UNIVERSITY OF COPENHAGEN
NIELS BOHR INSTITUTE

Polymer Melt Relaxation Following Fast Uniaxial Extension Probed with X-ray and Neutron Scattering Techniques

PhD thesis

Anine Laura Borger

Principal Supervisor:
Kell Mortensen
Niels Bohr Institute
University of Copenhagen

Co-supervisors:
Jacob J. K. Kirkensgaard
Qian Huang
Ole Hassager
Nicolas J. Alvarez

Submitted: April 3rd, 2019

Preface

The research presented in this thesis was carried out in the X-ray and Neutron Science section (XNS) of the Niels Bohr Institute (NBI) at the University of Copenhagen from the 1st of April 2016 to the 31st of March 2019 under supervision of Professor Kell Mortensen from XNS at NBI and co-supervision of Associate Professor Jacob Kirkensgaard from XNS NBI, Professor Ole Hassager and Researcher Qian Huang from the Danish Polymer Center at the Technical University of Denmark, and Assistant Professor Nicolas Alvarez from Drexel University, Philadelphia, USA.

The research presented in the thesis combines extensional rheology and scattering techniques to deepen our understanding of the relaxation processes in polymer melts exposed to fast uniaxial extensional flow and of how they depend on molecular architecture and molecular size distributions, which is interesting both from a fundamental scientific point of view but also related to application where the choice of processing conditions strongly depend on the relaxation of the melt.

Abstract

Understanding how the molecular conformation of polymer molecules change with uniaxial extension, relaxation, and molecular architecture as well as blend dispersity is relevant both from an application and fundamental science point of view: appropriate processing conditions depend strongly on the molecular conformation and detailed information about molecular conformations may provide tests for polymer models and theories for the molecular interactions in the melt. In this thesis we show three examples of how the combination of controlled non-linear uniaxial extension and controlled relaxation following extension in combination with scattering techniques can provide deep insight to the conformation of polymer molecules during flow and relaxation.

We study the relaxation of a mono-disperse melt of relatively short, but entangled, linear polystyrene using small-angle neutron scattering and show that the recently published framework of spherical harmonics expansion is sensitive enough to chain length changes during relaxation to resolve chain retraction as proposed by Doi and Edwards even for short molecules. We also study the relaxation of local orientation probed by wide-angle X-ray scattering in a bi-disperse polystyrene melt relative to that in the pure melt of the short component and find that the local orientation in the blend is larger and that the local orientation relaxes as a power law with the same exponent in both melts. Finally, we study end-deuterated three-armed polystyrene stars in small-angle neutron scattering to test the hypothesis that branched polymers take a quasi-linear molecular conformation during fast extensional flow and that the quasi-linear conformation last well into the relaxation. We find that at least the scattering patterns corresponding to short relaxation times are consistent with a quasi-linear conformation.

Resumé

En dybere forståelse af, hvordan polymeres molekylære konformation påvirkes af forlængelse, relaksation og molekylearkitektur såvel som af molekylemasse og dennes dispersitet, er vigtigt både fra et anvendelses- og et grundvidenskabeligt synspunkt: Passende processeringsparametre afhænger kraftigt af den molekylære konformation, og detaljeret information om denne kan bruges til at teste validiteten af modeller og teorier for polymerers molekylære vekselvirkninger i en smelte.

I denne afhandling demonstrerer vi gennem tre eksempler, hvorledes polymersystemer udsat for kontrolleret ikke-lineær forlængelse og efterfølgende relaksation, som dernæst undersøges ved hjælp af spredningsteknikker, kan give dyb indsigt i polymermolekylekonformation under strømning og relaksation.

Vi undersøger relaksationen af en monodispers smelte af relativt korte, men stadig sammenfiltrede, lineære polystyrenmolekyler i småvinkelneutronspredning og viser, at det nyligt udgivne dataanalyseværktøj baseret på udvikling i sfærisk harmoniske funktioner er følsomt nok for ændringer i kædelængde, selv for korte kæder, til at observere kædesammentrækning under relaksation som forudsagt af Doi og Edwards. Vi undersøger også, hvorledes den lokale orienteringsgrad relakserer ved at anvende vidvinkelrøntgenspredning på en bidispers polystyrensmelte og på en ren smelte af de korte kæder. Vi finder, at den lokale orienteringsgrad er højere i polymersmelten med både korte og lange kæder, og at graden af lokal orientering for begge smelter aftager som en potenssammenhæng med samme eksponent. Endelig studerer vi en smelte af endedeutererede trearmede stjerneformede polystyrenmolekyler ”mærket” med deuterium i enderne for at teste hypotesen, at de tager en kvasilineær molekylær konformation under hurtig forlængelsesstrømning, og at den kvasilineære konformation varer vel ind i relaksationen. Umiddelbart efter stræk finder vi, at neutronspredningsdata er konsistent med en kvasilineær molekylær konformation.

Acknowledgments

First and foremost I would like to thank my principal supervisor Kell Mortensen. Your advice, support, and help over the last three years has been invaluable to me. I would also like to thank my cosupervisors Jacob J.K. Kirkensgaard, Nicolas J. Alvarez, Ole Hassager, and Qian Huang for good support and advice during my PhD studies. I would like to thank all of you for your genuine interest both in my development as a scientist and my personal life.

This thesis is assessed by Daniel Read from the University of Leeds, Kristine Niss from Roskilde University, and Lars Øgendal from University of Copenhagen. Thank you for taking the time to evaluate my work.

The work has been funded by the Danish Council of Independent Research. The expenses related to scattering experiments were funded by DanScatt. The small angle neutron scattering data that was (re)analyzed as a part of this thesis work was obtained at Australia's Nuclear Science and Technology organization. Furthermore the Society of Rheology and the NNSP Soft-Bio network have funded presentations of parts of the thesis work at international conferences.

I have had the great pleasure of being part of three scientific environments: The X-ray and Neutron Science section (XNS) at the Niels Bohr Institute, Danish Polymer Center (DPC) at the Technical University of Denmark, and the Alvarez Group at Drexel University in Philadelphia. I would like to thank everyone who has been a part of XNS or DPC during the last three years or the Alvarez and Palmese lab during the summer 2017 for being wonderful colleagues and friends.

Thank you Cilie Hansen, Jonas Mathiassen, and Sofie Janas for prooofreading my thesis.

Finally I would like to thank my parents, family, and friends for their support - and patience - over the last three years. A great thanks to FysikRevy$^{\mathrm{TM}}$, Psykopatgangen at Studentergården, Kollektivet Havkikket, and my office buddy Viktor Holm. Last but definitely not least, thank you Jonas Mathiassen for your endless support.

Thesis Outline

The thesis consists of four chapters: Introduction, Wide Angle X-ray Scattering on Bi-disperse Polystyrene, Small Angle Neutron Scattering on End-labeled Three-Arm Stars, and Chain Retraction in Spherical Harmonics Expansion. Here I present the main findings of the chapters and specify my contributions to the work and who I collaborated with.

Chapter 1: Introduction

This chapter presents the research question of the thesis in the context of previous work combining extensional rheology and scattering techniques and provides the needed background knowledge on polymer physics and rheology, with emphasis on non-linear extension using the filament stretch rheometer (FSR), and scattering techniques. All three topics have many fascinating facets worthwhile to study and describe in detail. However, since many good introductions to the topics have been written already, I have decided to keep the chapter brief and focused on the content needed specifically for chapters 2-4.

Chapter 2: Wide Angle X-ray Scattering on Bi-disperse Polystyrene

This chapter presents our study on the relaxation following fast extensional flow of a bi-disperse polystyrene melt compared to the pure melt of short chains in wide angle x-ray scattering. It is known from a previous small-angle neutron scattering experiment that the short chains are stretched about 50 % more and remain stretched longer into the relaxation after flow in the blend with long chains, which was attributed to nematic effects, i.e. preferred alignment of neighboring molecules on Kuhn segment scale. Whereas the length scales probed by small angle neutron scattering scattering correspond to the overall size of the molecule, the length scales probed by wide angle x-ray scattering correspond to distances between neighboring monomers or Kuhn segments and may therefore serve as a test of the nematic interactions hypothesis. Furthermore, if a firm connection between the results obtained in small angle neutron scattering and wide-angle x-ray scattering can be established, it may be possible to continue the study of dispersity employing home source x-rays in stead of large scale facility neutrons. We quantify the local orientation by calculation of Hermans' orientation factor from the 2D WAXS patterns of FSR-filaments quenched at different relaxation times after fast extensional flow. We find a larger local orientation in the blend than in the pure melt and that the relaxation of the local orientation in both melts follow power laws with the same exponent suggesting that the relaxation of local orientation as measured by WAXS consists of several processes that are independent of chain length.

I have measured the WAXS-pattern for the samples and analyzed the data, partly in collaboration with our student Sidsel Lefmann. The interpretation of the results was done in collaboration with Kell Mortensen, Jacob Kirkensgaard, Ole Hassager, Qian Huang and Sara Wingstrand.

Chapter 3: Small-Angle Neutron Scattering on Three-Arm Stars

This chapter presents our work on the relaxation of an end-deuterated three-arm star following fast extensional flow. Previous experimental and theoretical work has suggested that in fast extensional flow, branched polymers behave like linear polymers because they take a quasi-linear molecular conformation. In this work we test the hypothesis by analyzing small angle neutron scattering patterns from a samples series of FSR-filaments of the end-deuterated star melt quenched immediately after cessation of the extensional flow and at different relaxation times. We find that the stars to some degree preserve their quasi-linear conformation at least up until a relaxation time of $t = 200$ s $\approx 0.5\tau_R$ where τ_R is the Rouse time of the star backbone.

The analysis and interpretation of the scattering pattern for the sample quenched immediately after cessation of flow and the scattering pattern for the fully relaxed star has been published in Mortensen et al. ”Structural Studies of Three-Arm Star Block Copolymers”.

I have calculated the RPA-structure factor, repeated the data analysis presented in the publication mentioned above and analyzed the remaining scattering patterns. The interpretation of the results was done in collaboration with Kell Mortensen, Ole Hassager, and Qian Huang.

Chapter 4: Chain Retraction in Spherical Harmonics Expansion

This chapter presents our work on studying chain retraction during polymer relaxation by expanding 2D small angle neutron scattering data in spherical harmonics, which has recently been proposed as a framework for analyzing 2D data for uniaxially extended polymer melts. We reach the conclusion that the spherical harmonics expansion is so sensitive to changes in the overall chain length that we see chain retraction for polystyrene chains of about six entanglement segments. I initiated the project, implemented the expansion framework, and analyzed the data. The quantitative comparison to the tube model predictions for chain retraction was done in collaboration with Ole Hassager, and the interpretation of the results was done in collaboration with Ole Hassager, Kell Mortensen, Qian Huang, Jacob Kirkensgaard, and Kristoffer Almdal.

Appendix 1: Small Angle X-ray Scattering on FSR filaments

This appendix contains preliminary work of small-angle X-ray scattering on filaments prepared on the filament stretch rheometer. The purpose of the project is to understand the origin of the often cross-shaped features at small q in the 2D scattering patterns from FSR-filaments first observed in small-angle neutron scattering. At first we thought it was due to surface cracks appearing during the fast quench procedure, later we have discussed whether it could be due to crazing or elongated bubbles in the stretched filaments. Currently, it is still an open question.

The work has been carried out in collaboration with Peter Jeppe Madsen, who prepared commercial polystyrene extracted with CO_2 and Wendi Wang who prepared the filaments specific for this project. The interpretation of the data was done in collaboration with Peter Jeppe Madsen, Wendi Wang, Ole Hassager, Qian Huang, and Kell Mortensen.

Appendix 2: Publications and manuscripts

This appendix contains a list of publications that I have contributed to during my PhD-studies and a list of future publications based on the work described in the thesis. Furthermore the appendix contains a reprint of the publication ”Structural Studies of Three-Arm Star Block Copolymers” by Mortensen et al. on the end-deuterated stars immediately after deformation and in the fully relaxed state and the draft manuscript for our coming publication on chain retraction seen in spherical harmonics expansion.

Contents

List of Figures

List of Tables

Chapter 1

Introduction

Polymer melts are viscoelastic and thus behave like solids on short time scales and simple fluids on longer timescales. The viscoelastic properties in polymer melts originate from their complex composition of macromolecules of varying size, size distribution and molecular architecture. Their mechanical response to external deformation is intimately linked with the molecular conformation in the melt, and the discipline of polymer melt rheology establishes the connection between external deformation and mechanical response and thus molecular conformation.

If we can establish the molecular conformation as a function of molecular parameters and external deformations, we may answer the fundamental question: How do polymer molecules interact in the melt? The behavior of polymer melts exposed to small deformations is well captured by the tube model, in which the motion of a single chain is modeled as if it moves in a tube instead of the complicated network of all the other chains. However, more experimental, theoretical, and numerical work is needed to understand polymer interactions under large deformations and during the following relaxation. In this thesis we expose polymer melts to uniaxial extension.

About fifteen years ago controlled extensional flow experiments on polymer melts able to go to large deformation, Hencky strains of at least five [1], were made possible with the filament stretch rheometer developed at the Technical University of Denmark[1] and the subsequent commercial version [2], which provide possibilities for new tests of polymer melt models and interaction theories. Bach et al. [1] measured the transient and steady state elongational viscosity of two monodisperse linear polystyrene melts, Nielsen et al. [3] for bidisperse polystyrene melts, and Nielsen et al. [4] for branched polymers. Experiments on stress relaxation are usually restricted to rather small strains due to progressive thinning of the sample leading to necking. The filament stretch rheometer can counteract the progressive thinning and thus allow for constant strain relaxation. Nielsen et al. [5] measured the stress relaxation of monodisperse linear polystyrene, Huang et al. [6] measured it for commercial low density polyethylene which is branched and polydisperse, and Huang et al. [7] measured the stress relaxation for very well defined branched polymers.

From the extensional viscosity and the stress relaxation, one can form hypotheses on the molecular conformation, e.g. [7, 8] and see whether the rheological response is consistent with a given model. However, these experiments are particularly powerful when combined with ex-situ scattering techniques that allow for an independent, and more direct, measurement of the molecular conformation. Hassager et al [9] studied the molecular stretching in polystyrene melts under fast elongation using the filament stretch rheometer and ex-situ small angle neutron scattering. They employed that deuterium scatters neutrons differently from hydrogen to label the center part of a fraction of the molecules. They found that the radius of gyration of the center labeled part parallel to the stretching direction scaled as a power law of the stretching rate showing that finite extensibillity of the chain does not affect the extensional stress behavior of linear polystyrene. In the papers Hengeller et al. [8] and Kirkensgaard et al. [10] the combination of filament stretch rheometer experiments and ex-situ small angle neutron scattering was used to study a bi-disperse polystyrene melt with a fraction of the short chains labeled using deuterium. They found that even though the stress in the melt was carried primarily by the long chains, the short chains were stretched more in the blend than in the pure melt and their relaxation was prolonged due to the presence of the long chains. The last example in particular is remarkable since it shows how scattering may provide information on molecular conformation that extensional rheology cannot for complex systems.

There is great potential in further experiments that combine filament stretch rheometry and ex-situ neutron scattering, e.g. on branched polymers to provide more data to test polymer melt models. It would also be interesting to see whether other ex-situ scattering techniques could provide new insights to the molecular conformation. In this thesis we demonstrate how wide angle X-ray scattering may supplement small angle neutron scattering in the studies of molecular conformation. We also show how the combination of filament stretch rheometry and small angle neutron scattering on well-defined branched polymers deuterated to provide information on the molecule ends reveal that branched polymers take a quasi-linear conformation during fast extensional flow and maintain that conformation into the relaxation. Finally we demonstrate how advanced analysis methods of small-angle neutron scattering data can lead to even more detailed information about the molecular conformation during extension and relaxation.

The remaining part of this chapter introduces basic concepts of polymer physics, a few polymer models, extensional rheology of polymer melts using the filament stretch rheometer, as well as concepts of small angle neutron and wide angle X-ray scattering techniques serving as a background for the next three chapters presenting our work.

1.1 Polymer Models

There are many good introductions to polymers and polymer molecules available. This section is based on two of them ”Polymer Physics” by Michael Rubinstein and Ralph Colby [11] and ”Introduction to Polymer Physics” by Masao Doi [12], and unless otherwise specified, these are the sources for the content presented here.

Polymers are macromolecules consisting of a large number N' of small repeated units, monomers, $N' > 100$ is required before a molecules is called a polymer[12] but N' may be much bigger, e. g. ultra high molecular weight polyethylene used in total joint replacements reach $N' \sim 200,000$ [13]. Polymer molecules can have different architectures such as linear, branched, or closed. In a linear molecule all monomers sit on the backbone of the molecule that has only two ends. A branched molecule on the other hand has branches growing from the backbone and may have many ends. In this thesis, we work with a specific type of branched polymers, namely stars where all the branches or arms grow from the same point, the branch point. In a closed architecture there are no free ends, where the simplest example is a ring. Polymers can be made up by only one type of monomers, a homopolymer, or two or more types, copolymers. Copolymers can have different sequences of the different types of monomers. In this thesis, we work with block copolymers of two different monomer types where the molecule consists of blocks containing only type A and blocks containing only type B. We use hydrogenous and deuterated styrene to form block copolymers.

Amorphous polymers have two states: The glass and the melt. In the glass at lower temperatures, the chains are frozen in, and in the melt, at higher temperatures, the molecules are free to move. The transition between the melt and the glass state occurs at the glass transition temperature T_g. The rheological properties of polymer melts, which we define below, depend on the size of the polymer molecules, i.e. the number of monomers and thus degree of polymerization N'. For scientific studies, we often desire a monodisperse melt where all chains have the same size. However, in a synthesized ensemble of molecules there will be a, potentially small, spread in molecule size, or molar mass M. The molar mass distribution is often characterized by two numbers, the number-average molar mass M_n and the weight-average molar mass M_w:

$$M_n = \sum_{N'} n_{N'} M_{N'} \tag{1.1}$$

$$M_w = \frac{\sum_{N'} n_{N'} M_{N'}^2}{\sum_{N'} n_{N'} M_{N'}} \tag{1.2}$$

where $n_{N'}$ is the number fraction of molecules with degree of polymerization N and M_N' is the molar mass of molecules with degree of polymerization N'. For a fully mono-disperse melt $M_n = M_w$. To characterize the deviation from monodispersity, the polydispersity, the polydispersity index PDI $= \frac{M_w}{M_n}$ is often used.

Not only do we need a statistical description when we characterize a melt, or ensemble of polymer molecules, but also when we characterize a single molecule due to the large number of monomers. In the next subsection we present a model for a single, ideal, polymer molecule.

1.1.1 Ideal Chain

The basic assumption in the description of an ideal chain is that monomers that are far apart along the backbone of the chain do not interact even if they are in close proximity to each other.

To characterize the ensemble of molecular conformations of the ideal chain, we could consider the end-to-end vector, $\vec{R}$. If we define the bond vector $\vec{r}_i$ as the vector pointing from monomer n_{i-1} to n_i, the end-to-end vector is simply

$$\vec{R} = \sum_{i=1}^{N'} \vec{r}_i. \tag{1.3}$$

Now the ensemble average, either over all molecules in a melt or all possible configurations of a single chain, of the end-to-end vector $\langle \vec{R} \rangle = 0$ since $\vec{R}'$ is as likely as $-\vec{R}'$. We therefore consider the mean-square end-to-end distance $\langle R^2 \rangle$ instead

$$\langle R^2 \rangle = \sum_{i=1}^{N'} \sum_{j=1}^{N'} \langle \vec{r}_i \cdot \vec{r}_j \rangle. \tag{1.4}$$

For a freely jointed chain where there are no correlations between the direction of different bond vectors each of length l, we find

$$\langle R^2 \rangle_{\text{Freely joint}} = N' l^2. \tag{1.5}$$

However, if we allow for correlations between monomers close to each other along the chain, one can show that

$$\langle R^2 \rangle \simeq C_\infty N' l^2. \tag{1.6}$$

where C_∞ is Flory's characteristic ratio that tends to be larger for polymers with bulky side groups such as polystyrene, which means that they are stiffer. Polymers have many universal properties that are independent of the type of monomers from which they are form. We therefore define the equivalently freely joint chain with longer, effective bonds, or Kuhn segments, of length b. The equivalent freely joint chain is defined such that it has the same mean square average end-to-end vector $\langle R^2 \rangle$ and contour length R_{max} as the actual chain such that

$$\begin{aligned} \langle R^2 \rangle_{\text{equiv}} &= N b^2 \qquad (1.7) \\ R_{\text{max}} &= N b \qquad (1.8) \end{aligned}$$

where N is the number of Kuhn segments.

Provided that N is large enough, the statistical properties of the chain does not depend on the detail of the model. We therefore choose the Gaussian model since it is mathematically simplest. The Gaussian model assumes that the individual bond vector $\vec{r}$ possesses some flexibility and is Gaussian distributed

$$p(\vec{r}) = \left(\frac{3}{2\pi b^2} \right)^{\frac{3}{2}} \exp\left(\frac{3\vec{r}^2}{2b^2} \right). \tag{1.9}$$

In terms of position vectors of the segments, $\vec{R}_n$, we may express the probability distribution as

$$P(\{\vec{R}_n\}) = \left(\frac{3}{2\pi b^2}\right)^{\frac{3}{2}} \exp\left(\frac{3\vec{r}^2}{2b^2}\right). \tag{1.10}$$

Using this probability distribution we determine the pair correlation function $g(\vec{r})$ as

$$g(\vec{r}) = \frac{1}{N}\sum_{m=1}^{N}\sum_{n=1}^{N}\left\langle \delta\left(\vec{r} - \left(\vec{R}_m - \vec{R}_n\right)\right)\right\rangle. \tag{1.11}$$

The structure factor $S(\vec{q})$ is the Fourier transform of the pair correlation function

$$S(\vec{q}) = \int \mathrm{d}\vec{r} g(\vec{r}) e^{i\vec{q}\cdot\vec{r}} = \frac{1}{N}\sum_{m=1}^{N}\sum_{n=1}^{N}\left\langle \exp\left[i\vec{q}\cdot\left(\vec{R}_m - \vec{R}_n\right)\right]\right\rangle. \tag{1.12}$$

It is measurable with small angle scattering as we describe below. With Eq. 1.10 and substituting the sums in Eq. 1.12 with integrals, one can show that

$$\begin{aligned} S(\vec{q}) =& \frac{1}{N}\int_0^N \mathrm{d}m \int_0^N \mathrm{d}n \exp\left(-\frac{\vec{q}^2|n-m|b^2}{6}\right) \\ =& N\frac{2}{q^4R_g^4}\left(e^{-q^2R_g^2} + q^2R_g^2 - 1\right) \\ =& Nh(qR_g) \end{aligned} \tag{1.13}$$

where $h(qR_g)$ is the Debye function and R_g is the radius of gyration of the polymer. The radius of gyration is defined as

$$R_g^2 = \frac{1}{2N^2}\sum_{m=1}^{N}\sum_{n=1}^{N}\left\langle\left(\vec{R}_m - \vec{R}_n\right)^2\right\rangle. \tag{1.14}$$

The radius of gyration is a more convenient measure of the polymer size than the end-to-end vector since it is directly measurable in experiments as we show below and since it can also be defined for branched polymers. For a linear chain the radius of gyration is given by

$$R_g^{\text{linear}} = \sqrt{\frac{Nb^2}{6}}. \tag{1.15}$$

In the next two subsections we discuss polymer dynamics and present the Rouse model that describes short, unentangled, polymer melts and the tube model for entangled polymer melts.

1.1.2 Rouse Model

The Rouse model captures the dynamics of short polymer molecules. In the Rouse model, the chain is represented by N beads connected by springs. The beads only interact through the connecting springs. Each bead experiences a drag force proportional to its velocity with friction coefficient, ζ, as it moves through the melt. One can show that the position of the beads, taken to be a continuous variable in the bead number n, the monomer position vector $\vec{R}(n)$ will fulfill the partial differential equation

$$\frac{\partial \vec{R}(n,t)}{\partial t} = \frac{-1}{\zeta} \frac{\partial \vec{R}^2(n,t)}{\partial n^2} + \vec{\eta}(n,t) \tag{1.16}$$

where $\vec{\eta}(n,t)$ is a random force. With the boundary condition $\frac{\partial \vec{R}}{\partial n} = 0$, the differential equation can be expressed in terms of a Fourier series where the p'th component fulfills

$$\vec{X}_p(t) = \frac{1}{N} \int_0^N \mathrm{d}n \cos\left(\frac{p\pi n}{2N}\right) \vec{R}(n,t). \tag{1.17}$$

It can be shown that the auto correlation of these Fourier modes is

$$\langle \vec{X}_p(t) \vec{X}(0)_p \rangle \sim e^{t/\tau_p} \text{ for } p = 1, 2, \ldots \tag{1.18}$$

The longest of the characteristic times, $\tau_{p=1}$, can be shown to equal the rotational relaxation time and the time it takes the polymer molecule center of mass to diffuse a distance comparable to the size of the molecule. This characteristic time, is called the Rouse time

$$\tau_R \approx \frac{\zeta b^2 N^2}{k_B T} \tag{1.19}$$

where k_B is Boltzmann's constant and T is temperature.

1.1.3 Tube Model

In a polymer melt of chains, the motion of an individual chain is hindered by the other molecules especially in the lateral direction. It was proposed by de Gennes[14] to explain the rheological response of a polymer melt by considering the motion of a test chain moving in a three dimensional

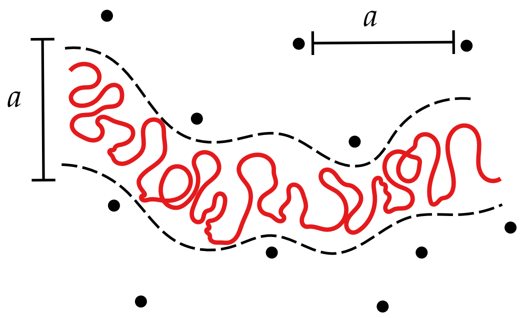

Figure 1.1: Tube model cartoon. In the tube picture, the motion of the polymer chain is described as if it takes place in a tube formed by the obstacles of the other chains.

network of obstacles that it cannot pass but move between in a snake-like motion, reptation. Doi and Edwards build on the tube concept of de Gennes in a series of papers describing the equilibrium state [15] and the non-equilibrium state [16] of polymer melts. The constitutive equation for times longer than the Rouse time, relating the stress in a given point to the local deformation in that point, is derived in Doi and Edwards [17]

In the tube model, the primitive chain is a freely joint chain, as described above, of step length a and arc length L. The averaged square end-to-end distance is in the tube picture Za and for the real chain, according to Eq. 1.7, Nb^2, which gives $Z = Nb^2/a$. The step length a is the characteristic spacing of the network of obstacles and the tube diameter. The steps in the freely joint chain is called entanglement segment and thus Z is also the number of entanglement segments. See Fig. 1.1 for a cartoon of a polymer melt in the tube picture.

Under rapid deformation, the tube is oriented and initially expanded. During relaxation, the initial expansion relaxes at a short time scale τ_R whereas the orientation relaxes on a longer time scale: the disentanglement or reptation time

$$\tau_d \approx \frac{\zeta b^4 N^4}{k_B T a^2}. \tag{1.20}$$

If $\tau_d \gg \tau_R$, the tube model predicts that the chain will retract during the initial $t \leq \tau_R$ relaxation. In Chap. 4 we test the chain retraction hypothesis.

GLaMM-model

Since the original work of de Gennes and Doi and Edwards, tube theory has been modified to include constraint release and contour length fluctuations due to discrepancies between the experimentally observed rheological behavior of polymer melts and that predicted by tube Doi-Edwards tube theory[18]. Constraint release is a modification to tube theory that takes into account that if one chain moves away from an entanglement, the lateral motion of the neighboring chain is also eased. In the linear regime, the motion of the chain is through reptation[18] and in the non-linear regime the chain motion releasing an entanglement could also be due to chain retraction[19]. Contour length fluctuations takes the fluctuations in chain length due to thermal fluctuations into account [20], which can also be seen as the inclusion of the higher order Rouse modes [21]. The GLaMM-model[18] is widely considered the state of the art tube theory [22]. It incorporates reptation, chain stretch, convective constraint release and contour length fluctuations in a microscopic stochastic partial differential equation, which describes the dynamics of polymer chains down to a length scale of the tube diameter.

1.2 Polymer Melt Rheology

Rheology is the science of general flow properties [23], and the aim of polymer melt rheology is to establish a relation between the flow deformation of a polymer melt and the stress induced in the melt. Polymer melts are viscoelastic due to complex microstructure of the macromolecules: Their chain lengths, architectures, and molecular weight dispersities, and their interactions, entanglements. Here we focus on extensional rheology.

For uniaxial extension we characterize the deformation by the stretch ratio λ and the Hencky strain ε

$$\lambda(t) = \frac{L(t)}{L_0} \tag{1.21}$$

$$\varepsilon(t) = \ln\left[\lambda(t)\right] \tag{1.22}$$

where $L(t)$ is sample length at time t and L_0 is the initial sample length. True stress, σ, is force per area which for a cylindrical sample gives

$$\sigma(t) = \frac{F(t)}{\pi R(t)^2} \tag{1.23}$$

where F is the magnitude of the force and R is the sample radius.

There is not yet a full theory of viscoelastic materials but in the regime of small deformations, their behavior is captured by linear viscoelasticity. The following account for linear viscoelasticity is based on the lecture notes [24]. Consider a shear deformation of magnitude γ occurring at $t = t_0$ where the particles in the material are shifted by

$$\begin{aligned} \Delta x =& x(t) - x(t_0) = \gamma y(t_0) \\ \Delta y =& \Delta z = 0. \end{aligned} \tag{1.24}$$

The shear stress as a function of time is then given by

$$\sigma_{xy}(t) = G(t - t_0)\gamma(t, t_0) \tag{1.25}$$

where $G(t - t_0)$ is the relaxation modulus. If multiple subsequent deformations are applied, the shear stress is given by

$$\sigma_{xy}(t) = \int_{-\infty}^{t} \mathrm{d}t' G(t - t')\dot{\gamma}_{xy}(t') \tag{1.26}$$

where $\dot{\gamma}_{xy}(t')$ is the instantaneous deformation rate.

In an experiment with constant shear rate, the shear viscosity is defined as

$$\eta_{\text{shear}} = \frac{\sigma_{xy}(t)}{\dot{\gamma}_{xy}} = \int_{-\infty}^{t} \mathrm{d}t' G(t - t') \tag{1.27}$$

The linear shear viscosity and extensional viscosity are related through Trouton's ratio [9]

$$\eta_{\text{extension}} = 3\eta_{\text{shear}} \tag{1.28}$$

and that is used to calculate the Linear Viscoelastic Envelope (LVE) for uniaxial extension. Deviations from the LVE show that the extensional rheology is non-linear.

We expect to see linear extensional rheology for Hencky strain rates $\dot{\varepsilon} < 1/\tau_d$, non-linear extensional rheology with tube orientation for $1/\tau_R > \dot{\varepsilon} > 1/\tau_d$ and with chain stretching for $\dot{\varepsilon} > 1/\tau_R$. These conditions may also be expressed in terms of the dimensionless Weissenberg number $Wi_i = \dot{\varepsilon}\tau_i$ that relates the deformation rate with the characteristic time of the material's relaxation mode i[8, 9, 25].

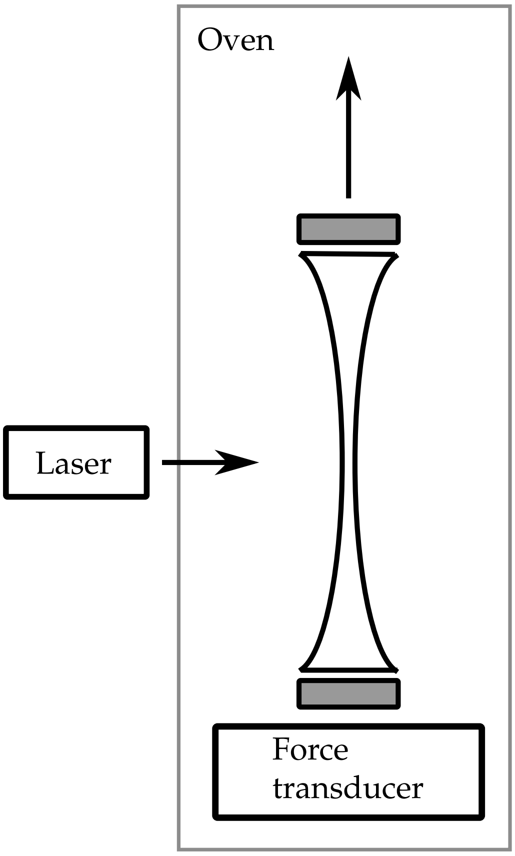

Figure 1.2: Schematic drawing of the filament stretch rheometer. The FSR consists of two plates, in gray, between which the filament is stretched, and a laser. The top plate is connected to a motor allowing for vertical motion, and the bottom plate in connected to a force transducer that measures the force. The filament diameter is measured from its shadow due to the laser. The filament and the plates are placed inside an oven to allow for experiments at elevated temperatures.

1.2.1 Filament Stretch Rheometer

In this thesis we use the Filament Stretch Rheometer (FSR) to create an extensional flow and measure the extensional rheology of polymer melts. The principle of the FSR and the experimental procedure is described in a number of publications, e.g. [1, 5, 4], and we base the following presentation of the instrument on those sources. Basically the FSR consists of two round plates, the top plate that is connected to a motor and the bottom plate connected to a force transducer, and a laser with which the diameter of the filament can be measured, see Fig. 1.2. The initial sample is disc-shaped with a diameter of approximately 8 mm and a height of about 2 mm. The sample is heated above T_g before the experiment starts.

If ideal extension could be obtained for the sample, the disc would be stretched to a cylinder, and the stretch ratio λ and Hencky strain ε would be defined relative to the full filament length as in Eq. 1.21 and 1.22. However ideal extension is not achievable for the entire sample do to the non-slip condition at the plates. For polystyrene, the stretched filaments have a shape similar to that in Fig. 1.2 where the center part of the filament is very close to a cylinder. Now in principle if we could keep track of the length change of this center part, we could still define λ as in Eq. 1.21. This however is still challenging so instead we use that polystyrene melt, and polymer melts in general, are to a good approximation incompressible, and so we measure the diameter $D(t)$ of the central part instead of its length. In this way

$$\lambda = \frac{D_0^2}{D(t)^2} \tag{1.29}$$

$$\varepsilon(t) = -2\ln\left(\frac{D(t)}{D_0}\right). \tag{1.30}$$

The implemented control scheme takes inputs from the diameter and force measurements and compute the next deformation step, i.e. the next movement of the top plate. In this way, it is possible to perform controlled stretching experiment, e. g. with fixed Hencky strain rate $\dot{\varepsilon}$ to a certain final Hencky strain ε_f, which is the procedure used in the work presented in this thesis.

Often the data is plotted in terms of the stress growth coefficient

$$\bar{\eta}^+ = \frac{\langle\sigma_{zz} - \sigma_{rr}\rangle_{\mathrm{corr}}}{\dot{\varepsilon}}. \tag{1.31}$$

The average difference between the axial and radial stress in the mid-filament plane for pure extension is obtained from a general force balance[26]. For large Hencky strains, a filament that is symmetric in the mid-filament plane and rotational symmetric, and negligible surface tension and inertia the average difference is given as

$$\langle\sigma_{zz} - \sigma_{rr}\rangle(t) = \frac{F(t) - \frac{1}{2}mg}{\pi R^2(t)}, \tag{1.32}$$

where $F(t)$ is the force measured by the force transducer, m is the mass of the filament, g is the gravitational acceleration, and $R(t)$ is the radius of the filament in the mid-filament plane.

At lower Hencky strains, the shear stress contributes due to the small initial ratio between length and ratio, or aspect ratio $\Lambda_0 = L_0/R_0$. The corrected average stress difference is [27]

$$\langle\sigma_{zz} - \sigma_{rr}\rangle(t) = \frac{F(t) - \frac{1}{2}mg}{\pi R^2(t)}\left(1 + \frac{D(t)/D_0 \cdot \exp\left(-\Lambda_0^{-3}\right)}{3\Lambda_0^2}\right) \tag{1.33}$$

To concentrate the stress in the mid-filament plane, the samples are often prestretched at a very low rate $\dot{\varepsilon} < 1/\tau_d$ to obtain a cylindrical center piece. The sample is annealed until no force is detected before the experiment is initiated [5].

Controlled Strain Relaxation

The control scheme is extended to perform constant strain relaxation experiments [5]. Due to the non-slip condition at the plates, the center part of the filament is elongated more than the parts closer to the end plates. For this reason, true stress relaxation of the center part is not measured simply by stopping the plate motion and collecting stress data since the parts of the filament with different elongations will relax differently. The different relaxation may even lead to flow and thinning of the center part. To counteract the thinning, the top plate is lowered at a suitable rate determined through the diameter measurements.

Quenching Samples for Ex-situ Scattering

We combine extensional rheology measured using the filament stretch rheometer with ex-situ scattering. To prepare samples for ex-situ scattering we utilize that polystyrene has a glass temperature of $T_g \sim 100°\text{C}$. The rheological measurement are carried out at temperatures above T_g, typically at $T \approx 130°$ C, and by rapidly cooling the filament at any point of the experiment, we may preserve the molecular conformation at that point for ex-situ scattering. It is reasonable to assume that the molecular conformation is preserved if that the rapid cooling, or quench, is fast enough compared to the molecular relaxation. We quench the filament by opening the oven and applying a soft flow of nitrogen to the filament. After opening the oven, the filament is cooled by 10 K/s [10], and so the filament is cooled below the glass transition in about 3 s. If the shortest characteristic relaxation time of the polymer molecules, i.e. the Rouse time τ_R, is much longer than the quench time, the molecular conformation is to good approximation preserved during quenching. If the amount of material permits, we often quench several filament for given experimental parameters to increase the sample volume for neutron scattering.

1.3 Scattering Techniques

In this thesis, we employ small angle neutron scattering and wide angle X-ray scattering to study the molecular conformation of polymer molecules.

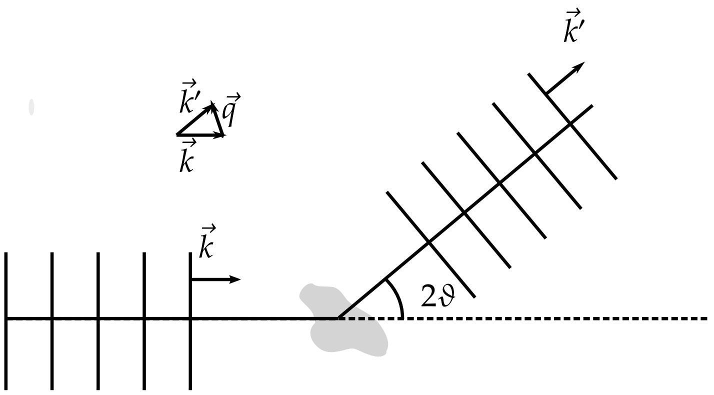

Figure 1.3: Scattering geometry. The incoming plane wave with wave vector $\vec{k}$ is scattered by the sample at the angle 2ϑ into a plane wave of wave vector $\vec{k}'$. The scattering vector $\vec{q}$ is defined as $\vec{q} = \vec{k}' - \vec{k}$.

There exist many good introductions to scattering techniques, see e.g. [28, 29] so here we provide only a brief overview of the most essential concepts that we use in Chap. 2, 3, and 4.

1.3.1 Scattering Geometry

The scattering geometry is illustrated in Fig. 1.3 were we see a incoming plane wave with wave vector $\vec{k}$ that hits the sample. Inside the sample the beam is scattered by multiple scatterers each of which emits a spherical wave. The emitted waves interfere and far from the sample the result of interference resembles an outgoing plane wave at an angle of 2ϑ[1] relative to the incoming beam with wave vector $\vec{k}'$. We call 2ϑ the scattering angle. If the scattering is elastic, which we assume throughout this thesis, energy and thus wave number, or wave vector length, is conserved $\left|\vec{k}\right| = \left|\vec{k}'\right| = \frac{2\pi}{\lambda}$, where λ is the wavelength of the incoming and outgoing plane wave[2]. It is convenient to express the scattered wave relative to the incoming wave in terms of the scattering vector $\vec{q}$. From the geometry in Fig. 1.3, we see that

---

[1] We choose the symbol ϑ for the scattering angle to avoid confusion with the polar angle in spherical coordinates in Chap. 4

[2] Note that we also use λ for the stretch ratio. The meaning of the symbol should be clear from the context.

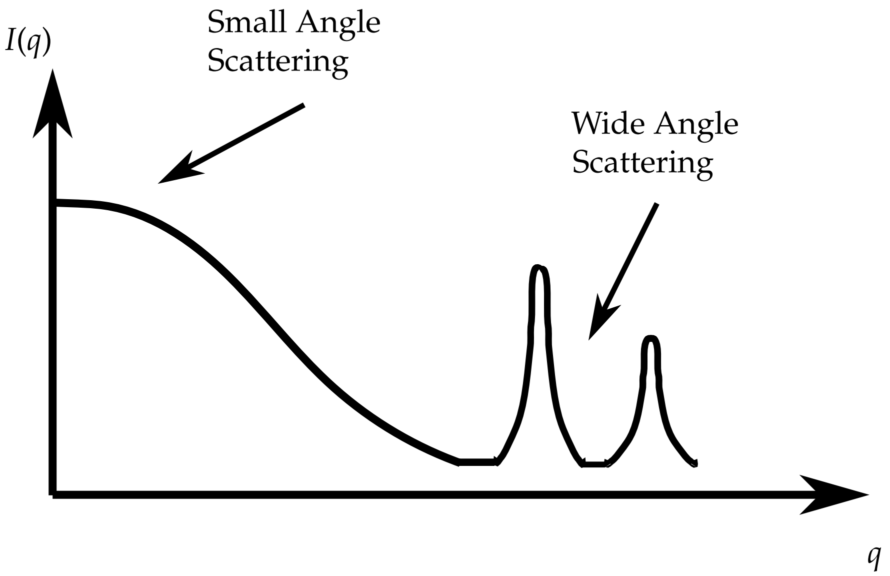

Figure 1.4: Scattering curve: Small and wide angle X-ray. The scattering intensity curve $I(q)$ at low q contain information about shapes and sizes of labeled polymer molecules, and high q data provide information about the internal structure.

$$\vec{q} = \vec{k}' - \vec{k} \tag{1.34}$$

$$q = \frac{4\pi}{\lambda} \sin \vartheta. \tag{1.35}$$

In Fig. 1.4 we show a generic scattering curve of a labeled polymer in the melt showing that the scattering intensity $I(q)$ at low q provide information of the large molecular scales whereas the scattering data at high q provide information of the small molecular scales.

In this thesis, we study polymer melts, which exposed to uniaxial extension in the FSR and subsequently quenched, in small angle neutron scattering and wide angle X-ray scattering. Small angle neutron scattering and wide angle X-ray scattering are the topics of the following sections.

1.3.2 Small Angle Neutron Scattering of Polymer Chains

In the small angle regime, the scattering intensity $I(q)$ from a polymer sample of a homogeneous mix of two types of monodisperse linear polymers with a relative scattering contrast, e. g. hydrogenous and deuterated polystyrene as we will work with later, is [22]

$$I(\vec{q}) = I(\vec{q})_{\text{coherent}} + I_{\text{incoherent}} \tag{1.36}$$

$$I(\vec{q})_{\text{coherent}} = (\Delta\rho)^2 \phi(1-\phi) n N^2 S(\vec{q}) \tag{1.37}$$

where $I(\vec{q})_{\text{coherent}}$ is the coherent scattering intensity that contain information about the molecular structure[29] and $I_{\text{incoherent}}$ is the incoherent scattering intensity that is a constant background. The coherent scattering intensity is proportional to the scattering length difference $\Delta\rho$ between the two polymer species in the sample, the fraction of the labeled species ϕ, the number density n, the number of monomers in the labeled species N, and the structure factor $S(\vec{q})$, which for an ideal Gaussian chain is given by Eq. 1.13.

Selective Deuteration

For the SANS experiments on polystyrene described in this thesis, the scattering contrast is provided by selective deuteration where hydrogen atoms are replaced by deuterium atoms in specific molecules or parts of molecules that one wishes to obtain information about. The coherent scattering length densities of hydrogenous polystyrene, $\rho_{\text{h-PS}}$, and deuterated polystyrene, $\rho_{\text{d-PS}}$, are

$$\rho_{\text{h-PS}} = 1.399 \cdot 10^{-6}\ \text{Å}^{-2} \tag{1.38}$$

$$\rho_{\text{d-PS}} = 2.544 \cdot 10^{-6}\ \text{Å}^{-2}. \tag{1.39}$$

The difference originates from the difference in coherent scattering lengths of hydrogen and deuterium: $b_{\text{coh, H}} = -3.741$, $b_{\text{coh, D}} = 6.671$. In Chap. 4 we use selective deuteration to label some chains in the melt. In Chap. 3 we use selective deuteration to label the ends of star polymers. In the latter case, the structure factor is no longer given by Eq. 1.13, and we therefore calculate the appropriate structure factor using the random phase approximation in Chap. 3.

Radius of Gyration

From small angle scattering experiments, the polymer radius of gyration can be extracted in a model independent way through Guinier analysis based on the low q limit, $qR_g \lesssim 1$, of the intensity

$$I(q) \approx e^{-\frac{1}{3}q^2 R_g^2}. \tag{1.40}$$

In practice however, the available q-range may not reach $qR_g \lesssim 1$ due to the large size of the polymer molecules and models such as Eq. 1.13 may be employed to extract R_g through fitting procedures.

1.3.3 Wide Angle X-ray Scattering

For larger values of q, the internal structure of the molecule appear in the scattering intensity. Characteristic distances , d, in the molecule or between molecules will appear as peaks in the scattering intensity $I(q)$ for certain q-values, q^*. The characteristic distance d that cause a peak in $I(q)$ at q^* can be determined as $d = \frac{2\pi}{q^*}$.

Scattering Contrast

X-rays interact with electrons and so there is no scattering contrast between hydrogenous and deuterated polystyrene, but scattering contrast between polystyrene and air. We use wide angle X-ray scattering to study the alignment of Kuhn segments between neighboring polymer chains in Chap. 2. On this length scale, the scattering contrast is due to variations in the electron density in polystyrene. In App. A, we use small angle X-ray scattering to study the excess scattering at small q, and on that length scale, the scattering contrast originates from larger domains of air relative to domains of polystyrene.

Chapter 2

Wide-Angle X-ray Scattering on Bi-disperse Polystyrene

In this chapter we present our results on the relaxation of local orientation of a bi-disperse polystyrene melt after exposure to fast extensional flow measured using wide angle X-ray scattering (WAXS). The purpose of the study is two-fold: From a previous small angle neutron scattering (SANS) experiment[10] it was found that the short chains were stretched 50 % more in the presence of the long chains in the blend relative to the pure melt of short chains, and that the stretching relaxation was significantly prolonged in the blend. As a hypothesis, the increased stretching and prolonged relaxation was attributed to nematic interactions, i.e. orientational coupling between Kuhn segments on neighboring chains[10]. The SANS-study probed length scales on the order of the over all size of the molecule whereas wide angle X-ray scattering probes length scales on the order of the distance between neighboring molecules and may therefore provide direct insight into the nematic interaction hypothesis. Furthermore, if it is possible to establish a close connection between the results from sans and WAXS, future studies of bi-disperse melts may be carried out using WAXS in stead of SANS which would be beneficial since an X-ray home source may be used instead of large scale facility neutrons.

2.1 Introduction

Studying bi-disperse blends is, apart from being interesting on its own, a stepping stone towards understanding polydisperse blends. From an application point of view, understanding and being able to model the effects of polydispersity on rheological behavior and chain conformation is paramount since commercial polymers are often polydisperse and that affects their viscoelatic properties strongly[30]. It is also an interesting problem from a fundamental science point of view since the original Doi-Edwards tube model [16] describes the behavior of infinite chains and therefore inherently cannot capture the effect of molecular weight distributions. Polydisperse melts of arbitrary molecular weight distributions are very complex and therefore model systems such as bi-disperse melts composed of two molecule lengths each with a narrow molecular weight distribution are studied instead. In the following we focus on studies of the extensional rheology and local orientation in bi-disperse melts.

2.1.1 Extensional Rheology of Bi-disperse Blends

Wagner et al. [31] studied polystyrene blends of a short polydisperse component to which a small volume fraction of super high molecular weight polystyrene was added. They found that the degree of strain hardening in the blends would increase with increasing amounts of the super high molecular weight component. Later, Nielsen et al. [3] studied the steady state extensional viscosity of bi-disperse blends and found a maximum as function of applied strain rate which increased with decreasing amounts of the long chain component. Though that opposes the conclusion of Wagner et al, the discrepancy is most likely due to the large difference in long chain lengths between the two studies where the long chain in Wagner et al. has M_w = 3320 kg/mol and M_w = 15400 kg/mol while in the work of Nielsen et al. the long chain has M_w = 390 kg/mol. Auhl et al. [32] studied the onset of chain stretch of long chains when diluted by shorter chains using two blend series of isoprene. They found that the long chains stretch at lower Hencky strain values in the blend than in the pure melt of long chains, which they explain using the concepts of ″fat″ and ″thin″ tubes, where the ″fat tube″ is made up by entanglements with other long chains only and the ″thin tube″ is made up by entanglements with both long and short chains. The constraint release rate, where some of the constraining chains move away, is larger for entanglements with short chains. In the situation where the strain is low enough that the thin tube has time to equilibrate to the long tube, the relevant long chain stretch is in relation to the fat tube, which can relax through the motion of the chain along the thin tube.

2.1.2 Local Orientation and Nematic Interactions

The hypothesis from the neutron scattering study by Kirkensgaard et al. [10] was that the increased stretching and longer relaxation time of the short chains was due to nematic interactions with the very stretched long chains. Other studies of bi-disperse melts[30, 33, 34] have also seen prolonged relaxation of short chains in a blend with long chains, and we get back to those in the next subsection. In this subsection we define nematic interactions. According to Doi et al. [35] nematic interactions lead to two, related, order parameters:$S_{\alpha\beta}$ for the tube segments and $Q_{\alpha\beta}$ for the Kuhn segments. They show, under the assumption that the orientational order of the individual bond is small or that they chain is still in the Gaussian regime[36], that the two order parameters averaged over the whole chain will be related as

$$\bar{Q}_{\alpha\beta}(t) = \frac{1}{1-\epsilon}\bar{S}_{\alpha\beta}(t) \tag{2.1}$$

where $\bar{}$ denotes an average over the full chain by integration along the contour length and the parameter giving the strength of the nematic interactions $\epsilon > 0$ in the case of nematic interactions.

For a bidisperse melt they introduce order parameters for each species, short S and long L: $\bar{Q}^L_{\alpha\beta}$, $\bar{Q}^S_{\alpha\beta}$, $\bar{S}^L_{\alpha\beta}$, and $\bar{S}^S_{\alpha\beta}$. Doi et al. find that for a blend of volume fraction ϕ_L of long chains and ϕ_S of short chains the order parameters are related in the following way

$$\begin{aligned}\bar{Q}^S_{\alpha\beta}(t) =& \bar{S}^S_{\alpha\beta}(t) + \epsilon\left(\phi_L\bar{Q}^L_{\alpha\beta} + \phi_S\bar{Q}^S_{\alpha\beta}\right)\\ \bar{Q}^L_{\alpha\beta}(t) =& \bar{S}^L_{\alpha\beta}(t) + \epsilon\left(\phi_L\bar{Q}^L_{\alpha\beta} + \phi_S\bar{Q}^S_{\alpha\beta}\right)\\ \phi_L\bar{Q}^L_{\alpha\beta}(t) + \phi_S\bar{Q}^S_{\alpha\beta}(t) =& \frac{1}{1-\epsilon}\left(\phi_S\bar{S}^S_{\alpha\beta} + \phi_L\bar{S}^L_{\alpha\beta}\right).\end{aligned} \tag{2.2}$$

These predictions can be tested experimentally if the four order parameters can be measured.

Experimental Studies of Nematic Interactions

The predictions of Doi et al. described in the previous section was used to explain the findings of Kornfield et al.[30] who studied bidisperse blends of polyisoprene, where also the short component holds several entanglements, in relaxation after step shear strain using infrared dichroism and birefringence. Their samples are bidisperse blends with varying mixing ratios of short and long chains. For each mixing ratio, two samples are prepared one where only short chains are deuterated and one where only long chains are deuterated. Each sample has 10 vol-% deuterated polymers. With infrared dichroism they can measure the bond orientation in the labeled chains and with birefringence they can measure the bulk orientation. Their shear strain is within the linear viscoelastic regime. They clearly see that for blends with $\phi_L < 0.5$, the longest relaxation of the long component is shortened and that the relaxation of the short component increases significantly with increasing ϕ_L, and for $\phi_L < 0.5$ the increase is at least two orders of magnitude. They interpret the prolonged relaxation of the short component as a combination of anisotropy in the orientation of Rouse segments and nematic interactions. They show that if both the bulk orientation and the orientation of the short component can be obtained for long relaxation times where the pure melt of the short component would be fully relaxed, any residual orientation of the short component will be due to nematic interactions and proportional to the bulk orientation with the parameter ϵ as constant of proportionality.

Infrared dichroism was also used to study the orientation of the components in a bidisperse melt in uniaxial extension by Tassin et al.[33]. They studied polystyrene blends with two different lengths of the short components M_w =10 kg/mol and M_w =27 kg/mol and two different lengths of the long component M_w =163 kg/mol and M_w =1190 kg/mol with 15 wt-% short chains. The molded films that were stretch to $\lambda = 4$ at $T = 115°$ C just above $T_g = 108°$ C. In accordance with the findings of Kornfield et al. They found that the orientation of the long component, M_w =1190 kg/mol, is independent of the length of the short component, but that the orientation of the short component, M_w =10 kg/mol, depend on the length of the long chains. Furthermore they established a connection between the residual orientation of the short component and the orientation of the long chains and from that they establish that $\epsilon = 0.26 \pm 0.03$ for polystyrene, see Eq. 2.2.

Hayes et al. [34] combined infrared dichroism and SANS to establish a connection between the local orientation of the short chain relative to the long chain and the resulting SANS pattern for deuterated short chains. They also worked with polystyrene and three different chain lengths, one long and two short: M_w =1920 kg/mol, M_w =180 kg/mol, and M_w =17 kg/mol also molded to films each with 15 wt-% deuterated short chains and stretched to $\lambda = 4$ at $T = 115°$ C. They find that in the mixture of the long and middle-length chain the local orientation of the two chain types in the blend is initially almost the same, whereas the short chain is clearly less oriented even from the start of relaxation. They too find residual orientation of the short chains after the pure material would have relaxed.

2.1.3 Motivation for Studying the SiS and SiL samples

Based on the previous studies, experimental data for the stress relaxation following steady state of extensional flow was missing for bi-disperse melts which motivated the extensional rheology study[8] of the bi-disperse blend of 50-50 wt-% M_w = 95 kg/mol and M_w = 545 kg/mol polystyrene and the pure melt of M_w = 95 kg/mol polystyrene, which we refer to as the Short-in-Long (SiL) and Short-in-Short (SiS) samples respectively. The extensional rheology study was followed by a SANS study[10] that focused on the chain conformation of the short chains in the blend relative to the pure melt of short chains since the relaxation of the blend indicated that the long chains carried most of the stress, and it was therefore interesting to see if and how the short chains were affected by the presence of the long chains. The current WAXS study is aimed at studying nematic interactions in fast extensional flow because it might explain the observations from SANS. As we learned from the experiments and theory described above, this will show up as prolonged local orientation of the short chains.

The chapter is structured in the following way: As background for the WAXS study we first review the earlier work on the Short-in-Short and Short-in-Long samples and present the WAXS pattern of polystyrene, its relation to the molecular structure, and how it is affected by uniaxial deformation. Then we present our experimental procedure, WAXS data for the Short-in-Short and Short-in-Long samples and our analysis. In the two following sections we discuss our results and conclude on our work.

2.2 Prior Studies of the Short-in-Short and Short-in-Long Blends

The samples have previously been studied in SANS which resulted in [10]: ”Nematic effects and strain coupling in entangled polymer melts under strong flow” in Phys Rev E in 2016 by J. J. K. Kirkensgaard et al.. The SANS study builds on a rheological study published in [8]: ”Stress relaxation of bi-disperse polystyrene melt - Exploring the interactions between long and short chains in non-linear rheology” in Rheol. Acta in 2016 by L. Hengeller et al.. In this section we describe the samples in detail and review the findings of the previous studies relevant for the WAXS study.

	h-PS545	h-PS95	d-PS86	d-PS80
SiS, SANS (wt-%)		90		10
SiL, SANS (wt-%)	50	40	10	
SiS, Rheo (wt-%)		100		
SiL, Rheo (wt-%)	48.9	50.1		
M_w (kg/mol)	545	95.1	86.3	80
PDI	1.12	1.07	1.02	1.02
Z	41	7		
τ_R (s)	705	20.1		
τ_d (s)	23000*	169		

Table 2.1: Sample composition Short-in-Short and Short-in-Long. SiS(L) is short for Short-in-Short (Long) and SANS (Rheo) mark the samples for SANS (Rheology) experiments. The blend composition are given as weight percentage of the four components that are characterized by their weight averaged molecular weight M_w and their polydispersity index PDI. The letter h or d in the component names indicate whether the component is fully hydrogenous or deuterated. The characteristic times of the components are for $T = 130°$ C, well above the glass transition temperature $T_g \simeq 100°$ C. The reptation time of h-PS545, marked by a *, is taken as the terminal relaxation time of the blend found through multi-mode Maxwell spectrum analysis. The table combines Tab. 1 from Kirkensgaard et al. [10] and Tab 1 and 2 from Hengeller et al. [8].

2.2.1 Materials

The samples consist of two polystyrene blends that we refer to as Short-in-Short and Short-in-Long or SiS and SiL for short. For the extensional rheology study, the Short-in-Short sample was pure hydrogenous polystyrene of a molecular weight M_w = 95 kg/mol, and the Short-in-Long sample was a 50-50 wt-% mixture of the same M_w = 95 kg/mol polystyrene and a M_w = 545 kg/mol polystyrene. The latter is about a factor of six longer than the short component and the blend thus has a ratio of one long to six short chains. For the later neutron scattering experiments, 10 wt-% of the blends consisted of short, deuterated chains with a molecular weight close to that of the hydrogenous short chains. The detailed compositions of the blends are summarized in Tab. 2.1.

The molecular weights are chosen such that the Rouse and reptation times of the two components are well separated, and the short chain carries at least a couple of entanglements.

2.2.2 Non-linear Extensional Rheology Study

The rheological study focused on the relaxation of a bi-disperse melt that has reached steady state after being exposed to non-linear uniaxial extension. The blend and the components were characterized in linear rheology using small amplitude oscillatory shear and in non-linear uniaxial extensional rheology both during stretching and the following relaxation.

Linear Rheology

From the linear rheology investigate by small amplitude oscillatory shear, it was found that the long chains relax faster in the blend than in the pure melt as estimated following the approach in ref. [3].

Non-Linear Rheology

From the non-linear extensional rheology during stretching it was found that steady state is reached for the blend at Hencky strains $\varepsilon > 3$.

The relaxation following non-linear extension to steady state was studied for several deformation rates. Only for the lowest rate $\dot{\varepsilon} = 0.003$ s^{-1} at $T = 130°$ it is possible to stretch the pure long component. The relaxation after reaching a final Hencky strain of $\varepsilon_f = 3.5$ for the pure long and pure short melt and blend is shown in Fig. 2.1a. It is apparent that the stress in the pure long component is more than one order of magnitude larger than the stress in the pure short component and that the stress in the blend is only about a factor of two lower than the stress in the pure long component. If the stress decay curve for the pure long component is scaled to superimpose the stress decay curve of the blend, it is clear that the stress relaxation of the blend is dominated by the stress relaxation of the long component.

The relaxation of the short component and the blend was also studied after a more rapid deformation of $\dot{\varepsilon} = 0.1$ s^{-1} up to $\varepsilon_f = 3.5$, see Fig. 2.1b. From this figure three relaxation regimes of the blend were identified: Fast relaxation ranging approximately up to 20 s, dominates, the intermediate regime approximately 20-700 s, and the terminal regime from approximately 700 s. The fast regime is characterized by a steep slope and a "knee". The time 20 s corresponds to the Rouse time of the short component, so the relaxation in this regime is interpreted as relaxation of stretching of both components. In the intermediate regime, the short chains are expected to reptate while the long chains are still retracting. In the terminal regime the stress decay coefficient follow a power law, and it is expected that in this regime the short chains are essentially equilibrated

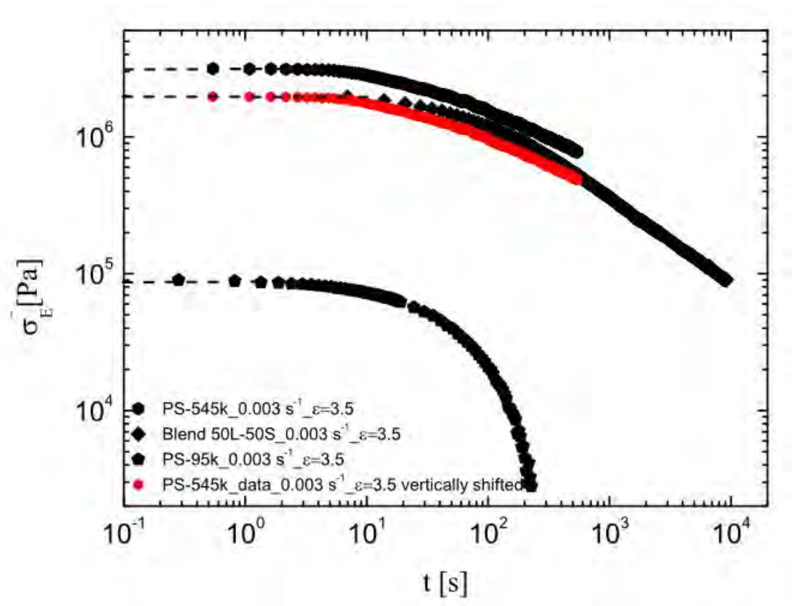

(a)

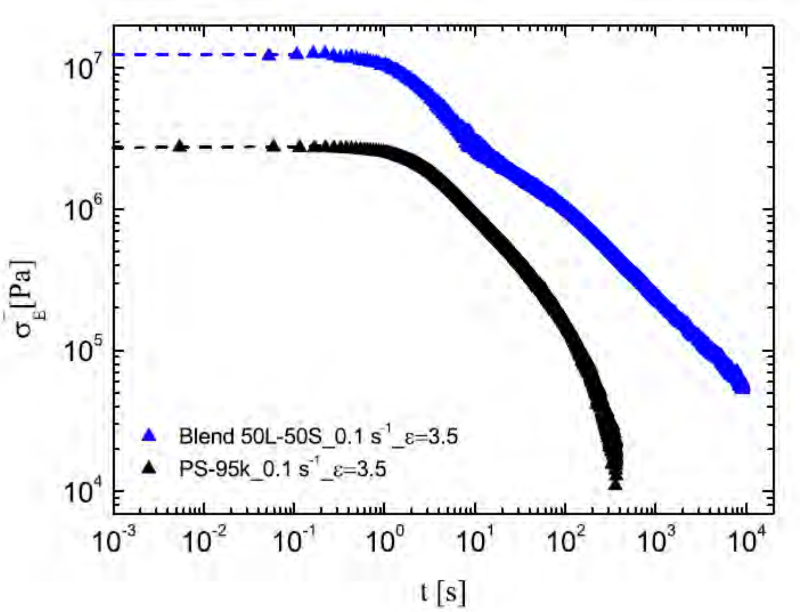

(b)

Figure 2.1: Extensional stress decay coefficient for the short and long components and the blend versus relaxation time. In a) the stress decay coefficient following a stretch of $\dot{\varepsilon} = 0.003\ \mathrm{s}^{-1}$ up to $\varepsilon_f = 3.5$ is plotted for the short and long components and the blend in black pentagons, hexagons, and rhombi respectively. The red hexagons are the data for the long component superimposed on the blend data. In b) The stress decay coefficient for the short component and the blend following a more rapid deformation of $\dot{\varepsilon} = 0.1\ \mathrm{s}^{-1}$ up to $\varepsilon_f = 3.5$ versus relaxation time. The figures are from [8]

while the long chains reptate. These observation raised the question: If the long chains carry the stress, what happens to the short chains? Are they in some way affected by the long chains, e.g. by an increased degree of stretching? And can we confirm the proposed relaxation mechanisms in the three regimes?

2.2.3 Small-Angle Neutron Scattering

The natural tool to answer these questions is small-angle neutron scattering where selective deuteration, see Sec. 1.3.2, can be used to highlight chain conformation of specific molecules, here we choose to focus on the short molecules. In the following we summarize the neutron scattering study by Kirkensgaard et al. with emphasis on the results that we will connect to the current WAXS study.

Quenched samples

For neutron scattering the samples were prepared as described in Sec. 1.2.1. Two sample series were prepared: a Hencky strain rate series and a relaxation time series. The sample series for varied Hencky strain rate contained SiS and SiL samples stretched with $\dot{\varepsilon} = 0.003, 0.03, 0.1\ \mathrm{s}^{-1}$. The rates are chosen such that they relate to the Rouse and reptation time of the short components as follows: $\dot{\varepsilon} = 0.003\ \mathrm{s}^{-1} < 1/\tau_d^S$, $1/\tau_d^S < \dot{\varepsilon} = 0.03\ \mathrm{s}^{-1} < \tau_R^S$, $\dot{\varepsilon} = 0.1\ \mathrm{s}^{-1} > \tau_R^S$. For the largest rate we thus expect the short chains to be oriented and stretched by the flow, for the intermediate rate we expect the chains to be oriented but not stretched, and for the lowest rate we expect the chains to remain in their equilibrium conformation. The samples for the relaxation time series are quenched immediately after stretching, after 10 s of relaxation, 20 s, 80 s, and 320 s for both samples, and 1260 s and 13000 s for the SiL samples. That corresponds to one sample for each material in the first relaxation regime, one on the border to the intermediate regime, two in the intermediate regime, and two samples in the terminal regime for the SiL-sample. All experiments were performed at $T = 130°$. For each neutron scattering sample a number of filaments were produced to increase the sample volume. Due to e.g. variations in filament diameter, some samples consisted of more filaments than others. The number of filaments per sample are listed in Tab. 2.2.

	SiS	SiL
$\dot{\varepsilon} = 0.003\text{s}^{-1}, t = 0$ s	1	4
$\dot{\varepsilon} = 0.03\text{s}^{-1}, t = 0$ s	2	7
$\dot{\varepsilon} = 0.1\text{s}^{-1}, t = 0$ s	6	9
$\dot{\varepsilon} = 0.1\text{s}^{-1}, t = 10\text{s}$	4	4
$\dot{\varepsilon} = 0.1\text{s}^{-1}, t = 20\text{s}$	4	9
$\dot{\varepsilon} = 0.1\text{s}^{-1}, t = 80\text{s}$	4	4
$\dot{\varepsilon} = 0.1\text{s}^{-1}, t = 320\text{s}$	3	4
$\dot{\varepsilon} = 0.1\text{s}^{-1}, t = 1260\text{s}$	-	4
$\dot{\varepsilon} = 0.1\text{s}^{-1}, t = 13000\text{s}$	-	1

Table 2.2: Number of filaments per SiS and SiL sample.

Experimental Settings and Data Correction

The SiS-samples were measured at QUOKKA at Australia's National Science and Technology Institute and the SiL-samples at SANS-1 at the Paul Scherrer Institute in Switzerland. At both instruments three overlapping settings were used to obtain a covered q-range of $0.005 - 0.25$ Å^{-1}. The data was corrected by adjusting detector efficiency using incoherent water scattering and subtracting a background sample consisting of non-deuterated polystyrene filaments[10]. The publication focused on the relaxation time series and the 5 m setting data sets were sufficient to cover the needed q-range. The other data sets are not yet published.

2D data

Kirkensgaard et al. plotted the corrected 2D data for the intermediate q-setting as iso-intensity curves, which is shown in Fig. 2.2 and 2.3 with 2D-fits described in the following section. The scattering patterns follow the general trends that the patterns corresponding to immediately after extension are most anisotropic, and as relaxation progresses, isotropy is regained. However the patterns for the SiL-samples remain anisotropic much further into the relaxation, visibly up to 80 s, compared to the SiS-samples. Also the anisotropy of the two samples look qualitatively different. For the SiL-samples the anisotropic scattering patterns have a clear lozenge shape whereas the scattering patterns for the SiS-sample look elliptical at least for $t \geq 10$ s.

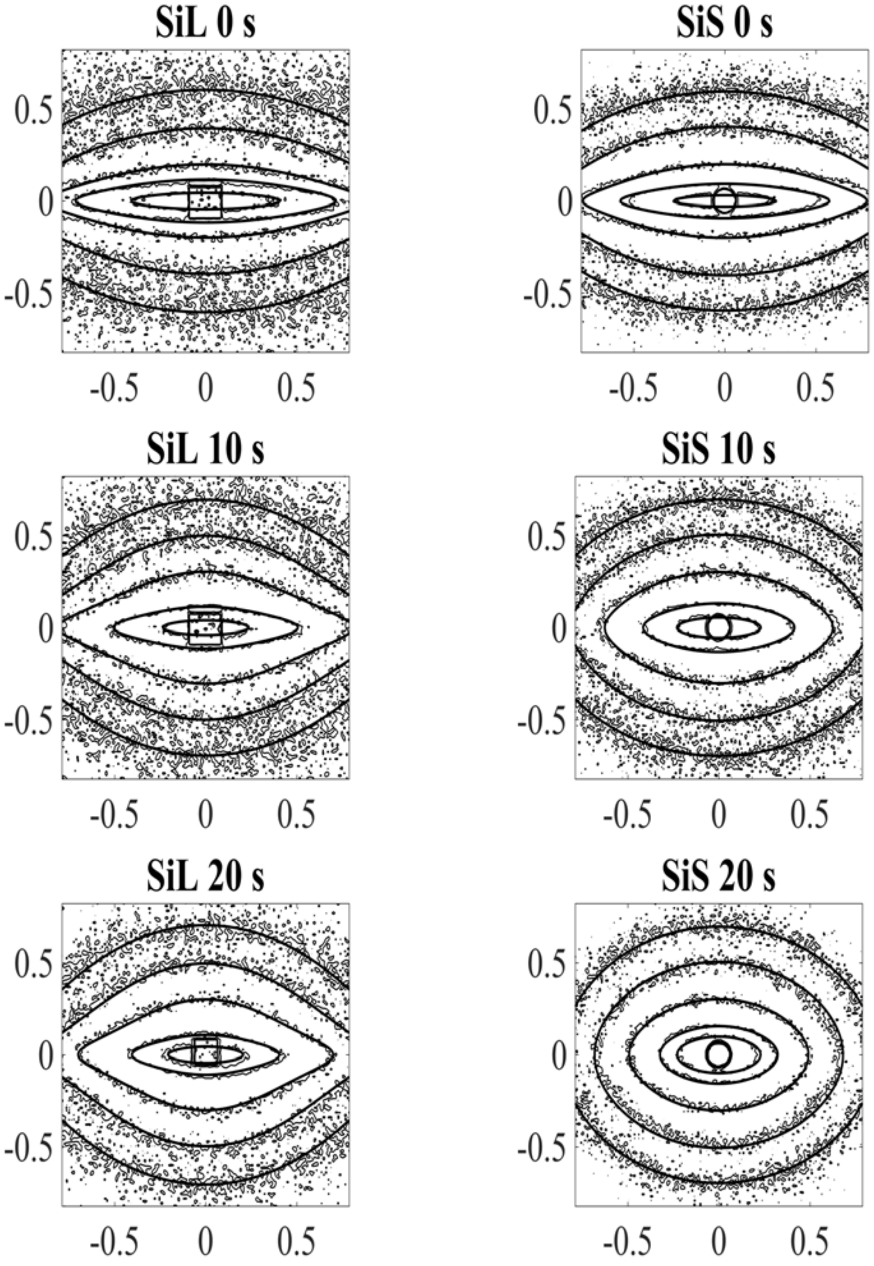

Figure 2.2: 2D SANS data for the Short in Short and Short in Long as a function of relaxation time. In the left column we present the data for the Short in Long sample and in the right column we present data for Short in Short. The Relaxation time increases from the top row to the bottom row. The units on the axes is nm^{-1}. The figure is from Kirkensgaard et al. [10].

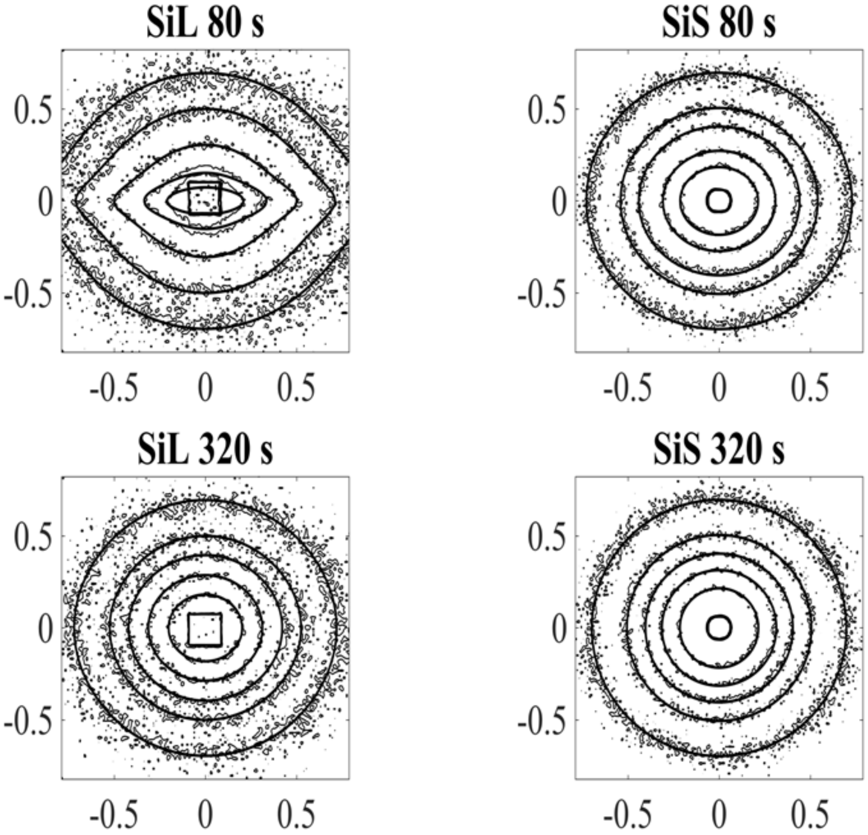

Figure 2.3: 2D SANS data for the Short in Short and Short in Long as a function of relaxation time. In the left column we present the data for the Short in Long sample and in the right column we present data for Short in Short. The Relaxation time increases from the top row to the bottom row. The units on the axes is nm^{-1}. The figures are from Kirkensgaard et al. [10].

Analysis

Kirkensgaard et al. fitted the data to the modified Warner-Edwards model with dangling ends [37] for the SiS and SiL samples respectively. The original Warner Edwards model derives the scattering pattern for a deformed polymer network containing some fully deuterated chains where the chains are confined to "tubes" of localizing potentials. The Warner-Edwards model was incapable of reproducing the Lozenge patterns in the scattering experiments by Straube et al.[38] who therefore modified the model phenomenologically by including deformed tube parameters. The potentially deformed tube parameters were included on the microscopic level in Read et al. [37] who also showed that the origin of the Lozenge patterns is that the outer parts of the chains can relax while the center remains confined in the tube described by the fraction of ”dangling ends” f. In this way, the tube diameter d in direction μ is given as $d_\mu = d_0\lambda_\mu^\nu$, where λ_μ is the strain in direction μ, and λ_μ^ν is the effective strain on the polymer tube. In ref. [37], fits to data from ref. [38] are performed with the value $\nu = 0$ corresponding to no deformation, and the value $\nu = 1/2$ that has been proposed for deformed tube potentials[39, 40].

Due to the much larger macroscopic stretch ratios applied in this study, the potential nematic interactions, and the extension to relaxation both the fraction of dangling ends and the coupling exponent ν was included as fitting parameters with constraints that the fraction of dangling ends, for the SiL samples, should increase monotonically during the relaxation, the tube diameter should tend towards isotropy $\nu = 0$, and the effective strain λ_z^ν felt by the short chains should decrease monotonically with relaxation[10].

The time evolution of the effective strain, λ_z^ν can be calculated from Tab. 2 in ref. [10]. The result is plotted in Fig. 2.4. It is evident that the short chain are stretched about a factor of 1.5 more in the presence of long chains than in the pure melt of short chains and that they remain stretched for quite some time longer reaching approximately the initial level of microscopic stretch ratio for the pure short material after 320 s of relaxation.

2.2.4 Nematic interactions hypothesis

The increased and prolonged stretching was explained by nematic interactions between the polymer chains meaning that the Kuhn segments of neighbouring chains prefer to align. Since the long chains are stretched by the flow, $Wi_R^L \sim 70 \gg 1$, the short chains will stretch more in the blend because they will prefer to align with their stretched surroundings. The WAXS study of the sample was initiated to test whether we could see this alignment on the Kuhn segment level. The section sets up the framework for answering this question by relating the scattering pattern of, stretched, polystyrene to its molecular structure and describing the mathematical description of segment alignment as measured by WAXS.

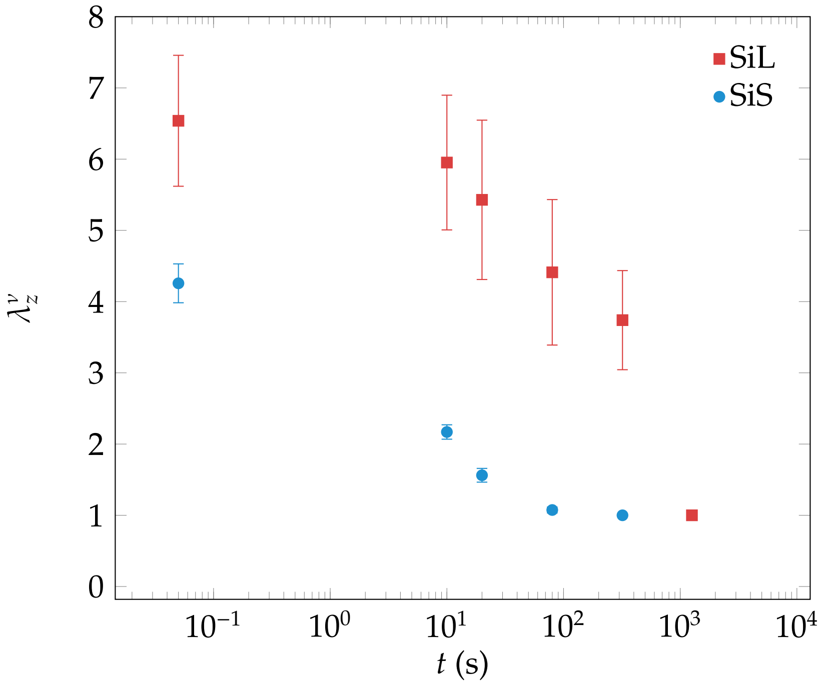

Figure 2.4: Relaxation of microscopic stretch ratio SiS and SiL. The microscopic stretch ratio λ_z^ν with errorbars as a function of relaxation time t_{rel} is calculated from Tab. 2 in ref. [10]. The upper red points correspond to SiL-data and the lower blue points correspond to SiS data. The data point at 0 s of relaxation is plotted at $t_{\text{rel}} = 0.05$ s.

2.3 Wide-Angle X-ray Scattering on Stretched Polystyrene

In the following section we will analyze the WAXS data for the samples above. In this section we describe the scattering pattern from polystyrene and discuss how it is affected by stretching. We also explain how orientation can be quantified from WAXS patterns for amorphous polymers. The knowledge about the origin of the scattering pattern and methods for quantifying the orientation is important to choose the right analysis method to test the nematic interaction hypothesis from the previous section with our WAXS measurements.

2.3.1 Scattering Pattern and Molecular Structure of Polystyrene

The scattering pattern of polystyrene in the $q = 0.2 - 2$ Å^{-1} range is characterized by two rings centered at approximately $q = 0.7$ Å^{-1} and $q = 1.3$ Å^{-1} corresponding to characteristic distances of approximately 9 Å and 5 Å. The scattering pattern of polystyrene is illustrated in the left panel of Fig. 2.5a. The right panel of the figure illustrates the effect on the scattering pattern when the sample is stretched, here along the vertical axis as illustrated by the filament cartoon in the middle of the figure. Stretching the sample causes the inner ring to split into two arcs and the outer ring has enhanced intensity parallel to the stretching direction and becomes visibly elliptical. In Fig. 2.5b we show 1D data to further illustrate the effect of stretching.

Early Experiments

That the WAXS pattern of polystyrene is affected by stretching has been known for almost a century. The origin of the X-ray scattering patterns of polymers, including polystyrene, was studied extensively by J. R. Katz from the late 1920s[41]. He compared the scattering patterns of polymers with those of about 400 non-polymerized liquids, e.g. the scattering pattern of polystyrene to that of liquid styrene. For some polymers, including polystyrene, he found that the scattering pattern of the polymer contains the same features as the scattering pattern from the monomeric liquid, the outer ring, with another ring added of corresponding to a larger distance, the inner ring for polystyrene. Due to this observation, Katz called the inner ring the polymerization ring. As he writes, the origin of this ring has been an unsolved question for a long time already in the 1930s, but the fact that the inner ring forms arcs upon stretching led to the conclusion that it corresponds to the distance between neighboring polymer molecules. To the best of our knowledge, the earliest experiment with stretching polystyrene was performed by M Hühnemörder 1927. She observed that upon stretching polystyrene heated above the glass transition temperature, T_g with 3000 to 4000 %, the inner ring was transformed into two arcs perpendicular to the stretching direction and that the outer rings turned elliptical, with the major axis parallel to the stretching direction and increased scattering intensity also parallel to the stretching direction[42] in agreement with our findings illustrated in Fig. 2.5.

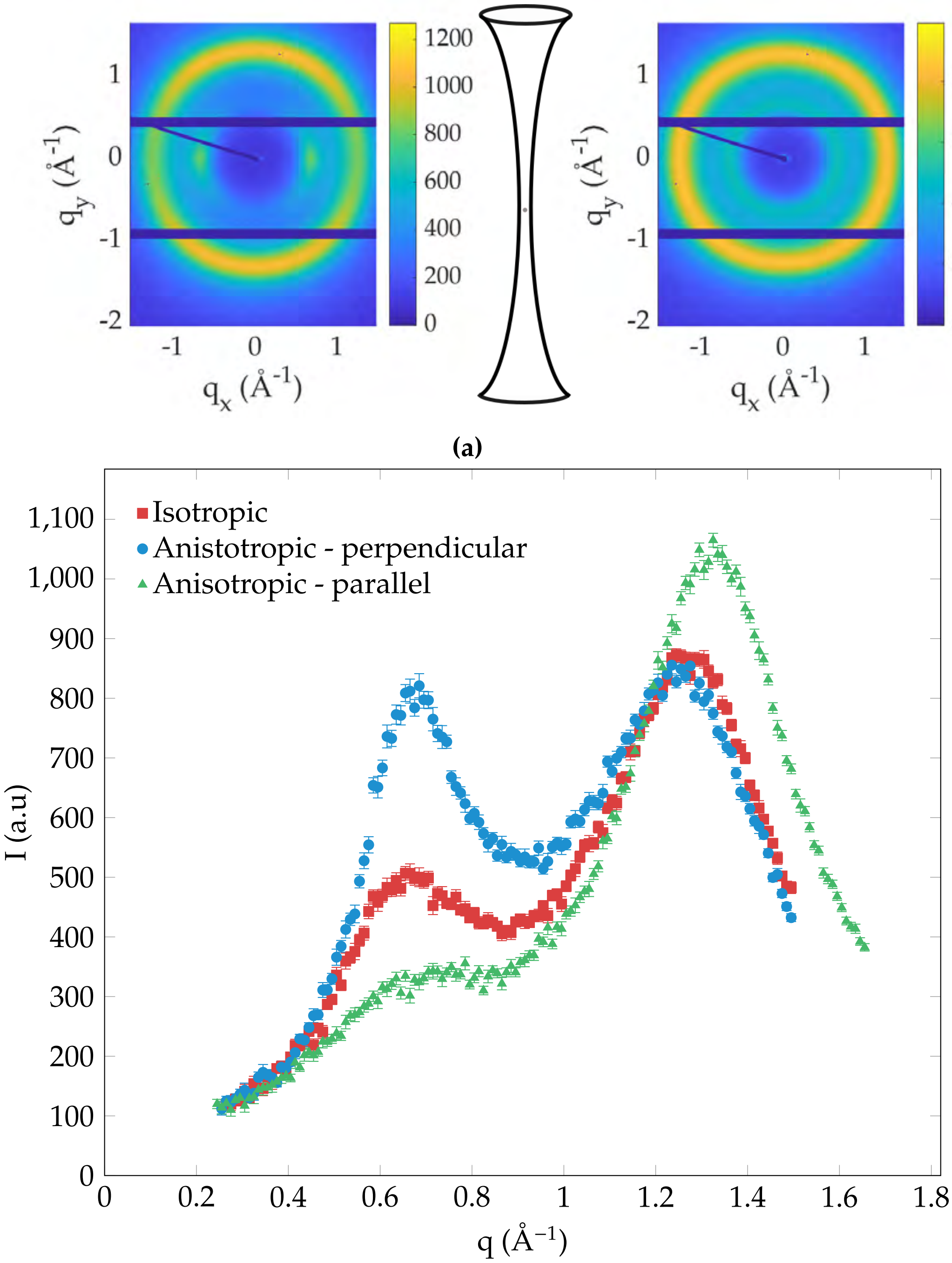

(a)

(b)

Figure 2.5: Scattering pattern from relaxed and stretched polystyrene. In a) the raw 2D patterns are shown for an isotropic sample, SiL 1260 s, and most anisotropic sample, SiL 0 s. The filament sketch illustrates the stretching direction and the tiny gray dot shows the X-ray beam hitting the filament. In b) we plot sector averages corresponding to (0.0 ± 2.5)° and (90.0 ± 2.5)° for the anisotropic and (90.0 ± 2.5)° for the isotropic samples.

Recent Molecular Dynamics Simulations

More recently the structure of polystyrene melts, i.e. the molecular conformations and molecules packing, has been investigated using Molecular Dynamics simulations e.g. [43, 44, 45]. The study by Ayyagari et al. ”Structure of Atactic Polystyrene: A Molecular Dynamics Simulation Study” in Macromolecules from 2000 [43] is especially interesting for establishing the connection between the molecular conformation and packing and their connection to the WAXS patterns of polystyrene. They perform a molecular dynamics simulation of atactic polystyrene and its dimer to investigate which inter- and intramolecular correlations that contribute to each of the rings in the WAXS pattern. As they write in the beginning of the paper, though polystyrene has been studied extensively over several decades, the origin of the ”polymerization” peak is not yet well understood. From their simulations of 16 chains containing 21 monomers each, Ayyagari et al. derive a scattering pattern that they find compares well to the experimental data from ref. [46], see Fig. 2.6a. Through their simulation they can also determine the correlations that contribute to each peak of the two most pronounced peaks in the scattering pattern at $q \approx 0.7$ Å^{-1} and $q \approx 1.3$ Å^{-1}, which we refer to as the inner and outer peak in the following. They conclude that the inner peak is dominated by backbone-backbone correlations between neighboring molecules and the outer peak dominated by phenyl-phenyl correlations, see Fig. 2.6b. They also find that the inner peak is present in the structure factor of the simulated dimers and so they question the validity of the polymerization peak” nomenclature.

In the following work we focus on the inner peak since backbone-backbone correlations are the most relevant for studying local orientation and thereby the potential nematic interactions.

2.3.2 Segment Orientation Distribution Function

Some of the first work quantifying the segment orientation in fibers was done by Hermans in the 1930s and 1940s through what is now known as Hermans’ orientation factor, and in the early 1940s Muller argued that Hermans’ orientation factor is the second moment of the orientation distribution function expanded in spherical harmonics functions of even order[47]. In this chapter we characterize the segment orientation in terms of Hermans’ orientation factor or the second moment of the distribution function only, but in Chap. 4, we characterize SANS patterns using spherical harmonics expansion to higher orders. As Winddle argues [48],

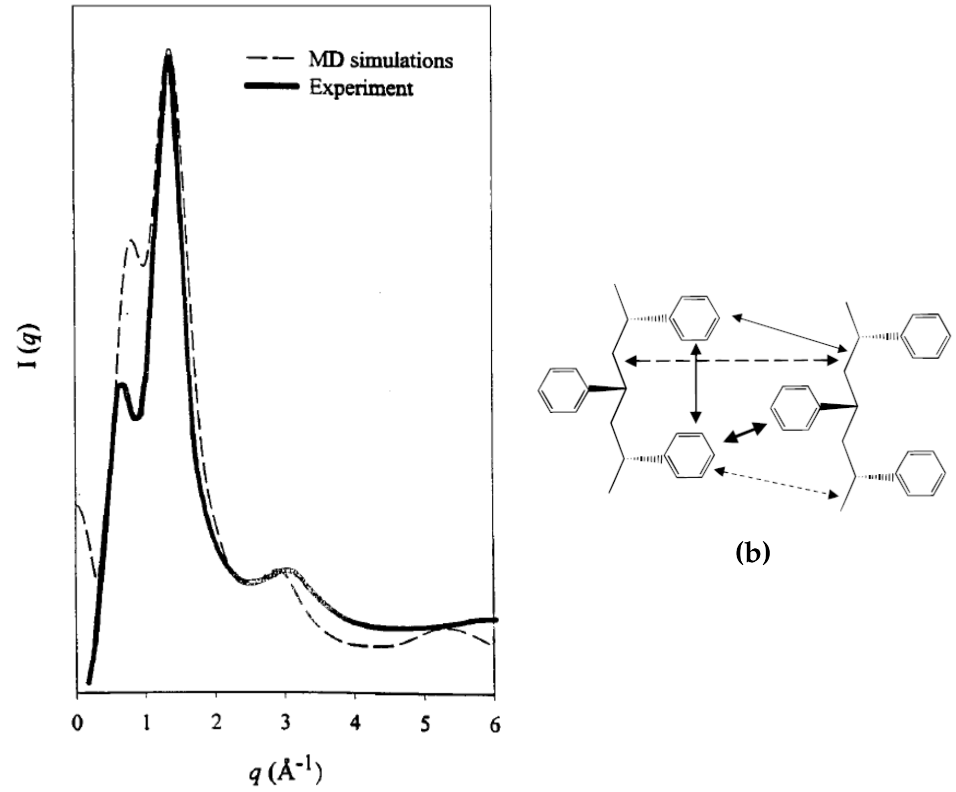

(a)

(b)

Figure 2.6: Results of MD simulation by Ayyagari et al. In a) the resulting scattering profile from the MD simulation is plotted with an experimental scattering profile from ref. [46] showing two pronounced peaks at small q, which are discussed in the following. In b) the inter- and intramolecular correlations are mapped to the peaks in the scattering pattern. Correlations marked with dashed arrows contribute to the inner peak at $q \approx 0.7$ Å^{-1}, and correlations marked with fully drawn arrows contribute to the outer peak at The arrow width represents the relative contributions. The figures are from Ayyagari et al. [43].

the orientation factor found through analysis of WAXS data not only provides information on semi-crystalline polymers with sharp peaks, but also for amorphous polymers with more diffuse and overlapping scattering peaks. Furthermore Winddle argues that information on chain packing of polystyrene can be obtained by studying the orientation of the inner ring as argued above. Pick et al. [49] argues that even though the diffuse scattering gives rise to challenges regarding background subtraction and a systematic underestimation of the orientation due to intrinsic disorder, WAXS has major advantages over other techniques that could be used because it is sensitive only to alignment and not e.g. side group rotation and there is no need for a specific model of the chain conformation to analyze the data.

We calculate Hermans' orientation factor or the second moment of the segmental distribution function relative to a chosen axis using

$$\begin{aligned} f(q^*) &= \frac{\sum_i I(q^*, \theta_i) P_2(\cos\theta_i) \sin\theta_i}{\sum_i I(q^*, \theta_i) \sin\theta_i} \\ P_2(\cos\theta) &= \frac{1}{2}\left(3\cos\theta^2 - 1\right) \end{aligned} \tag{2.3}$$

where $I(\theta_i)$ is the intensity at a given angle θ_i relative to the chosen axis for a specific q-value q^* or averaged over a specific q-range $q^* \pm \Delta q^*$. The two summations need identical limits and should cover an integer number of quadrants for Eq. 2.3 to be a meaningful quantity. In the following analysis we calculate the orientation relative to the filament axis, which we align vertically. If the scattering pattern is fully oriented parallel to the chosen axis, $f = 1$, if it is isotropic $f = 0$, and if it is fully oriented perpendicular to the chosen $f = \frac{-1}{2}$.

2.4 WAXS Analysis of SiS and SiL samples

In this section we described how we measured the samples in WAXS, reduced the data and extracted the second moment of the distribution functions. In the next section we compare our orientation factors with other studies that have looked at the orientation of stretched polystyrene in WAXS and the previous rheology and SANS study on the SiS and SiL samples.

2.4.1 Raw Data

2D data-patterns were measured on the SAXS-instrument at the Niels Bohr Institute. The wavelength is $\lambda = 1.54$Å and a sample-detector distance of 10 cm resulting in a maximal value of $q = 2.5$ Å. All filaments were measured in the mid-filament plane, see Fig. 2.5a. We plot one 2D data set for each sample, e. g. the 2D data for one out of nine filaments of SiL 0 s, in Fig. 2.7, 2.8, and 2.9. From Fig. 2.7 and 2.8, which show the 2D data for increasing relaxation time for the two materials, we see that SiL 0 s is the most oriented sample with clear ellipticity of the outer ring and the formation of arcs of increased intensity in both rings. The SiL-samples are more anisotropic, and for both materials the anisotropy decays rapidly with relaxation time. In Fig. 2.9 all filaments are quenched immediately after reaching a final Hencky strain $\varepsilon_f = 3$, but the Hencky strain rate $\dot{\varepsilon}$ varies. For all rates the SiL-filaments are more anisotropic than the corresponding SiS-filaments, and the degree of anisotropy decreases with decreasing rate.

2.4.2 Data Reduction and Analysis

The goal of the data analysis is to compute the degree of orientation using the second moment of the orientation distribution as presented in Sec. 2.3.2 and Eq. 2.3 with $I(q^*, \theta)$ corresponding to the inner ring as argued in Sec. 2.3.2. The goal of the data reduction is therefore to achieve $I(\theta)$ for the inner peak. A main obstacle is to estimate and subtract the background from the tail of the outer peak and other contributions such as thermal fluctuations. At first glance this seemed like a straight forward task, but it turned out to contain a number of challenges. Here we present the final data reduction procedure, but to argue why we made specific choices we also describe some earlier stages of the reduction and show their output. The first iteration of the reduction procedure relied on SAXSgui which is a Matlab based software package for data analysis provided by SAXSlab. In the later iterations we replaced many of the SAXSgui routines by our own which improved the outcome.

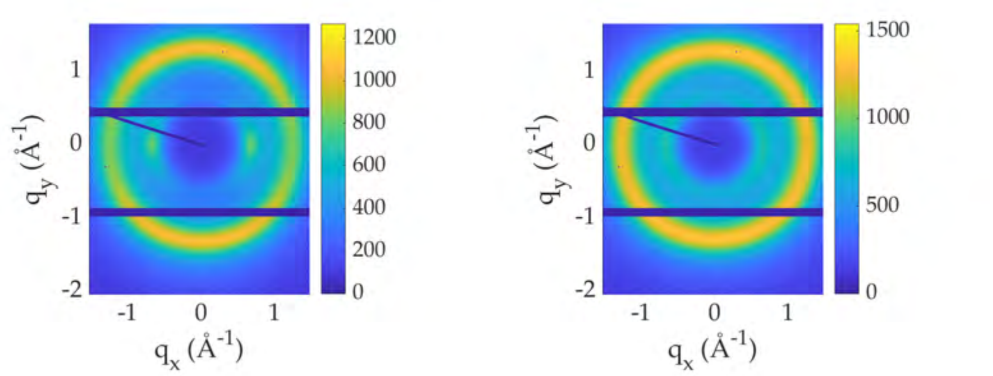

(a) SiL 0 s

(b) SiS 0 s

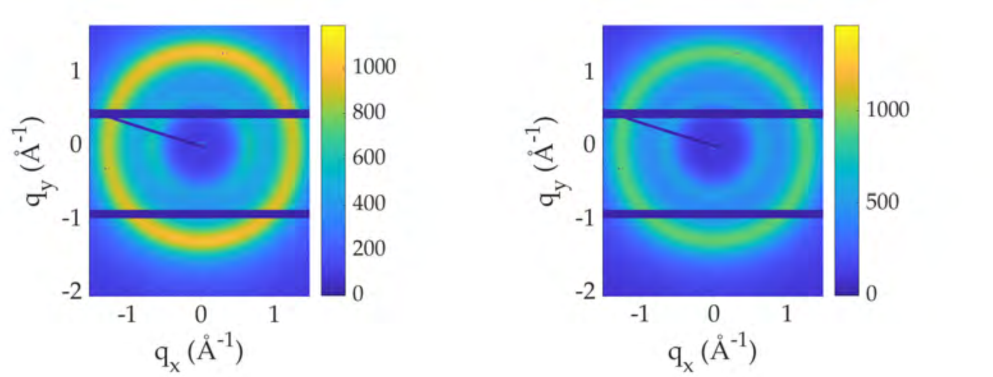

(c) SiL 10 s

(d) SiS 10 s

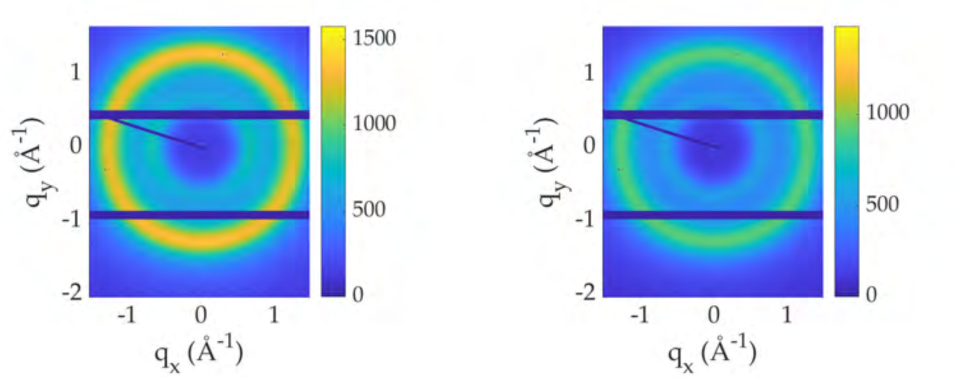

(e) SiL 20 s

(f) SiS 20 s

Figure 2.7: 2D WAXS data for SiL and SiS during relaxation 0 s to 20 s. Left panel is SiL-data and right panel is SiS-data.

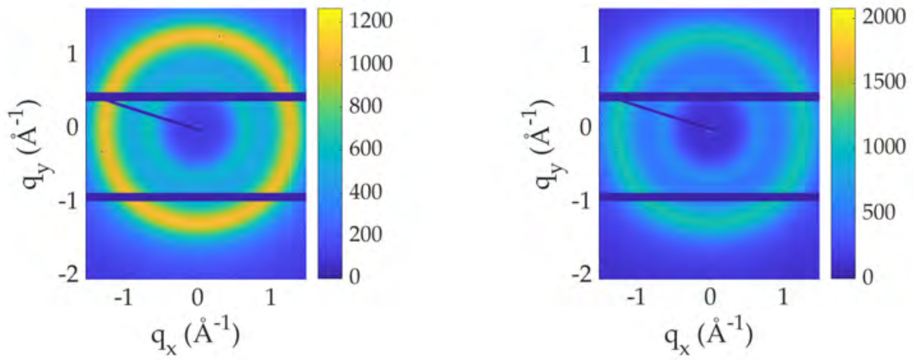

(a) SiL 80 s **(b)** SiS 80 s

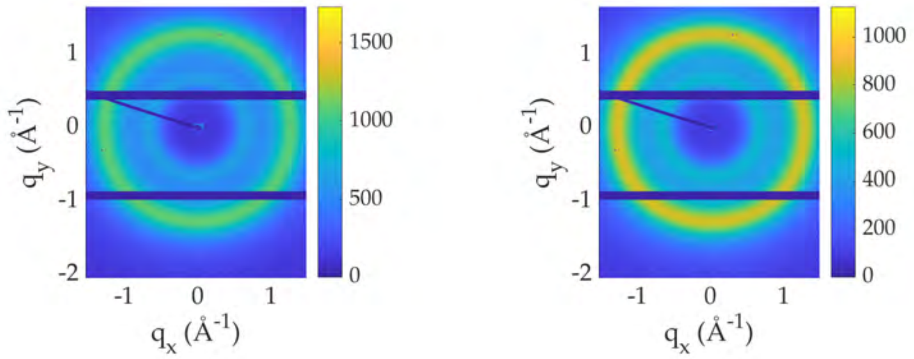

(c) SiL 320 s **(d)** SiS 320 s

Figure 2.8: 2D WAXS data for SiS and SiL during relaxation 80 s to 320 s. Left panel is SiL-data and right panel is SiS-data.

Reduction to $I(\theta)$ in SAXSgui

In our first approach we used SAXSgui for the full data reduction that consisted of finding the center of the detector image, q-calibration of the data set using silver behenate as standard, masking out the beamstop and the dead pixels, and reducing the 2D data $I(q, \theta)$ to two types of 1D data: $I(q)$ averaged for $\theta = \theta_0 \pm \Delta\theta$ and $I(\theta)$ averaged for $q = q_0 \pm \Delta q$. We call the first type of average a sector average and the second type a ring average.

At this point we measured only one filament of each sample assuming that the orientation is given to high precision based on the material and processing conditions. For each filament we performed a ring average without subtracting any background. We chose the summation range, $q = q_0 \pm \Delta q$, by using the in-built fitting routine to fit a Lorentzian on a sloped background to the inner peak of $I(q)$ averaged over the full

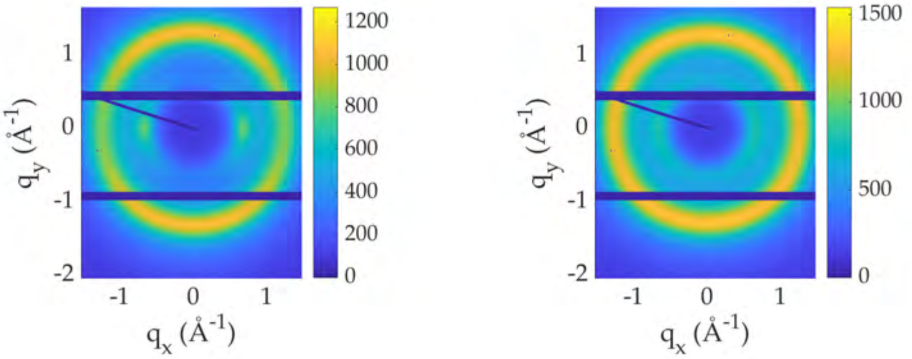

(a) SiL $\dot{\varepsilon} = 0.1\ \mathrm{s}^{-1}$ **(b)** SiS $\dot{\varepsilon} = 0.1\ \mathrm{s}^{-1}$

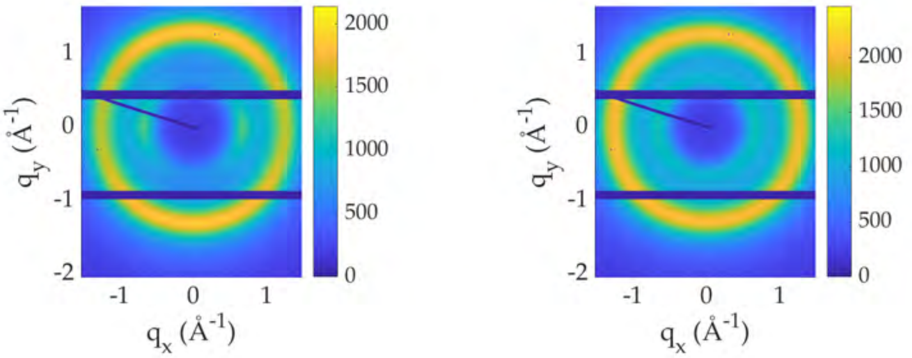

(c) SiL $\dot{\varepsilon} = 0.03\ \mathrm{s}^{-1}$ **(d)** SiS $\dot{\varepsilon} = 0.03\ \mathrm{s}^{-1}$

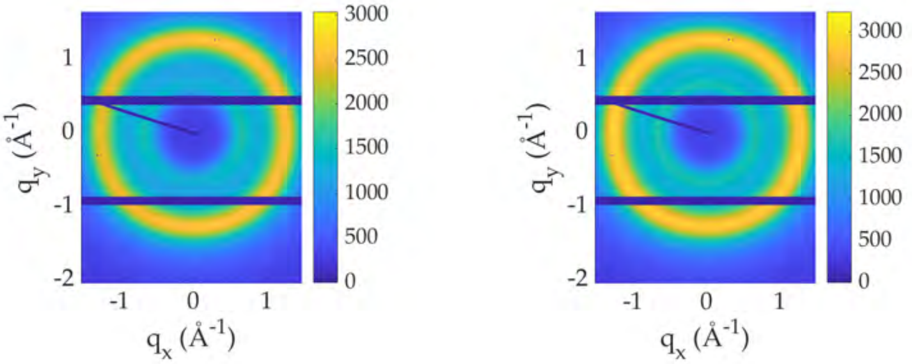

(e) SiL $\dot{\varepsilon} = 0.003\ \mathrm{s}^{-1}$ **(f)** SiS $\dot{\varepsilon} = 0.003\ \mathrm{s}^{-1}$

Figure 2.9: 2D data SiL and SiS for varying deformation rates. The left column is data for SiL and the right column is data for SiS. The Hencky strain rates are $\dot{\varepsilon} = 0.1\ \mathrm{s}^{-1} > 1/\tau_R^S$, $1/\tau_R^S > \dot{\varepsilon} = 0.03\ \mathrm{s}^{-1} > 1/\tau_d^S$, and $1/\tau_d^S > \dot{\varepsilon} = 0.003\ \mathrm{s}^{-1}$.

detector. The summation range of the ring average was then determined as $q^* \pm k\sigma_q$ were q^* is the center value and σ_q is the half width half maximum, HWHM. We chose several values of the factor $k = 0.25, 0.5, 1$ to investigate the effect of the width of the averaging window. The obtained $I(\theta)$ for SiL 0 s is plotted in Fig. 2.10a. It is evident that the data reduction is somehow flawed due to the non-smooth behavior at at $\theta \approx 50^\circ$, 70° and 310° corresponding well to the location of the beamstop, and the rows of missing pixels for read-out.

First Analysis of Reduced Data

The orientation factor was calculated using the data corresponding to 180°-270° and an approach very similar to that of Vancso et al. [50] who fitted their $I(\theta)$ found by peak-fitting, as described in the next section, to

$$y(\theta) = \sin(a\theta)^{2b} + k, \tag{2.4}$$

and used the integral version of Eq. 2.3 replacing $I(\theta_i)$ with the fit result $y(\theta)$ multiplied by a factor of -2 to correct for the fact that full orientation of the segments along the filament axis, i.e. full orientation of the scattering pattern perpendicular to the filament axis gives $f = -1/2$. The result of applying this method to our ring averaged data is plotted in Fig. 2.10b.

This first study showed that the initial degree of orientation differ for SiS and SiL. Comparing to the microscopic strain ratio from Fig. 2.4 the data for the SiS-samples qualitatively follow the same trend in the two plots whereas the SiL orientation from WAXS decays more rapidly than the microscopic strain ratio. However we knew that ignoring the background introduces a systematic error, and it was also unclear if the data points with very low degree of orientation did in fact have zero orientation within uncertainty. We therefore decided to measure all filaments for each sample in the mid-filament plane and to improve the data analysis by estimating and subtracting a background.

Our $I(\theta)$ Reduction Routine

We decided to estimate the background by fitting sector averages, $I(q)$ of the 2D data to a two-peak profile on a constant background. Then we could use the amplitude of the inner peak, A_1 as a function of θ to compute the orientation factor in this way removing the tail of the outer peak and the constant background. Even though SAXSgui has a batch mode, it is not capable of performing several sector averages on a single data in file in

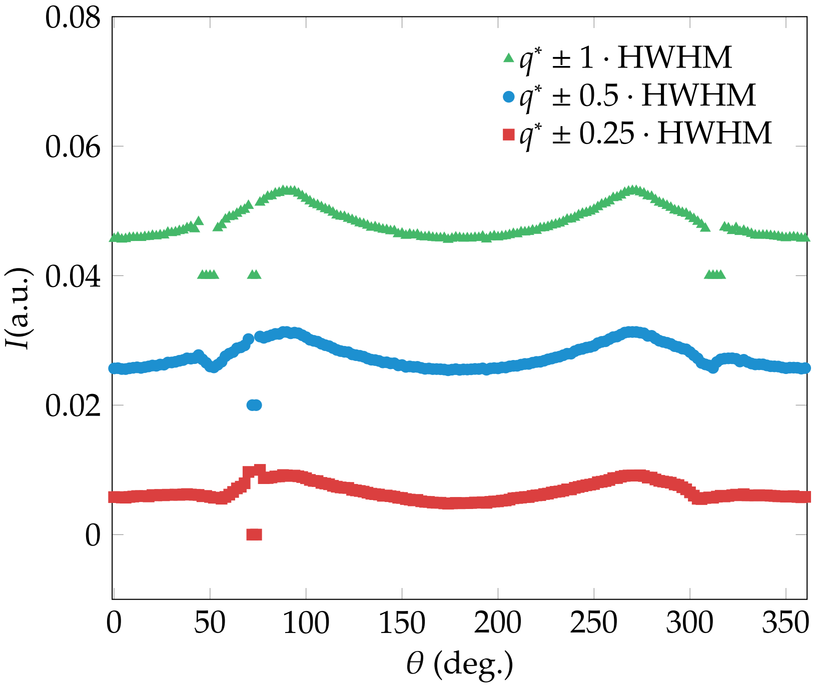

(a)

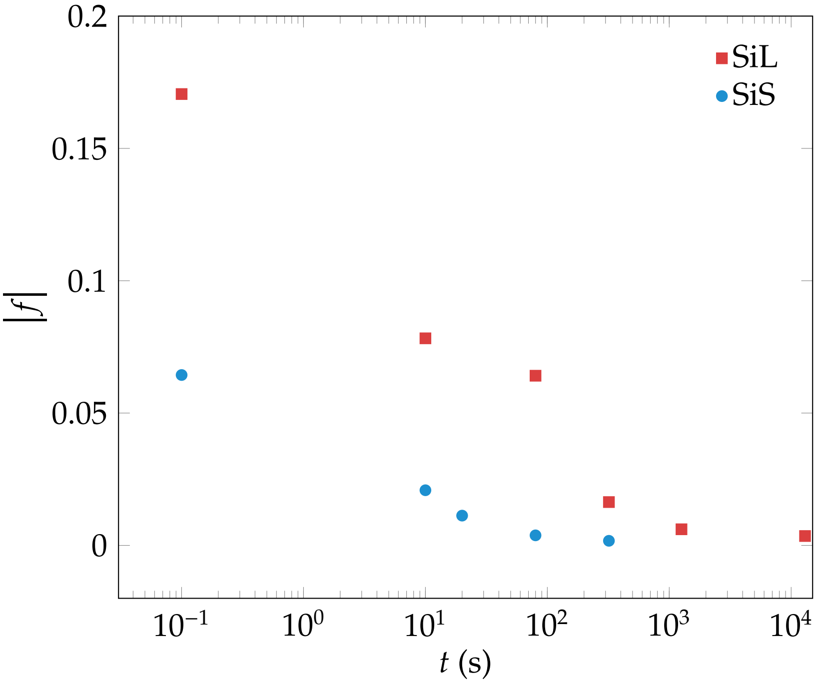

(b)

Figure 2.10: Data averaged in SAXSgui and resulting orientation factors. In a) data for SiL 0 s averaged in SAXSgui over the q-intervals specified by $q_1^* \pm k \cdot \mathrm{HWHM}$, where q_1^* is the coordinate of the peak center, k=1, 0.5, 0.25, and HWHM is the half width half maximum of a Lorentzian. Both q_1^* and HWHM are found using the fitting routine in SAXSgui for a Lorentzian peak on a sloped background. In b) the orientation factor for the time relaxation series of SiS and SiL using data averaged in SAXSgui over $q_1^* \pm 0.25 \cdot \mathrm{HWHM}$.

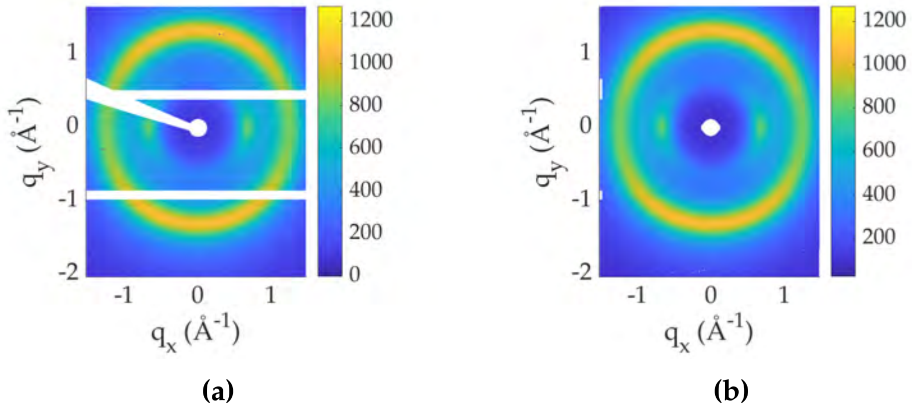

Figure 2.11: 2D data masked in a) and artificially filled in b) as described in the main text.

a batch mode sense, e.g. average the data in $360/\Delta\theta$ sectors of width $\Delta\theta$. Therefore performing sector averages of all data files in SAXSgui while potentially varying $\Delta\theta$ manually appeared as an inefficient approach with large probability of error, and so we put effort into the option of modifying the source code of SAXSgui, kindly provided by SAXSlab, to add the functionality or finding another readily made analysis software for the purpose, unfortunately without success. In the end we decided to write our own data reduction procedure using SAXSgui when convenient. In the next two subsubsection we describe our data reduction in two steps: Obtaining sector averages and obtaining $I(\theta)$ without background.

Sector Averages First we assign each pixel a q-value using silver behenate as a standard, the beam center read off through SAXSgui, and the size of each pixel and assign each pixel a θ-value relative to the vertical axis based on its position on the detector. We use the SAXSgui tool Maskmaker to make a mask to cover the dead pixels in the two stripes, the detector edge, the pixels covered by the beam stop and the few "dead" pixels on the detector, and apply the mask to our data. We then use fiber symmetry, i.e. that the scattering intensities in the four quadrants are related through a horizontal and a vertical mirror plane, to replace the masked out pixels by an average of the up to three pixels most closely related to it by fiber symmetry, see Fig. 2.11. After assigning a q- and θ-value to each pixel and filled the missing pixels after masking out data, we average the data in q and θ bins of width $2\Delta q$ and $2\Delta\theta$ respectively, where each pixel only counts in one bin based on the q and θ value of its center.

Background Estimation: Choice of Two-Peak Profile We decided to estimate the background by fitting a two-peak profile to each sector. Fitting both peak will allow us to subtract the tail of the outer peak from the inner peak. To account for the remaining background in a simple way, we decided to model it as a constant for each sector. Since we do not have theoretical knowledge of the peak profiles, we decided to work with simple models and therefore we restricted each peak to be modeled either as a Gaussian or as a Lorentzian thus excluding e.g. Voigt functions. The four potential two-peak profiles are then given as

$$\begin{aligned}
y_{\mathrm{GG}}(A_1, q_1^*, \sigma_1, A_2, q_2^*, \sigma_2, k) =& A_1 e^{-\frac{1}{2}(q-q_1^*)^2/\sigma_1^2} + A_2 e^{-\frac{1}{2}(q-q_2^*)^2/\sigma_2^2} + k \\
y_{\mathrm{GL}}(A_1, q_1^*, \sigma_1, A_2, q_2^*, \gamma_2, k) =& A_1 e^{-\frac{1}{2}(q-q_1^*)^2/\sigma_1^2} + A_2 \left(1 + \frac{(q-q_2^*)^2}{\gamma_2^2}\right)^{-1} + k \\
y_{\mathrm{LG}}(A_1, q_1^*, \gamma_1, A_2, q_2^*, \sigma_2, k) =& A_1 \left(1 + \frac{(q-q_1^*)^2}{\gamma_1^2}\right)^{-1} + A_2 e^{-\frac{1}{2}(q-q_2^*)^2/\sigma_2^2} + k \\
y_{\mathrm{LL}}(A_1, q_1^*, \gamma_1, A_2, q_2^*, \gamma_2, k) =& A_1 \left(1 + \frac{(q-q_1^*)^2}{\gamma_1^2}\right)^{-1} + A_2 \left(1 + \frac{(q-q_2^*)^2}{\gamma_2^2}\right)^{-1} + k
\end{aligned} \tag{2.5}$$

where the first capital letter G(L) means that the inner peak is modeled as a Gaussian (Lorentzian) and the second gives the model for the outer peak.

Some of the data files show a slight upturn at the smallest values of q. This could be included in the fit by assuming a more complicated model for the background, but to keep the model simple, we instead chose to only fit data for $q > 0.25$ Å^{-1}.

As a first attempt of choosing the most suitable two-peak profile, we fit the three sectors that we expect to be most extreme: A horizontal sector of the most oriented sample, a vertical sector of the most oriented sample, and a horizontal (or vertical) sector of the least oriented sample. The reason for this approach is the assumption that if a given two peak-profile fit these three sectors well, it should also fit all sectors in between well. The most oriented sample is SiL 0 s and we choose SiS 320 s as the least oriented sample. The resulting fits are shown in Fig. 2.12, 2.13 and, 2.14 and the χ^2-values of the fits are listed in Tab. 2.3. Overall, all four two-peak profiles describe the data reasonably well. However, closely inspecting the fits around the peak positions shown in the insets and taking the

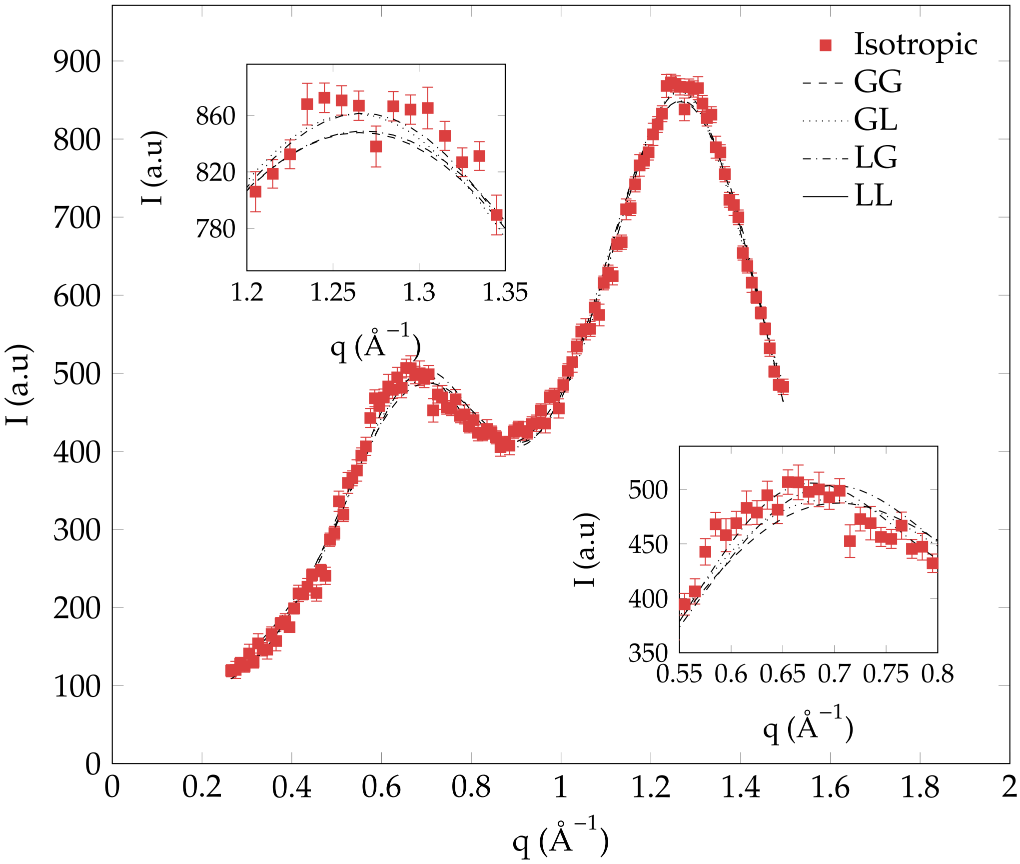

Figure 2.12: Isotropic data fitted to two-peak profiles. The two insets show zoom-ins on the two peaks. The letter combinations GG, GL, LG, and LL label the two-peak profiles: G for Gaussian and L for Lorentzian. The first letter gives the profile fitted to the inner peak.

χ^2-values for the vertical sector of the anisotropic data set into account, the double Lorentz profile performs best, but the Gauss-Lorentz profile is only slightly worse. Based on these considerations we only consider the double Lorentz and the Gauss-Lorentz profile in the following.

Background Estimation for All Sector Averages Before we test the two-Lorentz peak profile fitted to all sector averages of a single 2D set, we define what we expect of a successful two-peak profile. In Fig. 2.15 we plot representative $I(\theta)$ profiles, SiL 0 s - 320 s, from the averaged data obtained as described in Sec. 2.4.2. If a given two-peak profile successfully describes data, and we can subtract a meaningful $I(\theta)$ for the inner peak with the background subtracted, we expect the resulting profiles to look

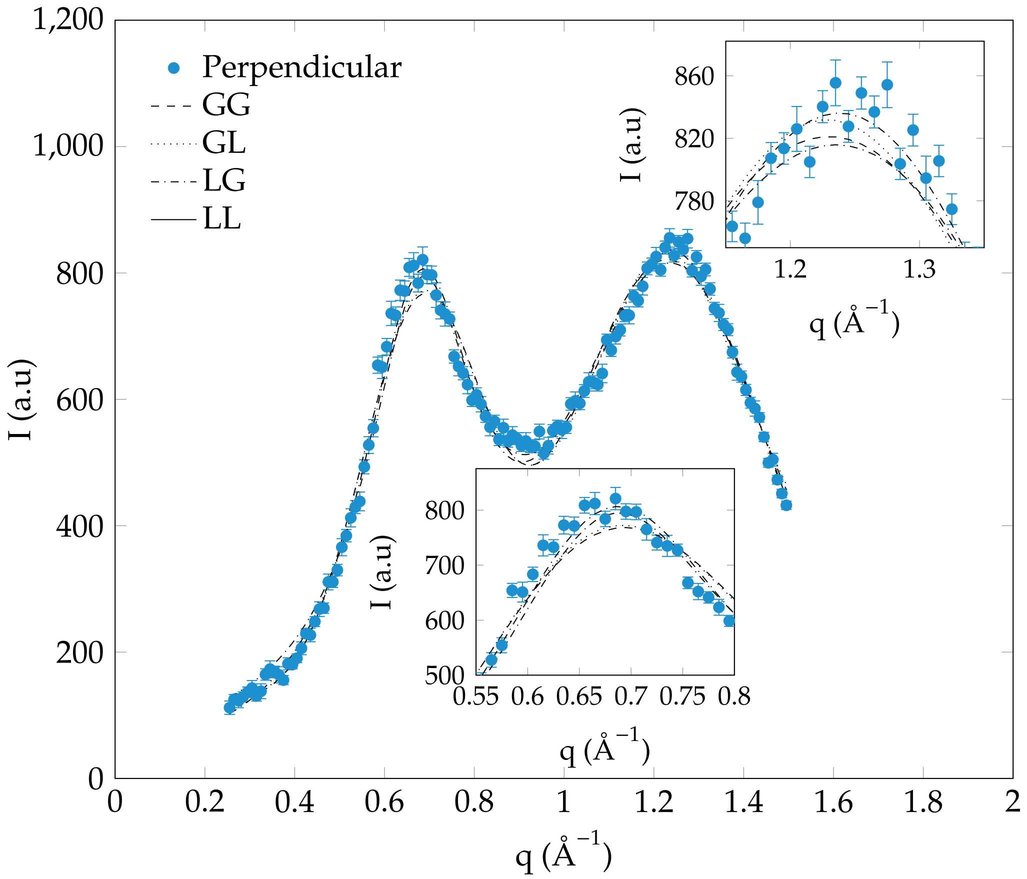

Figure 2.13: Perpendicular sector of anisotropic data fitted to two-peak profiles. The two insets show zoom-ins on the two peaks. The letter combinations GG, GL, LG, and LL label the two-peak profiles: G for Gaussian and L for Lorentzian. The first letter gives the profile fitted to the inner peak.

	G-G	G-L	L-G	L-L
Horisontal sector oriented	4.9	4.9	3.8	4.1
Vertical sector oriented	6.1	1.2	7.5	1.3
Isotropic	3.2	2.4	3.7	2.5

Table 2.3: χ^2 for the four two-peak profiles fitted to the perpendicular and parallel sector of anisotropic data and isotropic data.

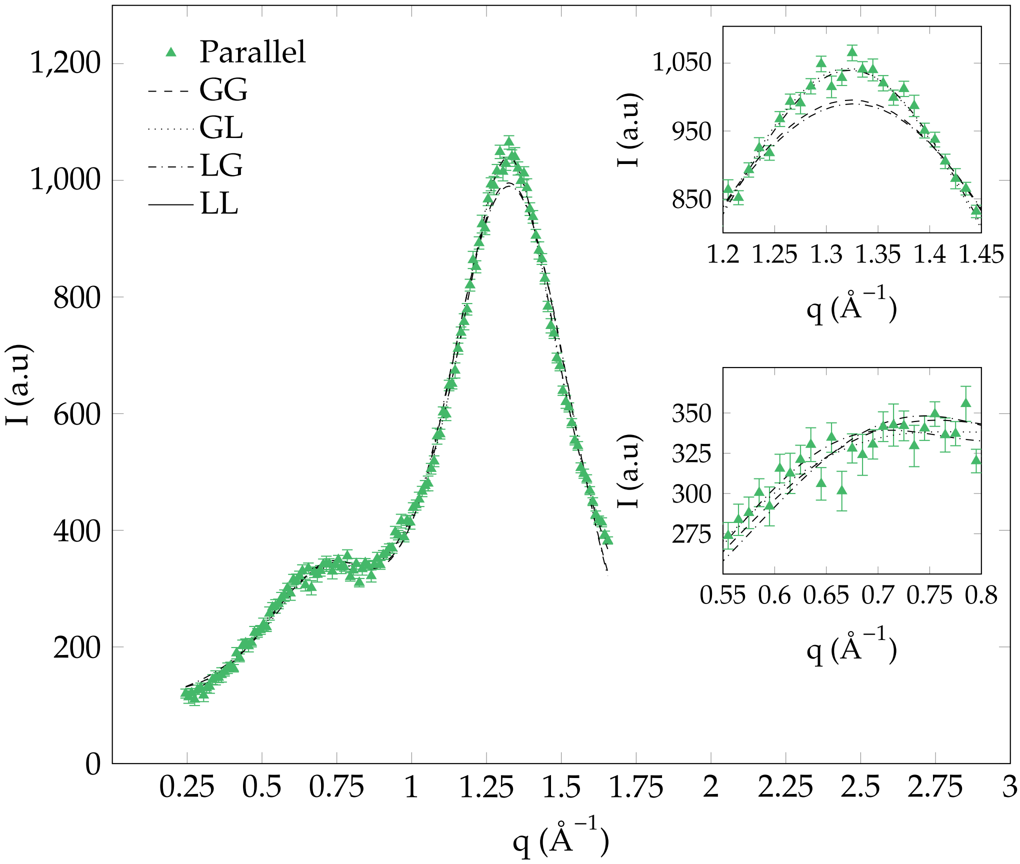

Figure 2.14: Parallel sector of anisotropic data fitted to two-peak profiles. The two insets show zoom-ins on the two peaks. The letter combinations GG, GL, LG, and LL label the two-peak profiles: G for Gaussian and L for Lorentzian. The first letter gives the profile fitted to the inner peak.

qualitatively like the data profiles but with a larger degree of orientation.

Fitting all sectors of given 2D data sets to the LL peak profile result in the following plots of the intensities of the inner and outer peak and their center q-value Fig. 2.16. The amplitudes of the inner peak show a strange upturn at the smallest and largest angles and the curves for the outer peak are not smooth. We therefore also fit the sectors to the GL peak profile, see Fig. 2.17. The upturn is smaller but still present and the curves are now less smooth. We believe this is due to a coupling of the fitting parameters, and to remedy this, we now estimate the constant background by fitting full azimuth averages of the data sets to the given two-peak profile. We then lock the value of the constant term in the following fits of the individual sectors to that determined from the fit to the full azimuthal average. For the LL-profile the result is plotted in Fig. 2.18 where the curve shape for $t \geq 10$ s differs from that of the actual data in Fig. 2.15. For the GL-profile the result is plotted in Fig. 2.19. The curves are smooth and look qualitatively like the data and the strange upturn is gone. We therefor consider the GL-fit with locked background as the best procedure for estimating the intensity of the inner peak.

The reduction procedure however still needs improvements. Fig. 2.19b show that the amplitude of the outer peak found by this procedure does not vary smoothly with θ, and the q value of the center of the peaks as a function of azimuthal angle $q_1^*(\theta)$ and $q_2^*(\theta)$ respectively vary in an irregular way, see Fig. 2.20. From the 2D data we expect the peak position of the outer ring to vary with maximum at $\theta = 0°, 180°$ and the position of the inner ring to be at least close to constant. However, from the data reduction we find that the peak positions shift in an irregular way. Nevertheless, for the current analysis we find that the peak amplitude $A_1(\theta)$ found from the GL profile with a locked background is sufficiently accurate for further analysis despite the inaccuracies described in this section.

2.4.3 Results

From the $A_1(\theta)$ profiles found as described in the previous section, we now calculate the orientation faction from Eq. 2.3 for each filament. In the following analysis we use one measurement for each filament taken in the mid-filament plane. For the most stretched filaments, it can be difficult to determine the mid-filament plane accurately since a large part of the filament is cylindrical. To test the influence of measuring away from the mid-filament plane, we scan a filament from SiL $t = 0$ s of relaxation sample in steps of 1 mm and calculate the orientation factor at each position. The result is plotted in Fig. 2.21. We see that the orientation factor varies slightly along the filament, and it seems to be systematically larger towards the ends of the filament. For consistency in measurements between filaments it is therefore important to measure at the middle. However the variation along the specific filament, $|f|_{\text{filament scan}} = 0.149 \pm 0.002$ is much smaller than the variation between all the SiL $t = 0$ s filaments $|f|_{\text{all SiL } t\,=\,0\text{ s filaments}} = 0.14 \pm 0.02$. Therefore it is not a concern if the measurement is taken slightly away from the mid-filament plane.

For samples with more than one filament, we take the mean and the standard deviation of the resulting orientation factors. In Fig. 2.22 we plot the orientation factors as function of Hencky strain rate, and in Fig. 2.23a we plot the orientation factor for the relaxation series of SiS and SiL stretched

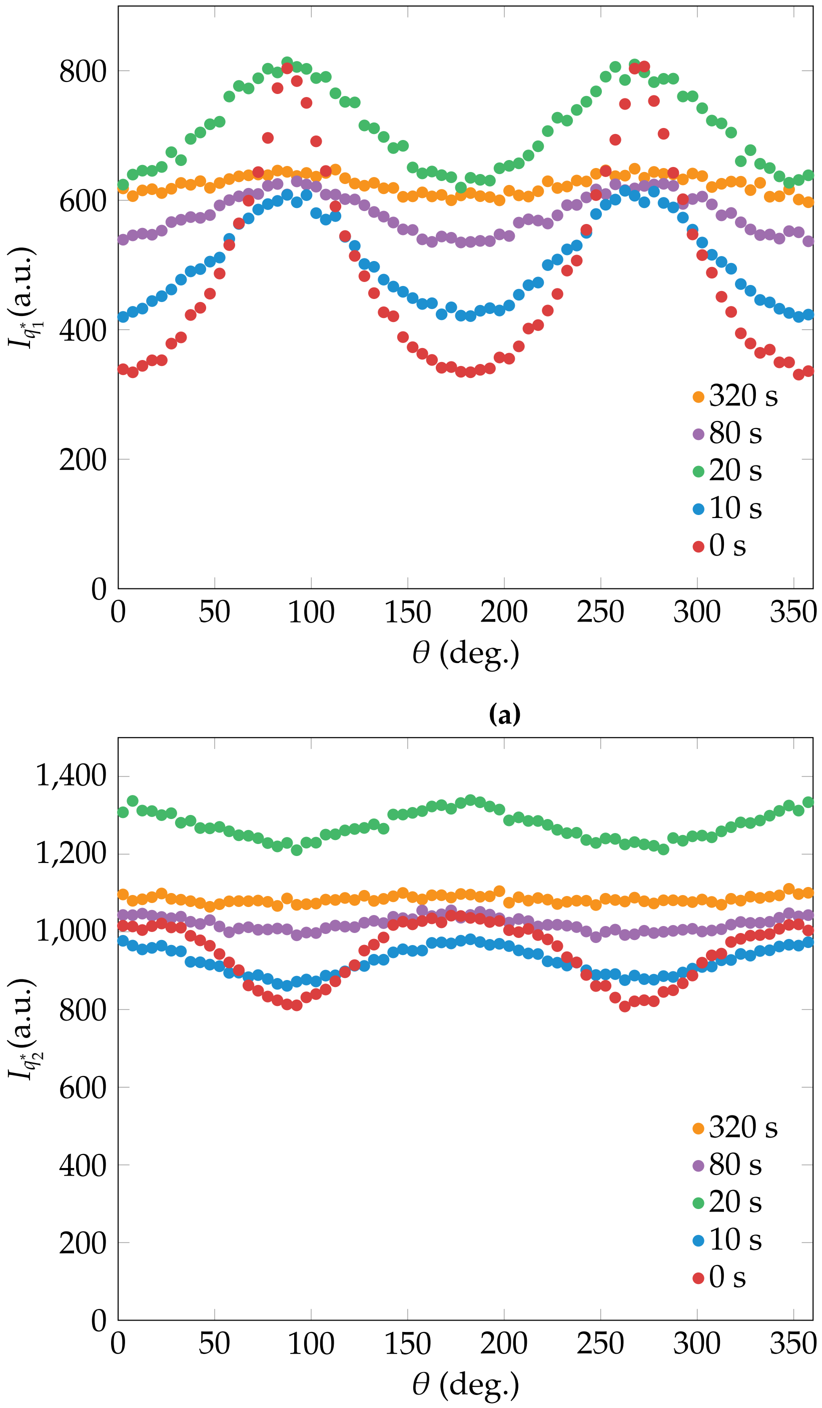

(a)

(b)

Figure 2.15: SiL data averaged over q = (0.6750 ± 0.0025) Å^{-1} in a) and q = (1.2850 ± 0.0025) Å^{-1} in b) for t =0, 10, 20, 80, and 320 s.

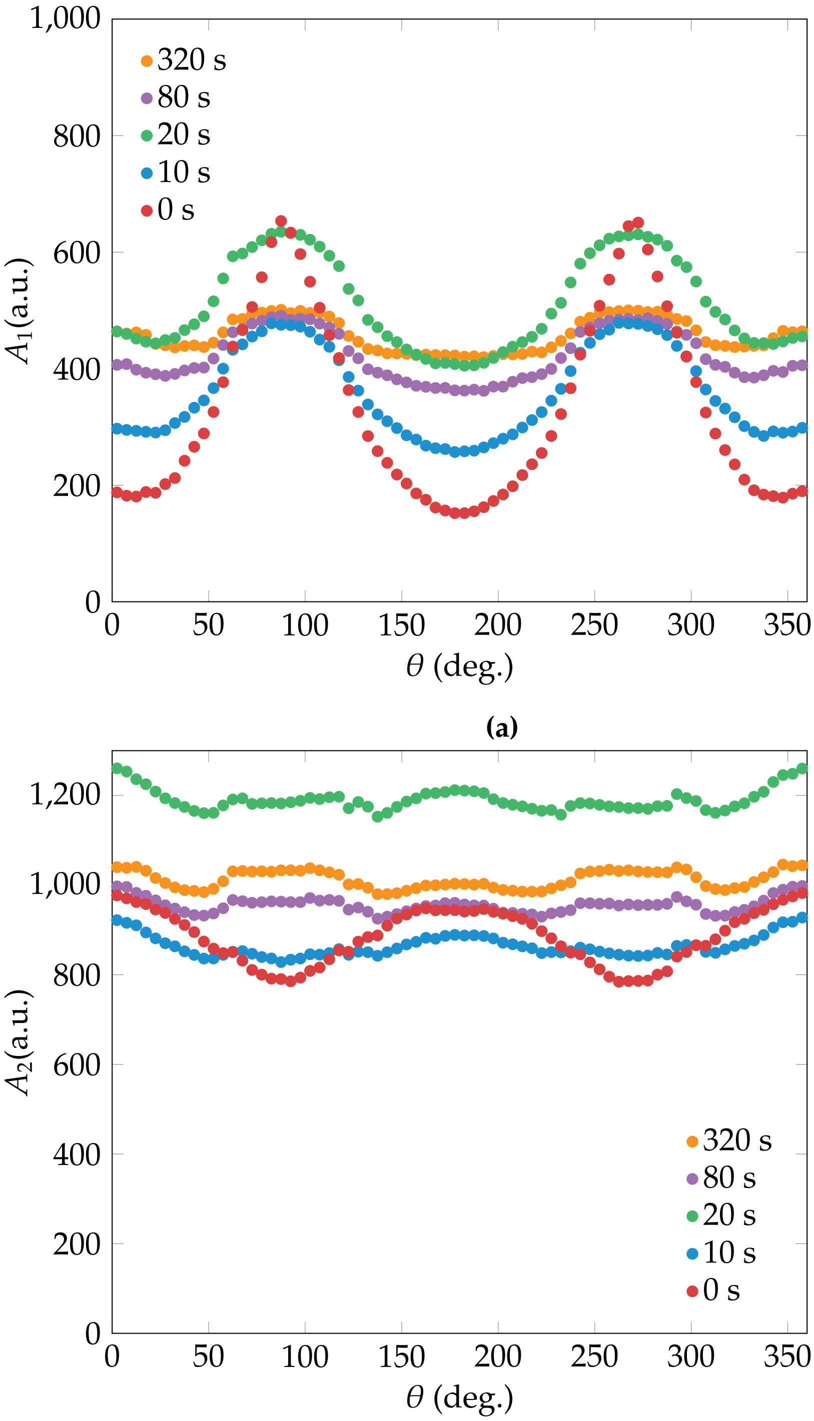

(a)

(b)

Figure 2.16: SiL peak amplitudes from LL-fit with free background. In a) the peak ampltude of the inner peak and in b) the peak amplitude of the other peak for 0, 10, 20, 80, 320 s.

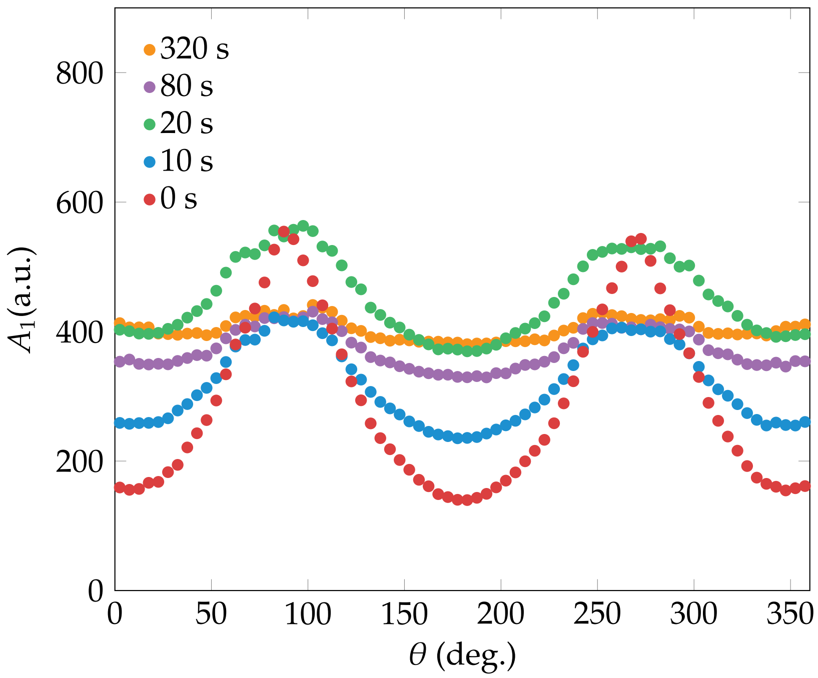

(a)

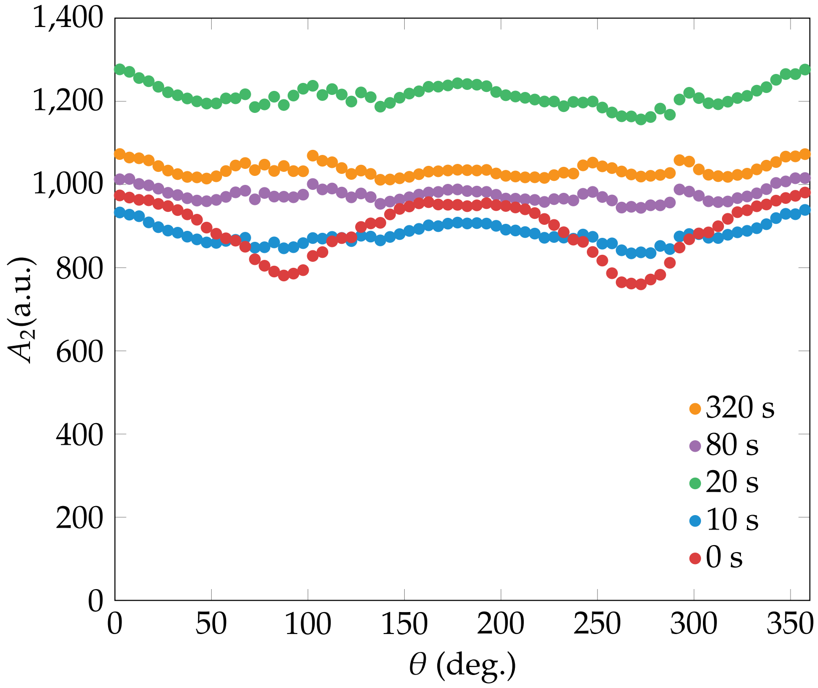

(b)

Figure 2.17: SiL peak amplitudes from GL-fit with free background. In a) the peak amplitude of the inner peak and in b) the peak amplitude of the outer peak for 0, 10, 20, 80, 320 s.

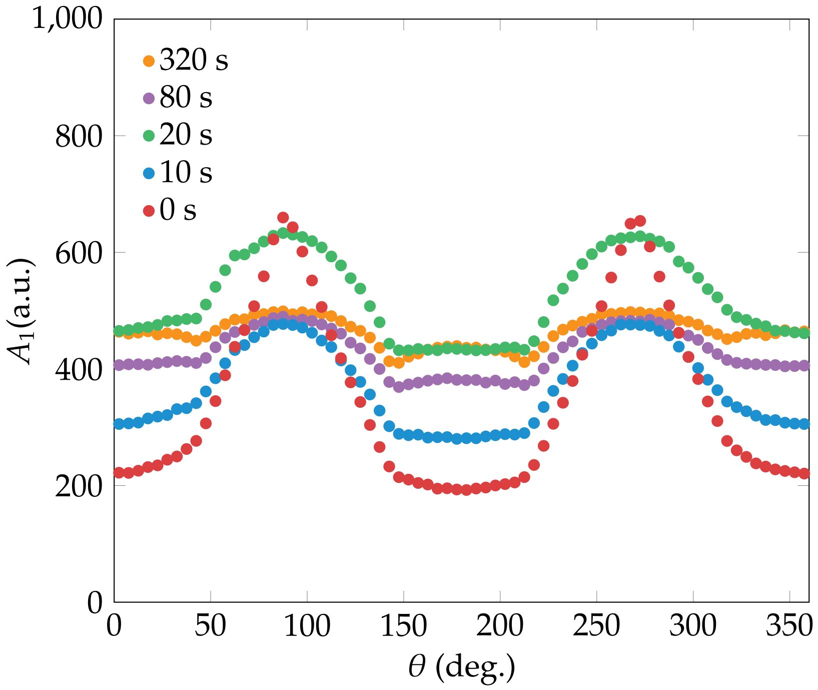

(a)

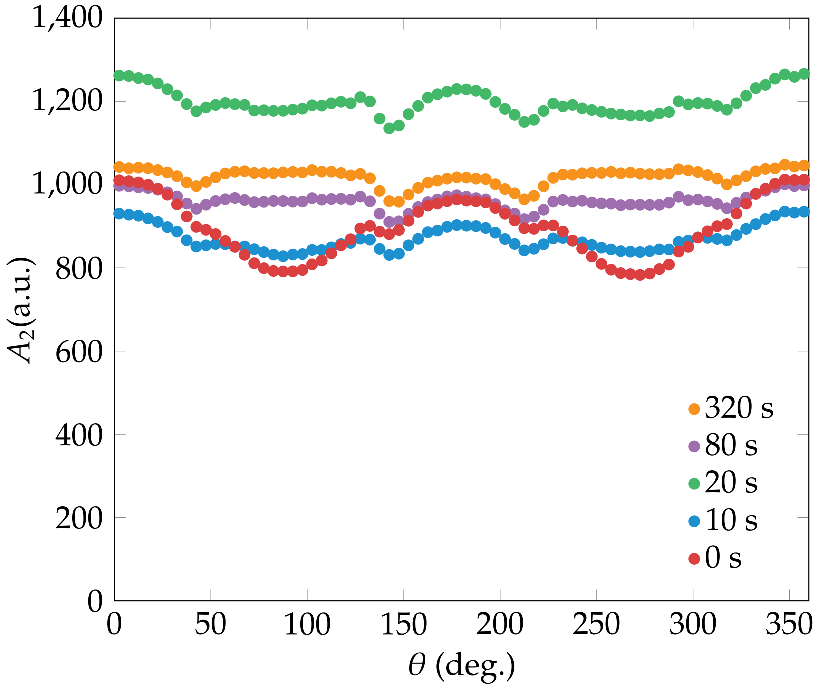

(b)

Figure 2.18: SiL peak amplitudes from LL-fit with locked background. In a) the peak ampltude of th inner peak and in b) the peak amplitude of the other plot for 0, 10, 20, 80, 320 s.

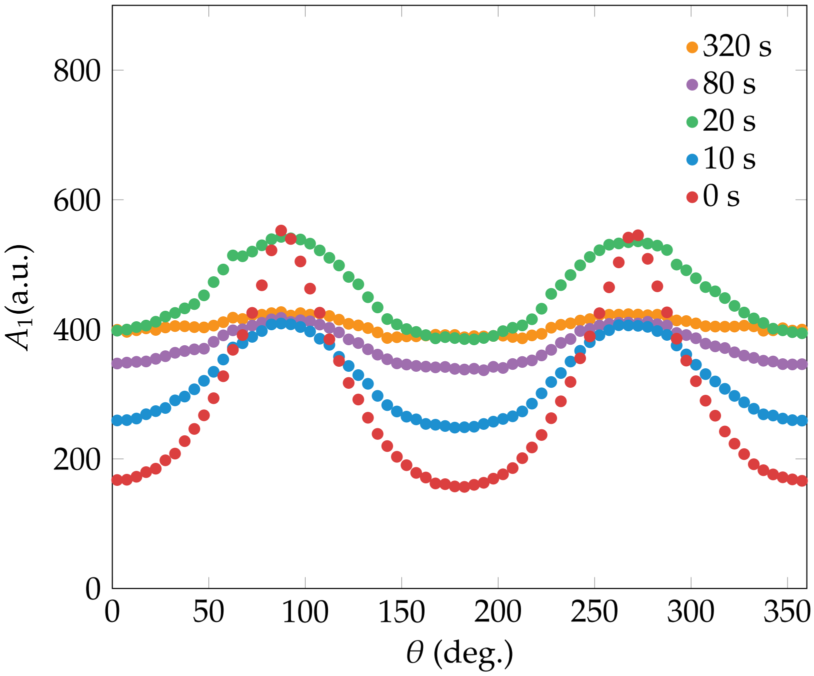

(a)

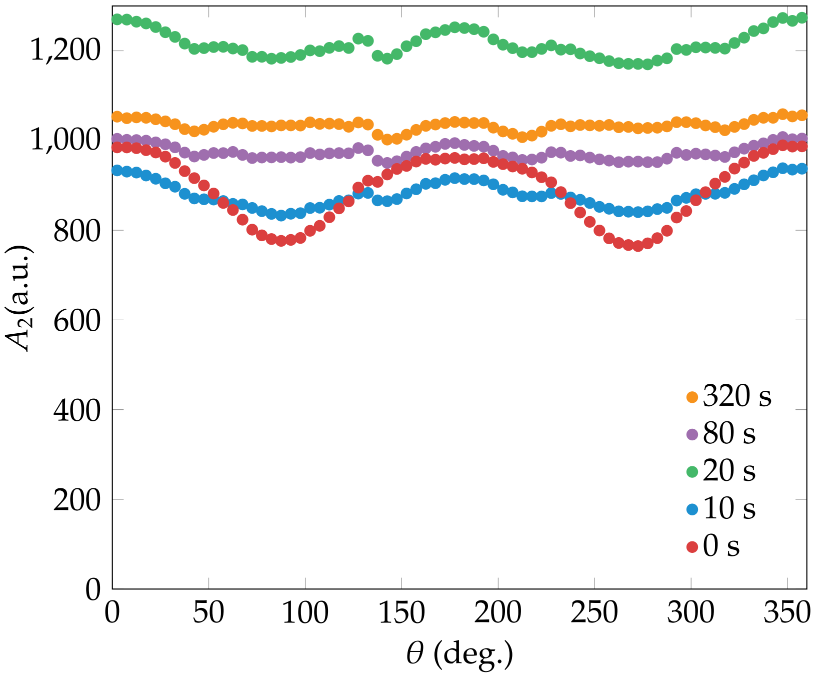

(b)

Figure 2.19: SiL peak amplitudes from GL-fit with locked background. In a) the peak ampltude of th inner peak and in b) the peak amplitude of the other plot for 0, 10, 20, 80, 320 s.

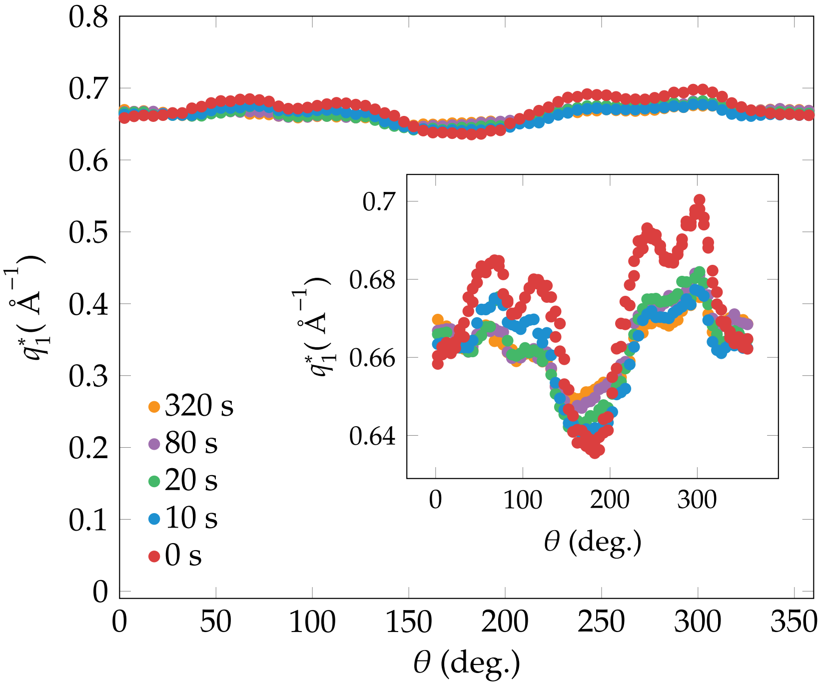

(a)

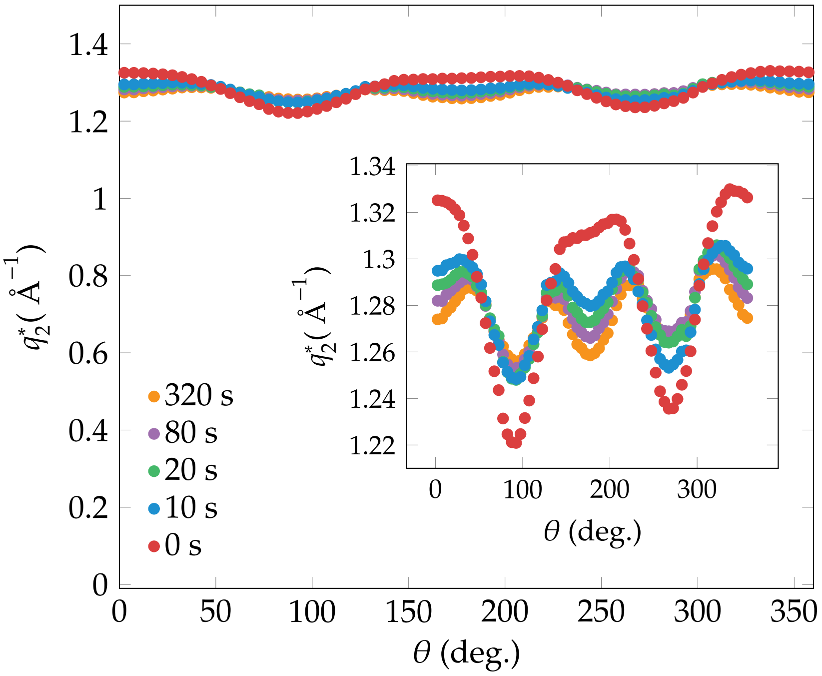

(b)

Figure 2.20: Peak positions determined through GL-fit with locked background. The position of the inner peak is plotted in a) and the position of the outer peak is plotted in b). The inset are zoom-ins.

	a	t_{quench}	b	χ^2
SiS	0.046±0.006	0.7±0.4	0.4± 0.03	5.4
SiL	0.17±0.03	1±1	0.39±0.03	4.0
SiL*	0.14±0.02	0.9±0.6	0.34±0.02	9.6

Table 2.4: Fitting parameters for power law decay of local orientation. In the SiL* row the data point at t =13000 s that consists of only one measurement was assigned the errorbar of the SiL 1260 s data point.

to $\dot{\varepsilon} = 0.1$ s^{-1}. We see that for all processing conditions, the SiL-samples are most oriented and that the orientation for both materials increases with increasing strain rate and decreases with increasing relaxation time. From Fig. 2.23 we thought it would be possible to determine a model for how the orientation decreases with time, and we found that it is well described by a power law if we allow for an additional constant quench time as a time off-set. We thus fit the data to

$$y = A * (t + t_{\text{quench}})^b \tag{2.6}$$

and obtain the fitting results listed in Tab. 2.4. In the first fit to the SiL-data the fitting routine excludes the last data point since it does not have errorbars associated because it consists of one measurement only. In the second fit to the SiL-data we gave the last data point the same errorbars as the orientation for t=1260 s. The fits are shown in Fig. 2.23b where $t^{S/L}_{\text{quench}} \sim 1$ s has been added to the relaxation time. As we see the exponents for the two first fits are consistent within the uncertainties. Comparing the first and the second fit to the SiL data we see that the exponent is sensitive to the last data point and in general to the orientation at the longer relaxation times. It is therefore possible that these results are sensitive to background subtraction.

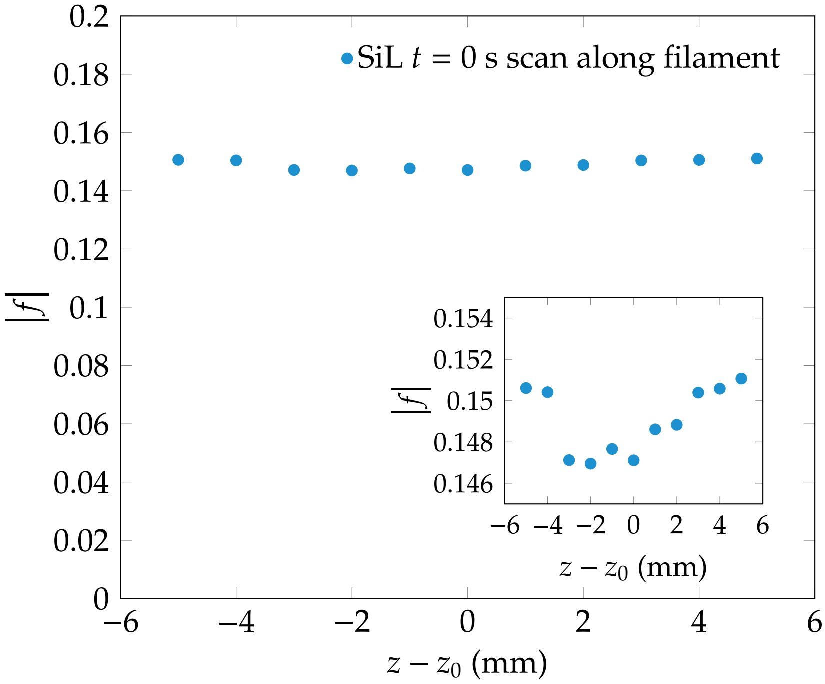

Figure 2.21: Orientation factor along SiL $t = 0$ s filament. The absolute value of the orientation factor $|f|$ as a function of position along the filament axis z relative to the center z_0. The inset shows a zoom-in on the data points to show the systematics.

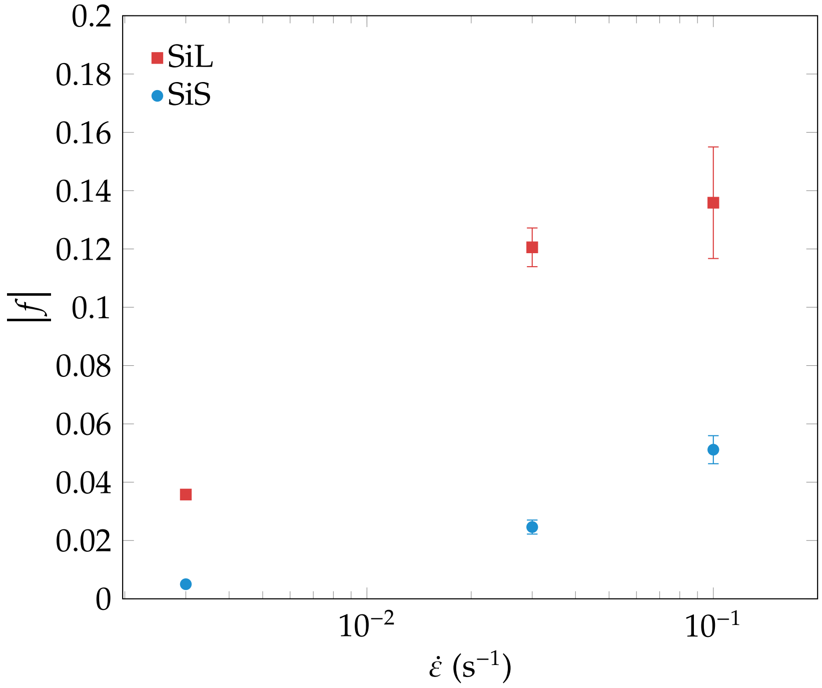

Figure 2.22: Orientation factor f as function of Hencky strain rate $\dot{\varepsilon}$. The rates relate to the characteristic time scales of the short chains in the following way: $\dot{\varepsilon} > 1/\tau_R^S$

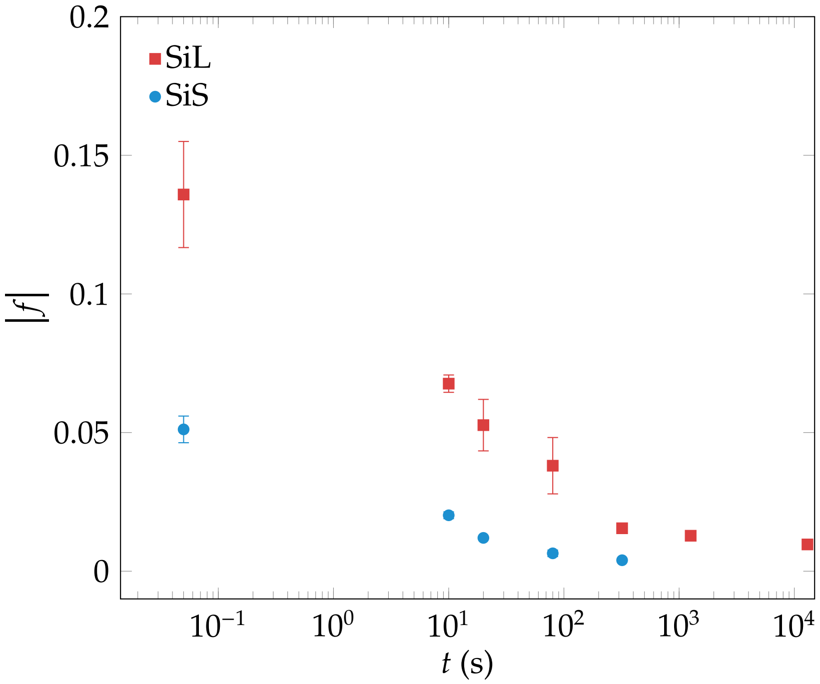

(a)

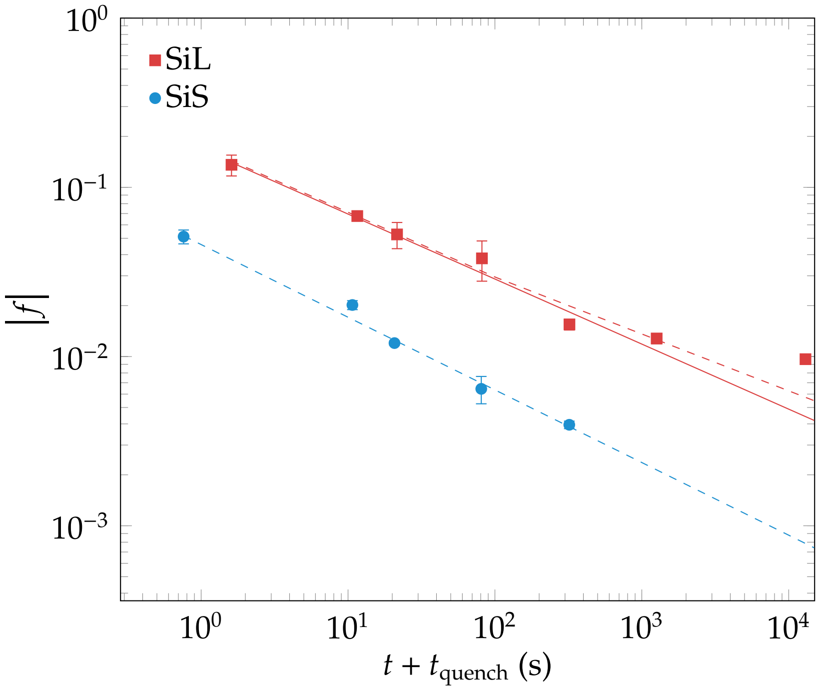

(b)

Figure 2.23: Orientation factor f as function of relaxation time t. In a) the absolute value of the orientation factor $|f|$ is plotted as a function of relaxation time log(t)t. In b) The data is plotted on double log scale and t_{quench} found from fitting to Eq. 2.3 has been added to the relaxation time. The last data point for the SiL-series is not included in the fully drawn fit but in the dashed.

2.5 Discussion

In this section we discuss the validity of the obtained orientation factors, how they compare to the effective strain derived from the SANS-study, and how they relate to the nematic interaction hypothesis.

2.5.1 Data Reduction

As mentioned in the previous section the data reduction procedure has room for improvements since it does not accurately capture the peak positions. This could be due to the simple peak models we have employed consisting of Gaussians and Lorentzian. Both Gaussians and Lorentzians are symmetric, but the peak profiles of the scattering pattern are not necessarily symmetric since each peak has contributions from two or more characteristic distances as argued in Sec. 2.3.1. It may also be due to errors or inaccuracies in the reduction procedure such as incorrect image centers, too simple an approach for replacing the masked pixels, or perhaps the procedure for locking the constant background or the choice of a constant background itself. However, by manual inspection of a selection of sector averages and their fitted profile, it appears consistent that the peak height, which we use in the further analysis, is captured well even though the position is not, and the suggested improvements of the analysis will therefore most likely not affect the conclusions.

2.5.2 Orientation Factors for Stretched Polystyrene in Literature

The found values of $\left|f\right| \leq 0.18$ where $\left|f\right| = 0.5$ would correspond to ideal perpendicular alignment. If we take the intrinsic disorder described in Sec. 2.3.2 into account and use the correction factor for polystyrene from ref. [50] we get $\left|f\right|_{\mathrm{corr}} \leq 0.22$ which shows that the material could be oriented more on this length scale. Fig. 2.22 show a clear correlation between the Hencky strain rate applied and the resulting orientation suggesting that if the SiL-material was deformed at a larger rate, the resulting orientation would increase. Given the three data points for each material, the orientation seems to increase linearly with applied rate, but more data points are needed to test this hypothesis.

To assess whether the orientation factors we found are reasonable, we compare to the values found in an earlier study by Vancso et al. in ref. [50]. They stretched flat tensile test specimens of polystyrene at temperatures very close to the glass transition temperature, $T_{\mathrm{exp}} = 108, 112°$

and $T_g = 107 - 114°$ determined by Differential Scanning Calorimetry, at different but constant clamp speeds. The material they use has $M_w = 287$ kg/mol and a PDI=2.4. They report values corrected for the intrinsic disorder of $\left|f\right|_{\text{Vancso}} \leq 0.3$. Though it is not straight forward to compare the stretching procedures, we do consider it reasonable that larger degrees of orientation can be obtained if the sample deformation is done at temperatures so close to the glass transitions where the sample relaxation is very slow.

2.5.3 Comparison of Orientation Factor and Effective Strain, and Stress

If we compare Fig. 2.4 and 2.23, we see that it is common for both the orientation factor relaxation and effective strain relaxation that the SiL-series has a larger initial value. To see whether the effective strain can also be described by a power law if the quench time is taken into account, we plot the effective strain on log-log scale and subtract one to account for the fact that $\lambda_z^v = 1$ in equilibrium whereas $f = 0$ in equilibrium, see Fig. 2.24. We clearly see that the effective strain and the local orientation relax qualitatively differently. Since we have not yet established a firm connection between the effective strain found from SANS and the local orientation found from WAXS, it is currently not possible for use WAXS instead of SANS to study the effect of polydispersity as we had hoped.

Nematic Interactions and Orientation from WAXS

The WAXS study was initiated to test the nematic interaction hypothesis from the previous SANS study. In the introduction, we described the experiments by Kornfield et al.[30], Tassin et al. [33], and Hayes et al.[34]. They all see a prolonged relaxation of the local orientation of short chains in blends with long chains and conclude it is due to nematic interactions so the hypothesis is supported by literature. However, it is not easy to interpret our results from WAXS in the context of nematic interactions due to the lack of scattering contrast between short and long chains in our experiment. We obtain information on on the local orientation of the short chains in the pure melt of short chains $\bar{Q}^S_{\alpha\beta}(t)$ through f, but for the blend we obtain information on the mix of local orders of the two species $\phi_L \bar{Q}^L_{\alpha\beta}(t) + \phi_S \bar{Q}^S_{\alpha\beta}(t)$ through f.

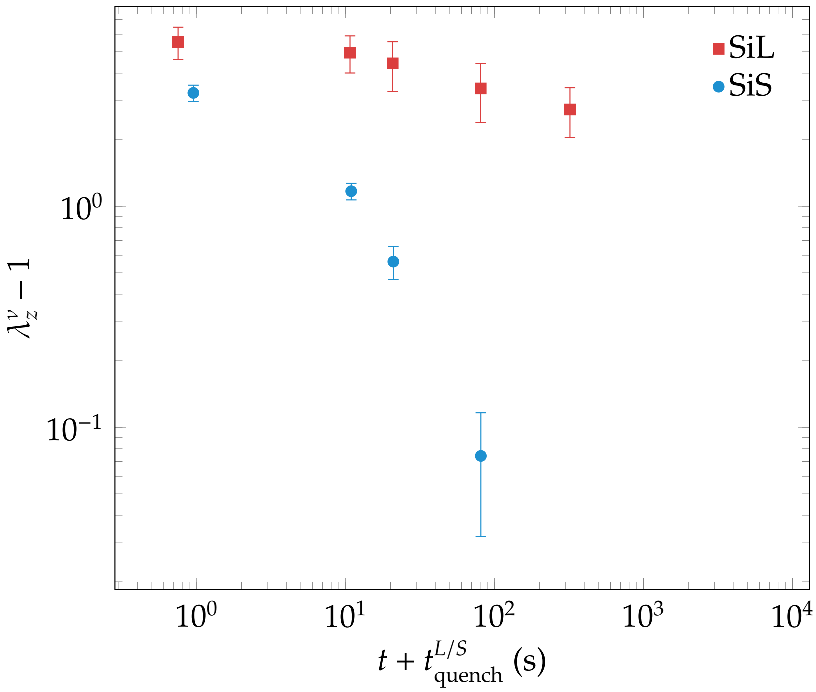

Figure 2.24: Relaxation of microscopic stretch ratio SiS and SiL. The microscopic stretch ratio λ_z^ν with errorbars as a function of relaxation time t_{rel} is calculated from Tab. 2 in ref. [10]. We subtract the equilibrium value $\lambda_{z,\text{eq}}^\nu = 1$. The upper black curve corresponds to SiL-data and the lower red curve corresponds to SiS-data. The relaxation times are shifted by $t_{\text{quench}}^{L/S} < 1$ s, see Tab. 2.4.

As stated in Sec. 2.1.2, the following relation between the order parameters $\bar{Q}_{\alpha\beta}^S(t)$, $\bar{Q}_{\alpha\beta}^L(t)$, $\bar{S}_{\alpha\beta}^S(t)$, and $\bar{S}_{\alpha\beta}^L(t)$ is expected in case of nematic interactions:

$$\phi_L \bar{Q}_{\alpha\beta}^L(t) + \phi_S \bar{Q}_{\alpha\beta}^S(t) = \frac{1}{1-\epsilon}\left(\phi_S \bar{S}_{\alpha\beta}^S + \phi_L \bar{S}_{\alpha\beta}^L\right). \tag{2.7}$$

From the sans experiment we obtain information on $\bar{S}_{\alpha\beta}^S$, but we still miss information on $\bar{Q}_{\alpha\beta}^L(t)$ and $\bar{S}_{\alpha\beta}^L(t)$ to determine whether nematic interactions could explain the increased stretching observed in neutron scattering.

2.5.4 Power Law Relaxation

That the orientation factors relax following power laws probably means that several relaxation mechanisms occur on different time scales, and that the exponents are the same for SiS and SiL suggests that the Kuhn segments relax similarly independent on whether they belong to short or long chain such that only the initial degree of stretching is affected by the chain length. Unlike in the SANS study, there is no scattering contrast between the short and long chains in X-rays and so it is hard to tell whether the higher initial orientation is the result of a simple mixture between less oriented short chains and more oriented long chains or whether there is an interaction between them. However it should also be noted that the exponent of the fit is quite sensitive to the orientation factors at long relaxation times and that the quality of the fit is quite sensitive to the fitted quench time, as described above, so it is very important to ensure that these values are as accurate as possible.

The stress relaxation of the blend also shows a power law behavior over at least two decades, see Fig. 2.1b though that has an exponent about twice as large $a_{\text{stress}} \sim -0.8$. The origin of this power law behavior is currently not understood either.

Segment Orientation and Tube Model Expectations

The lowest strain rate $\dot{\varepsilon} = 0.003\ \text{s}^{-1} < 1/\tau_d = 1/169\ \text{s}^{-1} \approx 0.05\ \text{s}^{-1}$ meaning that we do not expect orientation of the tube segments during deformation. With that in mind, it is interesting that even the SiS-filaments stretched at this rate show a slight degree of orientation. If it is true that there is orientation on the Kuhn segment level even though we do not expect orientation at the tube segment level, this could be due to nematic interactions. If it is an artifact of the data reduction, it could also be the case for the data points corresponding to long relaxation times, and as described above, the value of those influence the value of power law exponent a lot. It would therefore be an important check of the data reduction procedure to test if zero orientation can be reached in other, potentially unstretched, samples.

2.5.5 Future Experiments

It may be worthwhile to look into the potential of infrared dichroism for studying our samples, but care should be taken in designing the experiment since the techniques are sensitive to the optical path length which may be problematic with our cylindrical specimens.

To gain a better understanding of the relaxation of local orientation as measured by WAXS, it would be most interesting to repeat the study with a bi-disperse melt where the pure melt of the long component could be stretched at the same strain rate as the blend and the pure short component. This could be realized by stretching the current melt at a rate of up to at least $\dot{\varepsilon} = 0.01$ s^{-1} at $T = 130°$ C which was done in ref. [51]. It is still faster than the inverse of the reptation of the short component $1/\tau_d^S \approx 0.005$ s^{-1} but slower than the inverse of the Rouse time of the short chain $1/\tau_R^S \approx 0.05$ s^{-1} so we would expect only orientation of the tube segments and not stretching in the pure blend of short chains.

Another approach could be to prepare another blend where the long chain is shorter. With such a material, it would be interesting to see if the relaxation too follows a power law with the same exponent for both components and the blend, and how the initial level of orientation of the blend compares to that of both pure components. It would also be interesting to vary the composition of the blend and see how that affects the relaxation. The question is then which chain lengths to use. The short chain should probably not be much shorter since it currently holds only $Z \sim 6$ entanglements, and we would like to keep the long chain long enough relative to the short chain that the Rouse and reptation times of the two components are well separated. From Tab. 2.1, we know that the reptation time of the short chain $\tau_d^S = 169$ s and the Rouse time of the long chain is $\tau_R^L = 705$ s. Maybe a separation of $\tau_R^{L'} = 2\tau_d^S \approx 0.5\tau_R^L$ is sufficient, and in that case the long component could be shortened by a factor of $1/\sqrt{2}$ since $\tau_R \sim N^2$ and so have $M_w \approx$400 kg/mol. It should be possible to stretch this component at $\dot{\varepsilon} = 0.1$ s^{-1} at T=130° according to Nielsen et al. [3].

2.6 Conclusion

This chapter presented a wide-angle X-ray scattering study on a bi-disperse polystyrene blend that was previously characterized in non-linear extensional rheology and small angle neutron scattering. The thorough study combining several techniques is most relevant since a deep understanding of the bi-disperse melt will help us to understand the effect of polydispersity on the rheological behavior of polymer melts. The previous SANS-study, where some of the short chains were deuterated, showed that the short chains were stretched about 50 % more in the presence of the long chains for the same stretching parameters and that the stretching relaxed much slower than in the pure melt. Nematic interactions were put forward as a possible explanation for these observations, and the WAXS study was initiated to test this hypothesis. WAXS could be a suitable technique since it can probe length scales corresponding to the distance between neighboring molecules, but it is challenging since there is no scattering contrast between the long and short chains in WAXS unlike in SANS. The signal from the blend therefore contains contributions from both the long and short chains unlike SANS. In the WAXS study we quantified the local orientation using Hermans' orientation factor calculated for the peak at $q \approx 0.7$ Å^{-1} that is dominated by interchain correlations. We found that the orientation factor is always larger for the blend than for the pure short chain material, and that it increases with increasing strain rate and decreases with increasing relaxation time as expected. Surprisingly, if we correct for the quench time, we find that the orientation decreases as a power law of the relaxation time with the same exponent for both materials but different initial degrees of orientation suggesting that the relaxation of local orientation as measured by WAXS consists of several processes and is independent of chain length. We were not able to fully establish a connection between the previous SANS results and the new WAXS results suggesting that more experiments are needed. One such experiment could be to repeat the WAXS study for a system where also the pure long chain material can be stretched with the same stretching parameters.

Chapter 3

Small Angle Neutron Scattering on End-labeled Three-Arm Stars

In this chapter we present the results of our small angle neutron scattering (SANS) study on end-deuterated three armed star polymers in fast extensional flow. Theoretical work has predicted that in fast extensional flow, star polymers collapse into a quasi-linear conformation and thus have the same rheological behavior as a linear molecule of the same span, i.e. same backbone length [52]. This hypothesis was tested in a previous study on the extensional rheology during stretching and relaxation of a linear molecule and two stars: one with a short third arm and one with three arms of the same length [7]. It was found that during stretching at fast rates, the stars did in fact show the same rheological responses as the melt of linear molecules. Early in the relaxation, the melts showed the same response but for longer relaxation times, their behavior deviated. These works led to the hypothesis that in fast extensional flow, star molecules take a pseudo-linear conformation which remain some time into the relaxation. This SANS study was then initiated to track the molecular conformation during relaxation following fast extensional flow by analyzing a sample series quenched at varying relaxation times. The molecules were end-deuterated to obtain information on end-to-end correlations.

The analysis and interpretation of the scattering for the sample quenched immediately of the cessation of extensional flow and for the sample after full relaxation is previously published in Mortensen et al. [53], which is included in this thesis in App. B.

The chapter begins with an introduction to rheological and scattering experiments on branched polymers followed by a brief summary of the extensional rheology experiments that led to the hypothesis tested in this SANS study. Then we present the calculation of the random phase approximation structure factor for star block copolymers used for analyzing SANS data for the fully relaxed stars, the sans experiment and data reduction and analysis. Finally, we discuss our results and conclude on our findings.

3.1 Introduction

The molecular architecture, and the following molecular conformation, and rheological properties of polymer melts are closely related. The tube model has proven successful in the description of rheology of melts of linear molecules [54]. However, many commercial polymers such as low density polyethylene are branched, so apart from the fundamental question of how branching affects the rheological properties of polymer melts and the conformation of the molecules, a model that relates branching and rheological properties is also desired for application.

Branched polymers with several branching points and long, i.e., entangled, side chains are both very strain hardening and shear thinning. This behavior was captured by the molecular constitutive equation for the simple case of pom-pom molecules, which are molecules with a single backbone and two branch points from which several branches may grow [55]. Under sufficiently large strain where the tension in the backbone connecting the two branch points overcomes the entropic tension in the branches, the branch points are sucked into the tube of the backbone. This is called ″branch point withdrawal″ [56].

The theory of branch point withdrawal was tested in a set of SANS experiments on well defined H-branched molecules, i.e. pom-pom molecules with only two branches in each end. In ref. [57] and [54] end-deuterated H-branched molecules were studied and in ref. [58] backbone deuterated H-branched molecules were studied.

Branched polymers have also been studied using the filament stretch rheometer. Nielsen et al. stretched polystyrene melts of asymmetric stars with an average of 3.3 arms and pom-pom molecules with an average of 2.5 arms to steady state [4] each arm holding about two entanglements, and Huang et al. later studied a symmetric three arm star, an asymmetric three arm star and a linear molecule all of the same backbone span [7]. Also semi-crystalline, branched polymers have been studied, e.g. refs. [59, 60] showing that crystalline orientation in low density polyethylene is associated with backbone stretch and rather than macroscopic stretch and that flow induced nucleation and growth of elongated crystal structures, shishes, stabilize filaments elongated at temperatures slightly above the glass transition temperature respectively.

Based on the experiment by Nielsen et al., Ianniruberto and Marrucci suggested that in steady state of fast extensional flow, the branched polymers of Nielsen et al. take a quasi-linear chain conformation that for the stars is due to alignment with the flow [52].

3.2 Extensional Rheology of Stars and Linear Molecules of Comparable Backbone Length

Based on the work of Ianniruberto and Marrucci mentioned above, Huang et al. [7] decided to test the hypothesis that branched polymers (with a single branch point) behaves like linear molecules in fast extensional flow. The work resulted in ref. [7] "Dynamics of Star Polymers in Fast Extensional Flow and Stress Relaxation" by Q. Huang et al. published in Macromolecules in 2016. The hypothesis was tested by measuring the extensional rheology for increasing Hencky strain rates and the relaxation following extension for a linear molecule, and two stars all with the same backbone length, see next section. They found that for sufficiently large Hencky strain rates, the stress growth coefficient $\bar{\eta}^{+}(t)$ overlapped for melts of all three types of molecules and that the normalized stress curves also overlap initially during relaxation. In the following subsections, we describe the samples and the measurements of the extensional rheology.

3.2.1 Samples

The study involved three different molecular structures: A linear polystyrene Lin180, a symmetric polystyrene star Star90 and an asymmetric polystyrene Star20. The molecules are sketched in Fig. 3.1. All three molecules had a backbone with a molecular weight of approximately 180 kg/mol. For Star20 and Star90 a third arm branches out from a branch point in the middle of the backbone. . The third arm has a molecular weight of 20 kg/mol and 90 kg/mol respectively. The Rouse time, τ_R, of the molecules, which is determined by the backbone length, is about 87 s at $T = 130°$ [7] and 405 s at $T = 125°$ [53].

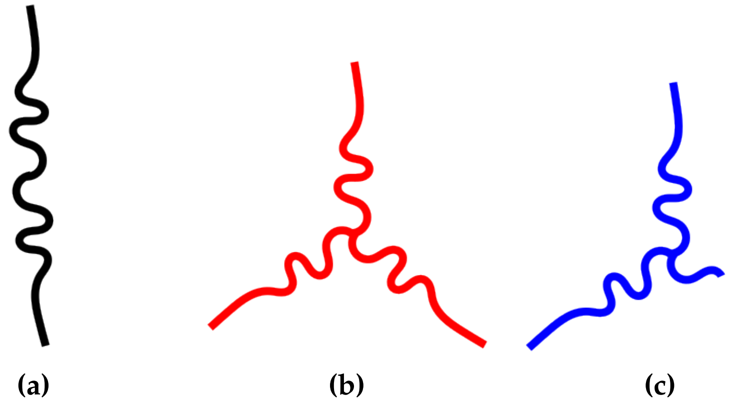

Figure 3.1: Molecular architecture of Lin180 in a), Star90 in b), and Star20 in c).

3.2.2 Extensional Rheology of Lin180, Star90, and Star20

This section presents the main findings of the above mentioned publication by Huang et al. in ref [7]. The extensional rheology for the three blends was measured on the filament stretch rheometer described in Sec. 1.2.1. The extensional rheology was measured at a range of Hencky strain rates $\dot{\varepsilon}$= 0.0003, 0.003, 0.01, 0.03, 0.1, 0.2 s^{-1}. All measurements except the lowest rate were performed at temperature T = 130° C. The measurement for the lowest rate was performed at T = 150°0 C and shifted to T = 130° C using time temperature superposition. The results of Huang et al. on the stress growth coefficient $\bar{\eta}^+(t)$ for the three materials and the different Hencky strain rates is shown in Fig. 3.2a. For increasing strain rate, the three curves overlap more and more. For $\dot{\varepsilon} > 0.03\ s^{-1}$, $1/\tau_R \approx 0.015$, the overlap is almost perfect. This figure supports the hypothesis of Ianniruberto and Marrucci from ref. [52] that entangled melts of branched polymers, single branch point i.e. stars or pom-poms, behave like linear polymers in fast extensional flow.

Huang et al. went further and measured the relaxation following to a final Hencky strain ε_f = 3.2 at Hencky strain rate of $\dot{\varepsilon}$ = 0.03 s^{-1}. Their [7] results on the normalized stress as a function of relaxation time is reproduced in Fig. 3.2b. The relaxation is described in terms of three regions: In region I, all three curves overlap, in region II, the relaxation of Star20 deviates from the other two curves, and in region III, all three curves differ. In terms on the Rouse time of the molecules, the transition from region I to II occur at $t \approx 0.2\tau_R$, and the transition from region II to III occur at $t \approx 6\tau_R$.

If the relaxation in region I is dominated by arm retraction and that the arms relax independent of each other and simultaneously, it is reasonable that the curves overlap. In region II, the short arm of Star20 is fully relaxed and acts like an solvent diluting the system, and therefore it relaxes differently than Lin180 and Star90 that continue to relax through arm retraction. In region III, the relaxation of all three melts is well described by the Doi-Edwards model using the multi-mode Maxwell relaxation modulus as memory function. Another interesting observation is that if the relaxation curve for Star20 is shifted vertically it overlaps well with the curve for Star90 from the middle of region II and into region III, see ref. [7], suggesting that the remaining two arms of Star20 relax through the same mechanisms as Star90 and Lin180 in this time interval. Based on this figure, the hypothesis was formed that Star90 remains in a quasi-linear, i.e. Lin180-like, conformation through region I and II in the relaxation. We aim to test this hypothesis with a small angle scattering experiments on a relaxation series of end-deuterated star melt following fast uniaxial extension.

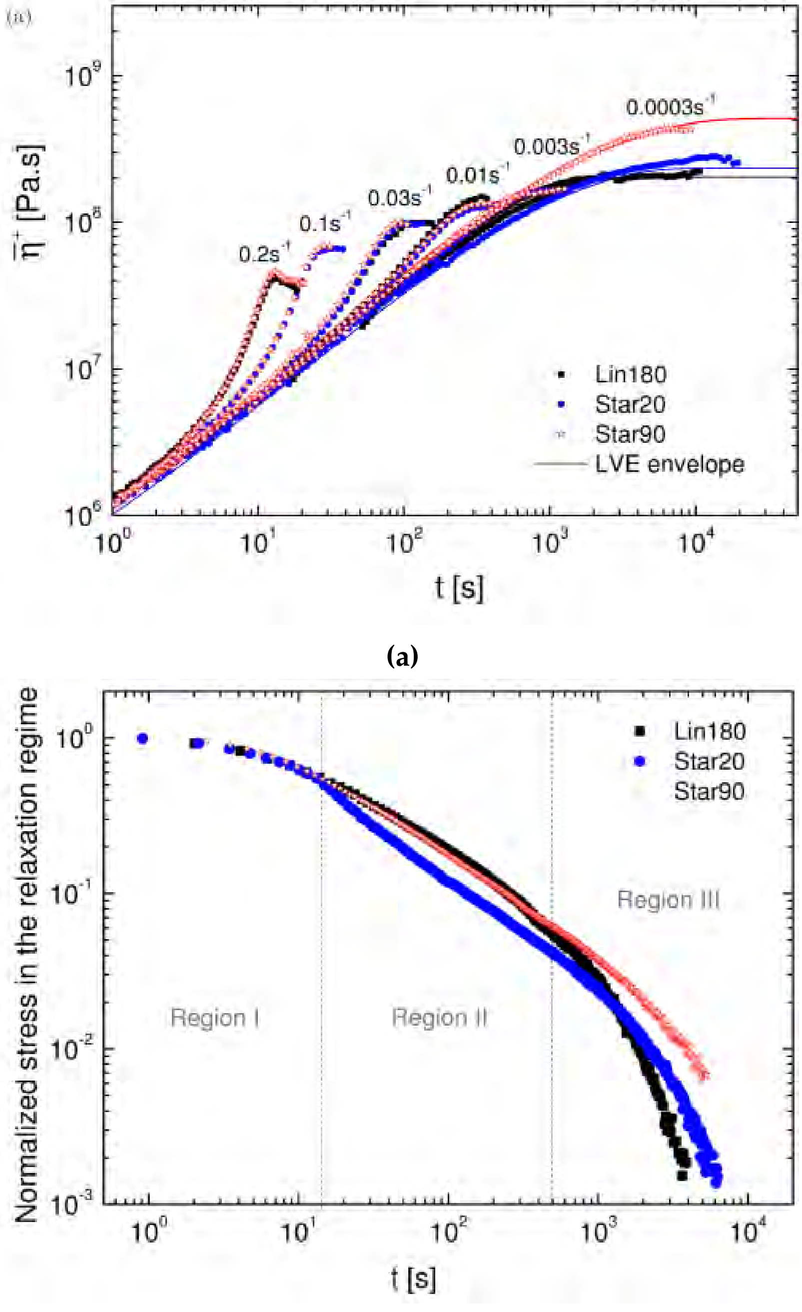

(a)

(b)

Figure 3.2: Extensional rheology for linear and star shaped molecules. In a) the stress growth coefficient $\bar{\eta}^+$ as function of time t after the onset of extension and in b) normalized stress as function of time after the onset of relaxation. All experiments were carried out at, or using the time-temperature superposition principle, shifted to $T = 130°$. The figures are from Huang et al. [7]

3.3 Random Phase Approximation Structure Factor

In the next section, we present the small angle neutron scattering study on melts of three-armed end-deuterated star polymers exposed to fast uniaxial extension and allowed to relax for different times. The end-deuterated stars of the SANS study are block copolymers where each arm has a large block of hydrogenous polystyrene by the branch point and a short block of deuterated polystyrene in the end, and all arms are symmetric in the sense that they have the same degree of polymerization N and same deuteration fraction f. One of the samples corresponds to the fully relaxed state of the end-labeled stars. We expect that the structure factor of this sample will be described by the random phase approximation structure factor, which we calculate in this section for a generalized g arm star with degree of polymerization N and fraction f of monomer type A and fraction $1 - f$ of monomer type B.

The simpler case of linear AB block copolymers shows an intriguing phase diagram where as a function of the fraction f of monomer type A and the product of the Flory-Huggins interaction parameter and the degree of polymerization, χN, a disordered and several ordered phases occur. In the ordered phase the block copolymers micro phase separate thus creating domains with a higher concentration of monomer type A or type B. Leibler wrote a microscopic theory that predicts the microphase separation transition, the transitions between the microphase separated states of different symmetry, and the structure factor in the disordered state using the random phase approximation (RPA) [61].

3.3.1 Structure Factor Calculation

We generalize the Leibler structure for linear AB diblock copolymers to symmetric stars where all g arms are AB diblock copolymers with the same degree of polymerization N and fraction of monomers of type A, f, see Fig. 3.3 for a sketch of the molecule. We follow the approach in ref. [12] in the calculation.

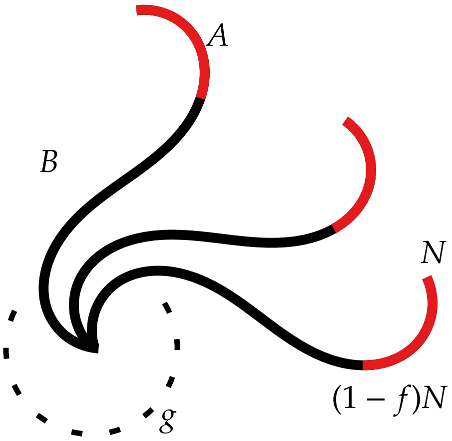

Figure 3.3: Sketch of g-armed end-labeled star. The star has g arms that each consists of N monomers. The outer fN monomers are deuterated.

The structure factor as function of scattering vector $\vec{q}$ is given as

$$S(\vec{q}) = \frac{1}{\frac{S_{AA}(\vec{q})+S_{BB}(\vec{q})+2S_{AB}(\vec{q})}{S_{AA}(\vec{q})S_{BB}(\vec{q})-S_{AB}^2(\vec{q})} - 2\chi} \tag{3.1}$$

and the contribution from correlations between $X, Y = A, B$ monomers, S_{XY}, is given as

$$S_{XY}(\vec{q}) = \frac{1}{N_X + N_Y} \sum_{n=1}^{N_X} \sum_{m=1}^{N_Y} \left\langle e^{i\vec{q}(\vec{R}_n - \vec{R}_m)} \right\rangle \tag{3.2}$$

where the average $\langle \ldots \rangle$ is for an ideal chain with Gaussian statistics and $\vec{R}_n$ is the position vector of the n'th monomer. If the total number of monomers is large, the summation can be replaced by an integral [12]. In the following, we employ this replacement to calculate the different contributions. We choose to keep the contributions for monomers belonging to the same and different arms separate. This explicit separation will be useful later when we calculate the limits of the structure factor for small and large qR_g.

We first calculate the contribution from correlations between monomers of type B, i.e. the inner block:

$$S_{BB}(q) = \frac{1}{gN}\left[\underbrace{g\int_0^{(1-f)N} \mathrm{d}n \int_0^{(1-f)N} \mathrm{d}n' e^{-\alpha|n-n'|}}_{\text{Intra-chain contribution, } S^{I}_{BB}(q)}\right.$$

$$\left. + \underbrace{g(g-1)\int_0^{(1-f)N} \mathrm{d}n \int_0^{(1-f)N} \mathrm{d}m\, e^{-\alpha(n+m)}}_{\text{Inter-chain contribution, } S^{II}_{BB}(q)}\right] \tag{3.3}$$

where we have defined $\alpha \equiv \frac{Nb^2}{6}q^2 = R_g^2 q^2/N$ for notational simplicity. The prefactors g and $g(g-1)$ arise due to combinatorics: There are g arms that each contribute with intra-chain correlations and each arm has inter-chain correlations with $g-1$ other arms.

We first calculate the intra-chain contribution

$$\begin{aligned}
S^{I}_{BB}(q) =& \frac{1}{N}\int_0^{(1-f)N} \mathrm{d}n \int_0^{(1-f)N} \mathrm{d}n' e^{-\alpha|n-n'|} \\
=& \frac{2}{N}\int_0^{(1-f)N} \mathrm{d}n \int_0^{n} \mathrm{d}n' e^{-\alpha(n-n')} \\
=& \frac{2}{N\alpha}\int_0^{(1-f)N} \mathrm{d}n\,(1-e^{-\alpha n}) \\
=& \frac{2}{N\alpha}\left[(1-f)N + \frac{1}{\alpha}\left(e^{-\alpha(1-f)N} - 1\right)\right] \\
=& \frac{2}{N\alpha^2}\left[e^{-\alpha(1-f)N} + (1-f)N\alpha - 1\right] \\
& x \equiv N\alpha \\
=& \frac{2N}{x^2}\left[e^{-(1-f)x} + (1-f)x - 1\right] \\
=& Nh(1-f, x)
\end{aligned} \tag{3.4}$$

where $h(f,x)$ is the generalized Debye function [61]:

$$\begin{aligned} h(f,x) =& \frac{2}{x^2}\left[e^{-fx} + fx - 1\right] && (3.5)\\ x =& \frac{N^2b^2}{6}q^2 = R_g^2q^2. && (3.6) \end{aligned}$$

Then we calculate the inter-chain contribution

$$\begin{aligned} S^{II}_{BB}(q) =& \frac{g-1}{N}\int_0^{(1-f)N} \mathrm{d}n \int_0^{(1-f)N} \mathrm{d}m e^{-\alpha|n+m|}\\ =& \frac{g-1}{N}\left[\int_0^{(1-f)N} \mathrm{d}n e^{-\alpha n}\right]^2\\ =& \frac{g-1}{N\alpha^2}\left[e^{-\alpha(1-f)N} - 1\right]^2\\ =& \frac{g-1}{N\alpha^2}\left[e^{-2\alpha(1-f)N} - 2e^{-\alpha(1-f)N} + 1\right]\\ =& \frac{(g-1)N}{x^2}\left[e^{-2(1-f)x} - 2e^{-(1-f)x} + 1\right]\\ =& \frac{(g-1)N}{2}\left[h(2(1-f),x) - 2h(1-f,x)\right] && (3.7) \end{aligned}$$

The calculation of $S_{AA}(q)$ and $S_{AB}(q)$ are carried out in the similar ways. For $S_{AA}(q)$ we get

$$\begin{aligned} S_{AA}(q) =& \frac{1}{gN}\left[\underbrace{g\int_{(1-f)N}^{N} \mathrm{d}n \int_{(1-f)N}^{N} \mathrm{d}n' e^{-\alpha|n-n'|}}_{\text{Intra chain contribution, } S^{I}_{AA}(q)}\right.\\ & \left. + \underbrace{g(g-1)\int_{(1-f)N}^{N} \mathrm{d}n \int_{(1-f)N}^{N} \mathrm{d}m e^{-\alpha(n+m)}}_{\text{Inter chain contribution, } S^{II}_{AA}(q)}\right]\\ S^{I}_{AA}(q) =& Nh(f,x) && (3.8) \end{aligned}$$

$$S^{II}_{AA}(q) = \frac{(g-1)N}{2}\left[h(2,x) + h(2(1-f),x) - 2h(2-f,x)\right], \tag{3.9}$$

and for $S_{AB}(q)$ we get

$$\begin{aligned} S_{AB}(q) = & \frac{1}{gN}\left[\underbrace{g\int_{(1-f)N}^{N} \mathrm{d}n \int_{0}^{(1-f)N} \mathrm{d}n' e^{-\alpha|n-n'|}}_{\text{Intra chain contribution, } S^{I}_{AB}(q)}\right. \\ & \left. + \underbrace{g(g-1)\int_{(1-f)N}^{N} \mathrm{d}n \int_{0}^{(1-f)N} \mathrm{d}m e^{-\alpha(n+m)}}_{\text{Inter chain contribution, } S^{II}_{AB}(q)}\right] \end{aligned}$$

$$S^{I}_{AB}(q) = \frac{N}{2}\left[h(1,x) - h(f,x) - h(1-f),x\right] \tag{3.10}$$

$$S^{II}_{AB}(q) = \frac{(g-1)N}{2}\left[h(2-f,x) - h(1,x) - h(2(1-f),x) + h(1-f,x)\right]. \tag{3.11}$$

The structure factor is found by combining Eq. 3.1, 3.4, 3.7, and 3.8-3.11.

3.3.2 Cases: $g = 1$, $g = 2$, and $g = 3$

To validate the found expression, we check that it reduces to the known expressions for $g = 1$ and $g = 2$ that are linear AB diblock copolymers and ABA triblock copolymers respectively. In the case of ABA triblock copolymers, the A blocks are symmetric.

Linear AB block Copolymer, $g = 1$

For $g = 1$, the molecule is a linear AB diblock as described by Leibler[61]. For a linear AB diblock, there are no inter-chain contributions, and we obtain the following expressions:

$$\begin{aligned} S_{AA}(q) &= Nh(1-f,x) \\ S_{BB}(q) &= Nh(f,x) \\ S_{AB}(q) &= N/2\left[h(1,x) - h(f,x) - h(1-f,x)\right] \end{aligned}$$

which is the same result as in refs. [61, 12].

Linear Triblock Copolymer, $g = 2$

The result for a two armed star, or linear triblock copolymer is given in ref. [9]. However, they use a slightly different notation where N^* is the total number of monomers in the triblock and the number of deuterated monomers in each end, f^*N^*, is also calculated relative to the total number of monomers in the molecule. Also they mix their triblocks with homopolymer molecules such that the volume fraction of triblocks is ϕ. To compare our result to theirs, we need to convert either of the expressions to the other notation. We choose to convert ours such that it is given in both notations if the other notation turns out to be more convenient in some context. We therefore first convert our expression to the notation of Hassager et al. and then evaluate the expressions for $g = 2$. The variables in the two notations are linked in the following way

$$\begin{aligned} x =& x^*/g \\ f =& f^* g \\ \text{Prefactor } N =& N^*/g \end{aligned} \tag{3.12}$$

which means that the Debye functions transform as follows

$$\begin{aligned} h(f,x) =& g^2 h(f^*,x^*) \\ h(1-f,x) =& g^2 h((1-gf^*)/g,x^*) \\ h(2(1-f),x) =& g^2 h(2(1-gf^*)/g,x^*) \\ h(2-f,x) =& g^2 h((2-gf^*)/g,x^*) \\ h(2,x) =& g^2 h(2/g,x^*) \\ h(1,x) =& g^2 h(1/g,x^*). \end{aligned} \tag{3.13}$$

In the notation of Hassager et al., the inter and intra-chain contributions to S_{AA}, S_{BB}, and S_{AB} for a g armed star are given as

$$\begin{aligned} S^I_{BB}(q) =& gN^* h((1-gf^*)/g,x^*) \\ S^{II}_{BB}(q) =& \frac{N^* g(g-1)}{2}\left[h(2(1-gf^*)/g,x^*) - 2h((1-gf^*)/g,x^*)\right] \\ S^I_{AA}(q) =& gN^* h(f^*,x^*) \\ S^{II}_{AA}(q) =& \frac{N^* g(g-1)}{2}\left[h(2/g,x^*) + h(2(1-gf^*)/g,x^*) - 2h((2-gf^*)/g,x^*)\right] \\ S^{II}_{AB}(q) =& \frac{N^* g}{2}\left[h(1/g,x^*) - h(f^*,x^*) - h((1-gf^*)/g,x^*)\right] \end{aligned}$$

$$\begin{aligned} S^{II}_{AB}(q) =& \frac{N^{*}g(g-1)}{2}\left[h((2-gf^{*})/g,x^{*})-h(1/g,x^{*})-h(2(1-gf^{*})/g,x^{*})\right. \\ & \left.+h((1-gf^{*})/g,x^{*})\right]. \end{aligned} \tag{3.14}$$

For $g = 2$ we get

$$\begin{aligned} S^{I}_{BB}(q) =& 2N^{*}h((1-2f^{*})/2,x^{*}) \\ S^{II}_{BB}(q) =& N^{*}\left[h((1-2f^{*}),x^{*})-2h((1-2f^{*})/2,x^{*})\right] \\ S^{I}_{AA}(q) =& 2N^{*}h(f^{*},x^{*}) \\ S^{II}_{AA}(q) =& N^{*}\left[h(1,x^{*})+h((1-2f^{*}),x^{*})-2h((1-f^{*}),x^{*})\right] \\ S^{II}_{AB}(q) =& N^{*}\left[h(1/2,x^{*})-h(f^{*},x^{*})-h((1-2f^{*})/2,x^{*})\right] \\ S^{II}_{AB}(q) =& N^{*}\left[h(1-f^{*},x^{*})-h(1/2,x^{*})-h((1-2f^{*}),x^{*})+h((1-2f^{*})/2,x^{*})\right], \end{aligned} \tag{3.15}$$

which when combining the inter and intra-chain contributions give

$$\begin{aligned} S_{BB}(q) =& S^{I}_{BB}(q)+S^{II}_{BB}(q) = N^{*}h((1-2f^{*}),x^{*}) \\ S_{AA}(q) =& S^{I}_{AA}(q)+S^{II}_{AA}(q) = N^{*}\left[2h(f^{*},x^{*})+h(1,x^{*})+h((1-2f^{*}),x^{*})\right. \\ & \left.-2h((1-f^{*}),x^{*})\right] \\ S_{AB}(q) =& S^{I}_{AB}(q)+S^{II}_{AB}(q) = N^{*}\left[h(1-f^{*},x^{*})-h(f^{*},x^{*})-h((1-2f^{*}),x^{*})\right] \end{aligned} \tag{3.16}$$

consistent with the expression in ref. [9] for $\phi = 1$.

Three Armed Stars, $g = 3$

For the current stud,y the relevant case is $g = 3$. For this case, we obtain

$$\begin{aligned} S^{I}_{BB}(q) =& Nh(1-f,x) \\ S^{II}_{BB}(q) =& N\left[h(2(1-f),x)-2h(1-f,x)\right] \\ S^{I}_{AA}(q) =& Nh(f,x) \\ S^{II}_{AA}(q) =& N\left[h(2,x)+h(2(1-f),x)-h(2-f,x)\right] \\ S^{I}_{AB}(q) =& \frac{N}{2}\left[h(1,x)-h(f,x)-h(1-f),x\right] \\ S^{II}_{AB}(q) =& N\left[h(2-f,x)-h(1,x)-h(2(1-f),x)+h(1-f,x)\right]. \end{aligned} \tag{3.17}$$

3.3.3 Limiting Behaviors

We also check the validity of the structure factor for a three armed star, Eq. 3.17 and 3.1, by examining its behavior in the limits $qR_g = x \gg 1$ and $qR_g = x \ll 1$ where we expect $S(q) \to 0$. In the low q limit, the structure factor tends to zero because we consider a region much larger than the length of the individual chains and the concentration of segments of type A (and B) is constant. The high q limit of the structure factor reflects the insensitivity to the interaction between monomers of type A and B on short length scales.

We test the structure factor expression in the limits of $qR_g = x \gg 1$ and $qR_g = x \ll 1$. In the high q-limit, the generalized Debye functions can be approximated as

$$h(f,x) = \frac{2}{x^2}\left(e^{-fx} + fx - 1\right) \approx \frac{2f}{x}. \tag{3.18}$$

With this approximation of the generalized Debye functions, the structure factor contributions are approximately given by the following expressions:

$$\begin{aligned}
S^{I}_{BB}(q) =& Nh(1-f,x) \approx N\frac{2(1-f)}{x} \\
S^{II}_{BB}(q) =& \frac{(g-1)N}{2}\left[h(2(1-f),x) - 2h(1-f,x)\right] \\
\approx& \frac{(g-1)N}{2}\left[\frac{4(1-f)}{x} - \frac{4(1-f)}{x}\right] = 0 \\
S^{I}_{AA}(q) =& Nh(f,x) \approx N\frac{2f}{x} \\
S^{II}_{AA}(q) =& \frac{(g-1)N}{2}\left[h(2,x) + h(2(1-f),x) - 2h(2-f,x)\right] \\
\approx& \frac{(g-1)N}{2}\left[\frac{4}{x} + \frac{4(1-f)}{x} - \frac{4(2-f)}{x}\right] = 0 \\
S^{I}_{AB}(q) =& \frac{N}{2}\left[h(1,x) - h(f,x) - h(1-f),x\right] \approx \frac{N}{2}\left[\frac{2}{x} - \frac{2f}{x} - \frac{2(1-f)}{x},x\right] = 0 \\
S^{II}_{AB}(q) =& \frac{(g-1)N}{2}\left[h(2-f,x) - h(1,x) - h(2(1-f),x) + h(1-f,x)\right] \\
\approx& \frac{(g-1)N}{2}\left[\frac{2(2-f)}{x} - \frac{2}{x} - \frac{4(1-f)}{x} + \frac{2(1-f)}{x}\right] = 0.
\end{aligned} \tag{3.19}$$

We thus find that, in the limit of $qR_g \gg 1$, the inter-chain correlations do not contribute to the structure factor, and the limiting value of the structure factor then becomes

$$\begin{aligned} S(q) \approx & \frac{S_{AA}S_{BB} - S_{AB}^2}{S_{AA} + S_{BB} + 2S_{AB}} \approx \frac{S_{AA}S_{BB}}{S_{AA} + S_{BB}} \approx \frac{N\frac{2f}{x}N\frac{2(1-f)}{x}}{N\frac{2f}{x} + N\frac{2(1-f)}{x}} \\ = & N\frac{4f(1-f)}{2x} = \frac{12f(1-f)}{b^2q^2} \end{aligned} \tag{3.20}$$

which is consistent with the result in Doi [12]. For $f = 0$ or $f = 1$, the block co-polymer is a homopolymer and the structure factor and thus scattering intensity is zero as required.

The low q limit $qR_g \ll 1$ is

$$S(q) \approx \frac{2}{3}f^2(1-f)^2Nx \tag{3.21}$$

which is also consistent with the result for one arm obtained in [12]. In both limits, the number of arms does not affect the structure factor, but it may affect the structure factor for $qR_g \sim 1$.

3.3.4 Plots of the Structure Factor

To gain intuition for the structure factor in the region $qR_g \sim 1$, we vary f, N, g through a few values and plot the results in Fig. 3.4 and 3.5. We study how the peak shifts as a function of the parameters. Later, we apply the RPA-structure factor to describe a star with parameter values $f = 0.075$, $g = 3$, and $N = 135$ and therefore these values are the starting points for all plots. The structure factor peaks at $qR_g \sim 1$ due to the correlation hole effect where the probability of two monomers of the same type belonging to different chains close to each other is slightly decreased [61]. In the following, we characterize the influence of the parameters f, g, and N through shifts in the peak position.

In Fig. 3.4, we see that the peak shifts slightly towards smaller q with increasing number of arms g or increasing degree of polymerization N which is reasonable since an increasing number of arms or increasing degrees of polymerization increases the radius of gyration, R_g. In Fig. 3.5, we see that the peak shifts to larger values of q for decreasing f which is consistent with the behavior for linear polymers in Leibler's work [61]. Though in principle, the RPA-structure factor for a g-armed star can be evaluated for any value of g, we only expect it to describe stars with few arms well because it does not take exclude volume interactions into account, and they become increasingly important as we increase the number of arms g.

In Fig. 3.6, we plot the structure factor and the high-q limit and see that for $q > 0.2$ Å^{-1}, they deviate with less than 5%. This will be important in Sec. 3.4.3 where we use the high-q limit of the structure factor to estimate the incoherent background in SANS data.

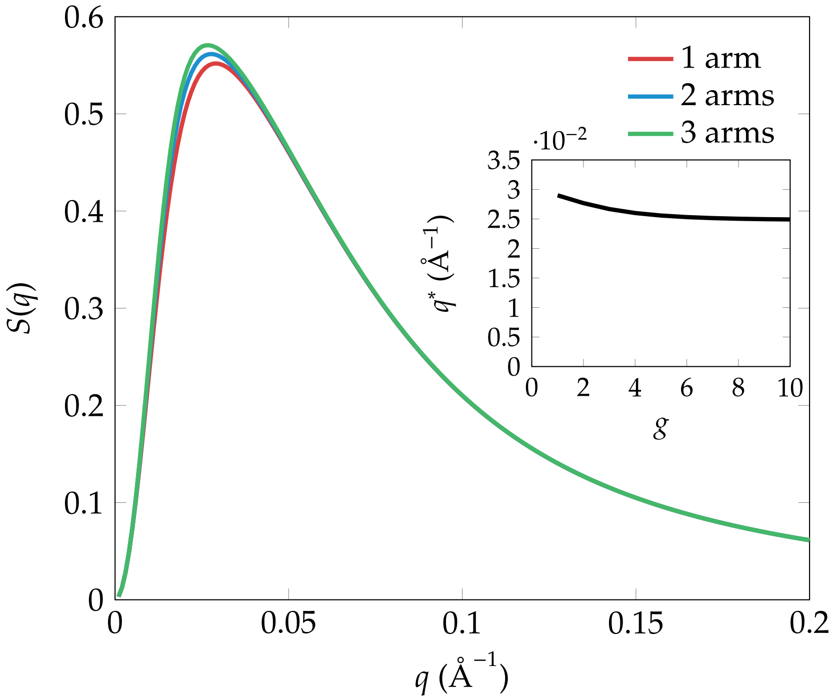

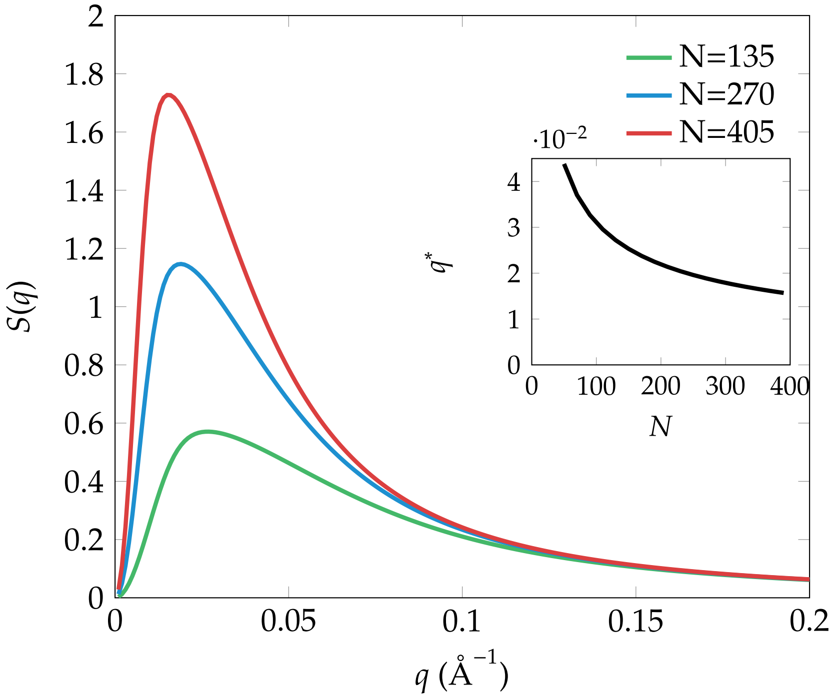

Figure 3.4: RPA-structure factor sensitivity to number of arms g and degree of polymerization in each arm N. In a) we increase the number of arms from one to three keeping $N = 135$ and $f = 0.075$ fixed, and in b) we vary N while keeping $g = 3$ and $f = 0.075$ constant. The insets show the peak position q^* as a function of the varied parameter g or N respectively.

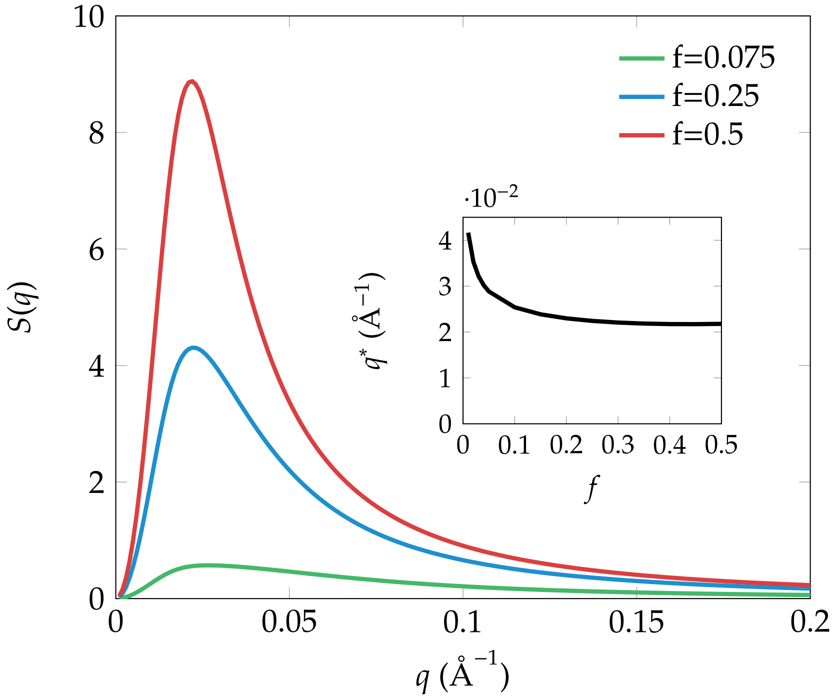

Figure 3.5: RPA-structure factor sensitivity to deuterated fraction f. We plot the structure factor $S(q)$ for three different deuteration fractions while keeping $g = 3$ and $N = 135$ fixed. The inset shows the peak position q^* as a function of f.

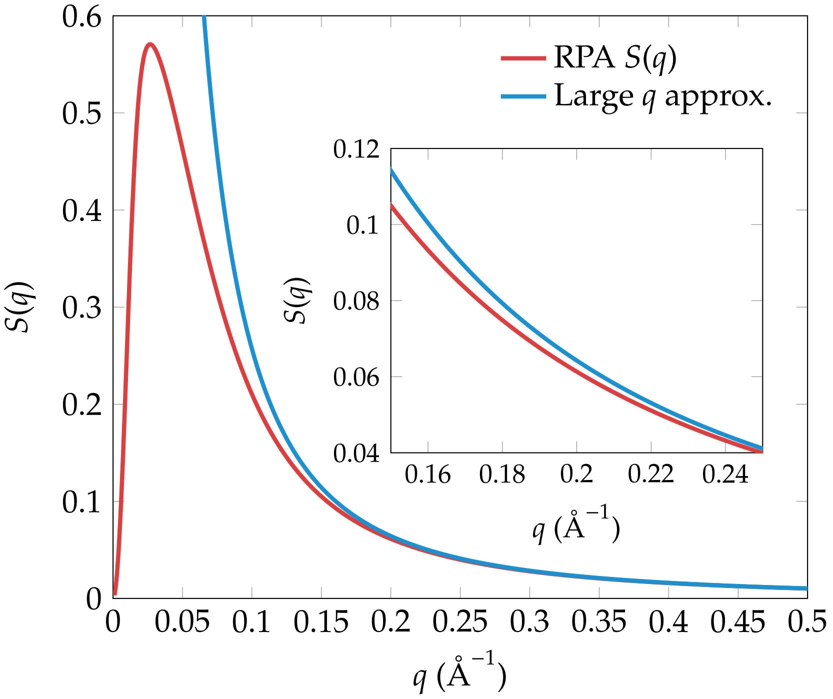

Figure 3.6: Comparison of RPA structure factor and high q-approximation. Inset shows that for $q > 0.2$ Å^{-1} the deviation between the structure factor and the approximation is 5% or less.

3.4 Small Angle Neutron Scattering

In this section, we introduce the samples for neutron scattering and the experimental setup at QUOKKA and present the 2D data and our results.

3.4.1 Samples

For studying three-armed stars in non-linear extensional flow using SANS end-deuterated stars were synthesized to obtain information on end-to-end correlations. The end-deuterated star is sketched in Fig. 3.7. The three armed stars have a molecular weight of M_w = 309.1 kg/mol and a polydispersity index of PDI=1.3. The end of each arm is deuterated corresponding to a deuteration fraction of 7.5 %. The molecules are synthesized and their molecular weight is measured by Ph.D. Andriy Dorokhin, see ref.[62].

Extensional Rheology

All samples were stretched using the filament stretch rheometer at a Hencky strain rate of 0.06 s^{-1} at T=125 ° C to a final Hencky strain of $\varepsilon_f = 3$ and quenched at different relaxation times ranging from no relaxation to full relaxation (FR) as listed in Tab. 3.1.

3.4.2 Experimental Settings

The SANS experiment was performed by Chris Garvey, instrument scientist at the small angle neutron scattering instrument QUOKKA at Australia's nuclear science and technology organization (ANSTO), using four instrument settings. The settings are summarized in Tab. 3.2.

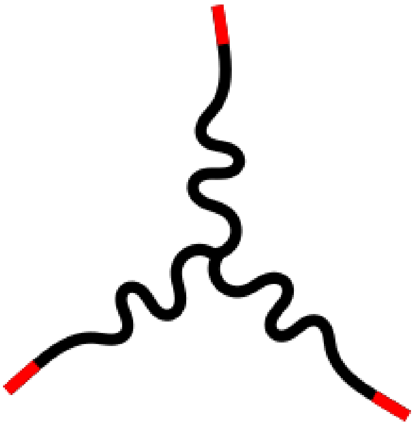

Figure 3.7: End-deuterated star. Black represents hydrogenous polystyrene and red deuterated polystyrene. The three arms are symmetric such that the deuteration fraction in each arm is the same.

Hencky strain rate (s^{-1}) at T=125 ° C	Relaxation time (s)
0.06	0
	5
	200
	4000
	Fully relaxed (FR)

Table 3.1: The sample series for end-labeled stars measured at ANSTO

	2 m	5 m	14 m	20 m
Wavelength (Å), $\Delta\lambda/\lambda = 0.1$	5	5	5	8
Source-Sample distance (m)	14	10	14	20
Sample-Detector distance (m)	2	5	14	20
Measurement time (h)	0.25	1	3	9
Covered q-range (Å^{-1})	0.25	1	3	9

Table 3.2: Instrument settings for QUOKKA. The end-labeled samples were measured at QUOKKA using the four instrument settings 2 m, 5 m, 14 m and 20 m.

3.4.3 Data Reduction

The obtained 2D SANS data was corrected for the measured scattering intensities for the blocked beam and the empty beam and for detector sensitivity using the QUOKKA-macro for Igor Pro. Furthermore, the data was rotated to account for the slight sample rotation, and the incoherent scattering was estimated and subtracted using code written for the purpose.

Data Reduction in Igor Pro

All 2D patterns, I_{SAM}, were corrected to obtain I_{COR} by subtracting the measured scattering intensities from the blocked beam, I_{BCK}, and empty beam, I_{EMP}, weighted by the respective transmissions $\tilde{T}$ using

$$I_{\mathrm{COR}} = (I_{\mathrm{SAM}} - I_{\mathrm{BCK}}) - \frac{\tilde{T}_{\mathrm{SAM}}}{\tilde{T}_{\mathrm{EMP}}} (I_{\mathrm{EMP}} - I_{\mathrm{BCK}}) . \tag{3.22}$$

The blocked and empty beam subtracted data is corrected for detector sensitivity, by dividing the 2D scattering data pixel by pixel with the 2D scattering pattern of an isotropic scatterer, here plexiglass. We present the resulting 2D patterns in the next subsection.

Qualitative Analysis

Looking first at the 2D data from the 2 m, 5 m and 14 m settings, Fig. 3.8, 3.9, and 3.10 we see that the scattering patterns change from highly anisotropic to close to ideally isotropic with relaxation time. The striking character of the anisotropy of the 0 s, 5 s and partly 200 s patterns is most clearly seen from the 5 m and 14 m settings. The 0 s and 5 s scattering patterns are characterized by four horizontal lines: Two with high intensity on the horizontal axis and two with lower intensity above and below the beamstop. The latter are most visible in the 14 m setting, Fig. 3.10. We sketch the scattering in pattern in Fig. 3.11 for clarity.

For the 200 s sample, the bright peaks on the horizontal axis are absent, and the peaks above and below the beamstop are shifted slightly towards larger q. We return to the quantitative interpretation of these features in Sec. 3.4.4. The lines are not perfectly horizontal due to sample rotation, which we discuss in Sec. 3.4.3. In the 14 m setting, it is also apparent that all five patterns have bright spots on each side of the beamstop on the horizontal axis and the fully relaxed sample also has excess scattering on the vertical axis. In the 20 m setting, we only see this scattering, see Fig. 3.12. It is the topic of Chap. A. Furthermore, there seem to be an issue with overestimation of the background for the 200 s and 4000 s samples in the 14 m setting. This is most likely due to issues with the transmissions of the samples leading to the subtraction of too much background. However, the results of this study rely, not on the absolute scattering intensity, but on the position of the maxima in intensity, and the following conclusions are therefore not affected by this issue.

Sample Alignment and Data Rotation

Most samples are made from several filaments. The individual filaments need to be aligned to each other to avoid smearing of the features in the scattering pattern. This is relatively easy to achieve for samples corresponding to larger final Hencky strains and short relaxation times since they are very close to cylindrical in shape and can therefore be packed closely. For filaments corresponding to longer relaxation times, the shape approaches an hour glass and thus relative alignment is more challenging. However this only posses a challenge at the longest relaxation times where the scattering patterns are isotropic. An example of filament alignment

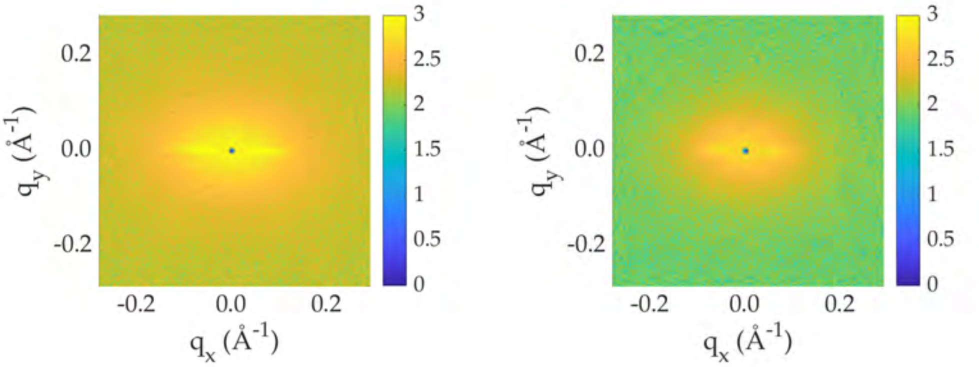

(a) t = 0 s

(b) t = 5 s

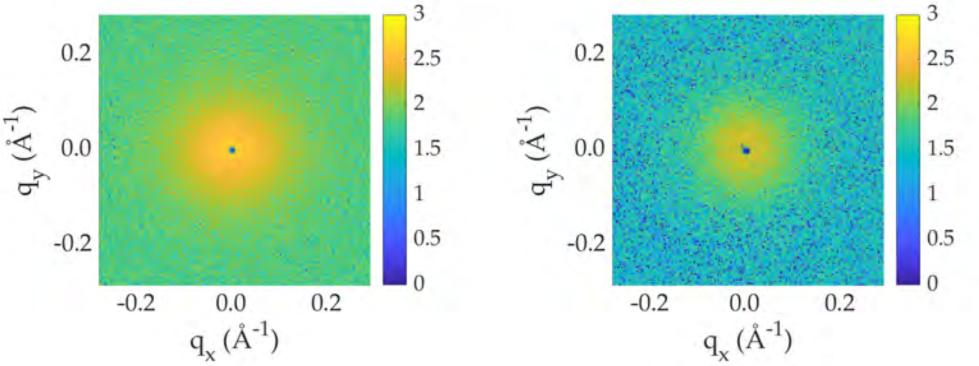

(c) t = 200 s

(d) t = 4000 s

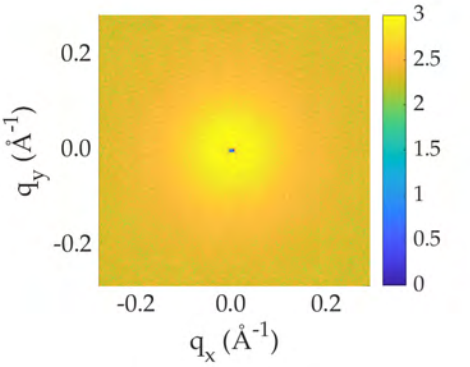

(e) FR

Figure 3.8: 2D data corrected for empty and blocked beam, 2 m setting.

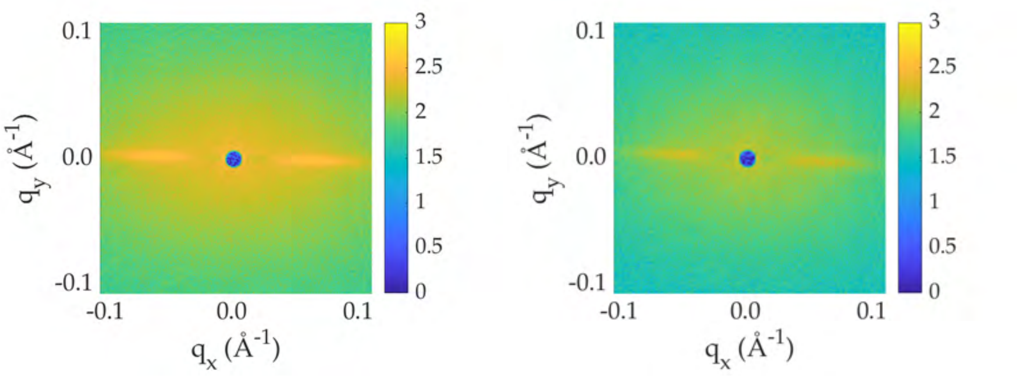

(a) t = 0 s **(b)** t = 5 s

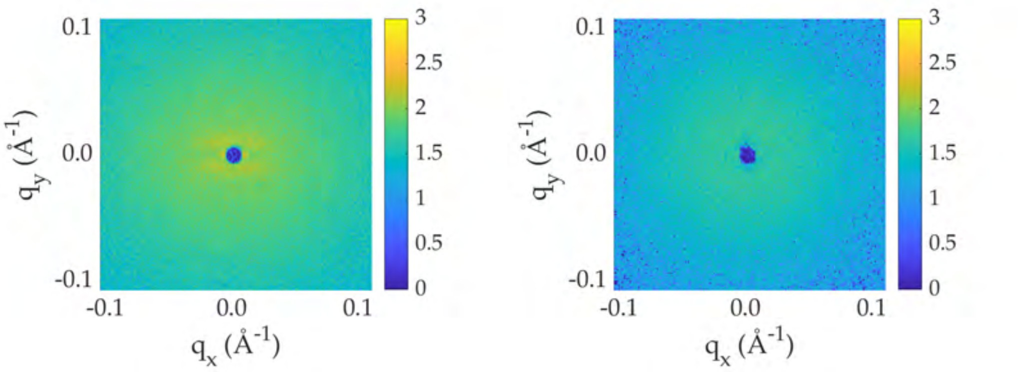

(c) t = 200 s **(d)** t = 4000 s

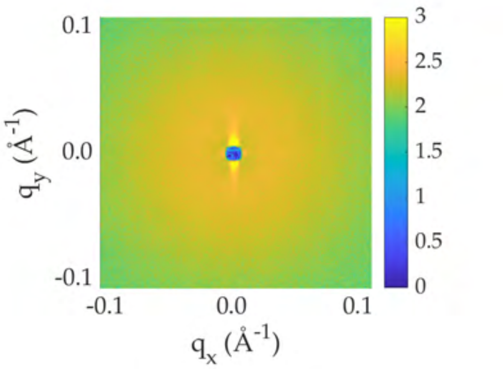

(e) FR

Figure 3.9: 2D data corrected for empty and blocked beam, 5 m setting.

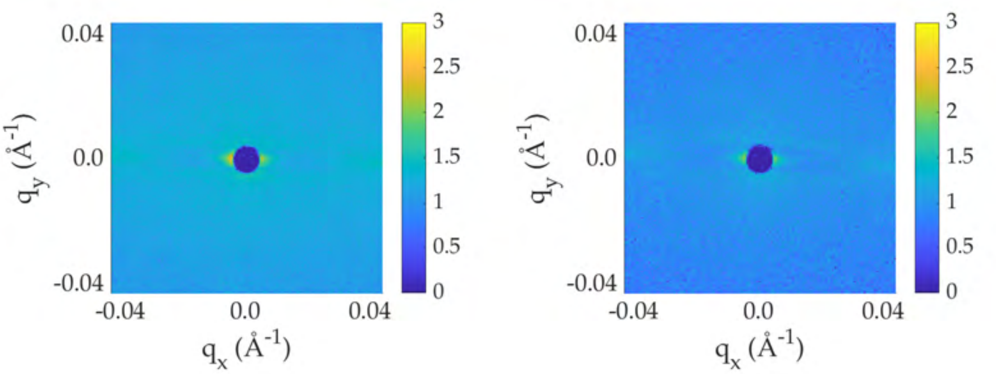

(a) t = 0 s

(b) t = 5 s

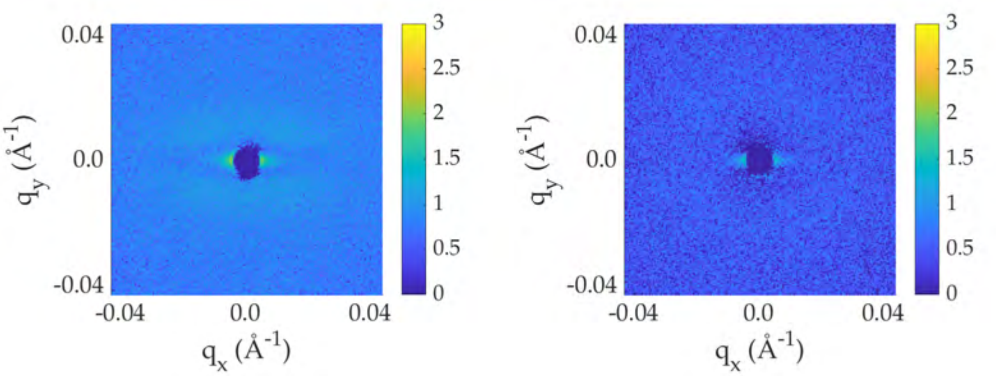

(c) t = 200 s

(d) t = 4000 s

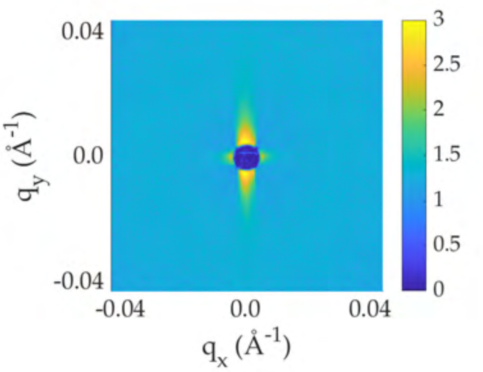

(e) FR

Figure 3.10: 2D data corrected for empty and blocked beam, 14 m setting.

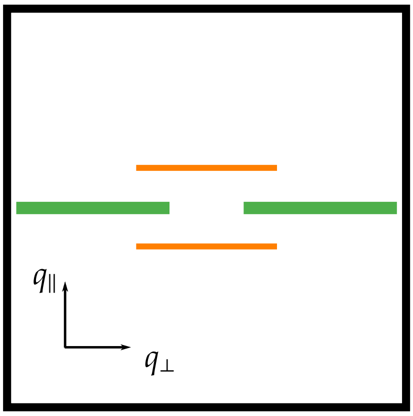

Figure 3.11: Schematic drawing of 0 s scattering pattern. The green lines show the peaks on the horizontal axis and the orange lines the peaks above and below the beamstop.

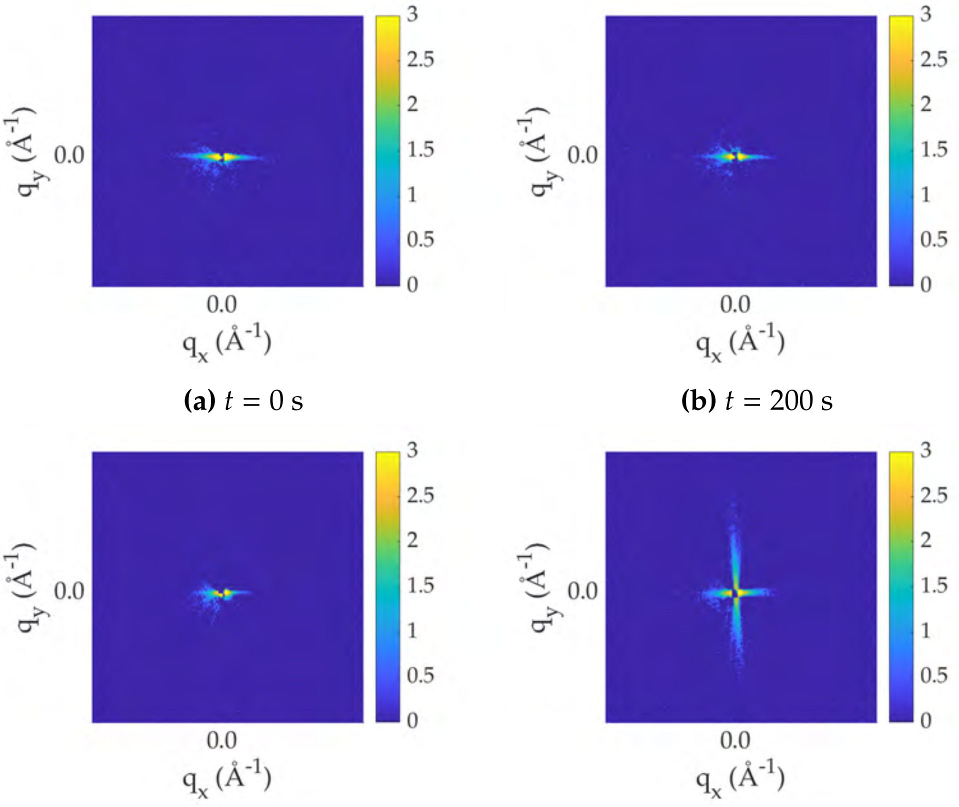

(a) t = 0 s **(b)** t = 200 s

(c) t = 4000 s **(d)** FR

Figure 3.12: 2D data corrected for empty and blocked beam, 20 m setting.

Figure 3.13: Samples for Neutron Scattering. The sample consists of several filaments aligned and attached to a cadmium ring and loaded in the sample holder. The sample is the end-labeled star for $t = 5$ s measured at QUOKKA in December 2016. Photo: Chris Garvey.

is shown in Fig. 3.13. When the filaments are aligned to each other the samples are attached to a cadmium ring that is mounted in a sample holder. In mounting the ring, perfect (vertical) alignment is difficult to achieve, see Fig. 3.13. For this reason, the peaks on the horizontal axis in e.g. Fig. 3.9 form lines slightly tilted from the horizontal axis.

In the following analysis, we need to take the sample rotation into account, and we choose to rotate the data before further analysis.

Determination of Rotation Angle For the end-labeled data sets corresponding to $t = 0$ s and $t = 5$ s the rotation angle is found using the peaks on the horizontal axis and the data sets from the 5 m setting The steps of the procedure are illustrated for the $t = 5$ s in Fig. 3.14. For single columns of the data, the intensity as function of pixel number is fitted to find the position of the center of the peak on the horizontal axis, see inset on Fig. 3.14a. The analytical expression fitted to data is not important as long as it captures the peak position well. We make a simple choice and fit the intensity for the center part of the pixel columns to the sum of two Gaussians with the same center but different

$$I_{\mathrm{fit}}(x) = A_1 \exp\left(-(x-x_0)^2/\sigma_1^2\right) + A_2 \exp\left(-(x-x_0)^2/\sigma_2^2\right) + k. \tag{3.23}$$

We show an example of the intensity for a pixel column fitted with the expression above in Fig. 3.14a.

Next, we plot the peak center found from the fits as a function of pixel column number to a first degree polynomial with slope a, see Fig. 3.14b. The sample rotation angle χ is found as $\chi = \arctan a$. In the case of the 5 s samples, $a = -0.0498 \rightarrow \theta = -2.8°$. We therefore rotate the scattering pattern by $-\theta = 2.8°$. The rotated data is shown next to the data before rotation for the 5 s sample in the 5 m setting in Fig. 3.15. The data sets for all detector settings for each sample are rotated by the same angle. We attempted to find the rotation angle for the t 200 s using the peaks above and below the beamstop and found that it was well aligned as is. The 4000 s and fully relaxed data sets were not rotated.

Sectors and Slabs

In the following sections, we will use two different averages over the area of the detector that we will call sectors and slabs. We define sectors as an area that spans an angular range from the beam center and out to the detector edge, like a slice of a pie, and slabs as vertical or horizontal rectangles. We illustrate sectors and slabs in Fig. 3.16. Due to the symmetry of uniaxial extension, the scattering intensities in the four quadrants are related and therefore we find up to four equivalent sectors or slabs illustrated in red and blue on the figure. By averaging over a sector or slab, we obtain 1D data $I(q)$.

Background Subtraction

In Sec. 3.4.3 we described how the measured scattering intensity was corrected for the blocked and empty beam and detector efficiency. Here, we show how we estimate and subtract the incoherent background originating from the sample.

Due to the cylindrical shape of the filaments and that a sample may consist of multiple filaments, the amount of material across the area of the sample and that makes it hard to choose a sample to estimate the incoherent background from. In principle, one could use a sample with the exact same distribution of fully hydrogenated filaments, but this is hard to realize in practice since it would require all samples to have identical dimensions, i.e. not vary in diameter or number of filaments, or a different background sample for each sample. In addition, the excess scattering at small q vary from sample to sample, see e.g. Fig. 3.10 and may also do so between background samples. Instead we use that the scattering intensity

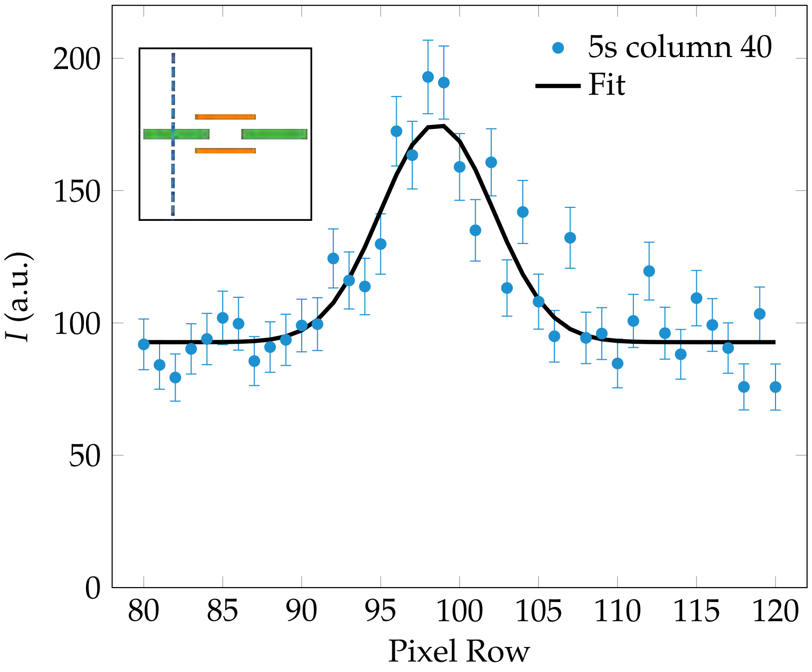

(a)

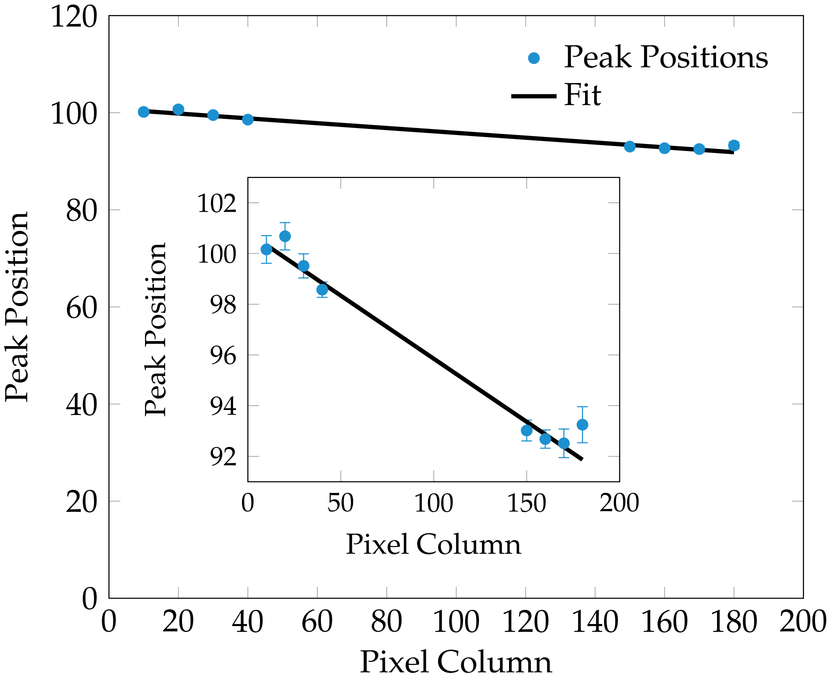

(b)

Figure 3.14: Intermediate steps for rotating 2D data, here 5 m setting for 5 s relaxation. In a) the scattering intensity in each pixel row is plotted for pixel column 40, see inset. The intensity is fitted to Eq. 3.23. In b) the found peak position is plotted as a function of pixel column and fitted to a straight line. The inset is a zoom of the same plot.

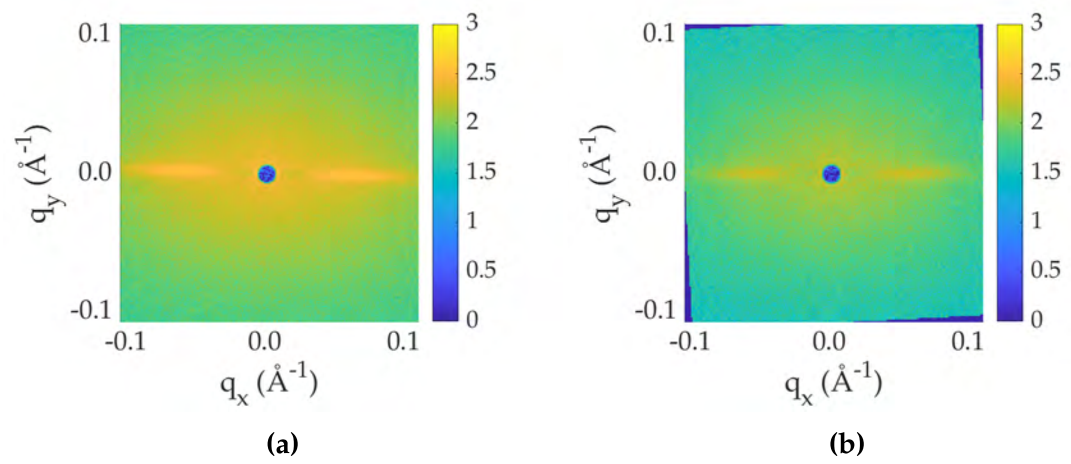

Figure 3.15: Rotation of end-labeled 5 s scattering pattern. In a) the original 2D data, in b) the rotated 2D data. See Fig. 3.14 for intermediate steps.

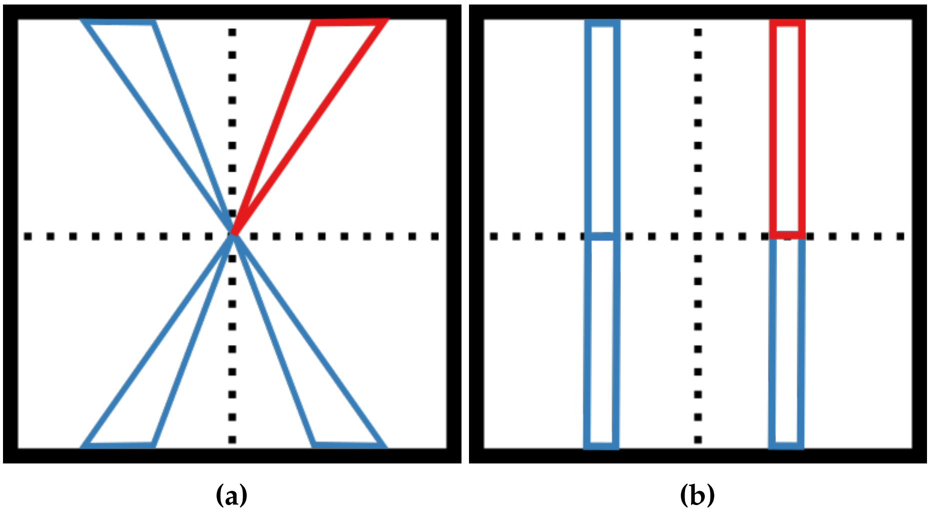

Figure 3.16: Illustration of sectors in a) and slabs in b).

is dominated by the incoherent scattering, which is independent of q, for sufficiently large values of q, .

To estimate the incoherent background for the end-deuterated star samples we use that the high q limit of the random phase approximation structure factor $S(q) \sim q^{-2}$ is within 5 % of $S(q)$ for $q > 0.2$ Å^{-1}, see Eq. 3.20 and Fig. 3.6, and fit $I(q)$ for sector averages at $(45 \pm 5)^\circ$ and $q > 0.2$ Å^{-1} to

$$y = Aq^{-2} + b, \tag{3.24}$$

and use b as our estimate for the incoherent background. We fit to the 45°-sector because we consider it the most neutral region for the stretched samples. In Fig. 3.17, we show the overlap of the 45°-sectors from the 2 m, 5 m, and 14 m setting after an arbitrary scaling. The 2 m data fulfilling $q > 0.2$ Å^{-1} is fitted to Eq. 3.24 . We then scale all data sets to account for varying material amounts in the different samples and subtract the scaled incoherent background. We do this by scaling the incoherent background from all 2 m sectors to the same, but otherwise arbitrary, value. For the 2 m data we then subtract the scaled incoherent background. For the 5 m and 14 m setting, we also scale by the arbitrary factor that gave the overlap in Fig. 3.17 before subtract. The resulting 2D patterns for the 5 m and 14 m setting are shown in Fig. 3.18 and 3.19.

3.4.4 Data Analysis

After the data reduction presented in the previous section, we are now ready to analyze the data. As mentioned in the beginning of the chapter, the data for the 0 s relaxation and fully relaxed samples and their interpretation are already published in Mortensen et al.[53]. Here, we give a brief summary of the findings of the publication and discuss the remaining three data sets in more detail.

Fully Relaxed Sample

For the fully relaxed scattering pattern, we assume that the hydrogenous and deuterated segments are uniformly mixed, i.e. that there is no microscopic phase separation. In this case, the scattering intensity is given by the random phase approximation structure factor, which we calculate in Sec. 3.3. Due to the extra scattering at small q, we omit the sectors $(0 \pm 20)^\circ$, $(180 \pm 20)^\circ$, $(90 \pm 10)^\circ$, and $(270 \pm 10)^\circ$, the remaining sectors are averaged for the 5 m and 14 m setting. The resulting $I(q)$ is plotted in

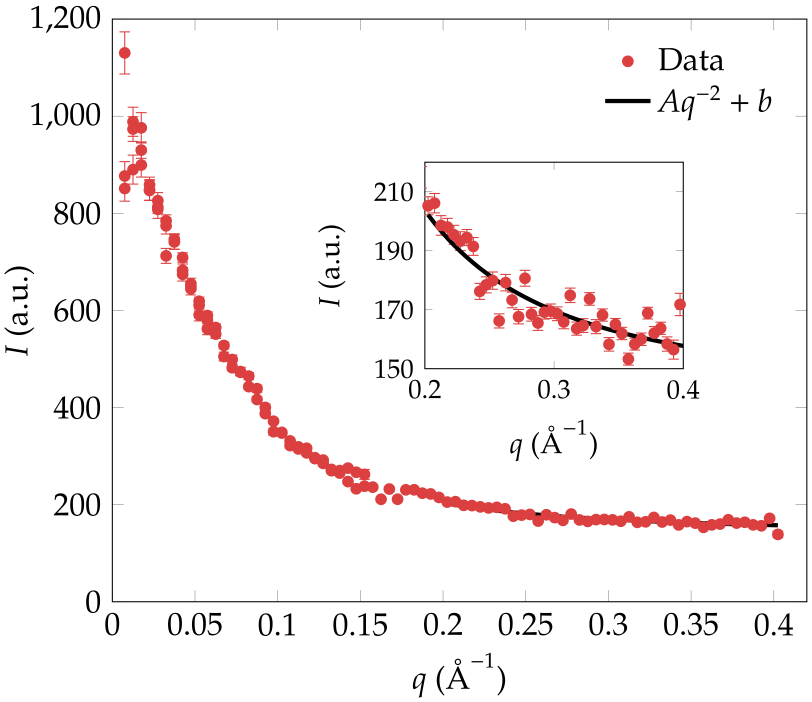

Figure 3.17: Overlap for 2 m, 5 m and 14 m setting and background estimation. For each detector setting the 45°-sector is plotted. The 5 m and 14 m data are arbitrarily scaled to match the 2 m setting data. The data for $q < 0.2$ Å^{-1} is fitted to Eq. 3.24 for incoherent background estimation.

Fig. 3.20 with two fits of the RPA structure factor from Eq. 3.1 to data. In the first fit, the structure factor is fitted with an overall amplitude as the only parameter, which we refer to as scaled, and in the second fit molecular parameters f and N and an overall amplitude were fitting parameters. The scaled RPA-structure factor describes the data for $q > q^*$, where q^* denotes the maximum of the structure factor, reasonably well though there are systematic deviations. The scaled RPA-structure factor predicts q^* to occur at smaller q than what we see in the data, and that may imply a slight overestimate of the molecular weight, see Sec. 3.3. Also we see a slight upturn at the smallest values of q. It could be due to remaining excess scattering or due to polydispersity though that should also shift the peak further towards small q [63, 64] and thus increase the discrepancy between the theoretical prediction and the experimental data. Interestingly in the same reference [63], Bates et al. find that RPA overestimates q^* for most of their linear diblock copolymers, which they explain by deviations from Gaussian statistics close to the spinodal curve. We, however, do not expect

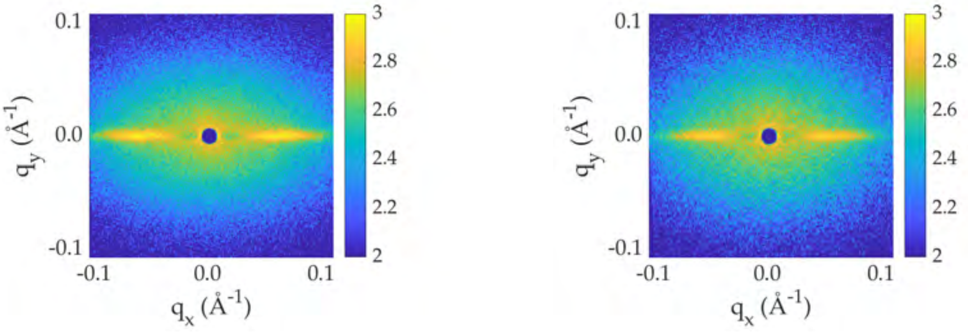

(a) *t* = 0 s **(b)** *t* = 5 s

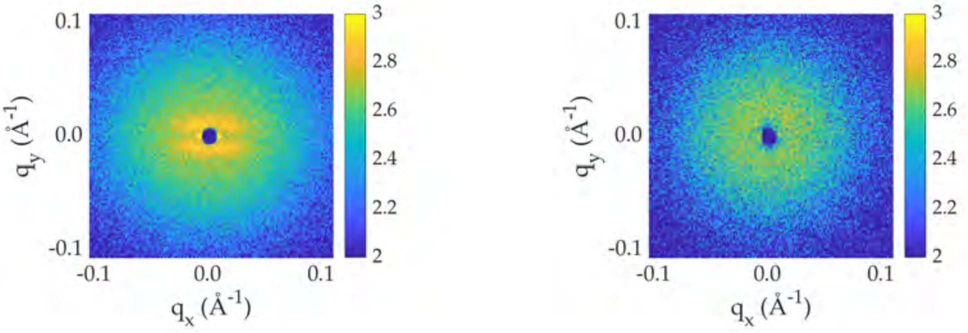

(c) *t* = 200 s **(d)** *t* = 4000 s

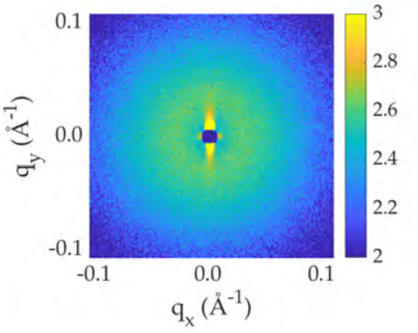

(e) FR

Figure 3.18: Background subtracted and scaled 2D data, 5 m setting. The subfigures show the 2D data for all five samples after rotation, background subtraction and scaling.

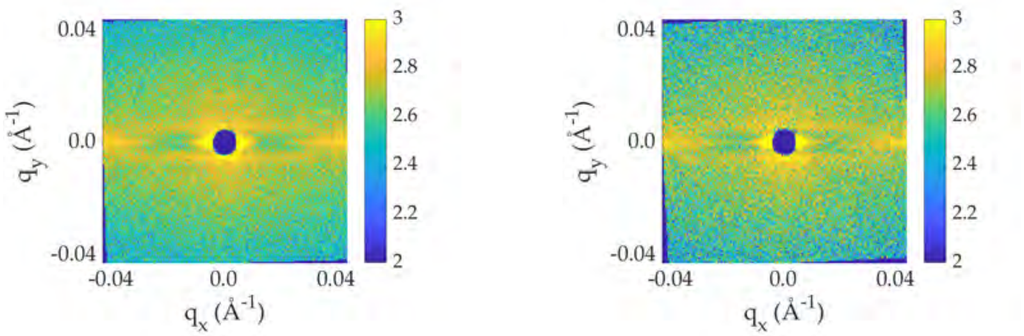

(a) t = 0 s

(b) t = 5 s

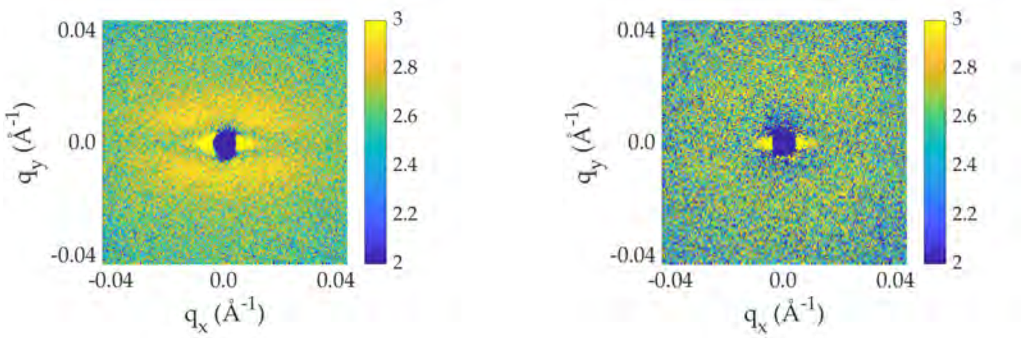

(c) t = 200 s

(d) t = 4000 s

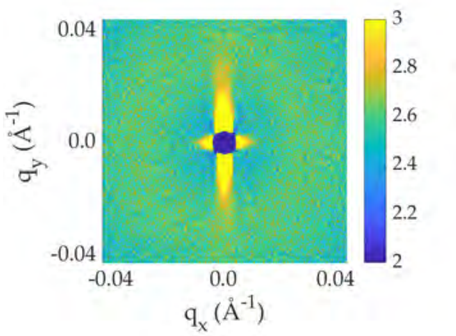

(e) FR

Figure 3.19: Background subtracted and scaled 2D data, 14 m setting. The subfigures show the 2D data for all five samples after rotation, background subtraction and scaling.

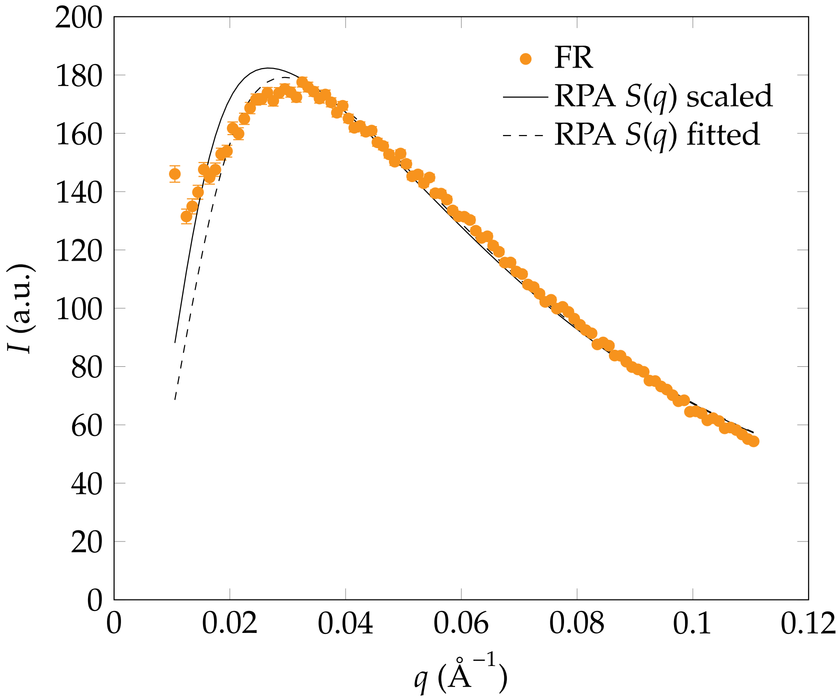

Figure 3.20: Scattering intensity from the fully relaxed sample compared to the RPA-structure factor. The scattering intensity, $I(q)$, is averaged over all sectors not affected by the excess scattering. The data is fitted to the RPA-structure factor twice. For the first fit, shown with a fully drawn line, only the overall scaling was included as a fitting parameter. For the second fit, shown with a dashed line, also the molecular parameters f and N were included as fitting parameters.

to be near the spinodal since we have relatively small χN. In further analysis, one could include polydispersity to see how it affects the result. To include polydispersity in a simple way, one could approximate the polydispersity by considering a finite number of molecular populations varying slightly in the length of the individual blocks as in ref.[58]. It would also be interesting to see how excluded volume effects impact the result.

Lastly, from the second fit where not only the over all scaling but also the molecular parameters f and N were fitted, we obtain the curve with the dashed line in Fig. 3.20, and find that $N = 99 \pm 1$ and $f = 0.104 \pm 0.002$.

Sample Relaxed for 0 s

As mentioned in Sec. 3.4.3, the scattering pattern is dominated by four stripes, two on the horizontal axis and two shifted away from the horizontal axis along the vertical axis, see Fig. 3.21 for a sketch of the idealized scattering pattern. The centers of the peaks on the horizontal axis, perpendicular to the direction of extension, are $q^*_\perp = \pm 0.06$ Å^{-1} corresponding to a characteristic distance $d_\perp$ ~100 Å, and the centers of the peaks shifted on the vertical axis, parallel to the direction of extension, are $q^*_{||} = \pm 0.005$ Å^{-1} corresponding to a characteristic distance of $d_{||}$ ~1300 Å. We assign the peaks to correlations between two deuterated ends. The horizontal peaks correspond to the distance between two deuterated ends of the molecule pointing in the same direction relative to the flow, $d_\perp$, and the vertical peaks correspond to the distance between two ends pointing in opposite directions relative to the flow, $d_{||}$. The horizontal width of the peaks on the vertical axis may simply reflect that the scattering domains are elongated along the stretching direction. The horizontal width of the peaks on the horizontal axis may have the same origin, but could also be caused by some variation in $d_\perp$. If we relate the characteristic distances to the molecular parameters, $d_\perp$ ~100 Å corresponds to the tube diameter for polystyrene of a = 85 Å, and $d_{||}$ ~1300 Å indicates that the tube segments of the star are not only aligned but also slightly stretched by the flow. We conclude that the segments are stretched from the following calculation: The tube contour length between two ends is

$$L_{\text{tube}} = 2Za \approx 1040 \text{ Å} \tag{3.25}$$

where a is the tube diameter and Z is the number of entanglements in one arm. The factor of 2 accounts for the fact that two deuterated ends are separated by two arms. The number of entanglement segments in one arm Z is calculated as the ratio of the molecular weight of one arm M_w = 101.7 kg/mol and the entanglement molar mass for polystyrene M_e=16.6 kg/mol:

$$Z = \frac{M_w}{M_e} \approx 6. \tag{3.26}$$

Since $d_{||} > L_{\text{tube}}$, the tube segments must be, slightly, stretched. For comparison, we also calculate the chain contour length

$$L_{\text{chain}} = 2Nb = 2\frac{\sqrt{\langle R^2 \rangle}}{b} = 2\frac{\sqrt{0.437 M_w[\text{g/mol}]}}{b} \approx 4940 \text{ Å} \tag{3.27}$$

where N is the number of Kuhn segments in one arm, b = 18 Å is the Kuhn segment length for polystyrene, and R is the end-to-end vector. We

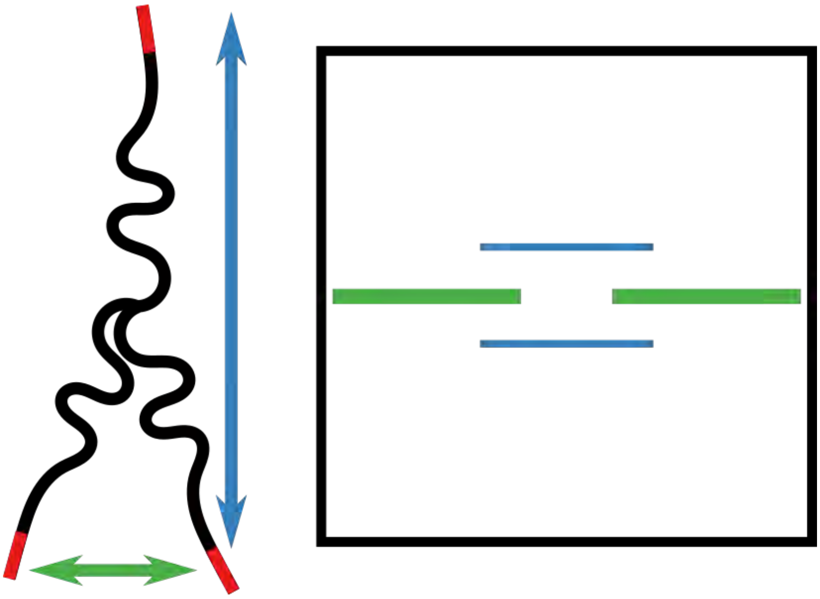

Figure 3.21: Idealized 0 s scattering pattern. The scattering pattern is dominated by two types of horizontal streaks

find that $L_{\text{chain}} > d_{\|} > L_{\text{tube}}$ and conclude that the chain is far from fully stretched.

The description of the molecular conformation in terms of a tube picture describes the data well, but it may be unclear how to think about tubes for the fully extended, and even slightly stretched, ”tubes” since there will be no entanglements in this situation. However, since we stretch the material so fast it may be that the chains have a memory of a virtual tube.

Scattering Patterns of Relaxation

Qualitatively the 5 s pattern looks very similar to the 0 s pattern, and the 4000 s pattern appears isotropic like the fully relaxed, omitting the scattering at small q from consideration though the ring of maximum intensity appear to be at slightly smaller q. The 200 s pattern is to some extend similar to the 0 s and 5 s pattern as it does not have the horizontal peaks but the vertical peaks, which are shifted to larger q. In the following, we reduce the data to $I(q)$-curves using the sector and slab averages shown in Fig. 3.16.

For the 5 s and 200 s patterns, we reduce the data over slabs corresponding to the horizontal peak and crossing the peak on the vertical axis respectively in Fig. 3.22. For clarity, we present the same slab averages of all data sets. We see that the horizontal peak shifts slightly towards smaller $q_\perp$ during the first 5 s of relaxation. For 200 s, there appear to be a peak at around $q = 0.02$ Å^{-1}. That there is a peak in the t=200 s data is supported by the more convincing presence of a peak at roughly the same q-value in the 4000 s data. However, the origin of these peaks is currently unknown. To determine the peak positions, we fit the slab averaged data. Since we do not have a model for the peak shapes, we choose a Gaussian on a sloped background for the horizontal peaks and a Gaussian on a constant background for the peaks on the vertical axis:

$$y_{\text{fit, horizontal}} = A_1 q^{-b} + A_2 e^{-\frac{(q-q_0)}{2\sigma^2}} \tag{3.28}$$

$$y_{\text{fit, vertical}} = A_2 e^{-\frac{(q-q_0)}{2\sigma^2}} + k. \tag{3.29}$$

The black lines representing the fit covers the data range used for the fit. In the figure insets, we plot the position of the peak centers as function of relaxation time. We see that the peak shifts non-monotonically from the position immediately after stretching to the equilibrium position at the longest relaxation time. We interpret the initial shift towards smaller q from the 0 s pattern to the 5 s pattern as the two arms oriented in the same direction relative to the flow moving somewhat further apart during the first 5 s of relaxation, which is consistent with our expectations. We come back to interpretation of the remaining horizontal slabs after discussing the relaxation of the peak on the vertical axis and the 4000 s scattering pattern.

For the peak on the vertical axis, the peak shifts towards larger values of $q_\parallel$ with relaxation time at least up to t=200 s. This is consistent with the molecule retracting from its oriented and slightly stretched state. The peak shift from 0 s to 200 s corresponds to a length change along the axis of stretching from $d_\parallel^{0\,\text{s}} \sim 1300$ Å to $d_\parallel^{200\,\text{s}} \sim 550$ Å. The distance of $d_\parallel^{200\,\text{s}} \sim 550$ Å is approximately twice the statistical end-to-end vector length for two star arms with $M_w = 203.4$ kg/mol which is $R_{2\text{ arms}} \sim 300$ Å calculated as $\sqrt{\langle R^2 \rangle} = \sqrt{0.437 M_w [\text{g/mol}]}$.

For the 4000 s data, we first conclude that pattern is in fact isotropic by plotting the sectors parallel and perpendicular to the flow in Fig. 3.23a and see that they are consistent within the errorbars for most values of q. For some small q-values the intensity of the horizontal and vertical sector deviate, but this is most likely due to the overall low scattering intensity recorded for this sample, see e.g. Fig. 3.10. Having concluded that the 4000 s scattering pattern is isotropic, we average the scattering

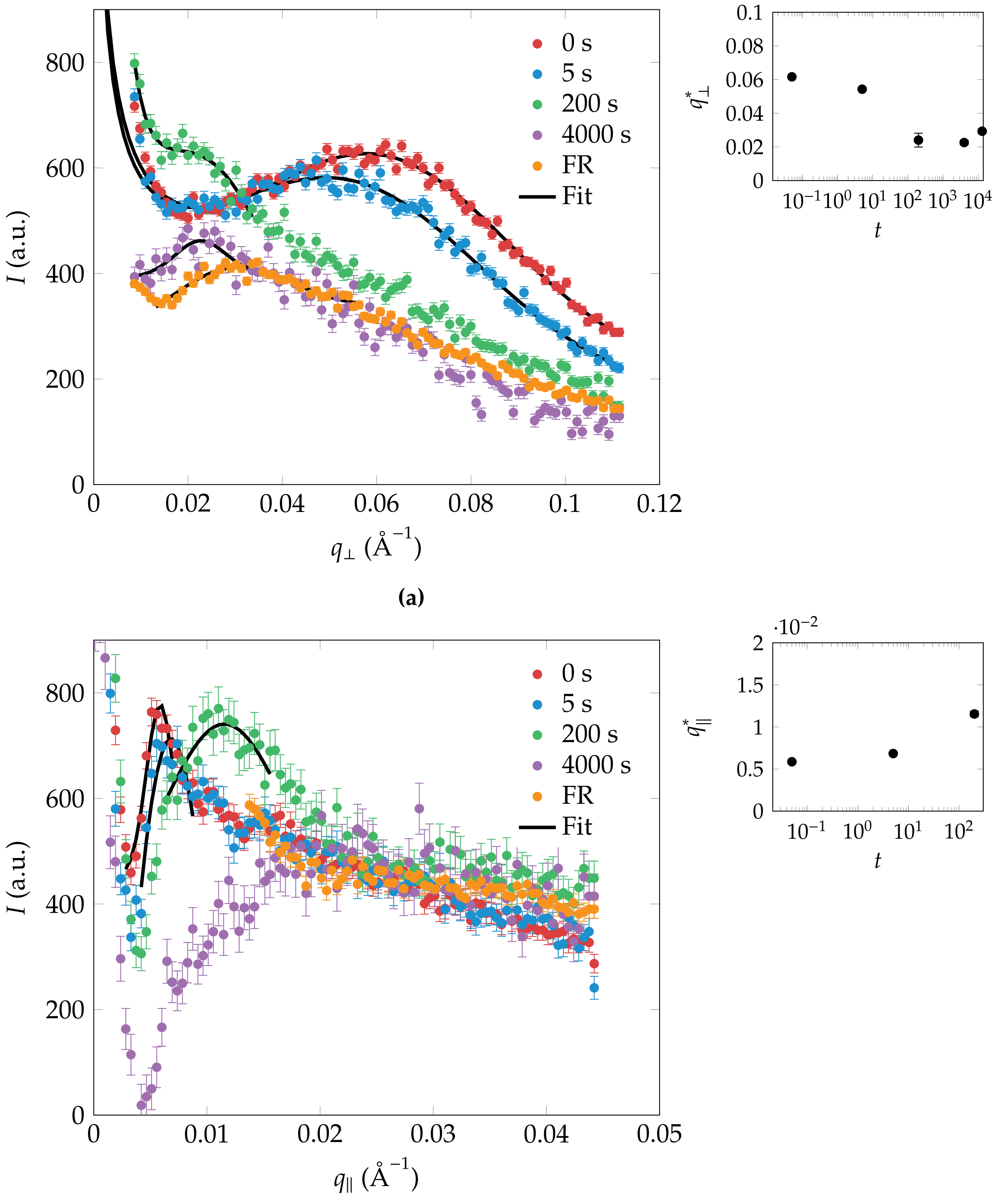

(a)

(b)

Figure 3.22: Horizontal and vertical slabs during relaxation. In a) intensity in the slab characterized by $q_\| = [-0.01, 0.01]$ Å^{-1} surrounding the horizontal peak is plotted as a function of $q_\perp$ for the relaxation steps using the 5 m setting data. In b) intensity in the slab characterized by $q_\perp = [-0.01, 0.01]$ Å^{-1} crossing the peak on the vertical axis is plotted as a function of $q_\|$ for the relaxation steps using the 14 m setting data. The FR-data is only shown for $q_\| > 0.015$ Å^{-1} due to the large amount of excess scattering at small q. Black lines are fits to Eq. 3.28 in a) and Eq. 3.29 in b). The insets show the peak positions found from the fits.

intensity over the full detector except the two horizontal sectors (0 ± 10)° and (180 ± 10)° and compare it to the RPA-structure factor where we fit a scaling factor only and not any molecular parameters. The result is plotted in Fig. 3.23b. Interestingly, we see that the maximum scattering intensity for the 4000 s pattern occurs at smaller q than the RPA-structure factor predicts on the contrary to the RPA-structure factor compared to the fully relaxed Fig. 3.20. We therefore conclude that after 4000 s the star conformations are isotropic as in equilibrium, but somehow swollen to a larger size.

The 200 s scattering pattern shares features with both the 0 s and 5 s patterns, apparent in the vertical direction, and the 4000 s pattern apparent in the horizontal direction. The clear peaks in the vertical direction shows that a characteristic separation between scattering domains pointing in opposite directions relative to the flow direction remains at least during the first 200 s of relaxation. The absence of the horizontal peaks show that there is no longer a characteristic distance between domains pointing in the same direction relative to the flow. That the neighboring domains are more free in their positions may also explain why the peaks on the vertical axis are broadened relative to the earlier relaxation times. The peak position on the 200 s horizontal slab has almost the same center as the corresponding peak on the 4000 s slab so the two peaks may have the same origin, and the 200 s pattern may therefore contain contributions from a population of molecules with isotropic conformations.

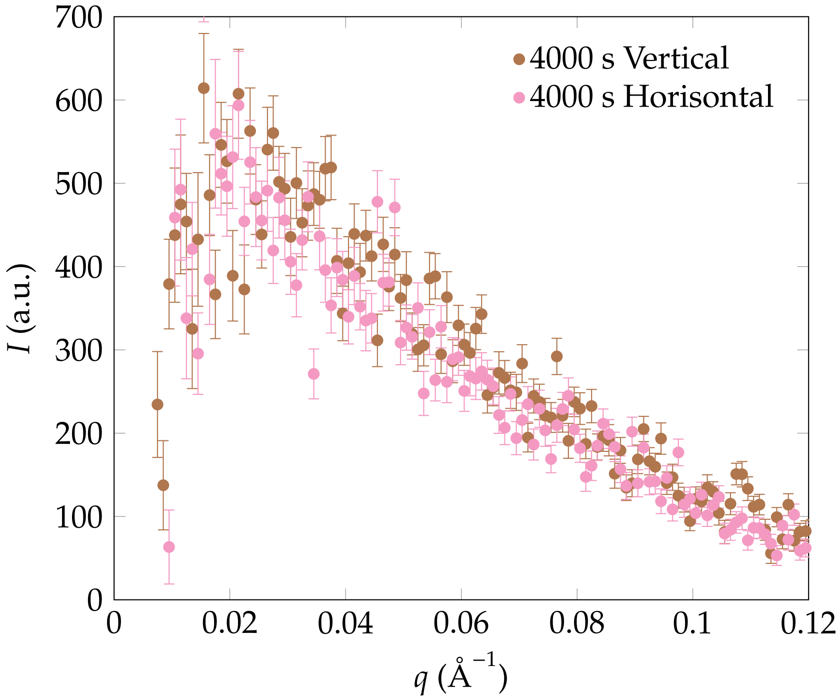

(a)

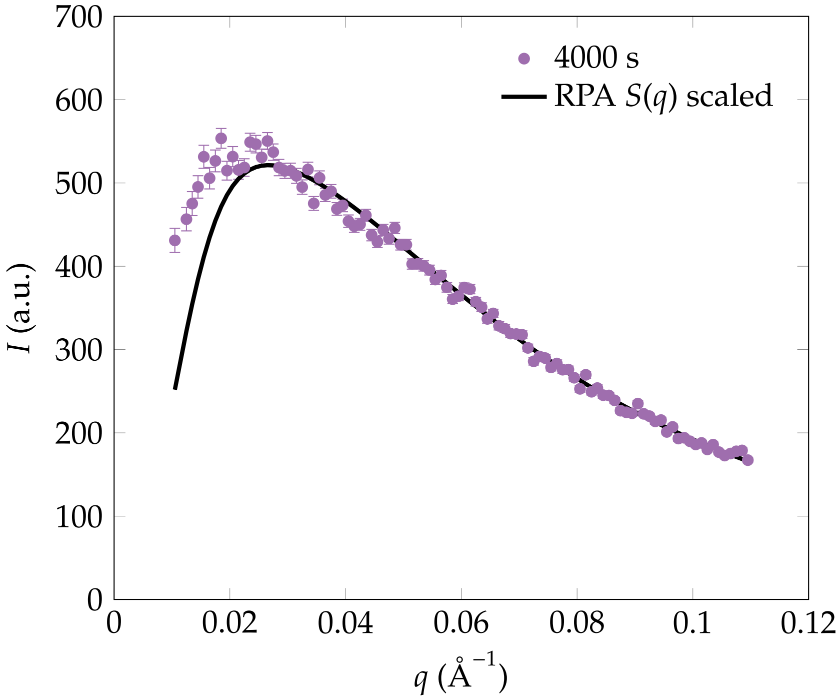

(b)

Figure 3.23: Analysis of the 4000 s pattern. In a) we show the overlapping horizontal and vertical sectors, and in b) we show how it compares to the scaled RPA-structure factor.

3.5 Discussion

It is most interesting to compare the conclusions from the stress relaxation in Sec. 3.2.2 to the conclusions based on the neutron scattering data in Sec. 3.4.4. The stress relaxation curves for Star90 and Lin180 follow each other through out region II which in terms of the Rouse time of the molecules at $T = 130^\circ$ C has an upper limit at $t \approx 6\tau_R$. This could lead us to think that the quasi-linear conformation of the star is preserved at all $t < 6\tau_R$. But from neutron scattering we learn that already at $t \approx 0.5\tau_R$ at $T = 125^\circ$ C, the correlation between the two ends aligned in the same direction relative to the flow is gone, and that suggests that the molecules no longer take a quasi-linear conformation. However, the rheological behavior may depend only on the stretching along the direction of flow, which could explain why the relaxation curves still follow each other.

To deepen our understanding of the relaxation apart from more data point for $5\ \text{s} < t < 200\ \text{s}$, it would be very interesting to perform a scattering experiment on a linear polymer of the same span and the same deuteration fraction to see how the scattering patterns compare. We would expect to see only the vertical peaks, and that they would relax in a similar way as the peaks on the vertical axis in the star patterns. Also, it would be interesting to perform scattering experiments on three-armed stars of comparable sizes with different deuteration schemes, i.e. an overall deuteration to provide information on the overall molecular conformation. Another approach to learn more about the relaxation of star polymers could be to perform simulations of star polymers in extensional flow and the following relaxation and generate scattering patterns from the simulation. If such a simulation for end-labeled stars could produce relaxation snap shots in agreement with the measured data, the simulation could give knowledge about the relaxation between our quench times.

3.6 Conclusion

Based on previous experimental and theoretical work, Huang et al.[7] studied two types of star molecules and a linear molecule of the same span in extensional flow and the following relaxation. Their findings confirmed that in fast extensional flow, the star molecules and the linear molecule had the same rheological response during deformation and in the initial relaxation, supporting the idea that the branched molecules take a quasi-linear conformation. To investigate this further, SANS on end-deuterated samples was conducted on samples representing a relaxation time series. We found that immediately after cessation of the flow the scattering pattern from the melt is consistent with the stars taking a quasi-linear conformation. However the scattering pattern soon after $t \approx 1/2\tau_R$ is no longer fully consistent with the quasi-linear conformation. More work is needed to obtain a quantitative understanding of the relaxation.

Chapter 4

Chain Retraction in Spherical Harmonics Expansion

The Doi-Edwards tube model[16] predicts chain expansion during deformation of linear polymers and subsequent chain retraction during the following relaxation. Deformation, such as extensional flow, will orient the molecules along the direction of flow and stretch the contour length of the molecules leading to an elongated molecular conformation. Stretching and orientation will relax through two mechanisms: Rouse relaxation and reptation. The characteristic time of the Rouse relaxation, τ_R, scales with the number of entanglement segments, Z, as $\tau_R \sim Z^2$ and the characteristic time of reptation or disentanglement τ_d, scales with the number of entanglement segments, Z, as $\tau_d \sim Z^{3.4}$[12]. As Z increase these relaxation modes become decoupled in time.

Doi and Edwards[16] showed that this decoupling of the relaxation leads to chain retraction. During the initial part of the relaxation, the molecule preserves its overall orientation but the contour length relaxes back to its equilibrium length. The contour length relaxation will cause the molecule to shrink in all dimensions during the Rouse relaxation. Interestingly, this will also cause the radius of gyration perpendicular to the flow direction to increase towards the equilibrium value in a non-monotonic way during relaxation with a minimum at $t \sim \tau_R$. Doi and Edwards propose to test this hypothesis using an experimental technique that can resolve the radius of gyration components as a function of relaxation time to test the hypothesis[16].

The chain retraction hypothesis has been tested in several experiments where polymer samples were stretched above the glass transition temperature and allowed to relax for different time before they were cooled below the glass transition. Ex-situ small angle neutron scattering (SANS) experiments[65, 66, 67] were used to measure the single chain structure factor for the different relaxation times through selective deuteration. The experiments lead to different results. Boue et al. [65] stretched a polystyrene sample of $M_w \sim 650$ kg/mol, corresponding to $Z \approx 45$, with 15 % deuterated chains to a stretch ratio of $\lambda = 3$. They samples were allowed to relax for different times before the samples were quenched. The determined the perpendicular radius of gyration as a function of relaxation time and found a monotonic increase and thus their findings contradict the chain retraction hypothesis. The authors suggested that the apparent monotonic increase could be due to insufficient separation of the characteristic times, i.e. the molecules are too small, or polydispersity smearing out the effect. Mortensen et al.[66] studied a sample of 2M-Dalton poly(polyethylenepolyethylene-co-ethylene) with 2% partially deuterium labeled polymers. They stretched polymer films by a factor of 3 and saw a non-monotonic increase in the perpendicular radius of gyration with a few data points. Blanchard et al. [67] worked with a polyisoprene sample of $Z = 58$ stretched to $\lambda = 1.7$, and they clearly see a non-monotonic increase in $R_g^\perp$. It was also reported necessary to include chain retraction in the model to fit the SANS data in the studies by Bent et al.[68] and Graham et al. [69] where the polymer deformation was created using a flow cell. In conclusion there seems to be experimental evidence for the chain retraction hypothesis.

However the conclusion that chain retraction occurs based on the results mentioned above was recently questioned by Wang et al. in ”Fingerprinting Molecular Relaxation in Deformed Polymers” published in Phys. Rev X in 2017[22]. They question whether the R_g, which is a coarse grained quantity giving information on the larger scales of the molecular conformation, is appropriate for testing the chain retraction hypothesis. Also it is an experimental challenge to determine at least the radius of gyration parallel to the direction of extension in a model independent way by Guinier analysis. In ref. [22] they combine and extend previous 2D scattering data analysis methods using spherical harmonics functions. They show how chain retraction, as defined by Doi and Edwards[16], will have a clear model independent signature in the spherical harmonics expansion. They perform an experiment on polystyrene with $Z \approx 34$ stretched to $\lambda = 1.8$, expand the relaxation series in spherical harmonics and find no signs of the predicted signature and conclude that either chain retraction does not occur or it is screened by other effects not included in the tube model.

Inspired by the potential strengths of the spherical harmonics framework in the analysis of 2D data for uniaxially extended polymer melts in general, we decided to implement the framework and reanalyze an old SANS data series for linear polystyrene. The data series was presented in Chap. 2 as the data for the Short-in-Short sample. The chains have approximately six entanglement segments, $Z \approx 6$, and the melt is stretched to a macroscopic stretch ratio of $\lambda = e^3 \approx 20$. We wondered how the differences in chain length and stretch ratio would show up in the spherical harmonics expansion and remarkably we found the signature of chain retraction that Wang et al. [22] derived from the Doi-Edwards model. [16]

In this chapter we first introduce the spherical harmonics expansion framework for single chain structure factors of uniaxially extended polymer melts, then we present the SANS-data sets and their expansions in spherical harmonics. Finally we present how the spherical harmonics expansion of the data sets show the signature of chain retraction and discuss our results.

4.1 Spherical Harmonics Expansion Framework

The framework is developed for structure factors for deformed polymer materials by Wang et al. [22]. However it may prove useful in the analysis of small angle scattering data from other soft matter or amorphous systems for which the structure factor is a smoothly varying function. Since the framework is so new and since we would like to end the chapter with a detailed analysis of what we learn from the expansion, it will be fruitful with a detailed description on how to set up the framework instead of a simple reference.

In this section we introduce the spherical harmonics expansion framework and employ the symmetry of uniaxial extension to simplify the expansion. While we establish the framework, we assume that the analytic expression for the structure factor, $S(\vec{q})$ is known. In the next subsection we describe how to employ the framework given an experimental scattering intensity $I(\vec{q})$.

4.1.1 General Framework

The starting point in setting up the framework is to write the single-chain structure factor $S(\vec{q})$ in a basis of spherical harmonics functions as

$$S(\vec{q}) = S(q, \theta, \phi) = \sum_{l=0}^{\infty} \sum_{m=-l}^{l} S_l^m(q) Y_l^m(\theta, \phi). \tag{4.1}$$

The integers l and m are the degree and order of the spherical harmonics functions $Y_l^m(\theta,\phi)$, and $S_l^m(q)$ are the q-dependent expansion coefficients, which we will later use to represent the structure factor. We follow the coordinate convention of physics such that $\theta \in [0,\pi]$ is the angle with respect to the positive z-axis, or the polar angle and $\phi \in [0,2\pi]$ is the angle from the positive x-axis in the xy-plane, or the azimuthal angle. To avoid confusion we stress that we labeled the scattering angle 2ϑ in Sec. 1.3.1.

Our basis functions the spherical harmonics can be represented as complex or real valued. Since the structure factor is a real valued function, it seems most natural to choose the real representation. However, the two representations coincide for $m = 0$ which, as we argue below, are the relevant harmonics when the series expansion has to fulfill the symmetries of uniaxial extension.

The real spherical harmonics functions are defined as:

$$Y_l^m(\theta,\phi) = \begin{cases} \sqrt{\frac{2(2l+1)(l-|m|)!}{4\pi(l+|m|)!}} P_l^{|m|}(\cos\theta)\sin\big(|m|\phi\big) & \text{for } m < 0 \\ \sqrt{\frac{(2l+1)}{4\pi}} P_l^0(\cos\theta) & \text{for } m = 0 \\ \sqrt{\frac{2(2l+1)(l-m)!}{4\pi(l+m)!}} P_l^m(\cos\theta)\cos\big(m\phi\big) & \text{for } m > 0. \end{cases} \tag{4.2}$$

Here $P_l^m(x)$ are the Legendre polynomials of degree l and order m and the prefactors are chosen to ensure orthonormality of the basis. Our definition deviate from that in ref. [22] by including the conventional $\sqrt{1/(4\pi)}$ in the refactors We show the orthonormality of the basis below after we have employed uniaxial symmetry to reduce the number of basis functions.

4.1.2 Uniaxial Symmetry Restricts the Basis

It is convenient to discuss uniaxial symmetry relative to a defined coordinate system. The natural choice is to orient the z-axis parallel to the axis of uniaxial extension and set up the experiment such that the incoming beam is perpendicular to the axis of extension, i.e. in the x,y-plane. We discuss the choice of coordinate system in more detail in the next subsection.

Uniaxial symmetry of the samples and therefore the structure factor both restricts the degree l and order m of the harmonics functions with a non-zero expansion coefficient in Eq. 4.1 and thereby greatly limit the number[1] of basis functions needed. The uniaxial symmetry of the structure factor means that it should be invariant under rotation around

---

[1] Though of course we still need infinitely many for an exact expansion

the extension axis, i.e. under change in ϕ, and invariant under reflection in the horizontal plane, i.e. under $\theta \rightarrow \pi - \theta$. The invariance under change in ϕ is achieved only if the orders of all terms in the expansion are $m = 0$, and the invariance under $\theta \rightarrow \pi - \theta$ is achieved only if the degrees of all terms in the expansion are even since the Legendre polynomials fulfill $P_l^0(-x) = (-1)^l P_l^0(x)$ or $P_l^0(\cos(\pi - \theta)) = (-1)^l P_l^0(\cos(\theta))$. The structure factors for unixially extended samples can then be expanded as

$$S(\vec{q}) = S(q, \theta) = \sum_{l=2l'} S_l^0(q) Y_l^0(\theta) = \sum_{l=2l'} S_l^0(q)\sqrt{2l+1} P_l^0(\cos\theta). \tag{4.3}$$

4.1.3 Measured Structure Factor

The measured coherent scattering intensity is proportional to a 2D cross section of the structure factor. As stated above, the experimental setup and our choice of coordinate system are such that the axis of extension is parallel to the z-axis and the axis of the incoming beam is in the xy-plane. It does not matter how we choose the axis of the incoming beam because $S(\vec{q})$ is independent of ϕ, but to make a choice, we follow ref. [22] and choose the coordinate system such that the axis of the incoming beam is along the y-axis, see Fig. 4.1. With this choice of coordinates, the two dimensional structure factor becomes

$$S(q_x, q_y = 0, q_z) = S(q, \theta, \phi = 0) = S(q, \theta) = \sum_{l=2l'} S_l^0(q)\sqrt{2l+1} P_l^0(\cos\theta). \tag{4.4}$$

In the following, when we refer to spherical harmonics expansion of the structure factor, it will be implicit that we refer to Eq. 4.4, i.e. we refer to the cross section that will be measured and we assume uniaxial symmetry of our sample.

Orthonormality of Spherical Harmonics Functions of degree $l = 2l'$ and order $m = 0$

To ensure that the expansion coefficients are unique, the chosen basis has to be orthogonal on the relevant interval, here $\cos\theta = [-1, 1]$ and $\phi = [0, 2\pi]$. The spherical harmonics functions relevant for the spherical harmonics expansion constitute an orthonormal basis such that

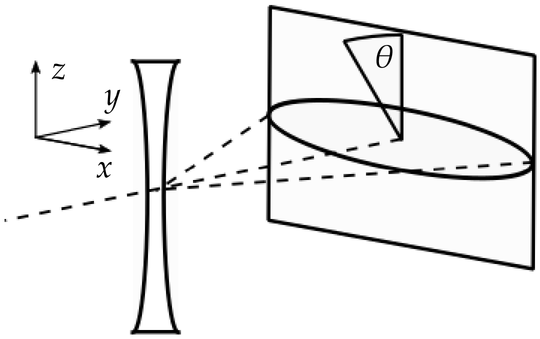

Figure 4.1: Sketch of experimental setup for SANS on filaments with choice of coordinate system illustrated. The sample is shown as a single, vertical filament. The dashed lines show the incoming and scattered neutron beam. The parallelogram represents the detector and the ellipsis illustrates the scattering intensity for a non-relaxed sample. The coordinate system is chosen such that the axis of uniaxial extension is parallel to the z-axis and the incoming beam parallel to the y-axis. With this choice of coordinate system, the measured cross section of the structure factor is given in Eq. 4.4. The angle θ is the polar angle in spherical coordinates and is defined relative to the positive z-axis.

$$\int_{-1}^{1} \mathrm{d}\cos\theta \int_{0}^{2\pi} \mathrm{d}\phi \left[Y_l^0(\theta,)\right]^* Y_{l'}^0(\theta) = \delta_{ll'}. \tag{4.5}$$

It can be seen because the integration over ϕ simply yields a factor of 2π and the integral over θ yields

$$\int_{-1}^{1} \mathrm{d}\cos\theta P_l^0(\cos\theta) P_{l'}^0(\cos\theta) = \frac{2}{2l+1}\delta_{ll'}. \tag{4.6}$$

The orthogonality of the Legendre polynomials can be shown using the Rodrigues formula for the associated Legendre polynomials and integration by parts[70]:

$$P_l(x) \equiv \frac{1}{2^l l!}\left(\frac{\mathrm{d}}{\mathrm{d}x}\right)^l \left(x^2-1\right)^l \tag{4.7}$$

Determination of Expansion Coefficients

Because the basis of spherical harmonics is orthogonal the q-dependent expansion coefficients in Eq. 4.4 can be determined uniquely and because the basis is orthonormal, the coefficients can be determined by integrals of the form

$$S_l^0(q) = \int_0^{2\pi} \mathrm{d}\phi \int_0^{\pi} \mathrm{d}\theta S(q,\theta) Y_l^0(\theta) \sin\theta. \tag{4.8}$$

Wang et al. [22] define the spherical harmonics functions with a slightly different prefactor containing the factor 2π from the ϕ-integral in Eq. 4.8 in which they need a prefactor of 1/2 to correct for the lack of normalization of their basis.

Legendre Polynomials of Degree $l \leq 10$ and order $m = 0$

Now we have our basis functions. As a reference, we write the first few out explicitly and plot them as a function of $\cos\theta$ in Fig. 4.2.

The spherical harmonics of degree $l \leq 10$ and order $m = 0$ are

$$\begin{aligned}
Y_0^0(\cos\theta) &= \sqrt{\frac{1}{4\pi}} \\
Y_2^0(\cos\theta) &= \sqrt{\frac{5}{4\pi}\frac{1}{2}}\left(3\cos^2\theta - 1\right) \\
Y_4^0(\cos\theta) &= \sqrt{\frac{9}{4\pi}\frac{1}{8}}\left(35\cos^4\theta - 30\cos^2\theta + 3\right) \\
Y_6^0(\cos\theta) &= \sqrt{\frac{13}{4\pi}\frac{1}{16}}\left(231\cos^6\theta - 315\cos^4\theta + 105\cos^2\theta - 5\right) \\
Y_8^0(\cos\theta) &= \sqrt{\frac{17}{4\pi}\frac{1}{128}}\left(6435\cos^8\theta - 12012\cos^6\theta\right. \\
&\quad \left.+6930\cos^4\theta - 1206\cos^2\theta + 35\right) \\
Y_{10}^0(\cos\theta) &= \sqrt{\frac{21}{4\pi}\frac{1}{256}}\left(46189\cos^{10}\theta - 109395\cos^8\theta + 90090\cos^6\theta\right. \\
&\quad \left.-30030\cos^4\theta + 3465\cos^2\theta - 63\right)
\end{aligned} \tag{4.9}$$

4.1.4 Summary

In this subsection we have set up the general framework for expanding structure factors in terms of spherical harmonics, using the symmetry of uniaxial extension to reduce the number of basis functions needed for our analysis, and shown how to determine the expansion coefficients. By

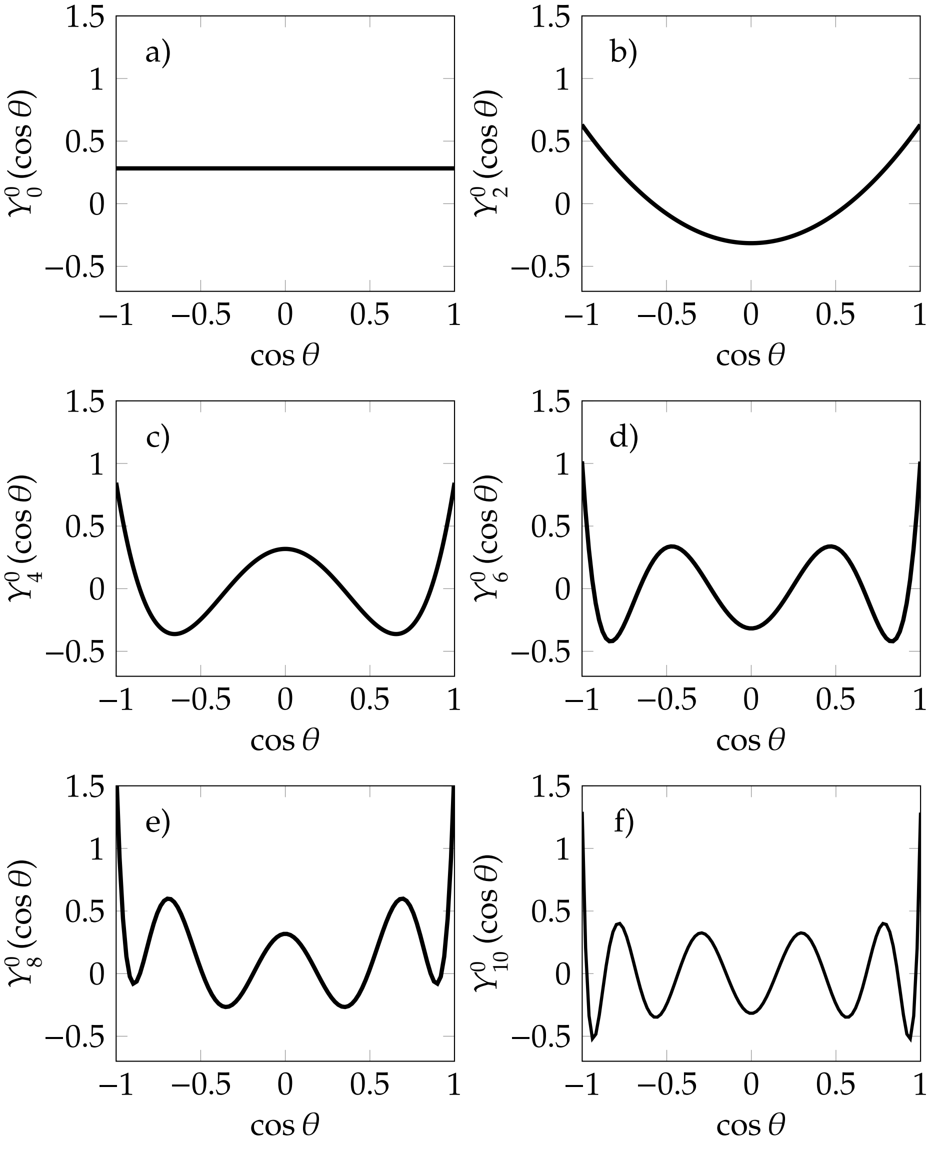

Figure 4.2: The low order Legendre polynomials of even degree $l = 2l'$ and order $m = 0$ consistent with the symmetry of uniaxial extension. The subfigures show the Legendre polynomials in ascending degree from a) to f).

determining the expansion coefficients, we can represent the structure factor in terms of the q-dependent expansion coefficients. As we will see below in Sec. 4.3.3, this data representation allows us to study the time evolution of the different modes in the data.

4.2 Experimental Data

In the precious section we established the framework of spherical harmonics expansion, and in the next we will apply it in the analysis of experimental data. In this section, we will describe the samples and reduction procedure used to obtain the reduced 2D data.

4.2.1 Samples

The samples for this study are the Short in Short-samples described in Chap. 2 and therefore we only give a short summary here. The samples are a relaxation series for a blend of 90% h-PS of M_w =95 kg/mol and 10% d-PS of M_w =80 kg/mol stretched in the Filament Stretch Rheometer with a constant Hencky strain rate of $\dot{\varepsilon} = 0.1\ \mathrm{s}^{-1}$ at a temperature of $T = 130°$ C to a final Hencky strain of $\varepsilon_f = 3$ and allowed to relax for 0 s, 10 s, 20 s, 80 s, or 320 s respectively at $T = 130°$ C. In terms of the Rouse time for the deuterated component, $\tau_R = 15$ s, the relaxation times are $0 \cdot \tau_R$, $0.7 \cdot \tau_R$, $1.3 \cdot \tau_R$, $5.3 \cdot \tau_R$, $21.3 \cdot \tau_R$. The deuteration percentage is chosen such that it is a reasonable assumption that the scattering pattern originates from the single chain structure factor and not composition fluctuations.

4.2.2 Measurements and Instrumental Settings

The samples were measured at the Small Angle Neutron Scattering instrument QUOKKA at Australia's Nuclear Science and Technology Organization in 2015. The samples were measured with neutrons of a wavelength of $\lambda = 5$ Å with a sample-detector distance of 14 m, 5 m, and 2 m respectively. The data from the 5 m setting is previously published in [10].

4.2.3 Data Reduction

The data was corrected for detector sensitivity and the measured intensity for blocked and empty beam as described in Sec. 3.4.3. The incoherent scattering was estimated and corrected for by subtraction as described in Sec. 3.4.3 with the only difference that the large q-data is fitted to the high q limit of the Debye structure factor. The Debye structure factor, see Sec. 1.1.1, and the high q limit is given by

$$S(q) = \frac{2}{q^4 R_g^4}\left(e^{-q^2 R_g^2} + q^2 R_g^2 - 1\right) \tag{4.10}$$

$$S(q) \approx \frac{2}{q^2 R_g^2} \quad \text{for } qR_g \ll 1. \tag{4.11}$$

We plot the Debye structure factor and the high parameters in Fig. 4.3. For $qR_g > 3$, the deviation between the high q-limit and the Debye structure factor is 10 % or less and so we fit data fulfilling $q > 3/R_g$ and $\theta = (45 \pm 5)^\circ$. The fitting parameters are an amplitude and a constant offset, and we thus fit to

$$y = Aq^{-2} + b. \tag{4.12}$$

The constant offset b is then our estimate of the incoherent background. All data sets were scaled arbitrarily to $b = 1$ before subtraction to account for varying material amount across samples.

The reduced 2D data are shown in Fig. 4.4 for the 14 m setting and Fig. 4.5 for the 5 m setting.

4.2.4 Qualitative Analysis

The overall trend in the data is that the scattering corresponding to no relaxation is most anisotropic and as the relaxation time increases, the isotropy of the equilibrium conformation, as described in Sec. 1.1.1, is regained.

Scattering at small q

However the scattering patterns also have a cross-shaped feature for the smallest values of q, which is most prominent for the scattering patterns corresponding to the longest relaxation times. However as we will argue in App. A, we are confident that it originates from voids or cracks formed in the filament during stretching and the subsequent quenching. Therefore it is unrelated to the molecular conformation which is the target of this analysis. For this reason we will base our conclusions regarding the molecular conformation on the data for $q \geq 0.008\text{Å}^{-1}$.

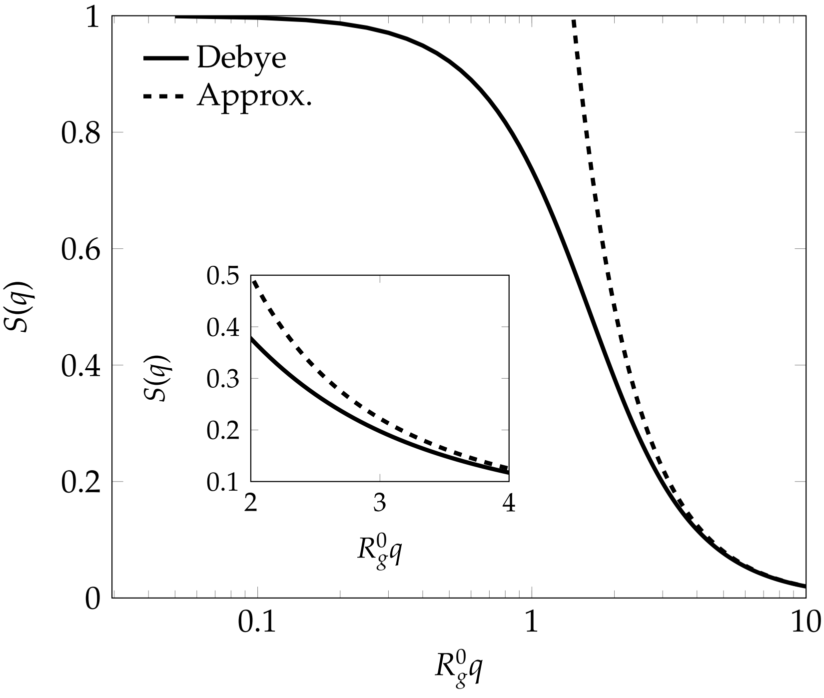

Figure 4.3: The Debye structure factor and its high q limit. The Debye structure factor is plotted as function of q with a fully drawn line. The dashed line show its high q limit as approximation. The inset shows a zoom-in around $qR_g^0 \approx 3$.

4.2.5 Summary

In this section we described how we obtained a reduced 2D data set that corresponds to a relaxation time series of 80 kg/mol deuterated polystyrene in a matrix of 95 kg/mol fully hydrogenous polystyrene. A qualitative analysis of the 2D patterns show that the degree of anisotropy in the patterns decrease with increasing relaxation time as expected. For further analysis of the data set, we implement the spherical harmonics expansion framework.

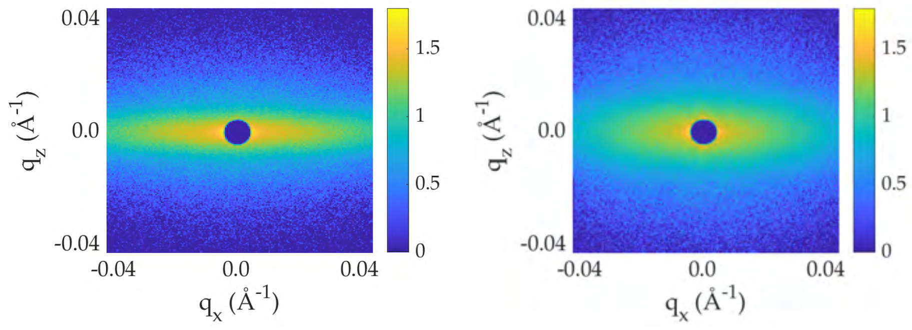

(a) $t = 0 \cdot \tau_R$ **(b)** $t = 0.7 \cdot \tau_R$

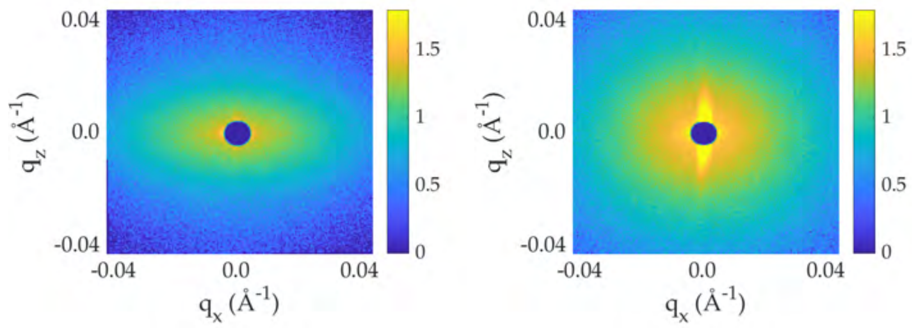

(c) $t = 1.3 \cdot \tau_R$ **(d)** $t = 5.3 \cdot \tau_R$

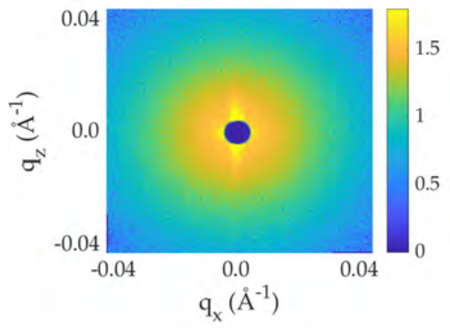

(e) $t = 21.3 \cdot \tau_R$

Figure 4.4: 2D SANS data 14 m setting for Short in Short-samples. The relaxation time increases from a) to e), and is given in terms of the Rouse time, $\tau_R = 15$ s. The data is plotted on $\log_{10}$ scale. All intensities less than one have arbitrarily been rounded up to one for the visualization on log scale.

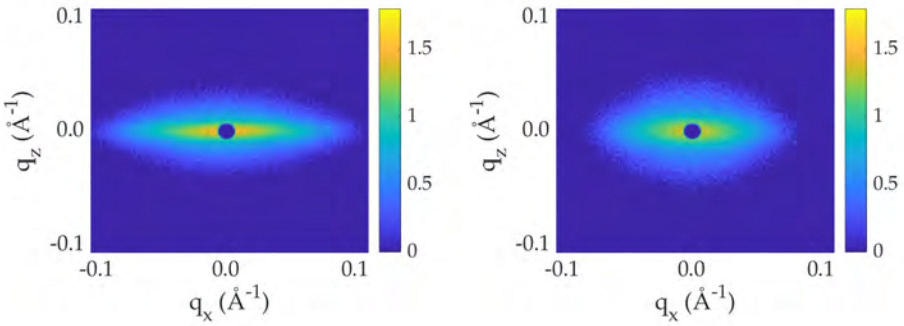

(a) $t = 0 \cdot \tau_R$ **(b)** $t = 0.7 \cdot \tau_R$

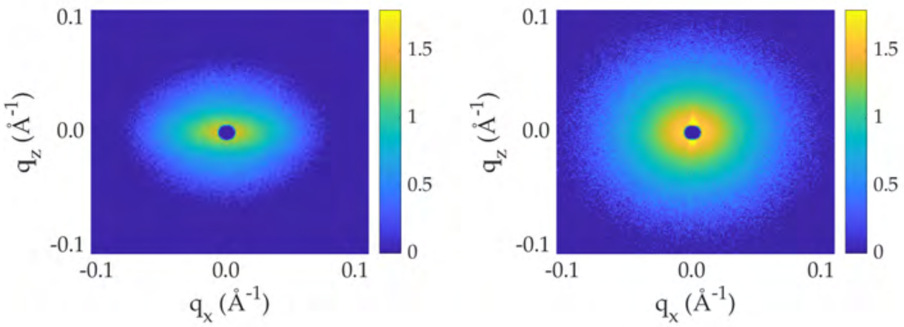

(c) $t = 1.3 \cdot \tau_R$ **(d)** $t = 5.3 \cdot \tau_R$

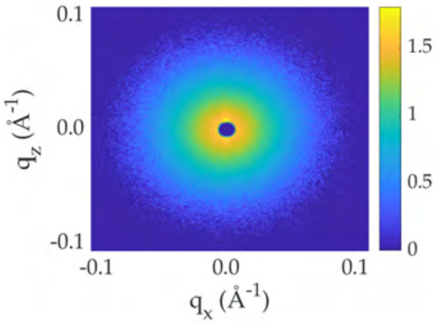

(e) $t = 21.3 \cdot \tau_R$

Figure 4.5: 2D SANS data 5 m setting for Short in Short-samples. The relaxation time increases from a) to e), and is given in terms of the Rouse time, τ_R = 15 s. The data is plotted on $\log_{10}$ scale. All intensities less than one have arbitrarily been rounded up to one for the visualization on log scale.

4.3 Spherical Harmonics Expansion of Experimental Data

In this section we implement the spherical harmonics expansion for experimental data, and show the representations of the 2D data sets in Fig. 4.5 and Fig. 4.4 in terms of the q-dependent expansion coefficients. In the following section we discuss chain retraction relative to the expansion of our data.

4.3.1 Extraction of Expansion Coefficients from Data

For experimental data we need to discretize Eq. 4.8 to obtain the q-dependent expansion coefficients $S_l^0(q)$. Also, as mentioned in Sec. 4.2.3 our data reduction adjusts the sample volume between samples so that we obtain $I(q,\theta) \propto S(q,\theta)$. For our experimental data we therefore determine the spherical harmonics expansion of the scattering intensity, $I(q,\theta)$, and we find the expansion coefficients by a sum instead of an integral :

$$S_l^0(q) = \sum_i^{\pi/\Delta\theta_i} I(q, \cos\theta_i) Y_l^0(\cos\theta_i) \sin\theta_i \Delta\theta. \tag{4.13}$$

The error on $S_l^0(q)$, $\sigma_{I(q,\cos\theta_i)}$, is found by error propagation:

$$\sigma_{S_l^0(q)} = \sqrt{\sum_i^{\pi/\Delta\theta_i} \left(\sigma_{I(q,\cos\theta_i)} Y_l^0(\cos\theta_i) \sin\theta_i \Delta\theta\right)^2}. \tag{4.14}$$

We obtain $I(q, \cos\theta_i)$ by assigning each pixel a q- and θ-value based on the position of its center relative to the beam center and averaging all pixels for which the centers fall in the same q,θ-bin. The chosen bin widths, Δq and $\Delta\theta$ respectively, should be large enough to avoid empty bins and small enough to not average out the features of interest. For this analysis, we settled on $\Delta q = 0.001$ and $\Delta\theta = 5$ as a compromise. We only calculate the expansion for q-values where no θ-bin is empty.

4.3.2 Spherical Harmonics Expansion of Data

With our choice of parameters, the 2D data presented in Fig. 4.5 and Fig. 4.4 can be represented in terms of the first six expansion coefficients as shown in Fig. 4.6 where data from both detector settings are shown.

We can see that although the data from the two detector settings have not been scaled, the expansion coefficient curves overlap nicely except for the sample corresponding to $t = 5.3\tau_R$, Fig. 4.6d, but it looks like the overlap would be ensured by scaling the two curves. We have not done it here to give the most honest demonstration of the framework. We also see that all expansion coefficients fulfill $S_l^0(q) \to 0$ for increasing q since $I(q) \to 0$. The tendency of the expansion coefficients for $q \to 0$ varies due to the excess scattering at small q that we discussed in Sec. 4.2.4 and will return to in Chap. A. The last observation we make is that the expansion coefficients can take both positive and negative values and that their magnitude decreases with increasing relaxation time, which is consistent with the molecules regaining their isotropic equilibrium conformation.

4.3.3 Time Evolution of Expansion Coefficients

In the previous section we described how the amplitude of the expansion coefficients of the anisotropic harmonics decreases as a function of relaxation time. However, the amplitude decrease is not the only change with relaxation time. As we see in Fig. 4.7, the $S_l^0(q)$ curves for the anisotropic modes have a maximal amplitude[2] for some value of q and the maximal amplitude shifts towards larger values of q with increasing relaxation time. This will be an essential point in Sec. 4.1.3 when we discuss chain retraction in the spherical harmonics expansion. We also see that the higher order modes decay more rapidly with relaxation time.

4.3.4 Modeling the Scattering Pattern from Expansion Coefficients

In figure Fig. 4.6 we represented the reduced data in terms of the expansion coefficients of the first six expansion terms. But how well do the truncated expansion series represent the measured data? To answer this question we model the $t = 0\tau_R$ data set from the 14 m setting, Fig. 4.4a. For clarity, we first plot the basis functions from Sec. 4.1.3 in 2D in Fig. 4.8. The modeled data sets are shown in Fig. 4.9. For each subfigure we include one more term in Eq. 4.13. In this way subfigure a) shows the result if we truncate the sum at $l = 0$, sub figure b) if we truncate at $l = 2$, and finally subfigure f) if we truncate at $l = 10$. As we add more harmonics, the modeled data approaches the experimental data. But the truncation of the expansion series introduces spurious wiggles in the reconstructed

---

[2] If we ignore the data points at small q that are dominated by the excess scattering.

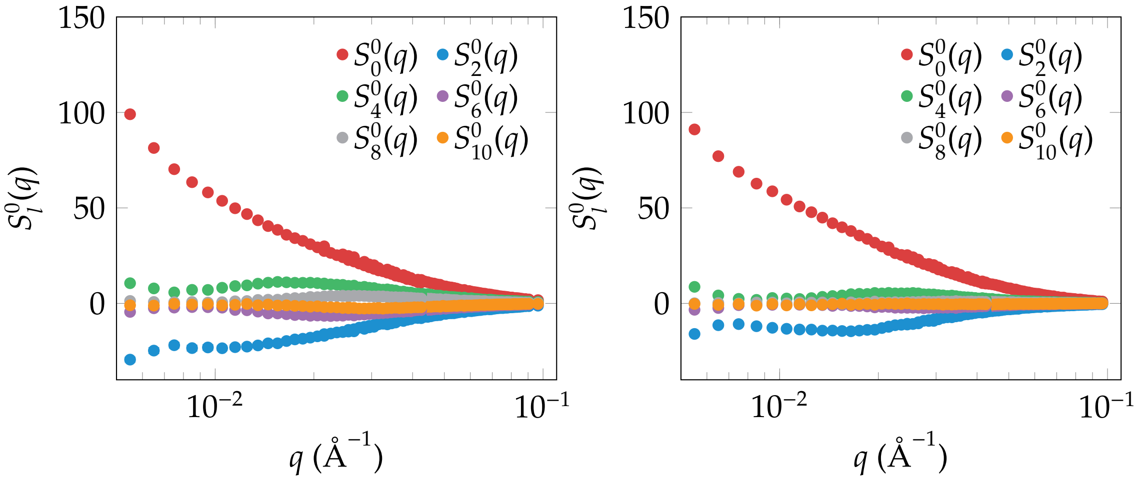

(a) $t = 0 \cdot \tau_R$ **(b)** $t = 0.7 \cdot \tau_R$

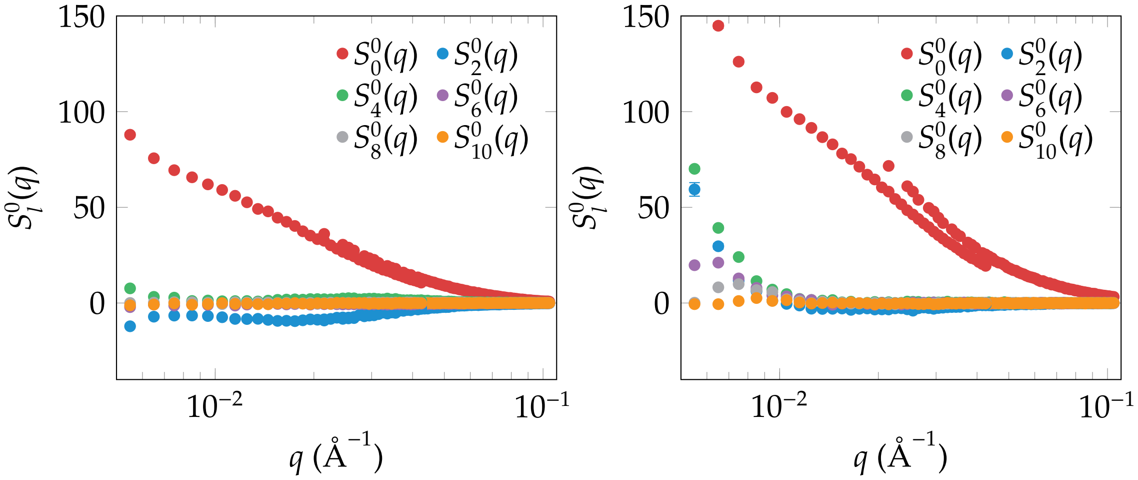

(c) $t = 1.3 \cdot \tau_R$ **(d)** $t = 5.3 \cdot \tau_R$

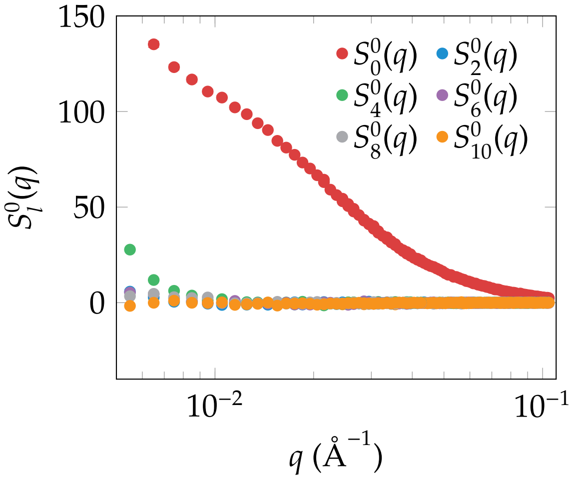

(e) $t = 21.3 \cdot \tau_R$

Figure 4.6: Expansion coefficient representation of data for relaxation time series. The subfigures show the relaxation time "snap shots". The relaxation times are given in terms of the Rouse time for the deuterated component, $\tau_R = 15$ s. The error bars are smaller than the markers and calculated using Eq. 4.14.

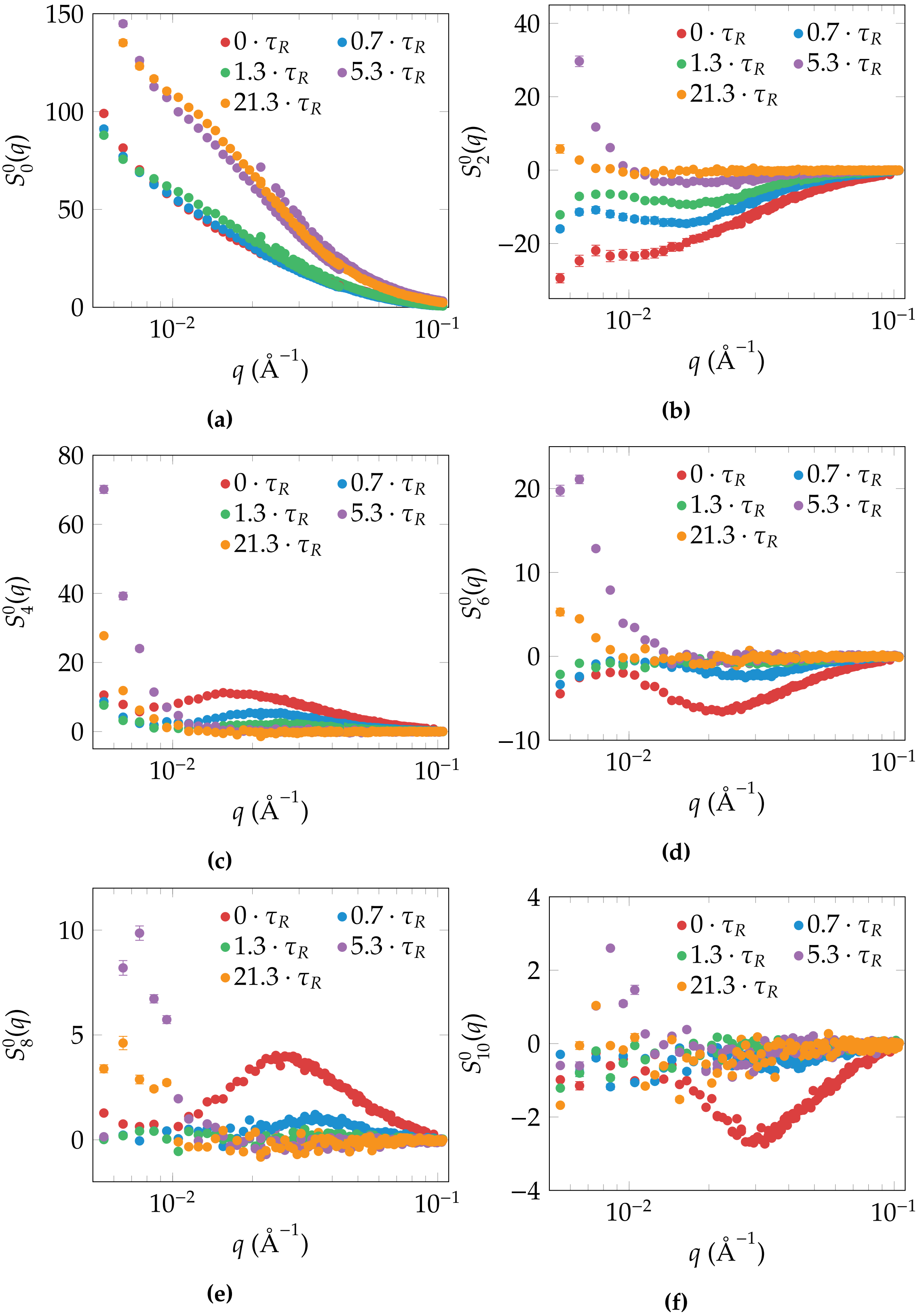

(a)

(b)

(c)

(d)

(e)

(f)

Figure 4.7: Expansion coefficients as function of relaxation time. The expansion coefficients $S_l^0(q)$ are plotted for increasing orders in subfigures a)-f).

scattering pattern even for $l = 10$. In Fig. 4.10 we plot the difference between the experimental $t = 0\tau_R$ data set and the modeled data sets shown in Fig. 4.9.

4.3.5 Qualitative Interpretation of Expansion Coefficient Plots

As we described in Sec. 4.3.2, the expansion coefficients may take both positive and negative values, and their profile amplitude decays with increasing relaxation time, in Sec. 4.3.3 we showed that the maximal amplitude shifts towards larger values of q with increasing relaxation time, and in Sec. 4.3.4 we reconstructed the scattering pattern using the expansion. In this section we discuss why some coefficients are negative while others are positive and how we can interpret the q-values of maximum amplitude magnitude. If we choose the 14 m $t = 0\tau_R$ data set, see Fig. 4.4a, as an example, the aim of this subsection is to understand why the expansion coefficient plot, see Fig. 4.11b, is as it is.

The scattering pattern is characterized by a horizontal streak. For small values of q the model of the scattering pattern including only $S_0^0(q)Y_0^0(\cos\theta)$ and $S_2^0(q)Y_2^0(\cos\theta)$, i.e. Fig. 4.9b captures the horizontal streak well, but $Y_2^0(\cos\theta)$, see Fig. 4.8b, has its maximum intensity on the vertical axis and minimum intensity on the horizontal axis. Therefore $S_2^0(q)$ must be negative. As we move out to larger q, the two-term reconstruction overestimates the intensity away from the horizontal axis, but adding increasing amounts of $Y_4^0(\cos\theta)$ will mend this and so $S_4^0(q)$ starts to increase. In this way the higher order spherical harmonics peak at increasing values of q, and their expansion coefficients have alternating signs. We interpret the peaks or dips in the expansion coefficients $S_l^0(q)$ as the q-range where the symmetry of $Y_l^0(\cos\theta)$ is most present in the data. In the following we loosely use peaks in $S_l^0(q)$ to refer to both dips and peaks because we are interested in the q-values where $Y_l^0(\cos\theta)$ contribute the most and not the sign of the expansion coefficient.

4.3.6 Fitting Approach as an Alternative to Summation

In the presented analysis we have found the expansion coefficients using the sum in Eq. 4.13, but in our first implementation, we instead fitted $I(q,\theta)$ to a linear combination of the basis functions. The linear combination fitted to $I(q,\theta)$ would then have a weight in front of each basis function as fitting parameters. These fitted weights should then be the expansion coefficients $S_l^0(q)$ according to Eq. 4.8 and the orthonormality of the basis functions

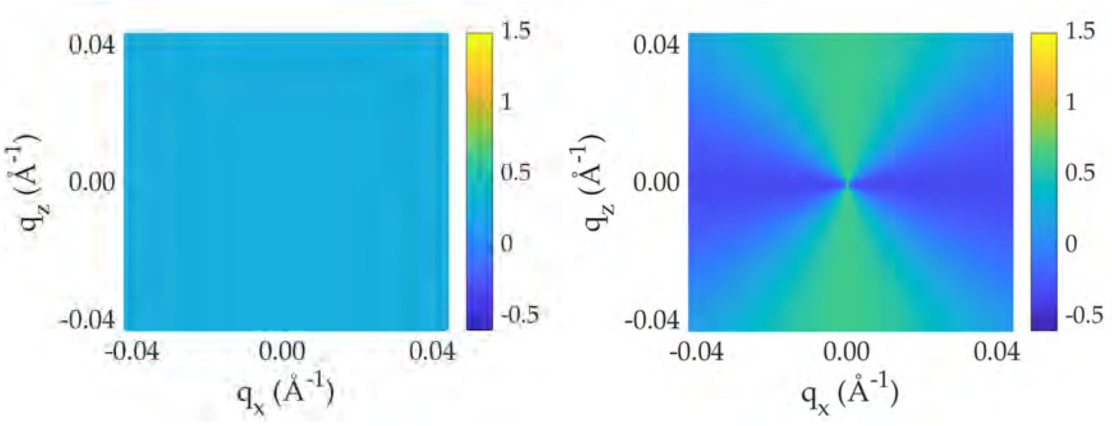

(a) $Y_0^0(q,\theta)$

(b) $Y_2^0(q,\theta)$

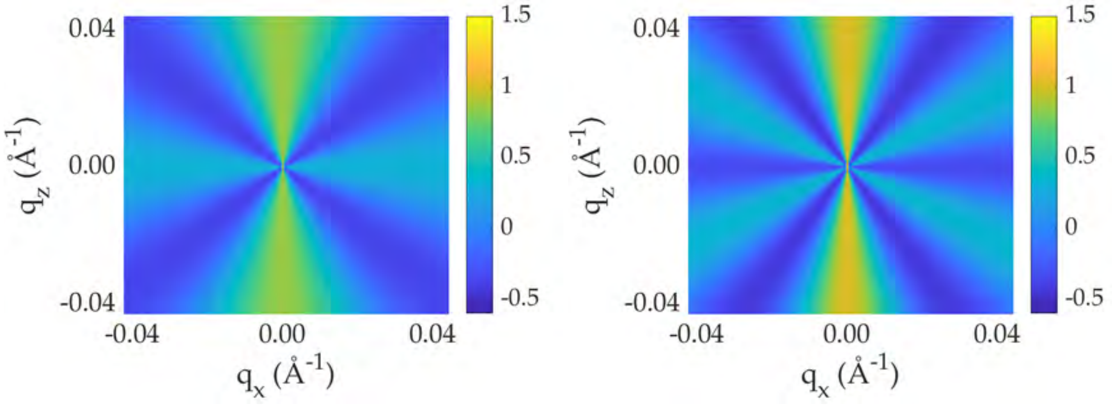

(c) $Y_4^0(q,\theta)$

(d) $Y_6^0(q,\theta)$

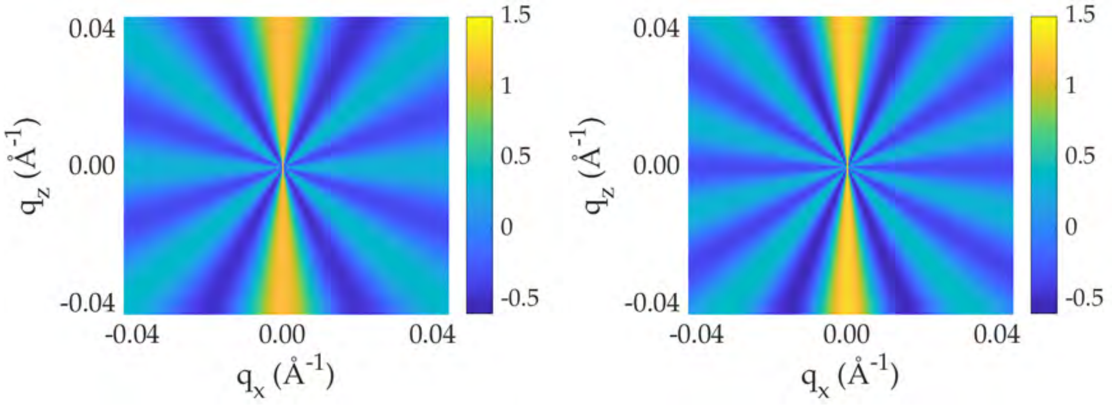

(e) $Y_8^0(q,\theta)$

(f) $Y_{10}^0(q,\theta)$

Figure 4.8: 2D basis functions for reconstruction of 2D scattering patterns plotted on linear scale.

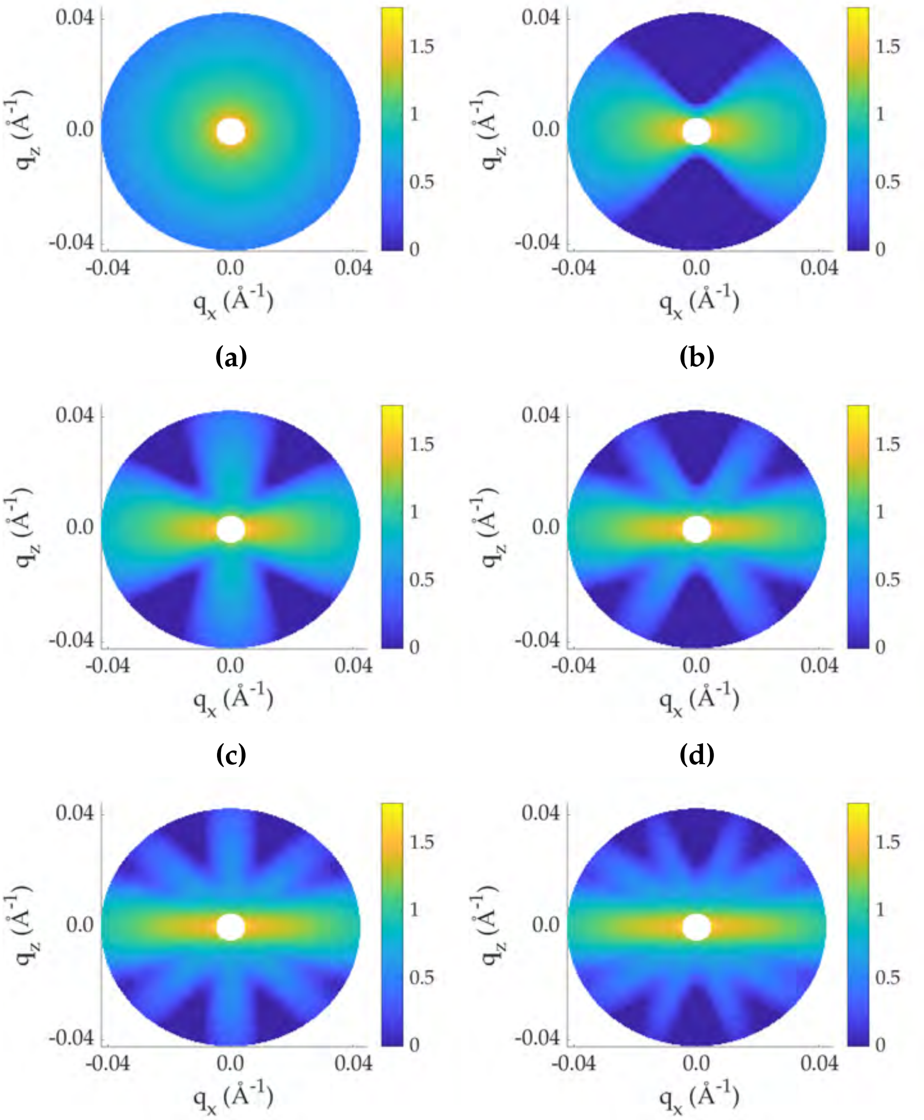

(a) (b) (c) (d) (e) (f)

Figure 4.9: Modeled scattering patterns on logarithmic scale. The scattering pattern corresponding to no relaxation measured in the 14 m setting Fig. 4.4a is modeled with Eq. 4.4 and Eq. 4.13. For each subfigure we add one more harmonic such that a) is the model only including $l = 0$, in b) the expansion is truncated at $l = 2$, and in f) we use all harmonics up to $l = 10$. The modeled patterns are plotted on $\log_{10}$ scale, and modeled intensities < 1 are artificially set to 1 for visualization on log scale.

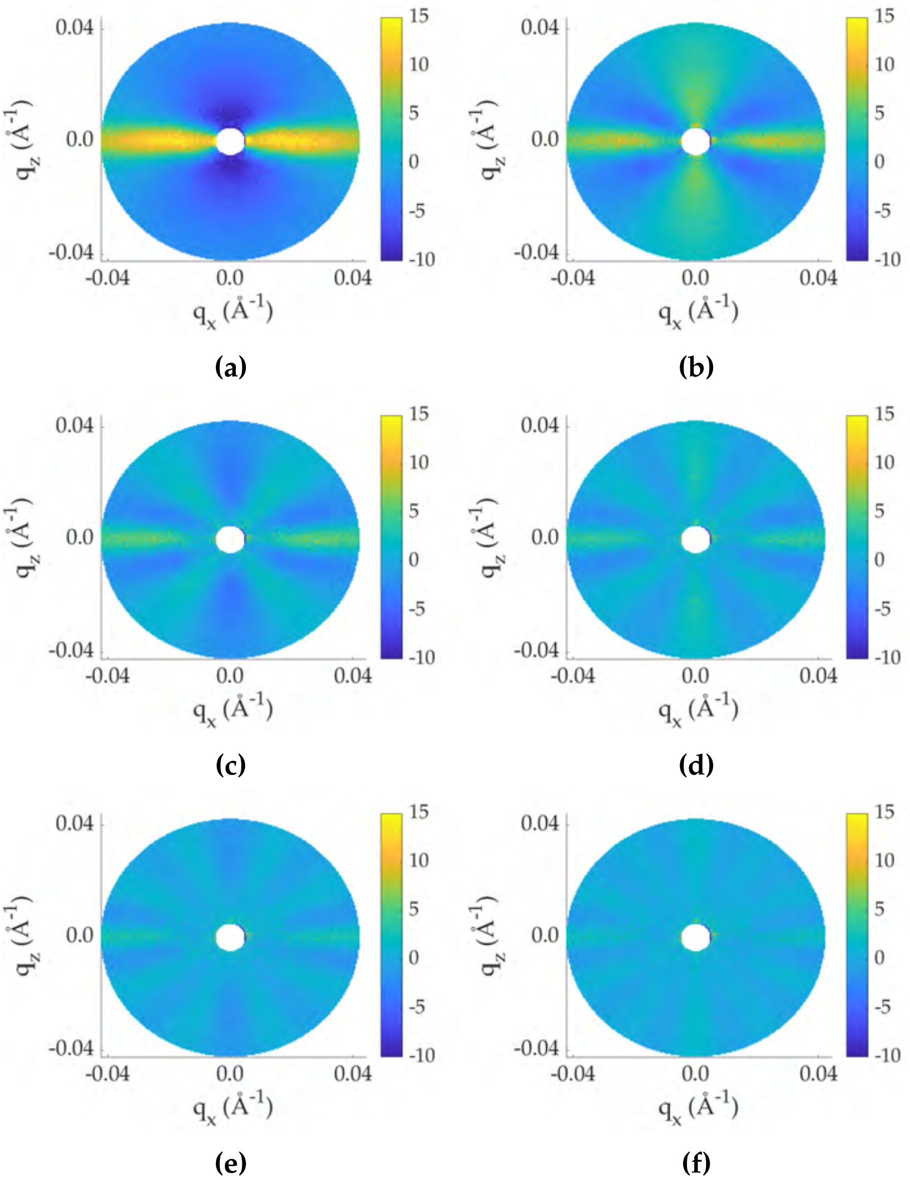

(a) **(b)**

(c) **(d)**

(e) **(f)**

Figure 4.10: Difference between experimental and modeled intensities. In each subfigure we plot the scattering pattern corresponding to no relaxation measured in the 14 m setting Fig. 4.4a with the modeled scattering pattern from Fig. 4.9. For each subfigure we add one more harmonic such that in a) we subtract only the $l = 0$ term in the expansion, in b) we subtract the $l = 0$ and $l = 2$ terms, and in f) we subtract all terms up to $l = 10$. The difference between the experimental data and the modeled data is plotted on linear scale.

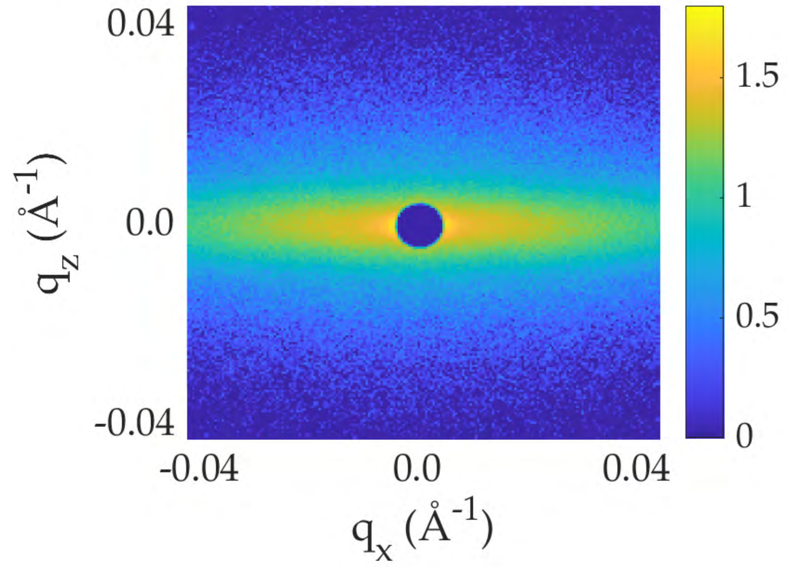

(a)

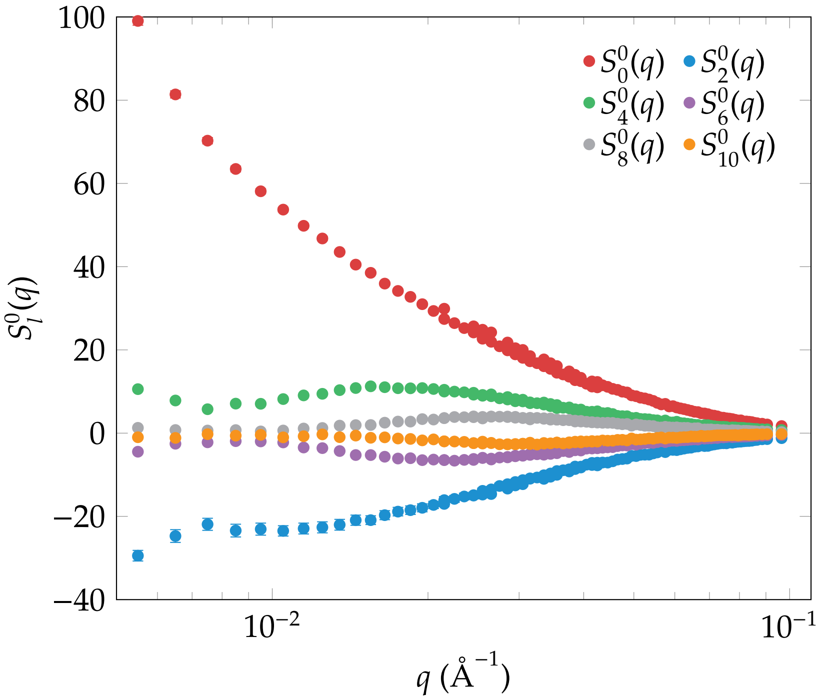

(b)

Figure 4.11: Comparison of 2D pattern and coefficient plot. In subfigure a) the reduced 2D scattering pattern corresponding to no relaxation is shown and in subfigure b) the expansion coefficient plot for the same data is shown.

in Eq. 4.6. This approach was originally chosen over the summation approach to provide a systematic way of determining the needed number of expansion coefficients to describe the data through the goodness of fit, e.g. the reduced chi-square parameter χ^2_{red}. However in the fitting approach, the resulting values of the different expansion coefficients vary with the number of harmonics functions included in the fit. We illustrate this in Fig. 4.12. This is not the case using the summation since each expansion coefficient is calculated independently. The fitting approach may still be justified in certain situations such as in the case of incomplete data, but one should be careful to include enough harmonics above the desired ones.

4.3.7 Summary

In this section we established the framework of spherical harmonics expansion from Sec. 4.1 for analysis of the experimental data presented in Sec. 4.2, and we may therefore represent the data in terms of the q-dependent expansion coefficients. In the next section we will see how this representation can help answering whether chain retraction occurs or not in our system.

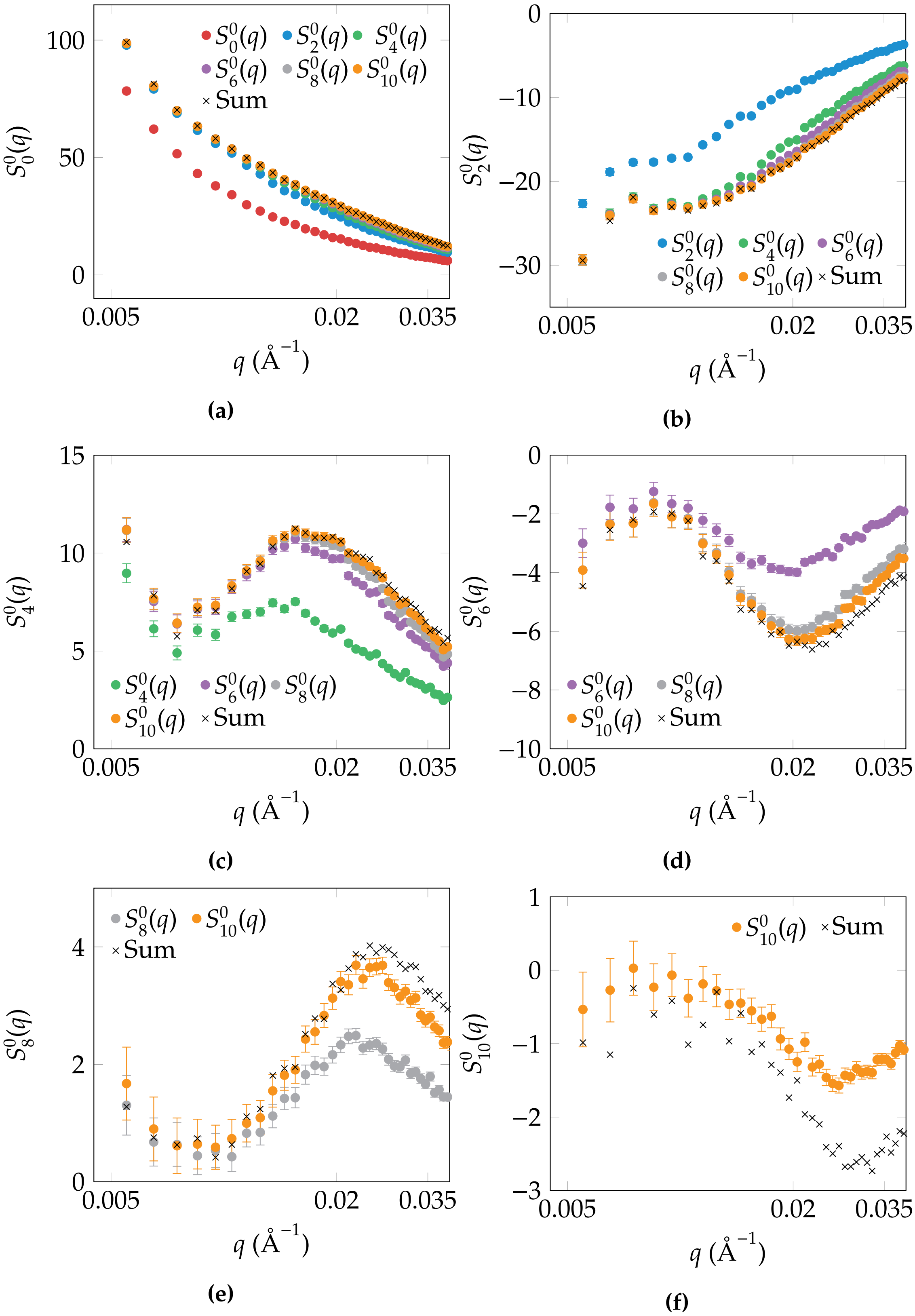

(a) **(b)** **(c)** **(d)** **(e)** **(f)**

Figure 4.12: Comparison of fit and sum extraction of expansion coefficients. The subfigures show the six expansion coefficients determined by fit (colored circles), and summation (crosses) in ascending order from $S_0^0(q)$ in a) and $S_{10}^0(q)$ in f). The legend in each figure indicate the harmonic of largest degree included in the fit.

4.4 Chain Retraction in Spherical Harmonics Expansion

In this section we present the quantitative predictions of chain retraction in the original Doi-Edwards tube model and show the expected finger print of chain retraction in the spherical harmonics expansion. Using our experimental data, we look for chain retraction in the relaxation of the radius of tension components and in the spherical harmonics expansion of the data. Towards the end of the chapter we relate our findings to those of Wang et al. [22] and molecular simulations by Hsu and Kremer [71], and finally we discuss and conclude on our findings.

4.4.1 Chain Retraction in the Tube Model

In the paper "Dynamics of Concentrated Polymer Systems, Part 2 - Molecular Motion under Flow" from 1978 [16], Doi and Edwards discuss polymer dynamics in the tube model under macroscopic deformation and the following relaxation. As described above chain retraction occur as a consequence of the initial chain expansion and the decoupling of the two relaxation modes, Rouse and reptation, should make it visible as a non-monotonic increase in $R_g^{\perp}$. In this section we present the findings of Doi and Edwards and show how they can be used to quantify the effect of chain retraction. We follow Doi and Edwards [16] closely and adapt their notation such that unprimed variables, e.g. x describe the system before deformation, primed variables, e.g. x', represent quantities immediately after deformation, and double primed variables, e.g. x'', represent quantities after the Rouse relaxation processes.

Regarding deformation, Doi and Edwards assume that the molecules deform affinely with the macroscopic deformation such that the end-to-end vector of the i'th tube segments, $\vec{r_i}$, changes during the deformation such that

$$\vec{r_i}' = E \cdot \vec{r_i} \tag{4.15}$$

where E is the macroscopic deformation tensor. In the following, we consider uniaxial extension along the z-axis and incompressibility, and then the macroscopic deformation tensor is

$$E = \begin{pmatrix} 1/\sqrt{\lambda} & 0 & 0 \\ 0 & 1/\sqrt{\lambda} & 0 \\ 0 & 0 & \lambda \end{pmatrix}. \tag{4.16}$$

As measures for the deformation of the molecule we first study the end-to-end vector and later the radius of gyration tensor. The tensorial average of the end-to-end vector V is defined as

$$\left\langle V_\alpha(t)V_\beta(t)\right\rangle = \left\langle \sum_{ij}^{N} r_{i\alpha}(t) r_{j\beta}(t)\right\rangle_0 \tag{4.17}$$

where N is the number of tube segments in equilibrium, $\alpha, \beta = x, y, z$, and subscript 0 indicates that the average is over the equilibrium segment distribution, which is isotropically distributed (in three dimensions) such that

$$\left\langle r_{i\alpha} r_{j\beta}\right\rangle_0 = \frac{a^2}{3}\delta_{ij}\delta_{\alpha\beta} \tag{4.18}$$

where a is the length of a tube segment and tube diameter.

The tensorial average of the end-to-end vector then becomes

$$\left\langle V_\alpha(t)V_\beta(t)\right\rangle = \sum_{ij}^{N}\left\langle r_{i\alpha} r_{j\beta}\right\rangle_0 = \frac{Na^2}{3}\delta_{\alpha\beta}. \tag{4.19}$$

After deformation the tensorial average becomes

$$\begin{aligned}\left\langle V'_\alpha(t)V'_\beta(t)\right\rangle &= \sum_{ij}^{N}\left\langle (E\cdot\vec{r}_i)_\alpha \left(E\cdot\vec{r}_j\right)_\beta\right\rangle_0 \\ &= \sum_{ij}^{N}\sum_{\gamma\delta} E_{\alpha\gamma}E_{\beta\delta}\left\langle r_{i\gamma} r_{j\delta}\right\rangle_0 \\ &= \frac{a^2}{3}\sum_{ij}^{N}\delta_{ij}\sum_{\gamma\delta} E_{\alpha\gamma}E_{\beta\delta}\delta_{\gamma\delta} \\ &= \frac{Na^2}{3}\sum_{\gamma} E_{\alpha\gamma}E_{\beta\gamma}.\end{aligned} \tag{4.20}$$

In the frame where E is diagonal, i.e. the Cartesian coordinates for the deformation defined in Eq. 4.16, the tensorial average of the end-to-end vector immediately after deformation becomes

$$\left\langle V'_\alpha(t)V'_\beta(t)\right\rangle = \frac{Na^2}{3}\lambda_\alpha^2\delta_{\alpha\beta}. \tag{4.21}$$

With this result it can be shown that the mean square end-to-end distance $\langle V'^2 \rangle_0$ is always larger than $\langle V^2 \rangle_0$ if the volume is conserved during deformation[16].

Now we calculate the tensorial average of the end-to-end vector after Rouse relaxation. To do that, we need to consider that the number of entanglements decrease during the Rouse relaxation. Doi and Edwards assumes that the monomer density per arc length of the chain goes back to the equilibrium value a/b^2 after the Rouse relaxation. As a consequence the average number of monomers per segment $\left\langle n_i'' \right\rangle$ increases relative to the state immediately after deformation and thus the number of entanglement segments N'' decreases

$$N'' = \frac{N_0}{\left\langle n_i'' \right\rangle} \tag{4.22}$$

where N_0 is the number of monomers in the chain. Doi and Edwards argue that the assumption of equilibrium monomer density per arc length leads to an average number of monomers per segment of

$$\left\langle n_i'' \right\rangle = \frac{a\left|\vec{r}_i\right|}{b^2}. \tag{4.23}$$

$$\tag{4.24}$$

Now introducing the isotropically distributed unit vector $\vec{u}$, we show that

$$\begin{aligned} \left\langle n_i'' \right\rangle &= \frac{a\left\langle \left|E \cdot \vec{r}_i\right| \right\rangle_0}{b^2}. \\ &= \frac{a^2\left\langle \left|E \cdot \vec{u}\right| \right\rangle_0}{b^2}. \end{aligned} \tag{4.25}$$

In this way we get the new number of entanglement segments

$$N'' = \frac{N_0}{\frac{a^2\left\langle \left|E \cdot \vec{u}\right| \right\rangle_0}{b^2}} = \frac{N}{\left\langle \left|E \cdot \vec{u}\right| \right\rangle_0}. \tag{4.26}$$

The resulting tensorial average of the end-to-end vector after the Rouse time is given by Eq. 4.20 with $N \to N''$:

$$\left\langle V_\alpha''(t) V_\beta''(t) \right\rangle = \frac{\left\langle V_\alpha'(t) V_\beta'(t) \right\rangle}{\langle |E \cdot u| \rangle_0} \tag{4.27}$$

And we thus see that the end-to-end vector shrinks during the first relaxation.

For the radius of gyration tensor $I_{\alpha\beta}$ that fulfills Tr$I = \left\langle \vec{R}_g^2 \right\rangle$, one can show that[16]

$$I_{\alpha\beta}(t=0) = \delta_{\alpha\beta}\lambda_\alpha^2 \frac{\langle S^2\rangle_0}{3} \tag{4.28}$$

$$I_{\alpha\beta}(t \simeq \tau_R) = \frac{I_{\alpha\beta}(t=0)}{\langle |E\cdot u|\rangle_0} \tag{4.29}$$

where $\langle S^2\rangle_0$ is the mean square radius of gyration in equilibrium. In conclusion the tube model predict that the characteristic dimensions of the molecules shrink by a factor of $1/\langle |E\cdot u|\rangle_0$ during Rouse relaxation and before reptation takes over. Note that e.g. $I_{\alpha\alpha} = R_{g,\perp}^2$ so therefore the radius of gyration components will shrink by $\sqrt{\langle |E\cdot u|\rangle_0}$ during the first $t \simeq \tau_R$ according to the Doi-Edwards tube model.

Molecular Shrink Factor

For later quantitative tests of the chain retraction hypothesis, we would like to evaluate $\langle |E\cdot u|\rangle_0$ for given values of λ and we therefore calculate $\langle |E\cdot u|\rangle_0$ here. We use that u is a unit vector and express it in spherical coordinates. Using the deformation matrix from Eq. 4.16 we obtain $|E\cdot u|$:

$$E\cdot u = \begin{pmatrix} \lambda^{-\frac{1}{2}}\cos\phi\sin\theta \\ \lambda^{-\frac{1}{2}}\sin\phi\sin\theta \\ \lambda\cos\theta \end{pmatrix} \tag{4.30}$$

$$|E\cdot u| = \sqrt{\lambda^{-1}\sin^2\theta + \lambda^2\cos^2\theta}. \tag{4.31}$$

The average $\langle \ldots\rangle_0$ is over the equilibrium distribution of u, which is isotropic:

$$\begin{aligned}\langle |E\cdot u|\rangle_0 =& \frac{1}{4\pi}\int_0^\pi \mathrm{d}\theta \int_0^{2\pi} \mathrm{d}\phi |E\cdot u|\sin\theta \\ =& \frac{1}{2}\int_0^\pi \mathrm{d}\theta\, \sqrt{\lambda^{-1}\sin^2\theta + \lambda^2\cos^2\theta}\sin\theta \\ =& \frac{1}{2\sqrt{\lambda}}\int_0^\pi \mathrm{d}\theta\, \sqrt{1+(\lambda^3-1)\cos^2\theta}\sin\theta. \end{aligned} \tag{4.32}$$

To solve the integral, we perform a series of substitutions. In the first substitution we define y

$$
\begin{aligned}
y =& \cos\theta \\
\mathrm{d}\theta =& -\frac{1}{\sin\theta}\mathrm{d}y \\
\langle|E\cdot u|\rangle_0 =& \frac{-1}{2\sqrt{\lambda}}\int_1^{-1}\mathrm{d}y\,\sqrt{1+(\lambda^3-1)y^2} \\
=& \frac{1}{\sqrt{\lambda}}\int_0^1\mathrm{d}y\,\sqrt{1+(\lambda^3-1)y^2}.
\end{aligned}
\tag{4.33}
$$

The second substitution is carried out by defining v

$$
\begin{aligned}
v =& \arctan\left(\sqrt{(\lambda^3-1)y^2}\right) \\
\mathrm{d}y =& \frac{\sec^2(v)}{\sqrt{\lambda^3-1}}\mathrm{d}v \\
\langle|E\cdot u|\rangle_0 =& \frac{1}{\sqrt{\lambda}}\int\mathrm{d}v\,\sqrt{1+(\lambda^3-1)\left(\frac{\tan v}{\sqrt{\lambda^3-1}}\right)^2}\,\frac{\sec^2(v)}{\sqrt{\lambda^3-1}} \\
=& \frac{1}{\sqrt{\lambda(\lambda^3-1)}}\int\mathrm{d}v\,\sqrt{1+\tan^2 v}\,\sec^2(v)
\end{aligned}
$$

In the next steps we use the following relation between sec(x) and tan(x) as well as the reduction formula for integrals over $\sec^n(x)$

$$
\begin{aligned}
\sec^2 v =& \tan^2 v - 1 \\
\int\mathrm{d}x\,\sec^n(x) =& \frac{n-2}{n-1}\int\mathrm{d}x\,\sec^{n-2}(x) + \frac{\sec^{n-2}(x)\tan(x)}{n-1}.
\end{aligned}
$$

We can now solve the integral

$$
\begin{aligned}
\langle|E\cdot u|\rangle_0 =& \frac{1}{\sqrt{\lambda(\lambda^3-1)}}\int\mathrm{d}v\,\sec^3(v) \\
=& \frac{1}{2\sqrt{\lambda(\lambda^3-1)}}\left(\int\mathrm{d}v\,\sec(v) + \sec(v)\tan(v)\right) \\
=& \frac{1}{2\sqrt{\lambda(\lambda^3-1)}}\left[\ln\left(|\tan(v)+\sec(v)|\right) + \sec(v)\tan(v)\right].
\end{aligned}
\tag{4.34}
$$

We now substitute back to the integral over y and obtain the final result

$$\begin{aligned}
\langle |E\cdot u|\rangle_0 =& \frac{1}{\sqrt{\lambda}}\int_0^1 \mathrm{d}y\sqrt{1+(\lambda^3-1)y^2}\\
=&\left[\frac{1}{2\sqrt{\lambda(\lambda^3-1)}}\left(\ln\left(\left|\sqrt{(\lambda^3-1)y^2-1}+\sqrt{(\lambda^3-1)y^2}\right|\right)\right.\right.\\
&\left.\left.+\sqrt{(\lambda^3-1)y^2-1}\sqrt{(\lambda^3-1)y^2}\right)\right]_0^1\\
=&\frac{1}{2\sqrt{\lambda(\lambda^3-1)}}\left[\ln\left(\left|\sqrt{\lambda^3}+\sqrt{(\lambda^3-1)}\right|\right)+\sqrt{\lambda^3}\sqrt{\lambda^3-1}\right]\\
=&\frac{1}{2}\left[\lambda+\frac{1}{\sqrt{\lambda(\lambda^3-1)}}\ln\left(\left|\sqrt{(\lambda^3-1)}+\sqrt{\lambda^3}\right|\right)\right]. \qquad (4.35)
\end{aligned}$$

We see that for $\lambda \gg 1$

$$\langle |E\cdot u|\rangle_0 \sim \frac{1}{2}\lambda. \qquad (4.36)$$

Our result is consistent with that of Boue et al.[65]. The molecular stretch factor $\langle |E\cdot u|\rangle_0$ is plotted as a function of macroscopic stretch factor λ in Fig. 4.13.

4.4.2 Tube Model Chain Retraction in Spherical Harmonics Expansion

In the previous section we established how the Doi-Edwards tube model predicts that the radii of gyration will change during relaxation. In this section we show the fingerprint of chain retraction in the Doi Edwards model. From Eq. 4.28 and an affine uniaxial extension along the z-axis of magnitude λ we know that the diagonal radius of gyration components will be given as

$$\begin{aligned}
R_g^x =& R_g^y = R_g^\perp = R_g^0/\sqrt{\lambda}\\
R_g^z =& R_g^\parallel = \lambda R_g^0. \qquad (4.37)
\end{aligned}$$

The structure factor will then be given by the Debye function, as in Sec. 4.2.3,

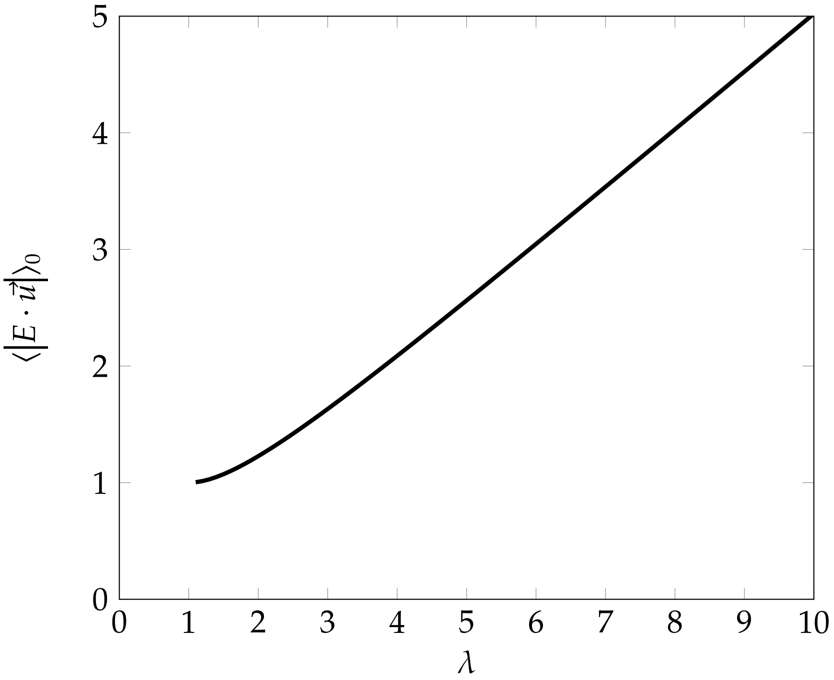

Figure 4.13: Molecular stretch $\left\langle \left| E \cdot \vec{u} \right| \right\rangle_0$ as function of macroscopic stretch λ for affine deformation.

$$S(\vec{q}) = \frac{2}{x^2}\left(e^{-x} + x - 1\right) \tag{4.38}$$

with a modification of x:

$$x = \left(q_{\|} R_g^{\|}\right)^2 + \left(q_{\perp} R_g^{\perp}\right)^2 \tag{4.39}$$

that takes the differences in radius of gyration into account. After completion of the Rouse relaxation all components of the radius of gyration tensor will shrink by the factor in Eq. 4.35 for $\tau_d \gg \tau_R$, see Eq. 4.29, which gives rise to the non-monotonic increase in $R_g^{\perp}$ as described in the previous subsection. To show the finger print of chain retraction we simulate the structure factor immediately after affine deformation of $\lambda = 3$ for molecules of $R_g^0 = 80$ Å and for the same molecules exposed to the deformation and allowed to complete the Rouse relaxation. The results are shown in Fig. 4.14a and 4.14b. The scattering pattern corresponding to complete Rouse relaxation share all features with the pattern from immediately after deformation except that they occur at larger q-values consistent with the molecule preserving its orientation while shrinking in all dimensions back to the equilibrium length. The similarity is much clearer in the spherical harmonics expansion of the two structure factors in Fig. 4.14c. All the expansion coefficients have the exact same shape for both patterns but is shifted horizontally after the Rouse relaxation. Here Wang et al. [72] point out not only the horizontal shift in i.e. the minimum of $S_2^0(q)$ as a sign of chain retraction but also the feature of "anisotropy inversion" where if we consider q-values somewhat larger than that of the minimum of $S_2^0(q)$, the degree of anisotropy increase with relaxation instead of decreasing as expected, but as we see from Fig. 4.14c for the same q-values also $S_0^0(q)$ increase. We therefore consider it to simply be a direct consequence of the horizontal shift.

4.4.3 Chain Retraction in Experimental Data

In this subsection we analyze our data for signs of chain retraction using first radius of gyration analysis and the spherical harmonics expansion.

Radius of Gyration Analysis

As described in the the beginning of the chapter, previous experimental tests of the chain hypothesis mostly consisted of radius of gyration analysis where the time dependence of $R_g^{\parallel}$ and $R_g^{\perp}$ is compared to the prediction in Eq. 4.28 and 4.29. Especially a non-monotonic increase in $R_g^{\perp}(t)$ with minimum at $t \approx \tau_R$ is taken as support for the chain retraction hypothesis.

As an initial test of whether we see signs of chain retraction in our data, we first determine $R_g^{\parallel}(t)$ and $R_g^{\perp}(t)$ from the relaxation series by fitting sector averages parallel to the stretch direction at $0 \pm 10^\circ$ and perpendicular to it at $90 \pm 10^\circ$ to the Debye function with the radius of gyration R_g and an arbitrary scaling factor A as fitting parameters:

$$y = A \cdot \frac{2}{q^4 R_g^4} \left(e^{-q^2 R_g^2} + q^2 R_g^2 - 1 \right). \tag{4.40}$$

Due to the excess scattering at low q, only data for $q > 0.015$ Å^{-1} was included in the fit. The resulting radii of gyration for each sample are then plotted as a function of relaxation time in Fig. 4.15. There are no indication of a non-monotonic increase in $R_g^{\perp}(t)$. Based on this analysis, we should conclude that chain retraction does not occur in our system. However, as we will see below we reach a different conclusion using the spherical harmonics expansion.

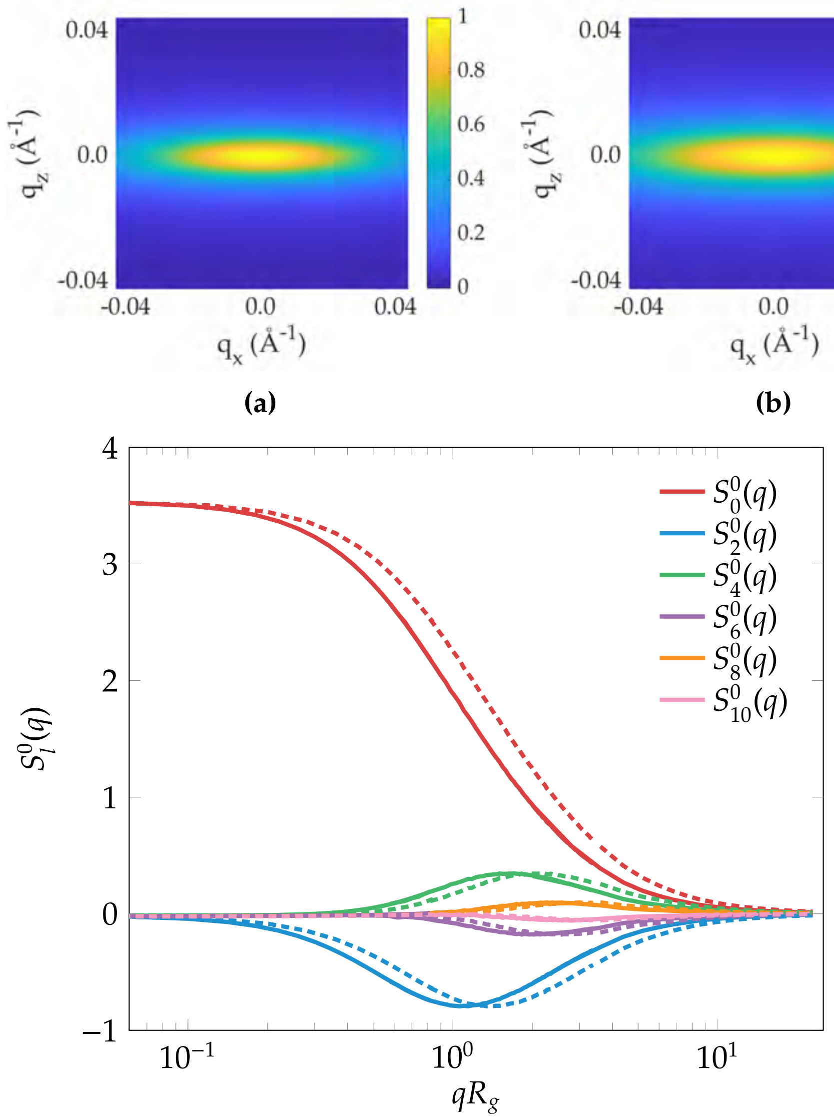

(a) **(b)**

(c)

Figure 4.14: Spherical harmonics expansion of the affinely deformed Debye structure factor before and after completion of Rouse relaxation. In a) we plot the Debye structure factor deformed affinely with macroscopic stretch of $\lambda = 3$ and and b) we plot the structure factor after completion of the Rouse relaxation, both on a linear scale. In c) we plot the spherical harmonics expansion of both structure factors where fully drawn lines are for the structure factor after deformation and the dashed lines are for the structure factor after completion of Rouse relaxation.

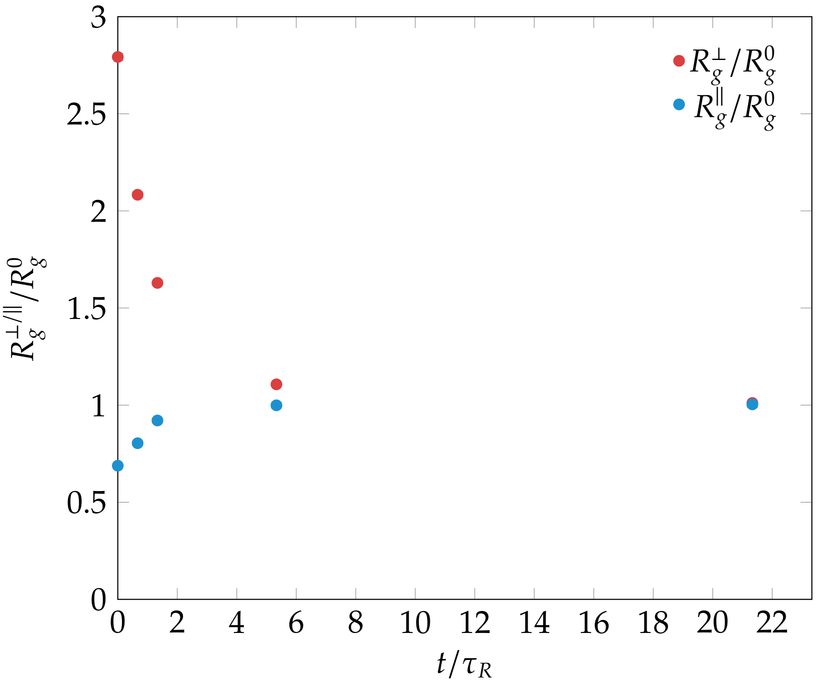

Figure 4.15: Radius of gyration tensor components $R_g^{\perp/\parallel}/R_g^0$ normalized to the equilibrium value $R_g^0 = 78.2$Å [10] as function of relaxation time t/τ_R normalized by the Rouse time $\tau_R \approx 15$ s.

Spherical Harmonics Expansion

In this section we present our results on spherical harmonics expansion of the data sets shown in Sec. 4.3.2 in the context of chain retraction. In this discussion we focus on the evolution of $S_2^0(q)$ which is the coefficient of the leading anisotropic contribution. We reproduce Fig. 4.7b in Fig. 4.16. As discussed above, we see that the dip in $S_2^0(q)$ shifts horizontally towards larger q and its amplitude decreases during relaxation. Here we compare the horizontal shift to the quantitative predictions of the tube model. To do that we need to determine the positions of the minima in $S_2^0(q)$ as a function of time and λ for our experiment. We determine the minima by fitting sixth degree polynomials to $S_2^0(q)$ for $t = 0 \cdot \tau_R$, $t = 0.7 \cdot \tau_R$, and $t = 1.3 \cdot \tau_R$. Using the fit coefficients, we and the result is plotted in the inset of Fig. 4.16.

To determine λ we first consider the measured macroscopic stretch ratio: we stretch the samples to a Hencky strain of $\varepsilon = 3$ leading to $\lambda_{\text{macro}} \approx 20$. The molecular stretch ratio λ in our case however must be smaller because we stretch to $\varepsilon = 3$ to make sure that we reach steady

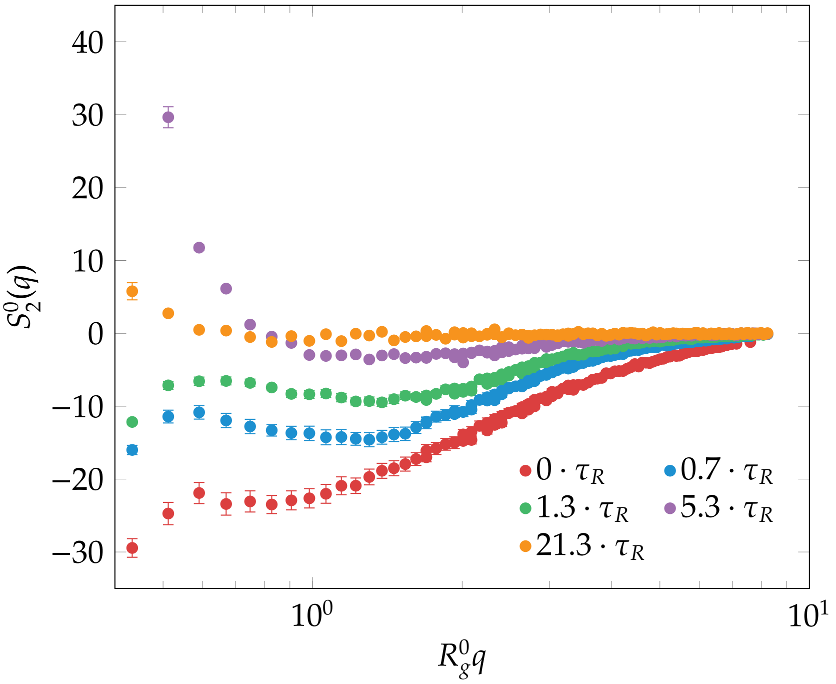

Figure 4.16: The expansion coefficient $S_2^0(q)$ for varying relaxation times as a function of qR_g^0 where the equilibrium radius of gyration is $R_g^0 = 78.2$ Å[10]. The inset shows the minima q^* as a function of relaxation time t.

state, i.e. the molecular stretch does not change with macroscopic stretch. Simply plotting (not shown here) the Debye function in Eq. 4.38 and comparing the result to the 2D pattern corresponding to $t = 0$ s relaxation, see e.g. Fig. 4.11a, reveal that we have $\lambda \sim 5$ and not $\lambda \sim 20$. That we stretch slightly past the point of steady state alone cannot explain the small value of λ relative to λ_{macro}, but a non-coupling between the macroscopic stretch and the molecular stretch has been proposed such that $\lambda = \lambda_{\text{macro}}^{\nu}$[40, 39, 37, 73] where the value $\nu = 1/2$ was proposed in [39, 40]. A non-affine coupling of the molecular and macroscopic stretch ratio with an exponent value of $\nu = 1/2$ would correspond to $\lambda \sim 4$. To determine the value of λ more accurately we first assume affine deformation, i.e. that the radii of gyration have the relations of Eq. 4.37 and fit the $t = 0\tau_R$ data set from the 14 m setting to the Debye function in Eq. 4.38 in a least squares sense with λ and an overall amplitude of the structure factor as fitting parameters. The resulting value of the molecular stretch is $\lambda_{\text{affine}} = 3.4$ and the difference pattern between the data set and the best fits is plotted in Fig. 4.17a where we see systematic deviations.

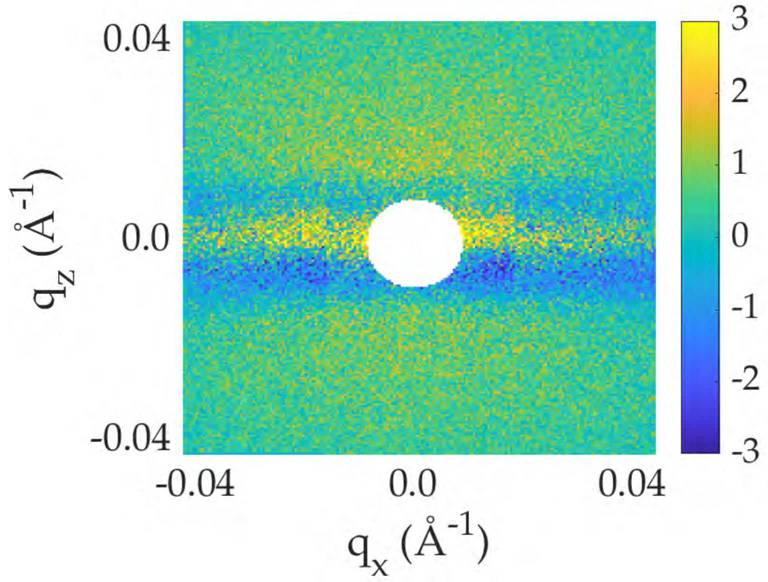

(a)

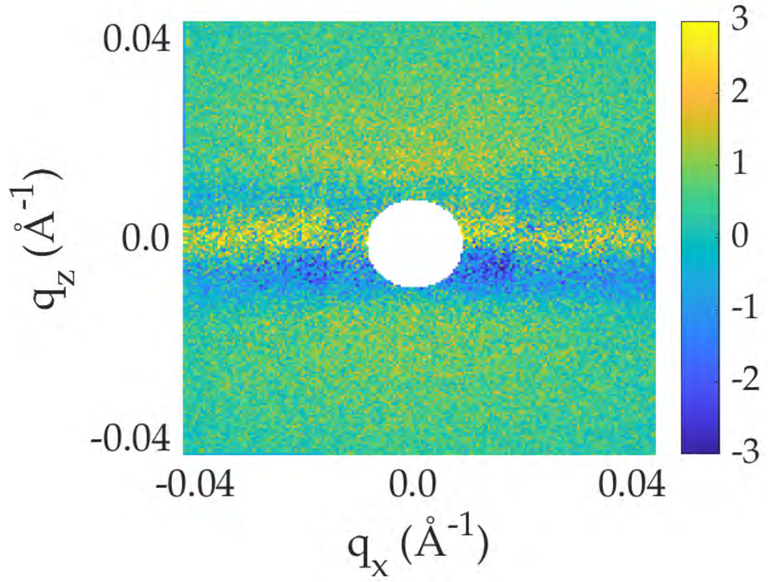

(b)

Figure 4.17: Difference between 14-m setting data set for $t = \tau_R$ and best fit to the modified Debye structure factor, affine and non-affine. In a) assuming affine deformation i.e. $R_g^\perp = \lambda R_g^0$ and $R_g^\parallel = 1/\sqrt{\lambda} R_g^0$ and in b) not assuming affine deformation i.e. $R_g^\perp = \lambda^\perp R_g^0$ and $R_g^\parallel = \lambda^\parallel R_g^0$ with $\lambda^\parallel \neq 1/\sqrt{\lambda^\perp}$.

We also fit to the Debye function in a non-affine sense where we allow for $\lambda^{\perp} \neq 1/\sqrt{\lambda^{\parallel}}$ thus having $\lambda^{\perp}$, $\lambda^{\parallel}$, and an overall amplitude of the structure factor as fitting parameters. The results are $\lambda^{\parallel}_{\text{non-affine}} = 3.5$ and $\lambda^{\perp}_{\text{non-affine}} = 0.60$ where $1/\sqrt{\lambda^{\parallel}_{\text{non-affine}}} = 5.3$. The difference between the data and the fit is shown in Fig. 4.17b. As we see in both plots of the difference between the data and the Debye functions there are systematic deviations and so neither describes the data at all length scales. Since the values of the λ are so similar in the two cases and since the introduction of an extra fitting parameter does not improve the fit significantly, we conclude that $\lambda = \lambda_{\text{affine}} = 3.4$ in our analysis. However, Kirkensgaard et al. found $\lambda = 4.3 \pm 0.3$ so in the following we compare the quantitative predictions of the tube model to the found minima in $S^0_2(q)$ using both $\lambda = 3.4$ and $\lambda = 4.3$. For these values of λ, the molecular shrink factors from Eq. 4.35 are

$$\sqrt{\langle |E \cdot u| \rangle_0 \, (\lambda = 3.4)} = 1.4 \tag{4.41}$$

$$\sqrt{\langle |E \cdot u| \rangle_0 \, (\lambda = 4.3)} = 1.5. \tag{4.42}$$

The ratio $q^*_{t=0.7\cdot\tau_R}/q^*_{t=0\cdot\tau_R} = 1.5$ and $q^*_{t=1.3\cdot\tau_R}/q^*_{t=0\cdot\tau_R} = 1.7$. If $\lambda = 4.3$, and we assume that Rouse relaxation is approximately completed at $t = 1.3 \cdot \tau_R$ the dip shift found from fitting the data curves is slightly larger than but yet consistent with the quantitative predictions of the Doi Edwards tube model. Comparing the experimental relaxation series of $S^0_2(q)$, Fig. 4.16, to the theoretical expectation, the blue dashed curve relative to the blue fully drawn curve in Fig. 4.14c, we do not have the ideal signature since we apart from the horizontal shift also see a decrease in the amplitude of the $S^0_2(q)$-profile during the initial relaxation $t \leq 1.3\tau_R$. This is probably due to the relatively short chain length leading to less separated Rouse and reptation times, $\tau_d \approx 10\tau_R$, than for longer chains.

4.5 Discussion

In the previous section we showed that the radius of gyration analysis of our data lead to the conclusion that chain retraction does not occur, meaning that the Doi-Edwards tube model is incorrect, whereas the spherical harmonics expansion analysis clearly support the Doi-Edwards model. In this section we compare our results to those of Wang et al.[22] who did not see chain retraction in the spherical harmonics expansion of their data and to those of Hsu and Kremer [71] who performed a molecular dynamics simulation and showed how the effect depends on the magnitude of the initial deformation and discuss the origin of our apparently contradicting findings on whether chain retraction occurs or not.

4.5.1 Comparison with Experiment by Wang et al.

In Wang et al.[22] where the compiled spherical expansion framework was first published, the authors too used the framework to test the chain retraction hypothesis. Their conclusion was that either chain retraction did not occur or it was somehow screened by other non-linear effects in the relaxation that were not included in the tube model[22], and in this way they challenged the tube model. That we reach opposing conclusions must be due to differences in the performed experiments and we therefore describe the experiment of Wang et al. in detail here.

Wang et al. also worked with a polystyrene melt but of a larger molecular weight $M_w = 450$ kg/mol. They stretched their melt at $T = 130°$ C at which temperature the Rouse time of there hydrogenous component is $\tau_R^{\text{Wang}} = 592$ s determined by the Osaki formula. They stretched their samples on a RSA-G2 Solids Analyzer from TA Instruments up to macroscopic stretch ratio $\lambda = 1.8$ at constant stretch ratio rate such that

$$\lambda(t) = l_0(1 + 40t/\tau_R) \tag{4.43}$$

where l_0 is the initial sample length. Our stretching scheme is graphically compared to that of Wang et al. in Fig. 4.18 in terms of Hencky strain $\varepsilon = \exp(\lambda)$, and Rouse Weissenberg number Wi_R both as functions of time. We see that both stretching schemes result in a Rouse Weissenberg number $Wi_R > 1$ which means that we expect chain stretch in both cases, see Sec. 1.2.

They used the GLaMM-model, see Sec. 1.1.3 to predict how $S_l^0(q)$ should change with relaxation time, i.e. how the dip should shift to larger values of q, see Fig. 4.19a, but when they analyzed their experimental data, see Fig. 4.19a, the predicted dip shift was absent. Based on the absence of the shift, they concluded that either chain retraction does not occur or it was somehow screened by other non-linear effects in the relaxation that were not included in the tube model[22].

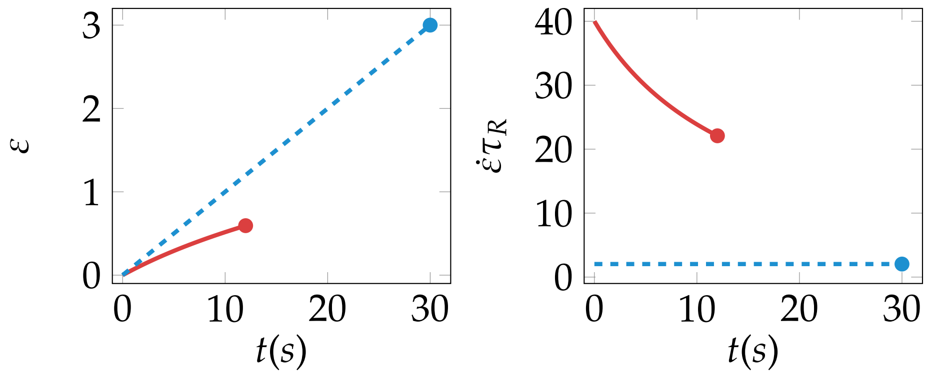

(a) **(b)**

Figure 4.18: Comparison of stretching schemes. In a) we plot Hencky strain ε as function of time t, and in b) we plot Hencky strain rate non-dimensionalized by the Rouse time $\dot{\varepsilon}\tau_R$. In both figures the dashed blue line illustrates our stretching scheme and the red line that of Wang et al..

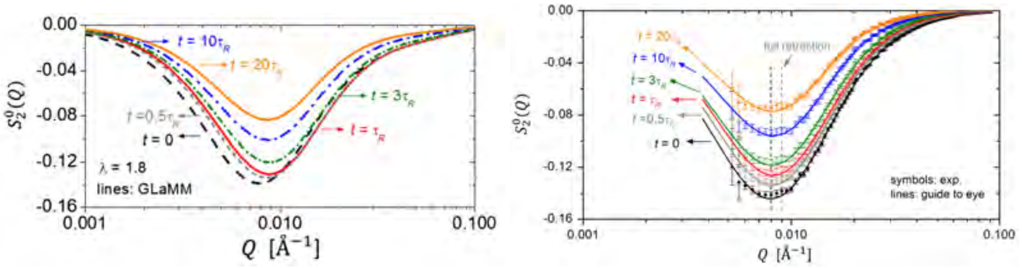

(a) **(b)**

Figure 4.19: Results of Wang et al.. The figure shows the results from Wang et al. using the spherical harmonics expansion. The plot in a) show the expansion coefficient $S_2^0(q)$ plotted for various lengths of relaxation times as calculated from the GLaMM-model, and the plot in b) show $S_2^0(q)$ for the same relaxation times as calculated from experimental data. The black dashed line show the q-value of the minimum for $t = 0\tau_R$ and the gray dashed line the GLaMM-prediction of the q-value of the minimum after full retraction. The figures are from [22].

4.5.2 Molecular Dynamics Simulations

The study of Wang et al. has been followed up by two molecular dynamics (MD) simulations papers. The first paper by Xu et al. [74] present a non-equilibrium molecular dynamics simulation that mimic the experimental conditions in Wang et al.[72] using a coarse-grained bead spring model for 250 chains with $Z \simeq 33$ using 2000 beads per molecule stretched to $\lambda = 1.8$ at constant $\dot{\lambda}$ with an initial Rouse Weissenberg number of $Wi_R(t = 0) = 41.8$. Their findings are in good agreement with the experimental results of Wang et al. namely that there is no horizontal shift in $S_2^0(q)$ and $R_g^\perp$ calculated in real space from the bead distribution increases monotonically to the equilibrium value.

Hsu and Kremer however also performed an MD-simulation covering a larger part of parameter space [71] where they vary both the number of entanglements $Z \approx 18, 36, 72$ and the stretch ratios varying between $\lambda = 1.0 - 5.0$. Regarding radius of gyration analysis, they find for $\lambda = 5.0$ and $Z \geq 36$, $R_g^\perp$ increases non-monotonically though the effect is not nearly as pronounced as predicted by the GLaMM-model. With respect to the spherical harmonics expansion of the structure factor, we show their findings in Fig. 4.20. From Fig. 4.20a we see that the anisotropy in the structure factor of the deformed polymers is more pronounced with increasing λ and shifts to smaller values of q. From Fig. 4.20b and c we see that the minimum of $S_2^0(q)$ shifts to larger values of q during relaxation but also that the GLaMM-model overestimates the effect relative to the simulated data and even more so for longer chains. Hsu and Kremer conclude that Wang et al. do not see chain retraction in their experiment either because the number of entanglements Z or the stretch ratio λ is not big enough.

4.5.3 Requirements for Observing Chain Retraction

Based on our results, the results by Wang et al. [22], and by Hsu and Kremer[71] we conclude that for observing chain retraction in the spherical harmonics expansion a sufficiently large λ is needed. In other experiments the spherical harmonics expansion was used to analyze scattering data for shorter polystyrene chains, $M_w = 197$ kg/mol in ref. [72] and $M_w = 101$ kg/mol in ref. [75] than in Wang et al. [22], stretched to $\lambda = 1.8$ also dip not show the signature of chain retraction.

To observe chain retraction in radius of gyration analysis seem to require $Z \gtrsim 58$[67] also consistent with the findings of Hsu and Kremer[71]

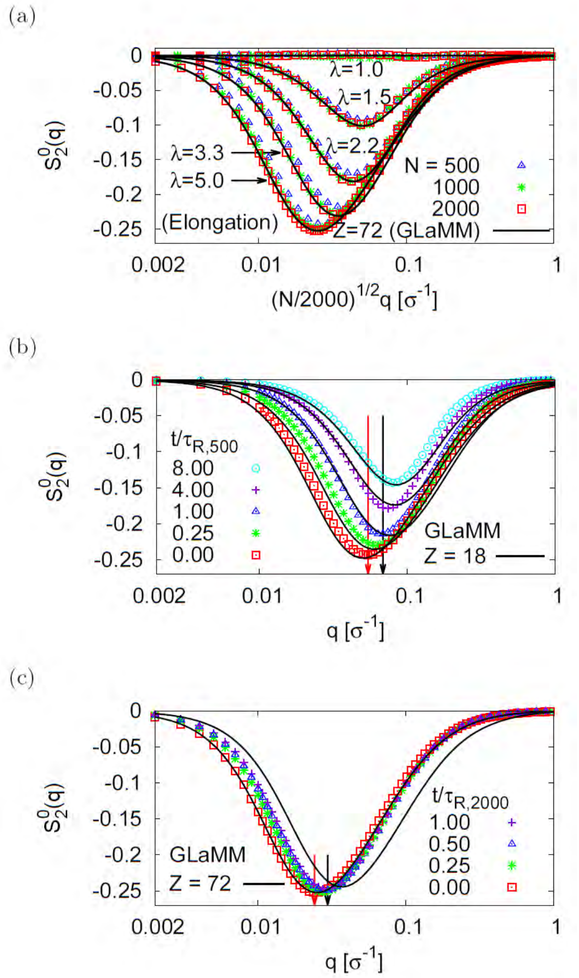

Figure 4.20: MD-results by Hsu and Kremer. In a) they show for varying numbers of monomers N, or number of entanglements Z, that the dip in $S_2^0(q)$ immediately after deformation increases in magnitude and shifts towards smaller values of q for increasing values of the stretch ratio λ. Subfigure b) and c) show that the GLaMM-model (lines) overestimates the dip shift relative to simulated data (varying markers) during relaxation. The figure is from Hsu and Kremer [71].

where the largest simulated molecule, $Z \approx 72$, at large strain show slight non-monotonic increase in $R_g^{\perp}(t)$.

It is remarkable that chain retraction is detectable even for as short molecules as we are working with $Z \approx 6$. However, this is only the case in the spherical harmonics expansion and not in radius of gyration analysis. This may be because the spherical harmonics expansion is sensitive to the full chain length and not only the change in radius of gyration. The end-to-end vector R of a linear polystyrene molecule of $M_w = 80$ kg/mol is $R = \sqrt{0.437 M_w[\mathrm{g/mol}]} \approx 190$ Å compared to the perpendicular radius of gyration immediately after deformation which we determined to $R_g \perp (t = 0) \approx 50$ Å. We know from Eq. 4.27 and 4.29 that the relative change in the two quantities is the same, but the absolute change in end-to-end vector length is clearly much larger, and that could be the reason why we see chain retraction in the spherical harmonics expansion and not in radius of gyration analysis.

4.5.4 Spherical Harmonics Expansion in General

From our results and the results of Wang et al.[22], Wang et al.[72], and Lam et al.[75] the spherical harmonics expansion framework seem to have a large potential for increasing our understanding of polymer melts under uniaxial deformation and the following relaxation since it appears to be more sensitive to changes in conformation than radius of gyration analysis. It will be most interesting to see what we will learn in the future by analyzing more data in this framework.

4.6 Conclusion

In this chapter we showed how to implement the framework of spherical expansion for analysis of 2D scattering patterns for polymer melts exposed to uniaxial extension. We applied the framework to the analysis of the relaxation of a relatively short polystyrene chain, with number of entanglements $Z \sim 6$, and saw that the spherical harmonics expansion framework is so sensitive to changes in molecular conformation that it can resolve chain retraction even for these relatively short chains. Based on other experiments and simulations we find that it is a requirement that the chains are stretched sufficiently in the initial deformation. From what we know from our and other experiments is that $\lambda = 1.8$ is insufficient and $\lambda \approx 4$ is sufficient.

Chapter 5

Conclusion and Outlook

The study of polymer materials under deformation is highly interesting both from an application point of view, since product properties depend on processing conditions, and from a fundamental scientific point of view because the interactions of polymer molecules under rapid deformation is not yet fully understood.

With the advance of the filament stretch rheometer, it is now possible to perform controlled, potentially large and fast, uniaxial extension and controlled relaxation following uniaxial extension of polymer melts. This provides completely new tests for polymer models and theories for their interactions.

Polymer rheology is intimately linked to molecular conformation and thus architecture and dispersity. Based on the rheological response of a polymer melt, hypotheses can be formed on the molecular conformation. The molecular conformation can be probed more directly using scattering techniques such small angle neutron scattering. The combination of extensional rheology and scattering techniques thus provide two independent measurements on molecular conformation

Here we presented work combining controlled extensional flow and the following controlled relaxation with small angle neutron scattering and wide angle X-ray scattering. We worked with three systems: mono-disperse linear polymers, a bi-disperse melt as a stepping stone towards polydisperse systems, and three-armed stars as a model system for branched polymers.

We studied the relaxation of a mono-disperse linear polystyrene using the recently published spherical harmonics expansion framework on small angle neutron scattering data. The Doi-Edwards tube model propose that due to the decoupling of the relaxation of stretching and orientation of the chain following deformation, the stretched chain will initialize retract to its equilibrium contour length causing it to shrink in all dimensions. This hypothesis was recently challenged due to the absence of the chain retraction signature predicted from the Doi-Edwards model in experimental data expanded in spherical harmonics. In our experiment however, the signature is clearly present. We believe the difference in conclusions is due to the fact that our stretching procedure stretches the molecules more.

The chains from the monodisperse sample described above was also mixed with longer chains to form a bidisperse melt. Previous small angle neutrons scattering studies showed that the short chains are stretched more and remain stretched longer in the blend on length scales of the full molecules, and that effect was attributed to nematic interactions, i.e. preferred orientational alignment of Kuhn segments. We set out to study the nematic interaction hypothesis in wide-angle X-ray scattering that probes distances on the order of the separation between neighboring Kuhn segments. The local orientation was more pronounced in the blend, but due to the lack of scattering contrast between long and short chains in wide angle X-ray scattering we could not infer nematic interactions in the system. An interesting observation is that the local orientation relaxation follows a power law with the same exponent for the pure melt and the blend indicating multiple relaxation processes on this length scale independent of chain length.

We also studied the relaxation of a three-armed end-deuterated star in small angle neutron scattering to the hypothesis that branched polymers behave like linear polymers in fast extensional flow because they adopt a quasi-linear conformation that remain well into the relaxation. The scattering patterns corresponding to very short relaxation time fully support the hypothesis, but deviations from the quasi-linear conformation appear at shorter relaxation times as seen by neutron scattering than as seen by rheology.

The presented projects opened new and exciting questions for future work such as: What mechanisms cause the relaxation of local orientation in pure melts and bidisperse melts to follow power laws with the same exponent? What is the range of validity for the structure factor of g-armed stars if we add more arms? What is the origin of the isotropic but swollen state, relative to equilibrium, of the three-armed stars at long relaxation times? If the spherical harmonics expansion is so sensitive to changes in the molecular conformation, what could we learn from applying it to data for other molecular architectures or dispersities? All molecules studied in this thesis have free ends, so another direction for future research could be to study the effect of free molecule ends e.g. by studying ring polymers that close on themselves and thus have no free ends.

Appendix A

Filament Scattering

Scattering techniques have proven most useful in testing hypotheses, potentially based on rheological data, regarding molecular conformation during extensional flow or the following relaxation. We routinely study molecules of M_n = 100 kg/mol or more corresponding to an equilibrium radius of gyration $R_g > 75$ Å. If we are to observe the Guinier region, we need reliable scattering intensities at small q meaning $q < 1/R_g = 0.015$ Å^{-1} in the case of $R_g = 75$. The data quality at small q in our experiments is currently limited by both the possible number of counts, which is controlled by the available amount of sample and to some extent the acquisition time of the experiment. However, the data quality at small q is also limited by excess scattering typically cross-shaped, which apparently comes from the sample itself. We hope to find the origin of this excess scattering in order to be able to eliminate it from future experiments or knowing its origin be able to include it in the data analysis in an educated way. This appendix presents our preliminary work on establishing the origin of the excess scattering.

A.1 Excess Scattering in Small-angle Neutron Scattering

The excess scattering was first observed in small-angle neutron scattering. It appeared in data sets for several samples measured both at SANS-1 at PSI and QUOKKA at ANSTO which made it clear that it was neither an issue with a single sample or instrumental background. Furthermore the excess scattering also appears in both blends of hydrogenous and deuterated polystyrene with a narrow molecular weight distribution and commercial polystyrene of hydrogenous polystyrene with a broad molecular weight

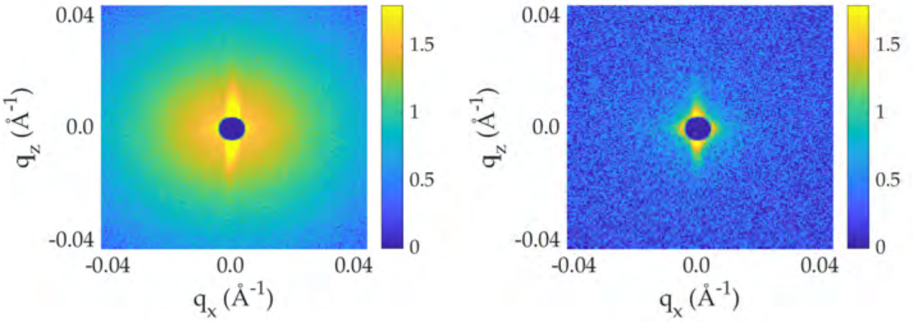

(a) SANS, deuterated **(b)** SANS, hydrogenated

Figure A.1: Examples of excess filament scattering as seen in neutron scattering. In a) the scattering pattern for a monodisperse melt of M_n = 95 k with 10 wt-% deuterated molecules, relaxed for 80 s or $t \approx 5.3\tau_R$ in b) the scattering pattern for commercial polystyrene, fully relaxed.

distribution, see Fig. A.1. The scattering contrast responsible for the scattering is thus not due to the scattering length density difference between hydrogenous and deuterated polystyrene, and so we propose that it originates from scattering contrast between polymer and air. This may be due to trapped air in the sample or surface cracks.

A.2 Surface Crack Hypothesis

Discussions with Professor Hiroshi Watanabe lead us to form the hypothesis that the scattering contrast was due to surface cracks appearing during the filament quench procedure where the oven is rapidly opened and the filaments cooled by a flow of nitrogen at room temperature. Rapid quenching could cause surface cracks because the density of polystyrene increases with decreasing temperature and during the rapid quenching the surface cools down faster than the center of the filament. If the density of the outer layer increases sufficiently, it may form cracks.

To test this hypothesis we compared two filaments of the same material and stretched in the same way. One filament was quenched following the above described procedure while the other filament was allowed to cool to room temperature before the oven was opened, which is a gentle cooling procedure. The filaments were prepared from commercial polystyrene that was dried in a vacuum oven and stretched very slowly as described as prestretching in Sec. 1.2.1. If the scattering contrast is in fact due to air in the samples, there will also be scattering contrast in Small-angle X-ray

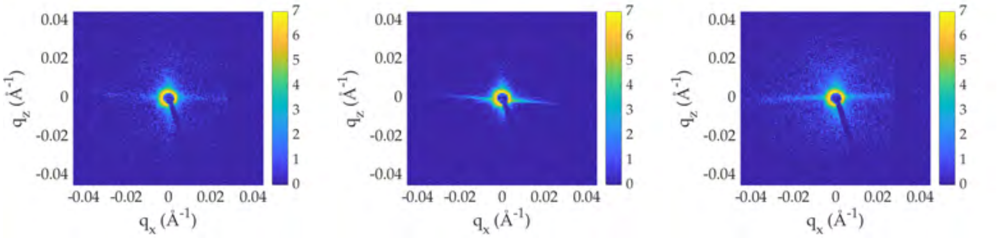

(a) SAXS, fast **(b)** SAXS, slow **(c)** SAXS, slow, wet

Figure A.2: Comparison of quench procedures. In a) we show the pattern from the sample rapidly quench, in b) the scattering pattern from the slowly cooled sample, in c) we see the pattern from a filament produced in the same way as that in b) only it was not dried as much in the vacuum oven. All three are qualitatively similar.

scattering (SAXS). We therefore performed the following measurements were performed using the home source X-ray setup at the Niels Bohr Institute. The scattering pattern for these samples are shown in Fig. A.2 a) and b). The pattern in Fig. A.2c was unintentionally produced by too short drying in the vacuum oven before stretching. All three scattering patterns qualitatively show the same excess scattering pattern, and we conclude that the rapid quenching is not the cause of the excess scattering. The less dried sample seem to scatter more overall, which we will come back to later.

A.3 Time Dependence of Excess Scattering

If we compare the scattering patterns presented in Chap. 3 and 4, i.e. Fig. 3.10 and 4.4, it looks like the vertical feature in the excess scattering appears with increasing relaxation time or, as in Fig. A.2, for samples stretched slowly. To test this hypothesis, we measure a single filament from each of the Short in Short-sample in the mid-filament plane with SAXS. The results are shown in Fig. A.3. There seems to be a weak time dependence. A time dependence in the vertical part of the excess scattering would be expected if it has its origin in air bubbles in the filament elongated by the extensional flow. For short relaxation times the bubbles may be so elongated that their scattering was hidden by the beam stop and for longer relaxation times they would relax back towards spherical bubbles, which would cause the excess scattering to appear at larger values of q and become detectable.

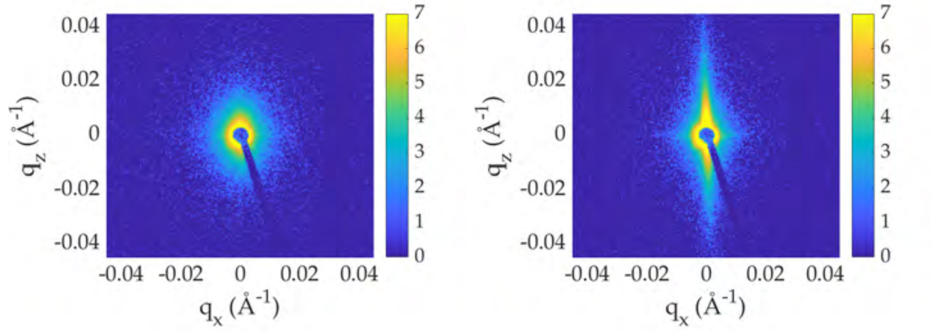

(a) 0 s **(b)** 10 s

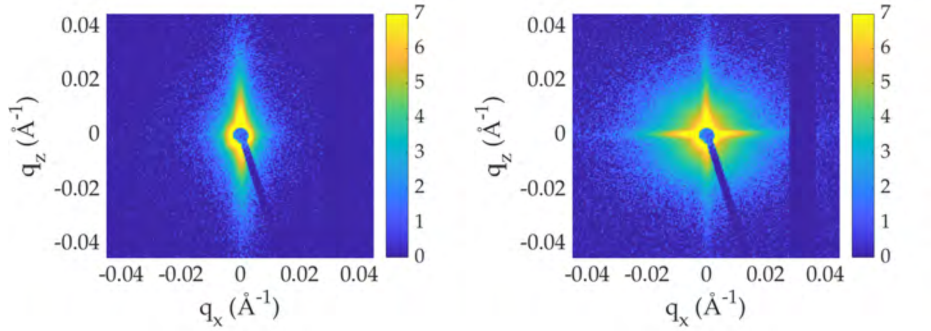

(c) 20 s **(d)** 80 s

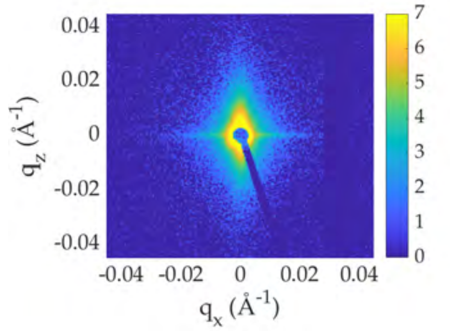

(e) 320 s

Figure A.3: Excess scattering and relaxation time. Scattering from the midplane of filaments corresponding to a relaxation series of a monodisperse 95 kg/mol melt.

A.4 Reproducibility of Filament Scattering

To test whether the excess scattering is a global or a local phenomenon we measured the remaining three 80 s-filaments in the mid-filament plane and scanned the first filament measuring SAXS patterns at different positions along the filament axis separated by 0.5 mm. The results are shown in Fig. A.4 and A.5. The scattering contrast leading to the excess scattering varies along a single filament and between filaments produced in the same way.

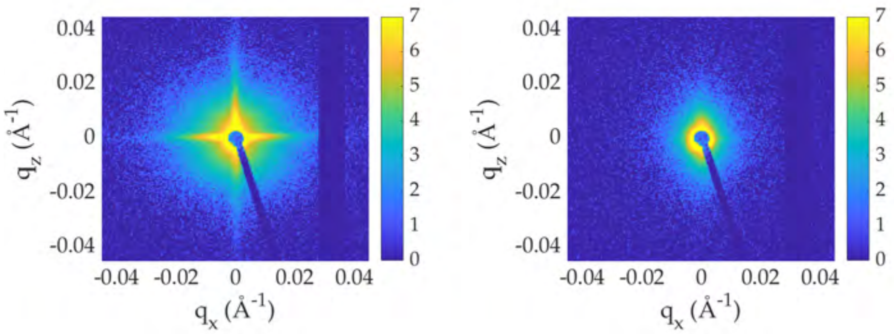

(a) t=80 s, sam. 1

(b) t=80 s, sam. 2

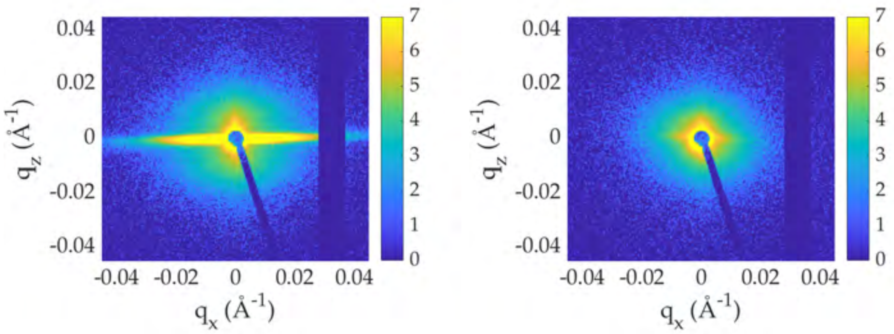

(c) t=80 s, sam. 3

(d) t=80 s, sam. 4

Figure A.4: Scattering from the mid-filament plane after 80 s of relaxation for four different filaments.

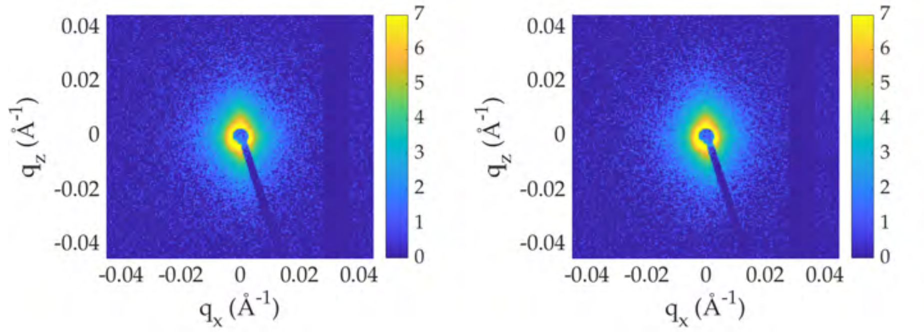

(a) t=80 s, sam. 1, pos1

(b) t=80 s, sam. 1, pos2

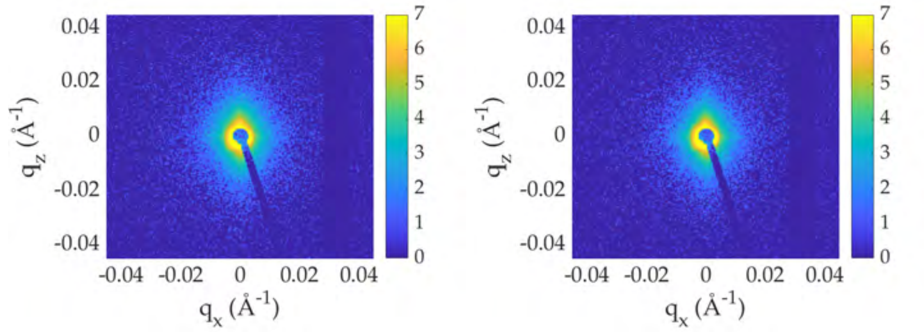

(c) t=80 s, sam. 1, pos3

(d) t=80 s, sam. 1, pos4

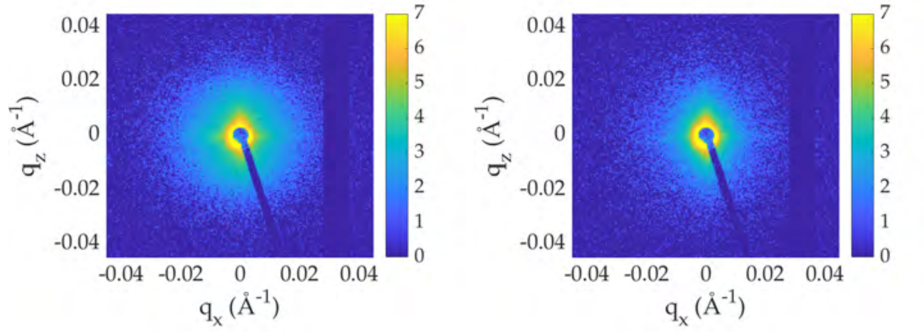

(e) t=80 s, sam. 1, pos5

(f) t=80 s, sam. 1, pos6

Figure A.5: Scan of 80 s filament 1. The positions are separated by 0.5 mm along the filament axis.

A.5 Craze Hypothesis

Potentially crazes, thin patches where the filament is kept together by thin threads of polymers, see e.g. [76] for images, or some precursor to crazes. We therefore also scanned a visually crazed polystyrene sample and the results are shown in Fig. A.6 and A.7. There clearly is a large variation along the crazed filament and we believe the prominent scattering patterns appear when we measure the scattering from a craze. However it looks qualitatively different with broad feature and it is therefore not convincing that crazes are the origin of the excess scattering.

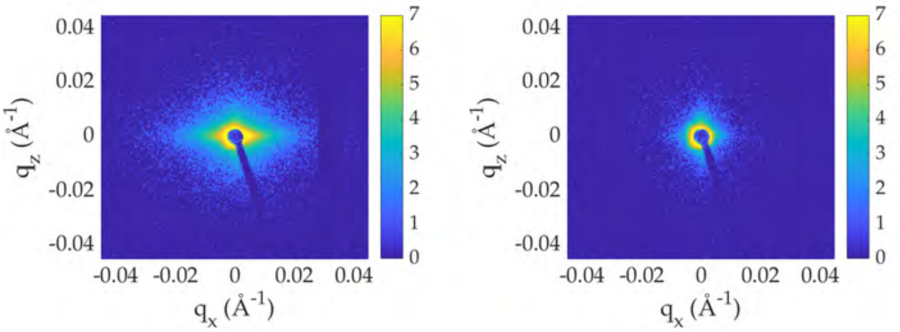

(a) position 19.3 **(b)** position 19.2 mm

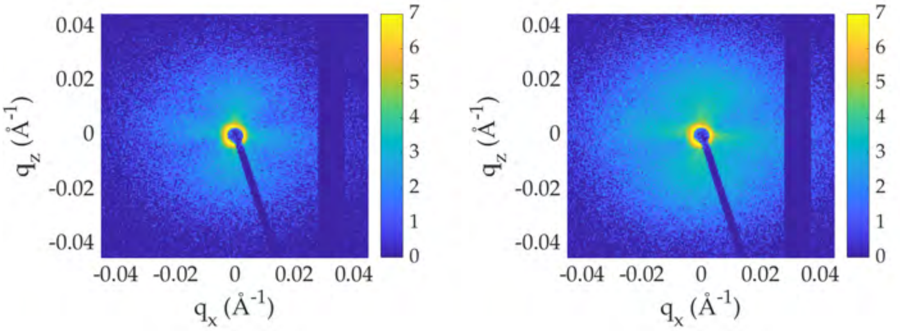

(c) position 19.1 mm **(d)** position 19.0 mm

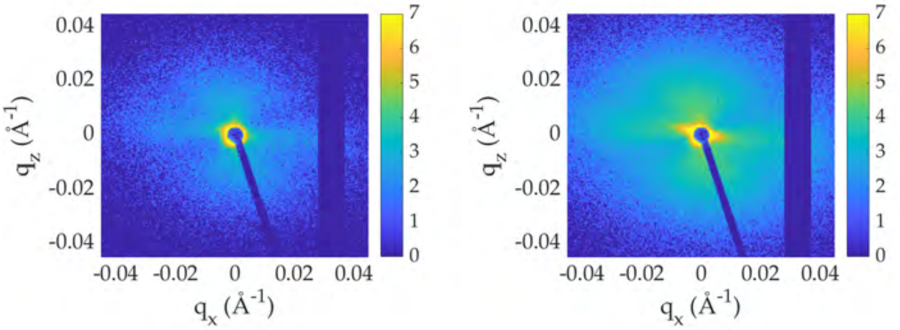

(e) position 18.9 mm **(f)** position 18.8 mm

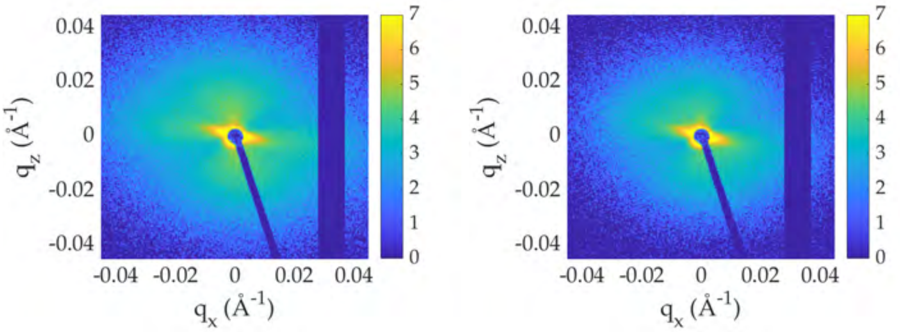

(g) position 18.7 mm **(h)** position 18.6 mm

Figure A.6: Scattering patterns for the crazed sample scan along filament axis 1/2

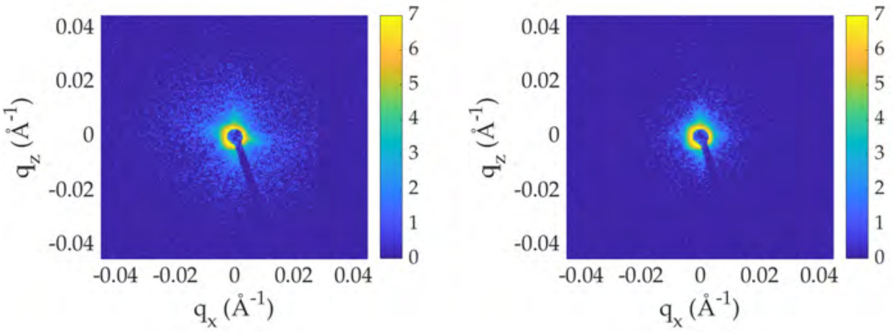

(a) position 18.5 mm **(b)** position 18.4 mm

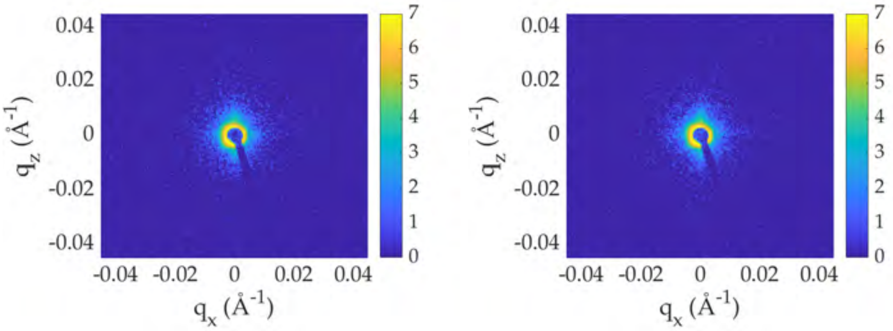

(c) position 18.3 mm **(d)** position 18.2 mm

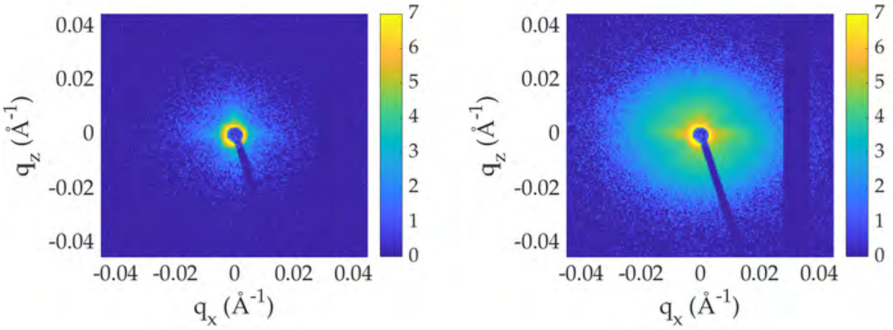

(e) position 18.1 mm **(f)** position 18.0 mm

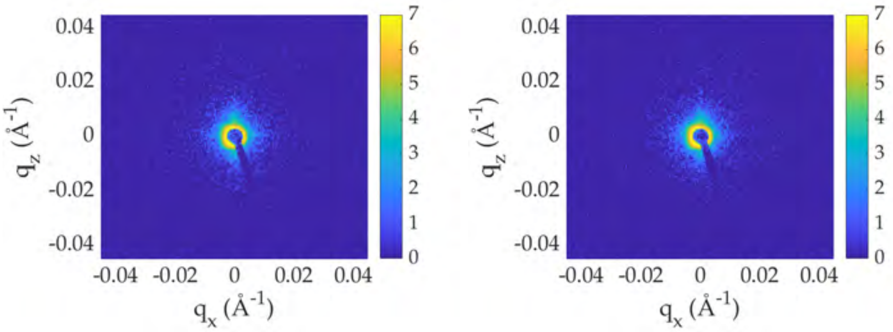

(g) position 17.8 mm **(h)** position 17.6 mm

Figure A.7: Scattering patterns for the crazed sample scan along filament axis 2/2

A.6 Residual Solvent

Though we still do not have a well supported hypothesis of the origin of the excess scattering we went back to the initial surface crack experiment where we saw that the less dried sample scattered more. No matter the origin of the scattering, could we avoid it by further minimizing the amount of residual solvent in the melt? For this purpose commercial polystyrene was treated with CO_2 to further extract solvent and a filament was prepared and scanned. The results are shown in Fig. A.8. The scattering patterns seem to have significantly less excess scattering that is more uniform along the filament than those from the scan of the 80 s filament in Fig. A.5 but there are still signs horizontal and vertical scattering, but this may very well be residual slit scattering from the instrument.

A.7 Discussion and Conclusion

At least part of this horizontal and vertical scattering is due to background from the collimation slits. Unfortunately, it is not straight forward to subtract a reliable instrumental background since the cylindrical geometry makes the effective transmission factor non-trivial to measure, and so we may compare scattering patterns within the same figure since they were measured at the same time and thus will have the same instrumental background and comparable sample geometries, but new measurements are needed to be able to compare e.g. the 80 s filament and the CO_2 extracted filament. We thus still believe that the amount of excess scattering depend on residual solvent in the filaments though further studies are needed for a final conclusion.

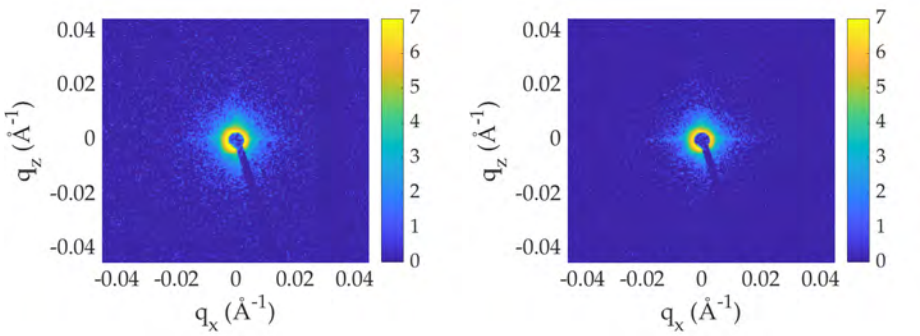

(a) position -0.5 mm **(b)** position 0 mm

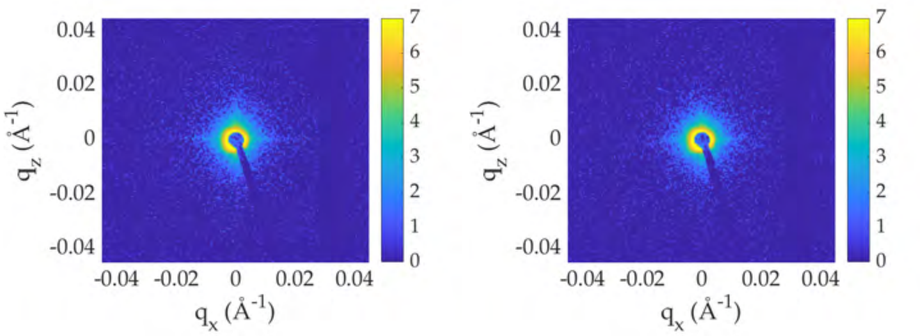

(c) position +0.5 mm **(d)** position +1.0 mm

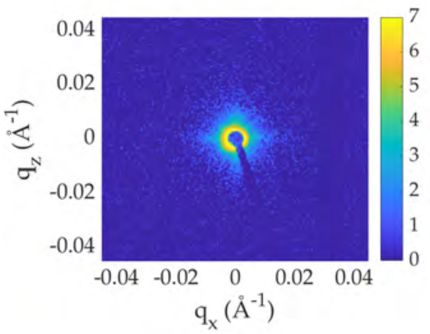

(e) position +1.5 mm

Figure A.8: Extracted sample scan along filament axis in steps of 0.5 mm.

Appendix B

Publication List

This appendix contains a description of the manuscripts that I have co-authored during my PhD-studies and list future publications based on the work presented in the thesis. Furthermore it contains reprints of the already published manuscript ″Structural Studies of Three-Arm Star Block Copolymers Exposed to Extreme Stretch Suggests a Persistent Polymer Tube″ and the soon to be submitted manuscript ″Chain Retraction during Polymer Relaxation Confirmed using Spherical Harmonics Expansion of Small Angle Neutron Scattering Data″.

Published Manuscripts Included in the Thesis

1: Structural Studies of Three-Arm Star Block Copolymers Exposed to Extreme Stretch Suggests a Persistent Polymer Tube. *Physical Review Letters*, vol. 120, p. 207801-(1-6), 2018. K. Mortensen, A. L. Borger, J.J.K. Kirkensgaard, C. J. Garvey, K. Almdal, A. Dorokhin, Q. Huang, and O. Hassager.

Manuscripts Soon to be Submitted

2: Chain Retraction during Polymer Relaxation Confirmed using Spherical Harmonics Expansion of Small Angle Neutron Scattering Data, in prep. for *Physical Review Letters*, A. L. Borger, J.J.K. Kirkensgaard, Q. Huang, O. Hassager, K. Almdal, and K. Mortensen.

Published Manuscripts not Included in the Thesis

I contributed with Wide-Angle X-ray scattering measurements and/or their interpretation to the following two manuscripts, which I also read carefully and revised critically.

3: Flow Induced Crystallization Prevents Melt Fracture of HDPE in Uniaxial Extensional Flow. *Journal of Rheology*, vol. 62, p. 1051, May 2018, S. L. Wingstrand, O. Hassager, D. Parisi, A. L. Borger, and K. Mortensen.

4: Highly Anisotropic Glassy Polystyrene Are Flexible *ACS Macro Letters*, vol 7, p. 1126-1130, 2018, Q. Huang, J. Madsen, L. Yu, A. L. Borger, S. R. Johannsen, K. Mortensen, and O. Hassager.

Future publications

5: Random Phase Approximation Structure Factor of Symmetric g-armed Block Copolymer Stars

6: Star Polymer Relaxation Following Fast Extensional Flow with Small-Angle Neutron Scattering

7: Local Orientation in Bi-disperse Polystyrene with Wide-Angle X-ray Scattering

8: Small q Scattering from FSR-filaments

B.1 Structural Studies of Three-Arm Star Block Copolymers Exposed to Extreme Stretch Suggests a Persistent Polymer Tube

The article presents our findings on the structure of an end-deuterated three-armed block copolymer star immediately after fast extensional flow and in equilibrium.

Abstract

We present structural small-angle neutron scattering studies of a three-armed polystyrene star polymer with short deuterated segments at the end of each arm. We show that the structure factor of the three-armed star molecules in the relaxed state agrees with that of the random phase approximation of Gaussian chains. Upon exposure to large extensional flow conditions, the star polymers change conformation resulting in a highly stretched structure that mimics a fully extended three-armed tube model. All three arms are parallel to the flow, one arm being either in positive or negative stretching direction, while the two other arms are oriented parallel, right next to each other in the direction opposite to the first arm.

My contribution

I calculated the random phase approximation structure factor and critically revised the manuscript.

PHYSICAL REVIEW LETTERS **120,** 207801 (2018)

Structural Studies of Three-Arm Star Block Copolymers Exposed to Extreme Stretch Suggests a Persistent Polymer Tube

Kell Mortensen,* Anine L. Borger, and Jacob J. K. Kirkensgaard
Niels Bohr Institute, University of Copenhagen, Copenhagen, Denmark

Christopher J. Garvey
Australian Nuclear Science and Technology Organisation, Lucas Heights, New South Wales 2234, Australia

Kristoffer Almdal and Andriy Dorokhin
Department of Micro- and Nanotechnology, Technical University of Denmark, 2800 Kongens Lyngby, Denmark

Qian Huang and Ole Hassager
Department of Chemical and Biochemical Engineering, Technical University of Denmark, 2800 Kongens Lyngby, Denmark

(Received 5 January 2018; revised manuscript received 16 March 2018; published 16 May 2018)

We present structural small-angle neutron scattering studies of a three-armed polystyrene star polymer with short deuterated segments at the end of each arm. We show that the form factor of the three-armed star molecules in the relaxed state agrees with that of the random phase approximation of Gaussian chains. Upon exposure to large extensional flow conditions, the star polymers change conformation resulting in a highly stretched structure that mimics a fully extended three-armed tube model. All three arms are parallel to the flow, one arm being either in positive or negative stretching direction, while the two other arms are oriented parallel, right next to each other in the direction opposite to the first arm.

DOI: 10.1103/PhysRevLett.120.207801

The flow and deformation of macromolecules are ubiquitous in nature as well as industry. A microscopic understanding of such macromolecular flow behavior has accordingly significant interest. Important parameters for the flow behavior include both the molecular chemistry and the molecular architecture, but also the exact flow condition. The tube model of polymers proposed and described by de Gennes [1] and Doi and Edwards [2] has proven to make a very good theoretical basis for the observed flow characteristics of linear chains [3,4], even though some modifications have been proposed to account for details in the experimental findings [4–8]. Large strain amplitudes can be expected to show further complications beyond the properties of the linear regime described in the tube model [9,10].

It has been questioned whether the tube model can describe branched and other types of complex polymer systems [11]. Star polymers, for example, have been the subject of several studies in both melts and solutions [11–20]. Dondos *et al.* discussed the elongation of star-shaped polystyrenes in flowing solutions, showing how the molecular deformation depends on their number of branches [13]. Ripoll *et al.* made mesoscale simulations showing that star polymers in shear flow change from linear-polymer-like to capsule-like behavior with increasing functionality [17]. Xu and Chen made a coarse grained molecular dynamic simulation, showing that star polymers align and deform for shear rates beyond a critical value [19]. Huang *et al.* measured the nonlinear rheology of three-arm star polymer melts in fast extensional flows [20], showing that the extensional viscosity of star polymers was identical to that of linear polymer in agreement with theoretical predictions [21]. While the agreement between the extensional viscosity and the model prediction is significant, it provides at best an indirect confirmation that branched polymers in strong extensional flows become quasilinear by aligning the arms.

In this Letter, we present experimental studies of the simplest complex polymer system that provides direct evidence from which the arm configuration in strong extensional flow may be tested. By using a deuterium labeled three-arm star, we show that the configuration corresponds very well to that of a fully extended three-armed tube. This does not necessarily imply that all dynamics of a star polymer can be associated to a tube model, and one may claim that the basis of the tube model, the entanglements, disappear when a tube becomes fully extended. However, it is striking how well the characteristics of a three-armed tube can explain our rather distinct experimental observations.

The Letter is restricted to the structure as measured in the relaxed state, and immediately after stopping the flow. The aim of the synthesis was for three-armed polystyrene star polymers labeled by hydrogen-deuterium exchange at the very end of each polymer arm, as sketched in Fig. 1, to

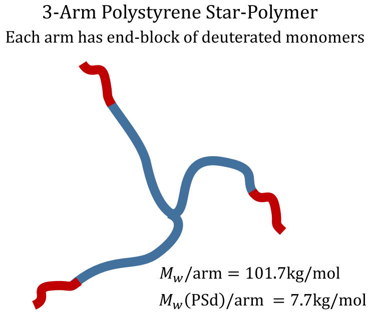

FIG. 1. Schematic illustration of the star copolymer where each arm is a polystyrene block copolymer of total 101.7 kg/Mol molar mass, made up of a 94 kg/Mol normal PS block near the star center, and 7.7 kg/Mol deuterated end blocks (PSd).

obtain contrast for neutron scattering experiments. The deuterated blocks are chosen to be relatively small to get more precise and easily accessible information on the star polymer deformation, even though the small size causes rather weak scattering and thereby somewhat noisy data. The resulting molar masses of the polystyrene samples were determined using size exclusion chromatography with nonstabilized tetrahydrofuran (THF) as the eluent and applying a column set consisting of a 5 μm guard column and two 300×8 mm^2 columns. The system was equipped with a triple detector system consisting of a combined Viscotek model 200 differential refractive index (DRI), a differential viscosity detector, and a Viscotek (LD 600) right angle laser light scattering detector (RALLS). The overall molar mass is calculated based on both the RALLS and DRI signal, whereas the polydispersity is based on calibration with polystyrene standards. The synthesis of three-arm polystyrene-*b*-polystyrene-d8 star block polymers was carried out in freshly distilled THF in three stages [22]. Synthesizing short narrow molar mass distribution polymer blocks is difficult in polar solvents due to high polymerization rates compared to the mixing rate and results in high polydispersity. The problem was minimized by performing the reactions of the labeled linear polystyrene-d8 polymer at −108 °C, close to the freezing point of the solvent. The resulting polymers have a molar mass of $M_w = 7.7$ kg/ mol with a polydispersity of 1.14. During the second stage the nondeuterated monomers were added while the reaction mixture was heated up to −78°C. The polydispersity of the full block copolymer arm is 1.40 due to incomplete homogeneity in the synthesis in this step. The resulting linear PS-PSd block copolymer has total molar mass M_w of 101.7 kg/mol corresponding to a mass fraction of deuterated polystyrene f equal to 0.075. The final star formation stage was made at −78 °C with methyltrichlorosilane as the coupling agent. The resulting polystyrene star polymer solution was fractionated and dried in vacuum at 50 °C for 24 h, resulting in an amorphous sample of three-arm block copolymer stars with molar mass equal to 309.1 kg/mol and polydispersity equal to 1.30. The relative large polydispersity may reflect a small amount long linear block copolymers, which may be the consequence of nonoptimal temperature during the polymer synthesis. The quality of the polymer was investigated further using rheology comparing the polymer of the present Letter with that of a well-defined low-PDI three-arm fully protonated PS star (PDI < 1.1) [20]. Rheology measurements show that the relaxation of the partly deuterated material is only slightly slower at low frequency, indicating some side product of a high-molar mass linear PS.

For polystyrene, the polymer end-to-end statistical length is $\sqrt{\langle R_\circ^2 \rangle}[\text{Å}] = \sqrt{0.437 M_w[\text{g/mol}]}$, the Kuhn segment length is $b = 18$ Å, the entanglement molar mass is $M_e = 16.6$ kg/mol and the tube diameter is $a = 85$ Å [23]. With the molar mass ($M = 101.7$ kg/mol) for each arm, the number of entanglements is $Z = 101.7/16.6 \approx 6$, and the equilibrium end-to-end length is $R_\circ(1\,\text{arm}) = \sqrt{0.437 \times 101.700}$ Å ≈ 210 Å. The number of segments in each arm is $N_{\text{arm}} = (R_\circ/b)^2 = (210/18)^2 = 135$, and thus the total number of segments in the star polymer, $N = 3N_{\text{arm}} = 405$.

The samples were stretched with the VADER 1000, Rheo Filament ApS. As shown by Hengeller *et al.* extensional steady state flow conditions are established beyond a Hencky strain of $\epsilon = 3$, which is the Hencky strain applied in the present study [24]. The applied strain rate for the stretched sample was $\dot{\epsilon} = 0.06$ s^{-1}, performed at $T = 125$ °C. The equilibrium Rouse time of a linear chain of the same span M_W is 450 s at 125 °C [20]. The nondimensional stretch rate based on this time constant is significantly greater than unity so we expect that the molecules are highly oriented and nonlinearly stretched. The samples were quenched with a cooling rate of about 10 K/s as described in Kirkensgaard *et al.* [10]. Since the glass transition temperature is 105 °C, the melt solidifies in a time much shorter than the Rouse time. Therefore, the molecular configurations in the solid samples are assumed to be identical to those in the melt at the time of quench. The large deformation does, according to previous related studies, not cause degradation of the complex polymer molecules [20].

The structural studies were performed using small-angle neutron scattering (SANS). SANS data were obtained using the SANS-1 instrument at PSI, Switzerland and Quokka at ANSTO, Australia. Results obtained by the two instruments agree perfectly. The results shown below are all obtained using the Quokka instrument, where two instrumental settings were applied, both with 5 Å neutrons with 10% wavelength resolution and the collimation defined by a source diameter of 50 mm and a pinhole in front of the sample with a diameter of 10 mm. One instrumental setting had 10 m collimation length and 5 m sample-to-detector

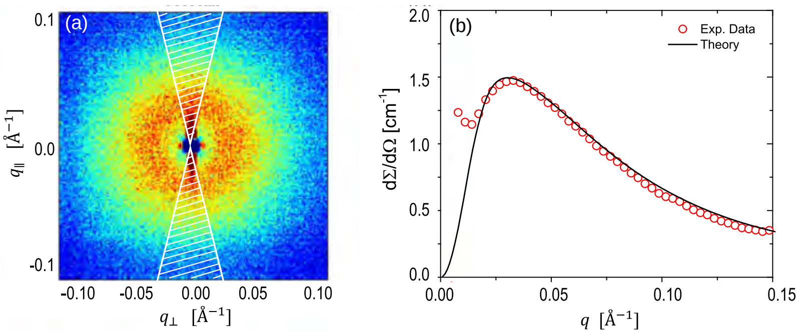

FIG. 2. Small-angle neutron scattering study of the relaxed star-polymer system. (a) The 2D scattering pattern as obtained in the SANS instrument. (b) The azimuthally averaged intensity versus scattering vector, as obtained from the nonstriped area in (a).

distance, giving a q range equal to $0.01 - 0.15$ Å^{-1}, while the second setting used collimation length and sample-to-detector distance both equal to 14 m, giving a q range of $0.004 - 0.06$ Å^{-1}.

Figure 2 shows the 2D scattering function of the fully relaxed star polymer. The rather poor statistics is due to a limited amount of material and only rather small scattering units in the labeled polymer. Unfortunately, this sample is affected by artificial small-angle scattering, which arises from the sample itself, but is likely related to cracks that we only realized after finishing the SANS measurements. The other measured samples do not have similar problems. Fortunately, the significant small-angle scattering does not disturb the main scattering characteristics of the correlation peak. The cylindrical shape of the sample gives further rise to some small angle scattering horizontally near the beamstop.

Figure 2(b) shows the azimuthally averaged structure factor $I(q)$, where $q = 4\pi/\lambda \sin(\theta)$ is the scattering vector, λ being the neutron wavelength and θ half the scattering angle. The averaged data exclude the striped area in Fig. 2(a) to limit the effect of artificial background. The incoherent scattering corresponding to pure polystyrene was subsequently subtracted [25], to show the pure star-block copolymer form factor. The SANS scattering pattern of the relaxed sample is characterized by a broad peak centered at $q^* = 0.03$ Å^{-1}, corresponding to a characteristic length scale of $d = 2\pi/q^*$ equal to 210 Å.

If we assume an ideal random position of the star molecules, there will be no intermolecular correlations. The scattering pattern will accordingly be dominated by the form factor of a single star molecule, which can be calculated based on a random phase approach equivalent to the calculation of a diblock copolymer melt developed by Leibler [26]. Using such a RPA method, strictly following the calculations of M. Doi [27], the form factor can be expressed as

$$I(q) = \frac{N}{S/W - 2\chi N} \tag{1}$$

with N being the total degree of polymerization, χ being the Flory-Huggins interaction parameter, and S and W are given by

$$S = S_{AA} + S_{BB} + 2S_{AB}$$

and

$$W = S_{AA}S_{BB} - S_{AB}^2$$

respectively, where the partial structure factors for a three-arm star polymer are given by [28–31]

$$\begin{aligned} S_{AA} &= -3h[(1-f)/3] + 3h[2(1-f)/3] \\ S_{BB} &= 3\{h(f/3) + h(2/3) + h[2(1-f)/3] \\ &\quad - 2h[(2-f)/3]\} \\ S_{AB} &= 3/2h[(1-f)/3] - 3/2h(1/3) - 3/2h(f/3) \\ &\quad + 3\{h[(2-f)/3] - h[2(1-f)/3]\}, \end{aligned} \tag{2}$$

where $h(x)$ is the generalized q-dependent Debye function introduced by Leibler:

$$h(x) = 2/(qR_{g,N})^4\{x(qR_{g,N})^2 + \exp(-x(qR_{g,N})^2) - 1\} \tag{3}$$

where $R_{g,N}$ is the radius of gyration of a linear polymer with similar degree of polymerization (N). Heinrich *et al.* made a corresponding analysis on end-labeled H-shaped molecules, studying the conformational changes upon more gentle stretching [32].

While small-angle neutron scattering is typically done on an absolute scale, this is not trivial for the cylindrical samples, where transmission and thickness vary over the beam. In attempt, anyway, to give our data on an absolute scale, we presuppose that the asymptotic high-q scattering is dominated by incoherent scattering from pure polystyrene [25]. The data shown in Fig. 2 have thus been

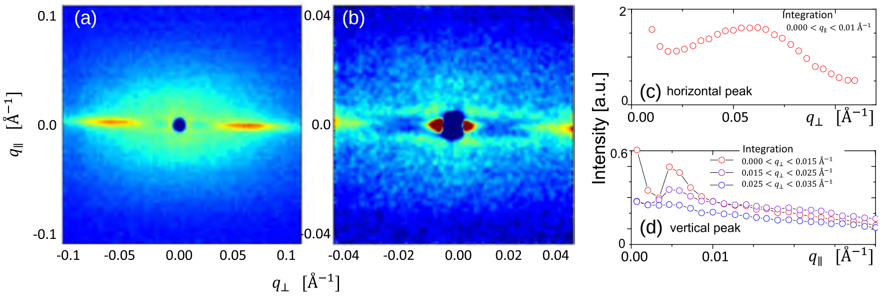

FIG. 3. Experimental small-angle neutron scattering results of a star-polymer system exposed to elongational stretching (vertically) using two instrumental settings at the Quokka instrument: neutron wavelength $\lambda = 5$ Å and sample to detector distance equal 5 m (a) and 14 m (b), respectively. (c) The horizontal peak intensity versus $q_\perp$ as averaged over a $q_\parallel$ slab. (d) The intensity of the vertical peak versus $q_\parallel$ as averaged over different $q_\perp$ slabs.

normalized using the incoherent scattering from polystyrene. The incoherent scattering was subsequently subtracted, to show the pure star-block copolymer form factor.

The solid line in Fig. 2 shows the RPA form factor calculated according to Eqs. (1) and (2) using the known molecular parameters given above, i.e., $N = 405$, $f = 0.075$. The Flory-Huggins interaction parameter $\chi(\mathrm{PS} - \mathrm{PSd}) = 0.004$ [33]; however, the scattering function is rather insensitive to changes in χ, reflecting that the system is far from any microphase separation. The theoretical scattering function is arbitrarily multiplied by 1.05, to fit the experimental data, which absolute intensity is anyway somewhat uncertain, according to the discussion above. The experiment and the theory agree very well, but the peak position is slightly shifted relative to the theoretical expectation, which can be explained by an effective segment-number N somewhat smaller than expected, or it may reflect a small fraction of two-arm stars.

The experimental 2D-SANS data, as obtained immediately after elongational flow, is shown in Fig. 3. The data show a very characteristic pattern dominated by two sets of correlation peaks: one pair at the horizontal axis around $q_\perp = \pm 0.06$ Å^{-1} [Figs. 3(a) and 3(c)] and another pair centered at the vertical axis around $q_\parallel = \pm 0.005$ Å^{-1} [Figs. 3(b) and 3(d)]. Both sets of correlation peaks have very large horizontal dispersions, i.e., perpendicular to the flow direction, while being highly confined vertically parallel to the flow. The characteristics are further clear from Figs. 3(c) and 3(d), showing intensity averaged over slabs parallel to, respectively, $q_\perp$ and $q_\parallel$, as expressed in the figures. The SANS pattern has additional horizontal scattering near the beamstop, which is attributed reflection from the thin, cylinder shaped samples. This scattering is not discussed further. The pattern is further characterized by an underlying close-to ellipsoidal contour pattern, which may reflect the form factor of the deformed deuterated chains.

To make the discussion more clear, we have combined the two data sets into one, and given a schematic illustration of the findings, as shown in Figs. 4(a) and 4(b), respectively. It is interesting to note that the two types of peaks do not merge; i.e., they are not part of a common ellipsoidal (or other simple) correlation ring as might have been expected to emerge from "deformation" of the relaxed pattern shown in Fig. 2. The peaks, on the contrary, make up four *stripes* running parallel in the two-dimensional detector plane, as also clear from Fig. 3(d) showing constant peak value $q_\parallel^* = \pm 0.005$ Å^{-1}. This strongly indicates that the two types of structures reflect properties of uncorrelated origin.

To discuss the origin of the scattering pattern, we note that the molecules must be highly stretched, implying that the RPA model should not be used. On the contrary, we propose a most simple model with geometrically simple, stretched objects where the scattering peaks as a consequence of the Fourier transformation simply reflect distances between the labeled blocks.

The two peaks centered on the vertical $q_\parallel$ axis at $q_\parallel^* = \pm 0.005$ Å^{-1} have character of horizontal streaks extending to rather large $q_\perp$ values (beyond the $q_\perp^*$ of the "horizontal" peaks discussed below). Such characteristics may have a very simple origin. The Fourier transform, and thereby the

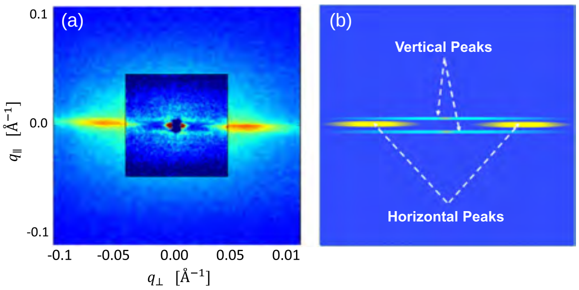

FIG. 4. Small-angle neutron scattering study of star-polymer system exposed to elongational stretching. (a) The 2D experimental scattering pattern as obtained in the SANS instrument. (b) A schematic illustration of the findings to clarify the discussion in the text.

scattering pattern, of a simple one-dimensional model with two elongated scattering domains aligned in the flow direction will have exactly such characteristics with the peak-width being relatively confined in the vertical direction parallel to flow, but broad perpendicular to the flow determined by the width of the deuterated block. The pattern thus reflects the correlation between two 7.5 kg/mol deuterated blocks parallel to the flow, one block in positive and one in negative stretching direction, where the center value $q_\parallel^* = 0.005$ Å^{-1} corresponds to a distance of roughly 1300 Å.

The two peaks centered on the horizontal $q_\perp$ axis are also very broad parallel to $q_\perp$ while being very confined in the $q_\parallel$ direction parallel to the flow. The center values $q_\perp^* = \pm 0.06$ Å^{-1} correspond to a distance of the order of 100 Å. The origin of these peaks must be correlations between two deuterated blocks that have oriented into the same direction relative to flow. The significant confinement in the vertical direction implies that the two scattering domains are positioned in the same plane perpendicular to flow, implying that in a given star molecule, both chains are stretched by the same factor. The large horizontal width of the reflections may have two origins: it may reflect diversity in distance between the domains and it may reflect the form factor of the stretched deuterated blocks. Some variation in the distance is reasonable, and the stretched chain may very well be relatively thin, as also argued for the horizontal width of the other pair of peaks.

To understand these findings on the molecular level, it is relevant to look into the characteristic polystyrene dimensions given above. The horizontal peaks are attributed to correlation between the deuterated domains of two arms that are stretched into the same direction relative to the flow (Fig. 5). The distance of roughly 100 Å resulting from the horizontal peaks is, with the given statistics, very close to the tube diameter $a = 85$ Å and thereby the tube center-to-center distance. While this may be fortuitous we suggest that the two arms do not constitute a common tube, but make up individual tubes separated with roughly two times their radius, thus giving rise to the pronounced correlation peak.

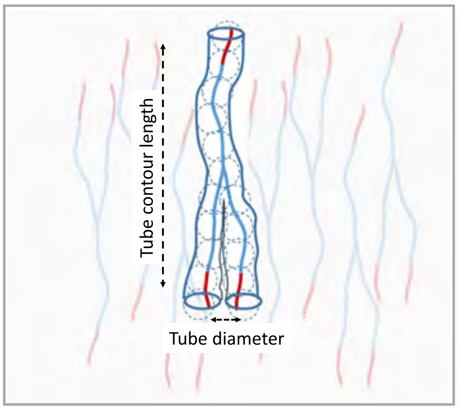

FIG. 5. Schematic figure of the stretched star block copolymer, illustrating the fully extended three-armed tube with two of the tube arms positioned right next to each other.

With the molar mass ($M_w = 101.7$ kg/mol), the one-arm chain contour length is $R_{\max}(1\,\mathrm{arm}) = R_\circ^2/b = 2480$ Å, while the tube contour length is $L_e = Za = 520$ Å. A fully stretched star polymer would have a total extension corresponding to two fully extended chains, i.e., $R_{\max}(\mathrm{star}) = 2 \times 2480$ Å $= 4960$ Å. The total length of a fully extended tube of the star polymer is correspondingly given by the sum of the tube length of two arms, $2L_e = 2Za = 1040$ Å. This value is, with our experimental resolution, very close to the experimental value obtained from the vertical peaks, equal to 1300 Å, though indicating slight stretching. Our interpretation of the experimental scattering pattern is thus that of a simple three-armed tube that retains the tube characteristics, while being fully extended parallel to the flow, as sketched in Fig. 5.

Even though our proposed tube picture may be somewhat naive, it describes very well the properties of the experimental findings. We should admit that the tube model may not make much sense for a fully extended tube, since such a system no longer has entanglements. The studied polymer system has, however, been exposed to a stretching that is fast relative to typical relaxation mechanisms, and one may accept that the chains still have the memory of a virtual tube, within which they appear confined. Without the physical tube, however, it is not clear what will happen during relaxation from the extended configuration; whether the chain relaxation will still be dominated by a virtual tube, or at which stage a new tube can be defined.

A simple comparison would be that of a simple two-arm star-block copolymer, i.e., a linear tri-block PSd-PS-PSd polymer. Exposed to a similar mechanical strain, we would predict that the resulting SANS pattern would be restricted to the two "vertical" scattering streaks. We are planning such experiments.

In summary, we have shown that three-armed star molecules of similar block copolymer arms behave in accordance with the random phase approximation of Gaussian chains in the relaxed state. Upon exposure to large extensional flows, the polymer arms change conformation to a highly stretched structure that mimics that of a fully extended three-armed tube model, with one arm in one direction and the two other arms in the opposite direction on the flow axis. The two arms pointing in the same direction are parallel and their associated tubes are right next to each other.

This work was funded from the Independent Research Fund Denmark, Technology and Production (DFF–4005-00112), and the Danish Research Infrastructure via DANSCATT (SFU–7055-00005B). Q. H. would like to acknowledge financial support from the Aage and Johanne Louis Hansen Foundation. The Paul Scherrer Institute and ANSTO are acknowledged for neutron beam time at, respectively, SANS-I and Quokka.

---

*kell@nbi.dk

[1] P. G. de Gennes, J. Chem. Phys. **55**, 572 (1971).
[2] M. Doi and S. F. Edwards, *The Theory of Polymer Dynamics* (Clarendon Press, Oxford, 1988).
[3] P. Schleger, B. Farago, C. Lartigue, A. Kollmar, and D. Richter, Phys. Rev. Lett. **81**, 124 (1998).
[4] V. G. Sakai, C. Alba-Simionesco, and S.-H. Chen, *Dynamics of Soft Matter, Neutron Applications* (Springer, New York, 2012).
[5] D. J. Read and T. C. B. McLeish, Phys. Rev. Lett. **79**, 87 (1997).
[6] A. E. Likhtman and T. C. B. McLeish, Macromolecules **35**, 6332 (2002).
[7] W. Pyckhout-Hintzen, S. Westermann, A. Wischnewski, M. Monkenbusch, D. Richter, E. Straube, B. Farago, and P. Lindner, Phys. Rev. Lett. **110**, 196002 (2013).
[8] Z. Wang *et al.*, Phys. Rev. X **7**, 031003 (2017).
[9] O. Hassager, K. Mortensen, A. Bach, K. Almdal, H. K. Rasmussen, and W. Pyckhout-Hintzen, Rheol. Acta **51**, 385 (2012).
[10] J. J. K. Kirkensgaard, L. Hengeller, A. Dorokhin, Q. Huang, C. J. Garvey, K. Almdal, O. Hassager, and K. Mortensen, Phys. Rev. E **94**, 020502(R) (2016).
[11] T. C. B. McLeish, Adv. Phys. **51**, 1379 (2002).
[12] G. S. Grest, L. J. Fetters, J. S. Huang, and D. Richter, *Star Polymers: Experiments, Theory, and Simulation*, Advances in Chemical Physics Vol. 94, edited by I. Prigogine and S. A. Rice (John Wiley & Sons, New York, 1996), ISBN 0-471-14324-3.
[13] A. Dondos, D. Papanagopoulos, P. G. de Gennes, and F. Brochard-Wyart, Macromol. Theory Simul. **8**, 147 (1999).
[14] X. Ye and T. Sridhar, Macromolecules **34**, 8270 (2001).
[15] D. Vlassopoulos, G. Fytas, T. Pakula, and J. Roovers, J. Phys. Condens. Matter **13**, R855 (2001).
[16] J. G. H. Cifre, R. Pamies, M. C. L. Martinez, and J. G. de la Torre, Polymer **46**, 6756 (2005).
[17] M. Ripoll, R. G. Winkler, and G. Gompper, Phys. Rev. Lett. **96**, 188302 (2006).
[18] N. H. Aloorkar, A. S. Kulkarni, R. A. Patil, and D. J. Ingale, Int. J. Pharm. Sci. Nanotechnol. **5**, 1675 (2012).
[19] X. Xu and J. Chen, J. Chem. Phys. **144**, 244905 (2016).
[20] Q. Huang, S. Agostini, L. Hengeller, M. Shivokhin, N. J. Alvarez, L. R. Hutchings, and O. Hassager, Macromolecules **49**, 6694 (2016).
[21] G. Ianniruberto and G. Marrucci, Macromolecules **46**, 267 (2013).
[22] A. Dorokhin, Entangled Polymer Melts in Extensional Flow. Synthesis, Rheology, Neutron Scattering, PhD Thesis, Technical University of Denmark, 2017.
[23] L. J. Fetters, D. J. Lohsey, and R. H. Colby, *Physical Properties of Polymers Handbook*, edited by J. E. Mark, 2nd ed. (Springer, New York, 2007), Vol. 3, pg. 25, ISBN 978-0-387-31235-4.
[24] L. Hengeller, Q. Huang, A. Dorokhin, K. Almdal, N. J. Alvarez, and O. Hassager, Rheol. Acta **55**, 303 (2016).
[25] NIST Center for Neutron Research, Neutron Scattering Lengths (2018), https://www.ncnr.nist.gov/resources/n-lengths/.
[26] L. Leibler, Macromolecules **13**, 1602 (1980).
[27] M. Doi, *Introduction to Polymer Physics* (Clarendon Press, Oxford, 1996), ISBN 198517726.
[28] M. O. de la Cruz and I. C. Sanchez, Macromolecules **19**, 2501 (1986).
[29] M. Guenza and A. Perico, Macromolecules **26**, 4196 (1993).
[30] M. Watzlawek, H. Löwen, and C. Likos, J. Phys. Condens. Matter **10**, 8189 (1998).
[31] A. Borger *et al.* (unpublished).
[32] M. Heinrich, W. Pyckhout-Hintzen, J. Allgaier, D. Richter, E. Straube, D. J. Read, T. C. B. McLeish, D. J. Groves, R. J. Blackwell, and A. Wiedenmann, Macromolecules **35**, 6650 (2002).
[33] J. D. Londono, A. H. Narten, G. D. Wignall, K. G. Honnell, E. T. Hsieh, T. W. Johnson, and F. S. Bates, Macromolecules **27**, 2864 (1994).

B.2 Chain retraction during polymer relaxation confirmed using spherical harmonics expansion of small angle neutron scattering data

The manuscript presents our findings on chain retraction during the relaxation of linear polymer chains after deformation using the spherical harmonics expansion framework recently proposed for analysis of 2D scattering patterns from uniaxially deformed polymer melts.

Abstract

Small-angle neutron scattering data on stretched polymer melt shows unambiguous chain retraction immediately after large uniaxial stretching. The sample was a linear polystyrene melt of 90 % 95 kg/mewl and 10 % 80 kg/mol deuterium-labeled chains exposed to a macroscopic stretch ratio of 20 resulting in a chain stretch ratio of about 4. The 2D small-angle neutron scattering data was analyzed using a spherical harmonics expansion that provides high sensitivity to polymer deformation. Our results and conclusion differ from previous experiments performed by another group analyzed using the same method, but our results agree with recent computer simulations. The difference in conclusions is likely a matter of different polymer sizes and stretch ratios.

My contribution

I initiated the project and implemented the spherical harmonics expansion framework. I am the driving force in the analysis and interpretation and I wrote the manuscript draft.

Chain Retraction during polymer relaxation confirmed using Spherical Harmonics Expansion of Small Angle Neutron Scattering data

Anine Borger, Jacob JK Kirkensgaard, and Kell Mortensen
Niels Bohr Institute, University of Copenhagen

Qian Huang and Ole Hassager
Chemical Engineering, Technical University of Denmark

Kristoffer Almdal
Nanotech, Technical University of Denmark

Small-angle neutron scattering data on stretched polymer melt shows unambigous chain retraction immediately after large uniaxial stretching. The sample was a linear polystyrene melt of 90 % 95 kg/mol and 10 % 80 kg/mol deuterium-labeled chains exposed to a macroscopic stretch ratio of 20 resulting in a chain stretch ratio of about 4. The 2D small-angle neutron scattering data was analyzed using a spherical harmonics expansion that provides high sensitivity to polymer deformation. Our results and conclusion differ from previous experiments performed by another group analysed using the same method, but our results agree with recent computer simulations. The difference in conclusions is likely a matter of different polymer sizes and stretch ratios.

The validity of the tube model [1] for non-linear rheology has been discussed for decades and was recently reapproached by Wang et al. [2] and Hsu and Kremer [3]. Wang et al. proposed a new analysis method for 2D small-angle scattering data from uniaxially extended polymer melts expanding the data in spherical harmonics. From the Doi-Edwards tube model and the GLaMM-model they predicted the signature of chain retraction in the spherical harmonics expansion, but in their subsequent analysis of data from a polystyrene melt the signature was absent. Therefore they concluded that either chain retraction does not occur or other nonlinear effects, not yet included in the tube model, screen chain retraction. However numerical studies of Hsu and Kremer showed that the predicted signature of chain retraction should occur, but also that its significance increases with increasing molecular stretching. In this paper we show experimentally that the predicted signature of chain retraction in the spherical harmonics expansion do occur for chains of $M_w = 80$ kg/mol under a macroscopic stretch ratio of about 20 and a resulting molecular stretch ratio of about 4.

Chain retraction during relaxation after a sufficiently rapid deformation means that the molecule initially shrinks in all dimensions and is a consequence of the decoupled orientation and stretching relaxation in the tube model. If the deformation of a polymer chain is fast enough compared to the chain relaxation dynamics, the chain will be both oriented and stretched by the deformation. To return to its equilibrium conformation, it thus has to relax both orientation and extension, and from the tube model it follows that the two relaxations are decoupled in time such that the molecular stretch relaxes on a short time scale, τ_R, in a Rouse-like manner and the chain orientation relaxes on a much longer time scale, τ_d, through reptation into a new tube. The reptation time scales as $\tau_d \approx 3Z\tau_R$ where Z is the number of entanglements so the decoupling is more significant for longer chains. The decoupling of the two relaxation modes leads to chain retraction where the molecule during the initial relaxation $t \lesssim \tau_R$ after deformation will to first approximation preserve its orientation, but shrink in all dimensions.

Doi and Edwards proposed to test the chain retraction hypothesis by by extracting the elements of the radius of gyration tensor corresponding to parallel, $R_{g\parallel}$, and perpendicular, $R_{g\perp}$, to the stretch direction from small angle scattering experiments.[1] If chain retraction occurs, all elements of the radius of gyration tensor will shrink during the Rouse-like relaxation. For $R_{g\perp}$ in particular this means that it will initially shrink before it increases to the equilibrium value. This has been attempted in several experiments and some see a non-monotonic increase in $R_{g\perp}(t)$[4, 5] whereas others do not.[6] The absence of signs of chain retraction in the latter experiments is explained by too short molecules or too larger polydispersity[6]. Other experiment report that including chain retraction in the model is needed to fit data.[7, 8]

Based on the differing conclusions in the previous experimental work, a new model-free approach more sensitive to changes polymer deformation is needed to test the chain hypothesis. The recent, detailed work of Wang et al. [2] offers a comprehensive and model free framework for analyzing anistropic 2D scattering data from uniaxially extended polymer melts using a spherical harmonics expansion. Their framework combines and refines earlier work using expansion techniques. The spherical harmonics expansion could be more suitable for testing the chain retraction hypothesis than radius of gyration analysis because it is sensitive to the overall chain length and the separation of the isotropic from the anisotropic contributions to the pattern increases the sensitivity to polymer deformation.

We use the spherical harmonics expansion on SANS data for polystyrene samples stretched using a filament stretch rheometer to test the chain retraction hypothesis. Our samples are melts of 10 wt-% of M_w = 80 kg/mol fully deuterated polystyrene with a polydispersity index of PDI=1.02 and 90 wt-% of M_w = 95 kg/mol hydrogenated polystyrene with PDI=1.07. The samples were previously studied and described in ref. [9, 10]. Both the 95 kg/mol hydrogenated PS and the 80 kg/mol deuterated PS were synthesized through anionic polymerisation as described in [9]. The calculated chain Rouse time for the deuterated component is $\tau_R^d = 15$ s and for the hydrogenated component $\tau_R^h = 20$ s for the hydrogenated component at $T = 130°$.

The filaments were stretched at elevated temperatures and allowed to relaxation a certain time after deformation before the rapidly cooled below the glass transition temperature to preserve the molecular conformation. The filaments where stretch on the commercial filament stretch rheometer VADER-1000, Rheo Filament ApS. The instrument consists of two plates and a laser in an oven. The bottom plate is connected to a force transducer and the top plate to a motor that allows for vertical motion. The laser tracks the diameter of the mid-filament, and the oven allows for controlled, elevated temperatures. We describe the deformation in terms of macroscopic stretch ratio λ_m and Hencky strain ϵ:

$$\lambda_m = \frac{L(t)}{L(0)} = \left(\frac{R(0)}{R(t)}\right)^2 \tag{1}$$

$$\epsilon(t) = \ln(\lambda_m) \tag{2}$$

where $L(t)$ is the length of the central part of the filament pre-stretched to an approximately cylindrical shape, and $R(t)$ is the radius of the filament both as a function of time t. Due to the non-perfect cylindrical shape, the filament radius provides a better measure of the mid-plane strain than the filament mid-segment length. A feed-back mechanism that allows for controlled deformation and relaxation has been implemented [11]. We stretched the samples at a constant Hencky strain rate of $\dot{\epsilon} = 0.1 s^{-1}$ at a temperature of $T = 130°$C up to a final Hencky strain $\epsilon = 3$ where steady flow is obtained [9], and allowed to relax under constant Hencky strain for 0, 10, 20, 80, and 320 s approximately corresponding to $0{\cdot}\tau_R^d$, $0.7 \cdot\tau_R^d$, $1.3{\cdot}\tau_R^d$, $5.3{\cdot}\tau_R^d$, and $21.3{\cdot}\tau_R^d$ before they were rapidly cooled below the glass transition temperature to preserve the molecular conformation as described in refs. [9, 10]. If the experimental parameters are such that the deformation is faster than the Rouse relaxation of the chains i. e. the deformation rate $\dot{\epsilon} = 0.1$ s^{-1} is larger than the inverse of the relaxation time $1/\tau_R^d = 0.15$ s^{-1} or the Rouse Weissenberg number $Wi_R = \dot{\epsilon}\tau_R > 1$ [12], we expect the chains to stretch during deformation. In our experiment $Wi_R = 1.5$.

For neutron scattering, the samples consisted of several aligned, quenched filaments attached to a Cadmium-ring. The SANS data was measured on QUOKKA at the Australian Nuclear Science and Technology Organisation. We include data from two detector settings with a sample detector distance of 14 m and 5 m respectively and a wavelength of 5 Å in our analysis. The data from the 5 m setting is previously published in [10]. The data was reduced by subtracting a blocked beam measurement and an estimate of the incoherent scattering intensity by assuming a constant incoherent background and Gaussian coil statistics. The data taken at $45 \pm 10°$ relative to the stretching direction for each sample was averaged, and the data fulfilling $qR_{g0} > 2.75$ was fitted to $I(q) = aq^{-2} + b$. Here $R_{g0} = 78.2$ Å [10] is the equilibrium radius of gyration and q the scattering vector. Before subtracting the incoherent background, b, the data sets were arbitrarily scaled to $b = 1$ to account for varying material amounts across samples. As can be seen in Fig. 1 the scattering patterns change from highly anisotropic, extending in the direction perpendicular to stretching, to isotropic as a function of relaxation time. Unfortunately, the scattering patterns have a cross-shaped contribution at very small q, most clear in the sample relaxed for 80 s. Fully understanding this part of the scattering pattern is ongoing work, but we are confident that the additional scattering at low q originates from cracks developed during the preparation of the filaments and thus has no relation to the polymer conformation. We therefore exclude the data corresponding to the smallest q-values as marked by rings in Fig. 1 from the spherical harmonics analysis.

The data is analyzed using the spherical harmonics expansion approach explained in detail in [2]. In the following we focus on our implementation and therefore only state the most essential equations from ref. [2]. The structure factor can be decomposed in an orthogonal basis of spherical harmonics $Y_l^m(\theta)$ with even l and $m = 0$ due to the symmetry of uniaxial extension:

$$S(\vec{q}) = \sum_{l,\text{even}}^{\infty} S_l^0(q) Y_l^0(\theta) \tag{3}$$

$$Y_l^0(\theta) = \sqrt{2l+1} P_l^0(\cos\theta) \tag{4}$$

where $S_l^0(q)$ are expansion coefficients, $P_l^0(x)$ are associated Legendre polynomials, and θ is the polar angle in the spherical coordinates and relates to data as defined in Fig. 1a, i.e. the scattering angle is 2ϑ, and the scattering vector magnitude is therefore defined as $q = 4\pi/\lambda \sin\vartheta$. The coherent scattering intensity is then proportional to the $q_y = 0$ cross section of the structure factor, $I_{\text{coh}}(\vec{q}) \propto S(q_x, q_y = 0, q_z)$, see Fig. 1a. By expanding $I_coh(\vec{q})$ in spherical harmonics , the isotropic and anisotropic contributions to the scattering pattern are separated. We implemented the spherical harmonics expansion by averaging the data in narrow q and θ intervals with $\Delta q = 0.001$Å^{-1} and $\Delta\theta = 5°$. For each q-interval, $I_{\text{coh}}(\theta)$ is fitted to eq. 3 truncated at $l = 8$ by minimizing the χ^2. The data can now be represented in terms of the q-dependent expansion coefficients $S_l^0(q)$.

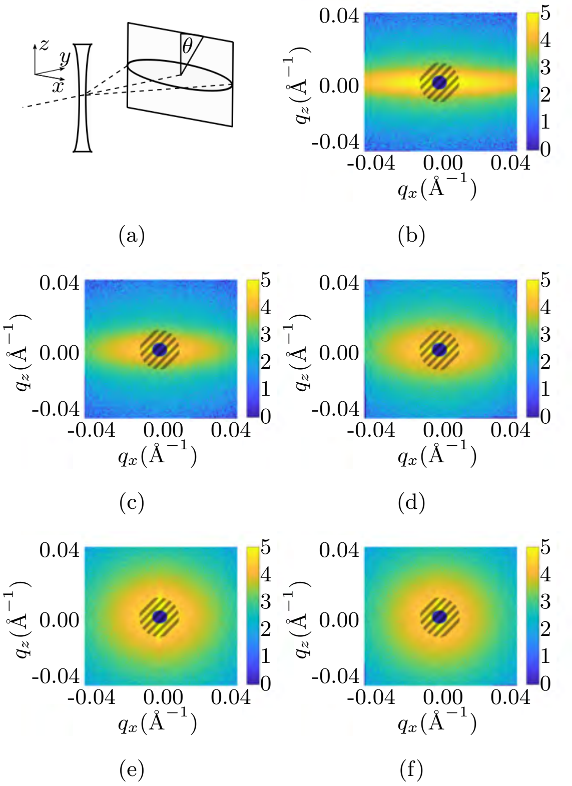

(a) (b)

(c) (d)

(e) (f)

FIG. 1: 2D SANS data on uniaxially extended polystyrene. The stretching direction and polar angle θ are defined in a). Subfigure b)-f) show data for relaxation time of $0{\cdot}\tau_R^d$, $0.7\cdot\tau_R^d$, $1.3{\cdot}\tau_R^d$, $5.3{\cdot}\tau_R^d$, and $21.3{\cdot}\tau_R^d$ all measured with a sample-detector distance of 14 m and wavelength 5 Å on QUOKKA at ANSTO.

To look for signs of chain retraction, we plot the expansion coefficient of the leading anisotropic component, $S_2^0(q)$ for all samples, see Fig.2. The center of the dip is to first approximation a measure of the overall chain length and only weakly dependent on anisotropy while the amplitude is highly dependent on the degree of anisotropy. Thus if chain retraction occurs, the center of the dip should shift to larger q during $t \lesssim \tau_R$[2] to reflect the molecule shrinking while preserving its orientation as mentioned above. From Fig. 2 it is evident that the dip shifts towards larger q during $t \lesssim \tau_R^d$ even though the exact location of the minimum for $t = 0 \cdot \tau_R^d$ is hard to determine due to the limited data at small q. We also observe that $S_2^0(q)$ relaxes quite fast. After $5.3 \cdot \tau_R^d$ the amplitude of $S_2^0(q)$ is very small, even though the reptation time is approximately $\tau_d \approx 8 \cdot \tau_R^d$. The innermost data points should not be fully trusted since they do not follow the expected trend that $S_2^0(q) \to 0$ for $q \to 0$ due to the additional scattering at small q. We assign the the dip shift to chain retraction.

Next we compare the magnitude of the dip shift to quantitative predictions on the tube model to determine how well the tube model captures the relaxation behaviour after extreme extension. The tube model predicts that the molecules deform affinely with the macroscopic stretch such that each bond vector u is transformed as $\tilde{u} = E \cdot u$ where E is the deformation matrix. For a uniaxial extension with stretch ratio of λ along the third coordinate we obtain

$$E = \begin{pmatrix} 1/\sqrt{\lambda} & 0 & 0 \\ 0 & 1/\sqrt{\lambda} & 0 \\ 0 & 0 & \lambda \end{pmatrix}. \tag{5}$$

We denote the stretch ratio λ here to prepare for a distinction between the macroscopic stretch ratio λ_m and the molecular stretch ratio λ motivated by the discussion below. The deformation λ will lead to an elliptical scattering pattern that can be modeled by a modified Debye function such that

$$\begin{aligned} S(\vec{q}) &= \frac{2}{x^2}\left(e^{-x} + x - 1\right) \\ x &= (q_\parallel R_{g\parallel})^2 + (q_\perp R_{g\perp})^2 \end{aligned} \tag{6}$$

where $R_{g\parallel} = \lambda R_{g0}$ and $R_{g\parallel} = 1/\sqrt{\lambda} R_{g0}$.

During Rouse relaxation the dip shifts to large values of q because all the bond vectors shrink isotropically by a factor of $\langle |E \cdot u| \rangle_0$[1]. As a consequence the ratio of the q-coordinates of the minima, q^*, will have the following relation: $q^*_{\text{R-relaxed}}/q^*_{t=0} = \sqrt{\langle |E \cdot u| \rangle_0}$ where the subscript R-relaxed means after full Rouse relaxation. As a function of λ using the deformation matrix in eq. 5 we find

$$\langle |E \cdot u| \rangle_0 = 1/2\left[\lambda + 1/\sqrt{\lambda^4 - \lambda}\ln\left(\sqrt{\lambda^3 - 1} + \sqrt{\lambda^3}\right)\right]. \tag{7}$$

Now we determine the dip shift in the experimental data and compare it to the theoretical expectations. The experimental data suggests a minimum in $S_2^0(q)$ for $t = 0\tau_R^d$ at $q^*_{t=0\tau_R^d} \le 0.011$ Å^{-1} given the data limit. We assume $q^*_{t=1.3\tau_R^d} \approx q^*_{\text{R-relaxed}}$ since the data set for $t = 5.3\tau_R^d$ is so affected by the cross-shaped scattering at small q. For $t = 1.3\tau_R^d$ we find $q^*_{t=1.3\tau_R^d} = (0.018 \pm 0.003)$ Å^{-1} where the uncertainty is due to the broad minimum of the curve, see fig. 2. These numbers give rise to a ratio of $q^*_{t=1.3\tau_R^d}/q^*_{t=0} = 1.4 - 1.9$ using the upper limit for $q^*_{t=0\tau_R^d}$ and $q^*_{t=1.3\tau_R^d} = (0.018 \pm 0.003)$ Å^{-1}. To compare to the theoretical predictions we need to firstly determine λ. As mentioned above the original Doi Edwards theory predicts that the molecules deform affinely with the macroscopic stretch ratio such that $\lambda_m = \lambda$. However, in later theoretical and experimental work it is proposed that the relation is non-affine [13–16]. In our experiment we even stretch until steady state where we assume that the molecular stretch is no longer affected by the macroscopic stretch. So to determine λ we therefore fit the data set corresponding to the smallest q values (14 m with the same exclusion of small q as above) for $t = 0 \cdot \tau_R^d$ to the modified Debye function, eq. 6, in a least squares sense including two free parameters: λ and an overall scaling factor to account for e.g. sample volume. We obtain an effective extension ratio for the chains $\lambda = 3.4$. However, the modified Debye function fitted to data shows minor but systematic deviations, and we therefore consider the found value of λ approximate. The mid-range q data (5m) was previously analyzed using the more advanced Warner-Edwards model in ref. [10] and that analysis lead to $\lambda = 4.2$. In the following we therefore compare experimental data to the theoretical expectations using both values of λ.

We determine the theoretical minimum $S_2^0(q)$ at $t = 0 \cdot \tau_R^d$ by expanding the modified Debye function of $\lambda = 3.4$ and $\lambda = 4.2$ respectively in spherical harmonics the same way as for the experimental data. The found minima are $q = 0.012\text{Å}^{-1}$ for $\lambda = 3.4$ and $q = 0.011\text{Å}^{-1}$ for $\lambda = 4.2$. The ratio $q^*_{R-relaxed}/q^*_{t=0}$ is determined by calculating $\sqrt{\langle|E(\lambda \cdot u|\rangle_0}$ for both values of λ. For $\lambda = 3.4$ we obtain $\sqrt{\langle|E(\lambda \cdot u|\rangle_0}$=1.3 and for $\lambda = 4.2$ we obtain $\sqrt{\langle|E(\lambda \cdot u|\rangle_0}$ =1.5. Both $q^*_{t=0\tau_R^d}$ and the ratio are more consistent with $\lambda = 4.2$ found using the Warner Edwards model than with $\lambda = 3.4$ though both ratios are low compared to the interval calculated from the data. However, the low ratios are most likely due to an overestimate of $q^*_{t=0\tau_R^d}$, but the assumption $q^*_{t=1.3\tau_R^d} \approx q^*_{\text{R-relaxed}}$ will also lead to a smaller ratio since $q^*_{t=1.3\tau_R^d} \leq q^*_{\text{R-relaxed}}$. The theoretical expectation from the description of the relaxation in the Doi Edwards tube model is consistent with the experimental data provided that the molecular stretch ratio is allowed to deviate from the macroscopic stretch ratio, i.e. the microscopic strain coupling is non-affine.

We have now analyzed our data using the spherical harmonics framework of Wang et al. and concluded that chain retraction occurs. This is a remarkable conclusion since Wang et al. used the same framework to look for chain retraction in a melt of much longer chains, but did not see it. We believe that the difference in conclusion is due to variations in the macroscopic stretch procedure, or the resulting molecular stretch factor λ.

Wang et al. performed a thorough analysis of experimental data on well-entangled polystyrene, $M_w = 510$ kg/mol, uniaxially extended to a final stretch ratio of $\lambda_m = 1.8$ using an RSA-G2 Solids Analyzer from TA Instruments at a temperature of $T = 130°\text{C}$ with constant crosshead velocity of $v = 40L(0)/\tau_R$ and thus constant stretch ratio rate and varying $\dot{\epsilon}$. Their stretch parameters and choice of chain length is such that they stretch at a Rouse Weissenberg number Wi_R of initially 40 and above 20 in the end of the experiment so as explained above, the chains are expected to stretch during the experiment. In our experiment $Wi_R = 1.5$ so more than a factor of 10 lower, but our macroscopic stretch ratio λ_m is more than a factor 10 larger.

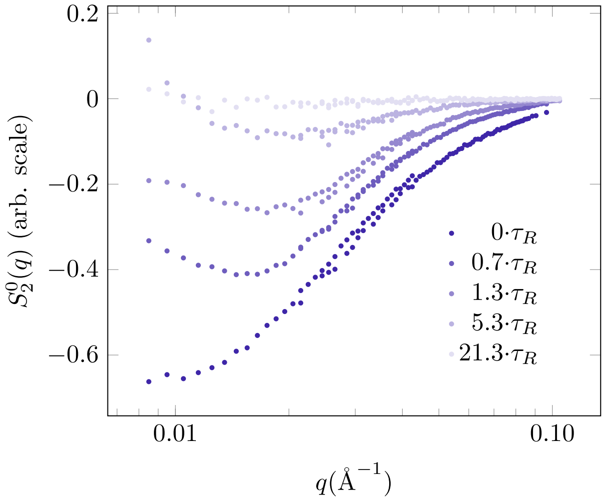

FIG. 2: Expansion coefficient of the leading anisotropic component $S_2^0(q)$ as function of scattering vector magnitude q during relaxation after uniaxial extension.

The findings of Wang et al. were supported by a non-equilibrium molecular dynamics simulation by Xu et al. [17] with parameters comparable to those in the experiment in Wang et al. [2]. They too reach the conclusion that the signature of chain retraction is absent. However, Hsu and Kremer performed a molecular dynamics simulation [3] covering a larger part of parameter space than the present and previous experiments and simulation. They do in fact see the signature of chain retraction in the spherical harmonics expansion for certain parameters. The simulation both shows that the dip in $S_2^0(q)$ at $t = 0$ increases for larger molecular stretch ratios and that the GLaMM-model [18], with which Wang et al. make quantitative predictions of the time evolution of $S_2^0(q)$, overestimates the dip shift magnitude during relaxation more severely for longer molecules. Potentially Wang et al. could have seen a dip shift for their system if they had stretched to larger values of λ_m. Hsu and Kremer suggest that there are other not yet understood relaxation modes in the nonlinear regime as an explanation for the overestimation.

We would also like to point out that it is remarkable how well the tube model captures the behaviour of our data when we consider that our chains are relatively short with a number of entanglements $Z \approx 5 - 6$ and that the Doi-Edwards tube model describes $Z \to \infty$ chains and therefore in general captures the behaviour better with increasing Z.

I. CONCLUSION

In conclusion, we shown chain retraction during polymer relaxation with the spherical harmonics expansion method to analyze anisotropic 2D small angle neutron scattering data from uniaxially deformed polymer samples proposed by Wang et al.. This is remarkable since the chain retraction hypothesis Most likely, the opposing conclusions originate from the differences in chain lengths and molecular stretch ratios between the two experiments. This interpretation is supported by a molecular dynamics simulation by Hsu and Kremer that further shows that the GLaMM-model overestimates the dip shift increasingly with increasing chain length. Our observation of the chain retraction signature in the spherical harmonics expasion viewed in relation to the work of Wang et al. and Hsao and Kremer, indicate that there may be other relaxation mechanisms at play than those already understood.

We thank ANSTO for beamtime, DanScatt and Danish Council for Independent Research for funding, Andriy Dorokhin for polymer synthesis and Ludovica Hengeller for rheological experiments and sample preparation.

---

[1] M. Doi and S. F. Edwards, J. Chem. Soc., Faraday Trans. 2 **74**, 1802 (1978).

[2] Z. Wang, C. N. Lam, W.-R. Chen, W. Wang, J. Liu, Y. Liu, L. Porcar, C. B. Stanley, Z. Zhao, K. Hong, and Y. Wang, Phys. Rev. X **7**, 031003 (2017).

[3] H.-P. Hsu and K. Kremer, Phys. Rev. Lett. **121**, 167801 (2018).

[4] K. Mortensen, O. Kramer, W. Batsberg, and L. J. Fetters, MRS Proceedings **79**, 259 (1986).

[5] A. Blanchard, R. S. Graham, M. Heinrich, W. Pyckhout-Hintzen, D. Richter, A. E. Likhtman, T. C. B. McLeish, D. J. Read, E. Straube, and J. Kohlbrecher, Phys. Rev. Lett. **95**, 166001 (2005).

[6] G. J. R. B. F. Boue, M Nierlich, JOURNAL DE PHYSIQUE **43**, 137 (1982).

[7] J. Bent, L. R. Hutchings, R. W. Richards, T. Gough, R. Spares, P. D. Coates, I. Grillo, O. G. Harlen, D. J. Read, R. S. Graham, A. E. Likhtman, D. J. Groves, T. M. Nicholson, and T. C. B. McLeish, Science **301**, 1691 (2003), http://science.sciencemag.org/content/301/5640/1691.full.pdf.

[8] R. S. Graham, J. Bent, L. R. Hutchings, R. W. Richards, D. J. Groves, J. Embery, T. M. Nicholson, T. C. B. McLeish, A. E. Likhtman, O. G. Harlen, D. J. Read, T. Gough, R. Spares, P. D. Coates, and I. Grillo, Macromolecules **39**, 2700 (2006), https://doi.org/10.1021/ma052357z.

[9] L. Hengeller, Q. Huang, A. Dorokhin, N. Alvarez, K. Almdal, and O. Hassager, Rheologica Acta **55**, 303 (2016).

[10] J. J. K. Kirkensgaard, L. Hengeller, A. Dorokhin, Q. Huang, C. J. Garvey, K. Almdal, O. Hassager, and K. Mortensen, Phys. Rev. E **94**, 020502 (2016).

[11] J. M. R. Marn, J. K. Huusom, N. J. Alvarez, Q. Huang, H. K. Rasmussen, A. Bach, A. L. Skov, and O. Hassager, Journal of Non-Newtonian Fluid Mechanics **194**, 14 (2013).

[12] J. Dealy, Rheol. Bull. **79**, 14 (2010).

[13] G. Heinrich and E. Straube, Polymer Bulletin **17**, 255 (1987).

[14] M. Rubinstein and S. Panyukov, Macromolecules **30**, 8036 (1997), https://doi.org/10.1021/ma970364k.

[15] D. J. Read and T. C. B. McLeish, Macromolecules **30**, 6376 (1997), https://doi.org/10.1021/ma970571k.

[16] W. Pyckhout-Hintzen, S. Westermann, A. Wischnewski, M. Monkenbusch, D. Richter, E. Straube, B. Farago, and P. Lindner, Phys. Rev. Lett. **110**, 196002 (2013).

[17] W.-S. Xu, J.-M. Y. Carrillo, C. N. Lam, B. G. Sumpter, and Y. Wang, ACS Macro Letters **7**, 190 (2018), https://doi.org/10.1021/acsmacrolett.7b00900.

[18] R. S. Graham, A. E. Likhtman, T. C. B. McLeish, and S. T. Milner, Journal of Rheology **47**, 1171 (2003), https://doi.org/10.1122/1.1595099.

Bibliography

[1] Anders Bach, Kristoffer Almdal, Henrik Koblitz Rasmussen, and Ole Hassager. Elongational viscosity of narrow molar mass distribution polystyrene. *Macromolecules*, 36(14):5174–5179, 2003.

[2] Nicolas Javier Alvarez and Ole Hassager. Scanning rheometer, 10 2015. WO2015144806; G01N 13/ 02 A I.

[3] Jens Kromann Nielsen, Henrik Koblitz Rasmussen, Ole Hassager, and Gareth H. McKinley. Elongational viscosity of monodisperse and bidisperse polystyrene melts. *Journal of Rheology*, 50(4):453–476, 2006.

[4] Jens Kromann Nielsen, Henrik Koblitz Rasmussen, Martin Denberg, Kristoffer Almdal, and Ole Hassager. Nonlinear branch-point dynamics of multiarm polystyrene. *Macromolecules*, 39(25):8844–8853, 2006.

[5] Jens Kromann Nielsen and Henrik Koblitz Rasmussen. Reversed extension flow. *Journal of Non-Newtonian Fluid Mechanics*, 155(1):15 – 19, 2008.

[6] Qian Huang, Henrik K. Rasmussen, Anne Ladegaard Skov, and Ole Hassager. Stress relaxation and reversed flow of low-density polyethylene melts following uniaxial extension. *Journal of Rheology*, 56(6):1535–1554, 2012.

[7] Qian Huang, Serena Agostini, Ludovica Hengeller, Maksim Shivokhin, Nicolas J. Alvarez, Lian R. Hutchings, and Ole Hassager. Dynamics of star polymers in fast extensional flow and stress relaxation. *Macromolecules*, 49(17):6694–6699, 2016.

[8] Ludovica Hengeller, Qian Huang, Andriy Dorokhin, Nicolas J. Alvarez, Kristoffer Almdal, and Ole Hassager. Stress relaxation of bidisperse polystyrene melts: Exploring the interactions between long

and short chains in non-linear rheology. *Rheologica Acta*, 55(4):303–314, 2016.

[9] Ole Hassager, Kell Mortensen, Anders Bach, Kristoffer Almdal, Henrik K. Rasmussen, and Wim Pyckhout-Hintzen. Stress and neutron scattering measurements on linear polymer melts undergoing steady elongational flow. *Rheologica Acta*, 51(5):385–394, 2012.

[10] Jacob J. K. Kirkensgaard, Ludovica Hengeller, Andriy Dorokhin, Qian Huang, Christopher J. Garvey, Kristoffer Almdal, Ole Hassager, and Kell Mortensen. Nematic effects and strain coupling in entangled polymer melts under strong flow. *Phys. Rev. E*, 94:020502, Aug 2016.

[11] M. Rubinstein and R. Colby. *Polymer Physics*. Oxford University Press, 2003.

[12] M. Doi. *Introduction to Polymer Physics*. Oxford University Press, 2006.

[13] M.C. Sobieraj and C.M. Rimnac. Ultra high molecular weight polyethylene: Mechanics, morphology, and clinical behavior. *Journal of the Mechanical Behavior of Biomedical Materials*, 2(5):433 – 443, 2009.

[14] P. G. de Gennes. Reptation of a polymer chain in the presence of fixed obstacles. *The Journal of Chemical Physics*, 55(2):572–579, 1971.

[15] Masao Doi and S. F. Edwards. Dynamics of concentrated polymer systems. part 1.—brownian motion in the equilibrium state. *J. Chem. Soc., Faraday Trans. 2*, 74:1789–1801, 1978.

[16] Masao Doi and S. F. Edwards. Dynamics of concentrated polymer systems. part 2.—molecular motion under flow. *J. Chem. Soc., Faraday Trans. 2*, 74:1802–1817, 1978.

[17] Masao Doi and S. F. Edwards. Dynamics of concentrated polymer systems. part 3.—the constitutive equation. *J. Chem. Soc., Faraday Trans. 2*, 74:1818–1832, 1978.

[18] Richard S. Graham, Alexei E. Likhtman, Tom C. B. McLeish, and Scott T. Milner. Microscopic theory of linear, entangled polymer chains under rapid deformation including chain stretch and convective constraint release. *Journal of Rheology*, 47(5):1171–1200, 2003.

[19] G Marrucci. Dynamics of entanglements: A nonlinear model consistent with the cox-merz rule. *Journal of Non-Newtonian Fluid Mechanics*, 62(2):279 – 289, 1996.

[20] Masao Doi. Explanation for the 3.4 power law of viscosity of polymeric liquids on the basis of the tube model. *Journal of Polymer Science: Polymer Letters Edition*, 19(5):265–273, 1981.

[21] Alexei E. Likhtman and Tom C. B. McLeish. Quantitative theory for linear dynamics of linear entangled polymers. *Macromolecules*, 35(16):6332–6343, 2002.

[22] Zhe Wang, Christopher N. Lam, Wei-Ren Chen, Weiyu Wang, Jianning Liu, Yun Liu, Lionel Porcar, Christopher B. Stanley, Zhichen Zhao, Kunlun Hong, and Yangyang Wang. Fingerprinting molecular relaxation in deformed polymers. *Phys. Rev. X*, 7:031003, Jul 2017.

[23] B. Lautrup. *Physics of Continous Matter, 2nd ed.* CRC Press, 2011.

[24] Polymer technology notes dtu course 28213, 2016.

[25] R J Poole. The deborah and weissenberg numbers. *Rheology Bulletin*, 2012.

[26] Peter Szabo. Transient filament stretching rheometer. *Rheologica Acta*, 36(3):277–284, May 1997.

[27] Henrik K. Rasmussen, Anca Gabriela Bejenariu, Ole Hassager, and D. Auhl. Experimental evaluation of the pure configurational stress assumption in the flow dynamics of entangled polymer melts. *Journal of Rheology*, 54(6):1325–1336, 2010.

[28] G. L. Squires. *Introduction to the theory of thermal neutron scattering*. Cambridge University Press, 1978.

[29] Des McMorrow Jens Als-Nielsen. *Elements of Modern X-ray Physics*. John Wiley & Sons Ltd., 2011.

[30] Julia A. Kornfield, Gerald G. Fuller, and Dale S. Pearson. Infrared dichroism measurements of molecular relaxation in binary blend melt rheology. *Macromolecules*, 22(3):1334–1345, 1989.

[31] M. H. Wagner, S. Kheirandish, K. Koyama, A. Nishioka, A. Minegishi, and T. Takahashi. Modeling strain hardening of polydisperse polystyrene melts by molecular stress function theory. *Rheologica Acta*, 44(3):235–243, Jan 2005.

[32] Dietmar Auhl, Pierre Chambon, Tom C. B. McLeish, and Daniel J. Read. Elongational flow of blends of long and short polymers: Effective stretch relaxation time. *Phys. Rev. Lett.*, 103:136001, Sep 2009.

[33] Jean Francois Tassin, Anne Baschwitz, Jean Yves Moise, and Lucien Monnerie. Relaxation of binary blends of long and short chains: evidence for orientational coupling. *Macromolecules*, 23(6):1879–1881, 1990.

[34] C. Hayes, L. Bokobza, F. Boué, E. Mendes, and L. Monnerie. Relaxation dynamics in bimodal polystyrene melts: A fourier-transform infrared dichroism and small-angle neutron scattering study. *Macromolecules*, 29(14):5036–5041, 1996.

[35] Masao Doi, Dale Pearson, Julie Kornfield, and Gerry Fuller. Effect of nematic interaction in the orientational relaxation of polymer melts. *Macromolecules*, 22(3):1488–1490, 1989.

[36] Jean-Pierre Jarry and Lucien Monnerie. Effects of a nematic-like interaction in rubber elasticity theory. *Macromolecules*, 12(2):316–320, 1979.

[37] D. J. Read and T. C. B. McLeish. Microscopic theory for the "lozenge" contour plots in scattering from stretched polymer networks. *Macromolecules*, 30(20):6376–6384, 1997.

[38] E. Straube, V. Urban, W. Pyckhout-Hintzen, D. Richter, and C. J. Glinka. Small-angle neutron scattering investigation of topological constraints and tube deformation in networks. *Phys. Rev. Lett.*, 74:4464–4467, May 1995.

[39] Michael Rubinstein and Sergei Panyukov. Nonaffine deformation and elasticity of polymer networks. *Macromolecules*, 30(25):8036–8044, 1997.

[40] G. Heinrich and E. Straube. Theoretical investigation of sans from elastomeric networks with topological constraints. *Polymer Bulletin*, 17(3):255–261, Mar 1987.

[41] J. R. Katz. X-ray spectrography of polymers and in particular those having a rubber-like extensibility. *Trans. Faraday Soc.*, 32:77–94, 1936.

[42] M. Hühnemörder. Röntgenographische studien an metastyrol. *Kautschuk*, pages 106–107, 1927.

[43] Chakravarthy Ayyagari, Dmitry Bedrov, and Grant D. Smith. Structure of atactic polystyrene: A molecular dynamics simulation study. *Macromolecules*, 33(16):6194–6199, 2000.

[44] V. A. Harmandaris, N. P. Adhikari, N. F. A. van der Vegt, and K. Kremer. Hierarchical modeling of polystyrene: From atomistic to coarse-grained simulations. *Macromolecules*, 39(19):6708–6719, 2006.

[45] Alexey V. Lyulin and M. A. J. Michels. Molecular dynamics simulation of bulk atactic polystyrene in the vicinity of tg. *Macromolecules*, 35(4):1463–1472, 2002.

[46] H. R. Schubach, E. Nagy, and B. Heise. Short range order of amorphous polymers derived by waxs. *Colloid and Polymer Science*, 259(8):789–796, Aug 1981.

[47] J. L. White and J. E. Spruiell. The specification of orientation and its development in polymer processing. *Polymer Engineering and Science*, 23, 1983.

[48] A. H. Winddle. X-ray scattering measurements of order in non-crystalline polymers. *Pure and Appl. Chem.*, 57:1627–1838, 1985.

[49] M. Pick, R. Lovell, and Winddle A. H. The specification of orientation and its development in polymer processing. *Polymer Engineering and Science*, 21, September 1980.

[50] D. Snétivy G. Vancso and I. Tomka. Structural changes during polystyrene orientation: A study of optical birefringende and wide angle x-ray scattering. *Polymer Engineering and Science*, 21, September 1980.

[51] Qian Huang, Olga Mednova, Henrik K. Rasmussen, Nicolas J. Alvarez, Anne L. Skov, Kristoffer Almdal, and Ole Hassager. Concentrated polymer solutions are different from melts: Role of entanglement molecular weight. *Macromolecules*, 46(12):5026–5035, 2013.

[52] Giovanni Ianniruberto and Giuseppe Marrucci. Entangled melts of branched ps behave like linear ps in the steady state of fast elongational flows. *Macromolecules*, 46(1):267–275, 2013.

[53] Kell Mortensen, Anine L. Borger, Jacob J. K. Kirkensgaard, Christopher J. Garvey, Kristoffer Almdal, Andriy Dorokhin, Qian Huang, and Ole Hassager. Structural studies of three-arm star block copolymers exposed to extreme stretch suggests a persistent polymer tube. *Phys. Rev. Lett.*, 120:207801, May 2018.

[54] M. Heinrich, W. Pyckhout-Hintzen, J. Allgaier, D. Richter, E. Straube, D. J. Read, T. C. B. McLeish, D. J. Groves, R. J. Blackwell, and A. Wiedenmann. Arm relaxation in deformed h-polymers in elongational flow by sans. *Macromolecules*, 35(17):6650–6664, 2002.

[55] T. C. B. McLeish and R. G. Larson. Molecular constitutive equations for a class of branched polymers: The pom-pom polymer. *Journal of Rheology*, 42(1):81–110, 1998.

[56] D. K. Bick and T. C. B. McLeish. Topological contributions to nonlinear elasticity in branched polymers. *Phys. Rev. Lett.*, 76:2587–2590, Apr 1996.

[57] T. C. B. McLeish, J. Allgaier, D. K. Bick, G. Bishko, P. Biswas, R. Blackwell, B. Blottière, N. Clarke, B. Gibbs, D. J. Groves, A. Hakiki, R. K. Heenan, J. M. Johnson, R. Kant, D. J. Read, and R. N. Young. Dynamics of entangled h-polymers: Theory, rheology, and neutron-scattering. *Macromolecules*, 32(20):6734–6758, 1999.

[58] M. Heinrich, W. Pyckhout-Hintzen, J. Allgaier, D. Richter, E. Straube, T. C. B. McLeish, A. Wiedenmann, R. J. Blackwell, and D. J. Read. Small-angle neutron scattering study of the relaxation of a melt of polybutadiene h-polymers following a large step strain. *Macromolecules*, 37(13):5054–5064, 2004.

[59] Sara Lindeblad Wingstrand, Martin van Drongelen, Kell Mortensen, Richard S. Graham, Qian Huang, and Ole Hassager. Influence of extensional stress overshoot on crystallization of ldpe. *Macromolecules*, 50(3):1134–1140, 2017.

[60] Sara L. Wingstrand, Ole Hassager, Daniele Parisi, Anine L. Borger, and Kell Mortensen. Flow induced crystallization prevents melt fracture of hdpe in uniaxial extensional flow. *Journal of Rheology*, 62(4):1051–1060, 2018.

[61] Ludwik Leibler. Theory of microphase separation in block copolymers. *Macromolecules*, 13(6):1602–1617, 1980.

[62] Andriy Dorokhin. *Entangled Polymer Melts in Extensional Flow*. PhD thesis, DTU Nanotech, Produktionstorvet, 423, 2800 Kongens Lyngby, Denmark, 7 2018.

[63] Frank S. Bates and Mark A. Hartney. Block copolymers near the microphase separation transition. 3. small-angle neutron scattering

study of the homogeneous melt state. *Macromolecules*, 18(12):2478–2486, 1985.

[64] C. Burger, W. Ruland, and A. N. Semenov. Polydispersity effects on the microphase-separation transition in block copolymers. *Macromolecules*, 23(13):3339–3346, 1990.

[65] F. Boue, M. Nierlich, G. Jannink, and R. Ball. Polymer coil relaxation in uniaxially strained polystyrene observed by small-angle neutron-scattering. *JOURNAL DE PHYSIQUE*, 43:137–148, 01 1982.

[66] Kell Mortensen, Ole Kramer, Walther Batsberg, and L. J. Fetters. Coil relaxation in uniaxially deformed polymer melt. *MRS Proceedings*, 79:259, 1986.

[67] A. Blanchard, R. S. Graham, M. Heinrich, W. Pyckhout-Hintzen, D. Richter, A. E. Likhtman, T. C. B. McLeish, D. J. Read, E. Straube, and J. Kohlbrecher. Small angle neutron scattering observation of chain retraction after a large step deformation. *Phys. Rev. Lett.*, 95:166001, Oct 2005.

[68] J. Bent, L. R. Hutchings, R. W. Richards, T. Gough, R. Spares, P. D. Coates, I. Grillo, O. G. Harlen, D. J. Read, R. S. Graham, A. E. Likhtman, D. J. Groves, T. M. Nicholson, and T. C. B. McLeish. Neutron-mapping polymer flow: Scattering, flow visualization, and molecular theory. *Science*, 301(5640):1691–1695, 2003.

[69] R. S. Graham, J. Bent, L. R. Hutchings, R. W. Richards, D. J. Groves, J. Embery, T. M. Nicholson, T. C. B. McLeish, A. E. Likhtman, O. G. Harlen, D. J. Read, T. Gough, R. Spares, P. D. Coates, and I. Grillo. Measuring and predicting the dynamics of linear monodisperse entangled polymers in rapid flow through an abrupt contraction. a small angle neutron scattering study. *Macromolecules*, 39(7):2700–2709, 2006.

[70] K.F. Riley, M. P. Hobson, and S. J. Bence. *Mathematical Methods for Physics and Engineering, third edition*. Cambridge University Press, 2006.

[71] Hsiao-Ping Hsu and Kurt Kremer. Chain retraction in highly entangled stretched polymer melts. *Phys. Rev. Lett.*, 121:167801, Oct 2018.

[72] Zhi-Yuan Wang, Dejia Kong, Lincan Yang, Hongwei Ma, Fengmei Su, Kanae Ito, Yun Liu, Xuewu Wang, and Zhe Wang. Analysis of small-angle neutron scattering spectra from deformed polymers with the spherical harmonic expansion method and a network model. *Macromolecules*, 51(21):9011–9018, 2018.

[73] W. Pyckhout-Hintzen, S. Westermann, A. Wischnewski, M. Monkenbusch, D. Richter, E. Straube, B. Farago, and P. Lindner. Direct observation of nonaffine tube deformation in strained polymer networks. *Phys. Rev. Lett.*, 110:196002, May 2013.

[74] Wen-Sheng Xu, Jan-Michael Y. Carrillo, Christopher N. Lam, Bobby G. Sumpter, and Yangyang Wang. Molecular dynamics investigation of the relaxation mechanism of entangled polymers after a large step deformation. *ACS Macro Letters*, 7(2):190–195, 2018.

[75] Christopher N. Lam, Wen-Sheng Xu, Wei-Ren Chen, Zhe Wang, Christopher B. Stanley, Jan-Michael Y. Carrillo, David Uhrig, Weiyu Wang, Kunlun Hong, Yun Liu, Lionel Porcar, Changwoo Do, Gregory S. Smith, Bobby G. Sumpter, and Yangyang Wang. Scaling behavior of anisotropy relaxation in deformed polymers. *Phys. Rev. Lett.*, 121:117801, Sep 2018.

[76] Elio Passaglia. Crazes and fracture in polymers. *Journal of Physics and Chemistry of Solids*, 48(11):1075 – 1100, 1987.